UNIVERSITA' DEGLI STUDI DI VERONA

DIPARTIMENTO DI BIOTECNOLOGIE

SCUOLA DI DOTTORATO IN SCIENZE DELLA VITA E DELLA SALUTE

DOTTORATO DI RICERCA IN
BIOTECNOLOGIE MOLECOLARI INDUSTRIALI E AMBIENTALI

CICLO
XXVII

Prokaryotic and eukaryotic expression systems for the production of recombinant proteins and nanoparticles for research and bio-industry

S.S.D. BIO/04

Coordinatore:
Ch.mo Prof. Roberto Bassi

Relatore:
Ch.mo Prof. Roberto Bassi

Correlatore:
Dott. Alessandro Alboresi

Dottorando:
Dott. Leonardo Ghin

a Lucia

a Lucia

Table of contents:

Summary

Living organisms can produce complex structures with specific functions for their metabolism that are used in a range of bio-industry and research activities. Biotechnology exploits prokaryotic and eukaryotic systems for expression of recombinant proteins, vaccines and antibodies as well as nano-structures. Indeed a number of nanoparticle-based products have been approved for diagnostics and therapeutics and more are currently under clinical trials.

In this thesis work, the possibility of using different expression systems for the preparation of bio-products has been exploited. On one handprokaryotic systems have been used for production of magnetosomes, magnetic nanoparticles used in diagnosis and therapy. On the other hand eukaryotic systems have been utilised for production of an important membrane protein LHCSR, which have a crucial role for the regulation of photoprotection in eukaryotic photosynthetic organisms such as algae and have been challenging researchers because of the difficulty of its purification from homologous systems.

Multifunctional nanostructured magnetic particles, MNP, and ferrofluids have been proposed for use in biomedicine with specific advantages in a large variety of industrial applications. MNP applications rely on their sensing, moving and heating properties, based on their superparamagnetism. In this context magnetosomes are magnetic nanoparticles gestated by magnetotactic bacteria (MTB) by a complex, genetically controlled biomineralization process. For example magnetosomes from *Magnetospirillum gryphiswaldense* consist of single-magnetic-domain sized nanocrystals of chemically pure magnetite, which are formed in plasma membrane invaginations within the cell wall in specialized membranous compartments. They are naturally coated by biological membranes and present physical-chemical properties with high bio- and nanotechnological potential.

In section A the results of using magnetosomes for thermoablation of tumours are reported. In magnetic hyperthermia a small amount of magnetic nanoparticles delivered to tumours releases heat upon application of a suitable alternate magnetic field in the range 100-500 KHz. The thermal shock consequent to bringing the cancer cells up to 40-45°C causes apoptosis and regression of tumour development. Magnetosomes (MNs) extracted from *M.ghryphiswaldense* as long chains have been tested for their interaction with cellular elements and anti-neoplastic activity both *in vitro* and *in vivo*, with the aim of testing their therapeutic potential against neoplastic model of Human Colon Carcinoma HT-29 cells and Human Glioblastoma U87MG cell cultures. MNs underwent efficient uptake with no evidence for cytotoxicity. *In vivo*, a model of subcutaneous tumours in mice was employed with MNs being administered by direct injection in the tumour volume. Upon three exposures to an AMF rated at 187 kHz and 23kA/m carried out on alternate days for a week we could report a decrease of tumour mass.

In section B, attention has been focused on the use of plant eukaryotic expression systems for the production of an intrinsic membrane protein which is present in trace amounts in plant chloroplasts and yet have a dramatic effect on the efficiency of light energy conversion into biomass. Despite many attempts so fa no expression system for this protein has been described thus hampering the possibility of revealing the molecular details of its function. Among different expression systems, plants offer many advantages. Previous work showed that recombinant proteins can be produced at 2–10% of the cost of microbial fermentation systems and at 0.1% of the cost of mammalian cell cultures, although this depends on the product yield. Plant systems seem to be a good choice for studying membrane proteins involved in the light phase of photosynthesis, like LHC-like proteins, for biochemical and spectroscopic analysis. In fact, plant cell systems have the unique property of being endowed with the synthetic pathways for the biosynthesis of the chromophores (Chlorophyll a, Chlorophyll b, xanthophylls) essential for the folding of pigment-binding photosynthetic proteins. Light harvesting complex (LHC) proteins function in photosynthesis by binding chlorophyll (Chl) and carotenoid molecules that absorb light and transfer the

energy to the reaction centre of the photosystem. Besides their role as light energy collection proteins, LHC proteins also have a second important role when solar irradiation exceeds the photosynthetic capacity. In this case, LHC proteins can help to dissipate excess absorbed light energy as heat rather than producing toxic ROS species.

Until now the properties of different LHC proteins has been studied in detail using *in vitro* reconstitution allowing the production of complexes yielding information on the properties of individual chromophores and their role in light harvesting and photoprotection. However only few LHCs proteins have been purified from thylakoids in their native state because of the complexity of the protein family whose members have very similar physical-chemical properties, making their resolution difficult using most analytical and preparative methods.

I have attempted the alternative strategy of expressing a LHC-like protein, namely LHCSR essential for the detection of low lumenal pH of the chloroplast, a symptom of excess illumination, and for triggering the photoprotective excess energy dissipation.

In order to shed light on LHCSR1 biochemical and spectroscopic properties an heterelogous expression of LHCSR1 in *Nicotiana tabacum* and *Nicotiana benthamiana* was established..

LHCSR1 is the only protein so far known to comprise the whole set of functions needed for NPQ into the same structural unit. Nevertheless, until now information regarding its structural and spectroscopic propertiesis not yet clarified. Until now attempts to over-express and purify LHCSR1 from *P.patens* have not given satisfactory results, so a different strategy has been adopted: the possibility of over-express it in heterologous system. Stable and transient expression of LHCSR1 in *N.tabacum* and *N.benthamiana* has been realized, leading to the isolation of LHCSR in the form of native chlorophyll a/b–xanthophyll-binding, correctly localized in thylakoids membrane and expressed as monomer LHC protein as reported for LHCSR1 in *P.patens*. The correlation of NPQ activity and LHCSR1 stable expressed in *N.tabacum* was also demonstrated.

In the last chapter, it has been exploited the possibility of LHCSR1 purification from *N.benthamiana* thylakoids by taking advantage of a histidine tail present at the C-terminus of the protein. Applying this strategy LHCSR1 has been purified in its native state from thylakoid membranes allowing description for the first time of its principal biochemical and spectroscopic characteristics.

Section A

Magnetosomes nanoparticles for thermotherapy of tumors

Introduction of section A

1. Nanoparticles and nanomedicine: brief introduction

According to the lexicology of science the prefix “nano” refers to the one-billionth of a unit, usually used for a variety of biological entities such as proteins, antibodies, viruses and bacteria, usually defined “biological nanomaterials”. The special functions and properties of biological nanomaterials provide much inspiration for the design of non-biological nanomaterials; meanwhile, due to their suitable sizes, non-biological nanomaterials can be used to access or manipulate biological nanomaterials. In this contest nanotechnology deals with the design, production and application of devices and systems by controlling their shapes and sizes at the nanometer scale.

Nanomaterials offer a lot of advantages as they have high surface-to-volume ratios when compared with larger particles, resulting in more reactive chemical properties affecting the mechanical or electrical properties of the materials. By regulating the surface of nanoparticles the scientist may be able to modulate their fates once introduced in the human body. Furthermore, the addition of targeting ligands that provides specific nanoparticle–cell surface interactions can play a vital role in the ultimate location of the nanoparticle (Davis et al., 2008).

In the recent years these nanomaterials found a applications in different fields among which nanomedicine. In contrast to conventional therapies—surgery, radiation, and chemotherapy—where the basic approach is to remove diseased cells faster than healthy cells, nanomedicine attempts to use sophisticated approaches to either kill specific cells or repair them at a time by using a biosensor to detect, for example, when a drug should be released (Riehemann et al., 2009) Nanomedicine includes different type of materials like polymers (e.g. biodegradable polymeric nanoparticles, dendrimers), lipids (e.g. solid-lipid nanoparticles, liposomes), inorganic materials (e.g. metal nanoparticles, quantum dots), and biological materials (e.g. viral nanoparticles, albumin nanoparticles). Among these nanomaterials magnetic nanoparticles is growing rapidly, and there is already a broad range of applications including cell separation, biosensing, studies of cellular function, as well as a variety of potential medical and therapeutic uses. The nanomaterials used in magnetic nanomedicine can be generally classified into magnetic thin films and magnetic nanoparticles which include nanospheres, nanowires and nanotubes.

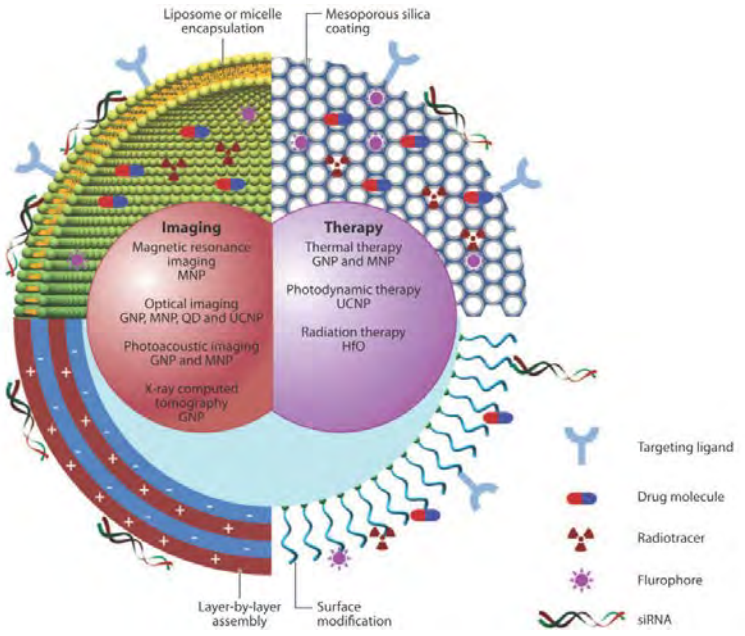

Figure. 1: Schematic diagram of multifunctional nanoparticles. Multifunctional nanoparticles can be generated by either combining nanocrystals with different functions or combining nanocrystals with functional small-molecule cargos through different surface engineering strategies. Four typical coatings developed for inorganic nanocrystals are liposome or micelle encapsulation, mesoporous silica coating, layer-by-layer assembly, and surface modification. Abbreviations: GNP, gold nanoparticles; HfO, hafnium oxide nanoparticles; MNP, magnetic nanoparticles; QD, quantum dot; UCNP, upconversion nanoparticles.

2. Magnetic nanoparticles: physical properties and applications

In the last decades, much attention has been devoted to multifunctional nanostructured magnetic particles, MNP, and ferrofluids with the aim of obtaining compounds suitable for several uses in biomedicine (Roca et al., 2009). The high interest in using MNP is based on the specific characteristics of magnetic nanomaterials and the benevolent relationships between magnetic fields and biological systems. Indeed the strength of magnetic field required for manipulating magnetic nanoparticles does not have harmful effects on biological tissues, and the biotic environment does not interfere with the magnetism of magnetic particles (Gould, 2004). The principal application of MNP regarding both diagnosis and therapy and rely on the use of iron oxide particles (usually Fe_2O_3 or Fe_3O_4). These particles available with diameters ranging from ~300 nm to less than 10 nm exhibit superparamagnetic behavior, magnetizing strongly under an applied field but retaining no permanent magnetism once the field is removed. Superparamagnetic behavior is extremely useful in hyperthermia treatment: when excited by an external magnetic field these MNP are able to transfer thermal energy to the surrounding allowing for local heating of nearby tissues where they are delivered, the so-called magnetic fluid hyperthermia (MFH) effect.

Generally magnetic effect is due to the movements of particles that have mass and electric charge. A spinning electric-charged particle creates a magnetic dipole, so-called magneton. When all magnetons in a material are aligned along the magnetic field it is possible to determine a magnetic domain. Fine particle magnetism comes from size effects, which are based on the magnetic domain structure of ferromagnetic materials. It assumes that the state of lowest free energy of ferromagnetic particles has uniform magnetization for particles smaller than a certain critical size and has non uniform magnetization for larger particles. The former ones are referred to as single domain particles, while the latter are called multidomain particles. The reaction of ferromagnetic materials on an applied field is well described by a

hysteresis loop as represented in figure 2.A. By applying an external magnetic field all the spins within a magnetic material align with the applied magnetic field reaching the maximum magnetization value called saturation magnetization (M_s). When the field becomes weaker the spins align with the external magnetic field and so the total magnetization decreases. For ferromagnetic materials a residual magnetic moment is retained even when the field is zero and this value is called the remaining magnetization (M_R). To bring the material back to zero magnetization, a magnetic field in the negative direction should be applied, and the magnitude of the field is called the coercive field (H_C). The coercivity is the single property of most interest, and it is strongly size-dependent (Fig.2.B). It has been found that as the particle size is reduced, the coercivity increases to a maximum and then decreases toward zero, particles with a coercivity of zero are called superparamagnetic. In superparamagnetic particles, thermal fluctuations are strong enough to spontaneously demagnetize a previously saturated assembly; therefore, these particles have zero coercivity and have no hysteresis. Placing superparamagnetic iron oxide in altering current [AC] magnetic fields randomly flips the magnetization direction between the parallel and ant parallel orientations, allowing the transfer of magnetic energy to the particles in the form of heat, a property that can be used *in vivo* to increase the temperature of tumor tissues to destroy the pathological cells by hyperthermia. Among materials used for hyperthermia magnetosomes, nanoparticles gestated by magnetotactic bacteria, has gained attention in recent studies. In the following sections magnetotactic bacteria and magnetosomes will be discussed and analyzed, understanding their properties and used in research and therapy.

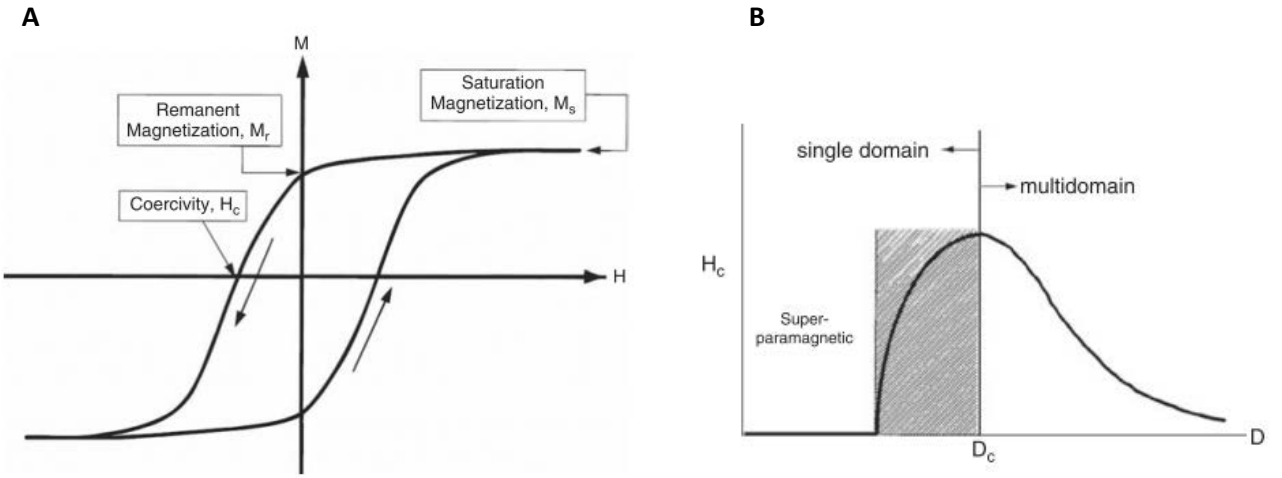

Figure.2: (A) A typical magnetization vs field (M–H) hysteresis loop of a ferromagnetic material. Several important parameters are shown: saturation magnetization Ms, remanent magnetization Mr,and coercivity Hc. **(B)** The relationship between the coercivity in ultrafine particle systems and particle sizes. (Leslie-pelecky and Rieke, 1996)

3. Magnetotactic bacteria and magnetosomes nanoparticles.

The term magnetotactic bacteria indicates a heterogeneous group of prokaryotes with different morphology, including coccoid, rod-shaped, vibroid, spirilloid and multicellular. All of them are gram-negative, motile by flagella, all exhibiting a negative tactic and/or growth response to oxygen concentration, all of them have a respiratory form of metabolism and are able to produce magnetic inclusion called magnetosomes (Bazylinski and Frankel, 2004). Magnetotactic bacteria usually are localized in the oxic-anoxic interface in aquatic habitats and, as shown by the physiological studies, they have the potential to participate in the biochemical cycle of iron, nitrogen and sulfur (Bazylinski and Blakemore, 1983; Toshifumi Sakaguchi, 2002). Magnetotactic bacteria are generally difficult to grow in pure culture although nowadays different strains are available for genetic and biochemical studies. Most described culture strains belong to the genus *Magnetospirillum* like *M.magnetotacticum* MS-1, *M.gryphiswaldense* MSR-1 and *M.magneticum* AMB-1. Other cultured magnetobacteria include the marine vibrio strains MV-1 and MV-2, a marine spirillum strain MMS-1, and strain MC-1. The last cultured strain belong to *Deltaproteobacteria ,* the magnetite-containing sulfate reducing strain *DesulfoVibrio magneticus* RS-1.

The main characteristic of all these bacteria is the ability to mineralize either iron oxide magnetosomes, containing magnetite crystal (Fe_3O_4), of iron sulphide magnetosomes , containing greigite crystals (Fe_3S_4). The particle morphology of Fe_3O_4 and Fe_3S_4 crystals is variable but consistent within cells of a single magnetotactic bacterial species of strain. Three general crystal morphologies have been reported in magnetotactic bacteria on the basis of their two-dimensional projections in the electron microscope: roughly cuboidal; elongated prismatic (roughly rectangular) and tooth-, bullet- or arrowhead-shaped (C.T. Lefèvre et al 2011) (Fig.3). All mature magnetosomes crystals falls within a narrow size range of about 35-120 nm (Schüler, 2008), except the very large magnetite crystals with length up to 250 nm produced by an uncultured coccus (Lins et al., 2006). Several factors influence Fe_3O_4 mineralization, the most important are oxygen concentration and the presence of nitrogen oxides. It has been reported that microaerobic conditions are required for Fe_3O_4 mineralization by *M.magnetotacticum* (Blakemore et al., 1985). Cells of this organism could grow in sealed, unshaken culture vessels with 0.1–21% oxygen in the headspace; maximum Fe_3O_4 production and cellular magnetism occurred with an oxygen concentration of 1%, whereas oxygen concentrations >5% were inhibitory. Fe_3O_4 mineralization in *M.magnetotacticum* is also increased by addition of nitrate to the growth medium as an additional terminal electron; indeed it has been shown that *M. magnetotacticum* is a microaerophilic denitrifier that converts nitrate to nitrous oxide (N_2O) and di-nitrogen, but which cannot grow under strict anaerobic conditions with nitrate. The dependence of oxygen and Fe_3O_4 mineralization has been also shown for other strains of magnetotactic bacteria. *M.gryphiswaldense* is able to induce Fe_3O_4 mineralization at very low oxygen concentration ~2-7 µM at 30°C (Schüler and Baeuerlein, 1998); *M.magneticum* synthesizes Fe_3O_4 either microaerobically or anaerobically using nitrate as the terminal electron acceptor and finally the magnetic vibro strain MV-1

synthesize Fe_3O_4 microaerobically in semi-solid agar oxygen-gradient cultures, and anaerobically under 1 atm of N_2O, which it uses as a terminal electron acceptor in respiration (Bazylinski et al, 1988).

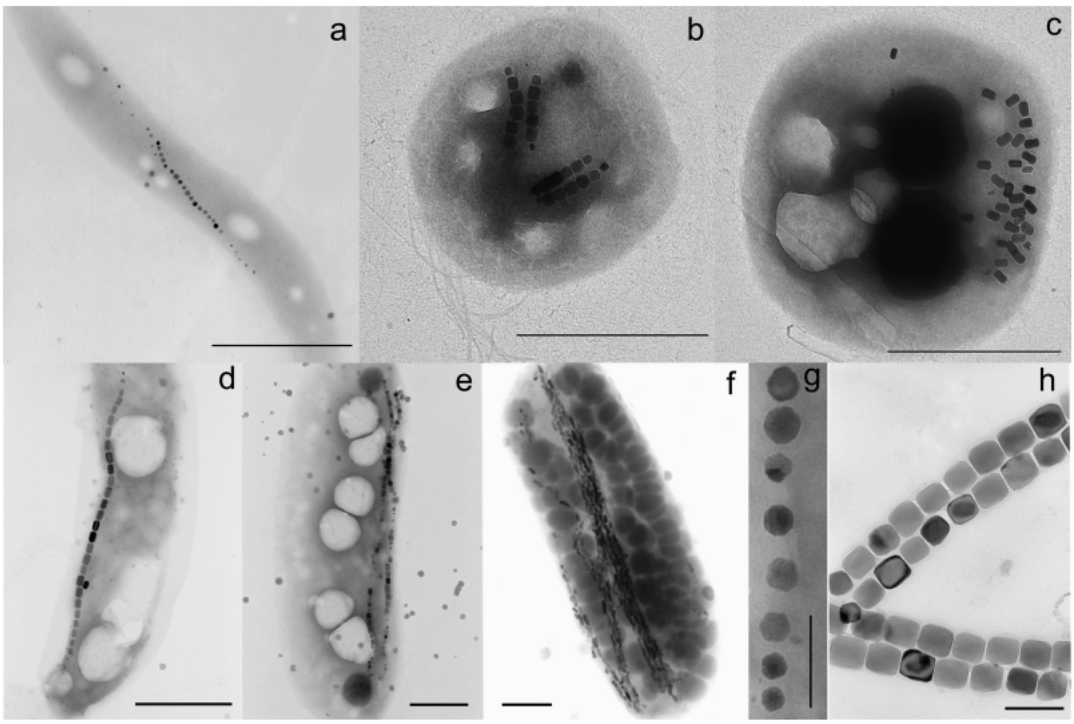

Figure.3. Electron micrographs of various magnetotactic bacteria and magnetosome chains. These images show the diversity of the cell morphology, of the magnetosomes, and of the arrangement of magnetosomes in bacteria: (A) a spirillum with a single chain of cubooctahedral magnetosomes, (B) a coccus with two double chains of slightly elongated prismatic magnetosomes, (C) a coccus with clustered, elongated magnetosomes, (D) a vibrio with elongated prismatic or cubooctahedral magnetosomes arranged in a single chain, (E) a vibrio with two chains, and (F) a rod-shaped bacterium with bullet-shaped magnetosomes arranged in a multitude of chains (Faivre and Schuler, 2008).

Due to their low dimension, magnetosomes are stable single-magnetic domain (SD) and are permanently magnetic at ambient temperature. Because each crystal is uniformly magnetized with the maximum possible magnetic dipole moment per unit volume, magnetosome crystals behave as if they were tiny permanent magnets. Usually magnetosomes are organized in long chains (Bazylinski and Frankel, 2004) which are responsible for the alignment of magnetic dipole moments of magnetosomes parallel to each other along the length of the chain. Thanks to this special organization the total magnetic moment of the cells is the sum of the permanent magnetic dipole moments of the individual magnetosome particles. The sum of single magnetosome dipole moments is large enough that its interaction with magnetic field overcomes the thermal forces that randomize the orientation of the cell. Indeed, cells exhibit magnetotaxis behavior which could be described as a passive alignment of the cell along geomagnetic field lines while it swims. Originally the first classic model of magnetotaxis was based on the assumption that all magnetotactic bacteria have a fixed polar preference to their swimming direction (Frankel and Blakemore, 1980). According to the Earth's magnetic field two different type of magnetic behavior could be described: bacteria from northern-hemisphere sites known as north-seeking (NS) swim preferentially parallel to the magnetic field, which corresponds to a northward migration in the geomagnetic field; while bacteria from

southern-hemisphere sites swim preferentially anti-parallel to the magnetic field and are known as south-seeking (SS) (R.P Blakemore; R.B Frankel; Ad. J. Kalmiin , 1980). Recently this first hypothesis on magnetotaxis has been revised introducing two different types of magnetotaxis: “polar magneto-aerotaxis” where the cell sense the direction of the field and the “axial-magneto-aerotaxis” where the cell sense the axis of the field (Frankel et al., 1997). In the polar magneto-aerotaxis cells moves according a two-state mechanisms resulting in an efficient aerotactic response in vertical oxygen gradients, as found in chemically stratified sediments or water bodies. Instead, according to axial magneto-aerotaxis cells are able to align along the magnetic field but they don’t display a preferred North- of South-seeking polarity. In both cases, magnetotaxis increases the efficiency of aerotaxis in vertical concentration gradients by reducing a three-dimensional search to a single dimension (Frankel and Blakemore, 1980).

These two mechanisms can be distinguished when magnetotactic bacterial cells are placed in a flattened open-ended capillary tube in a magnetic field that is oriented parallel to the tube’s long axis (Fig. 4). Oxygen diffusing into the two ends of the tube forms a double gradient with the oxygen concentration increasing from the center towards both ends of the tube. Cells of axial strain form bands below the menisci at both ends of the tube, whereas those of polar strain form a band only at the one end of the tube for which the direction of increasing oxygen concentration is opposite to the magnetic field. Thus the magnetic field provides only an axis of motility for axial magneto-aerotactic bacteria, whereas it provides both an axis and a direction for motility for polar magneto-aerotactic bacteria.

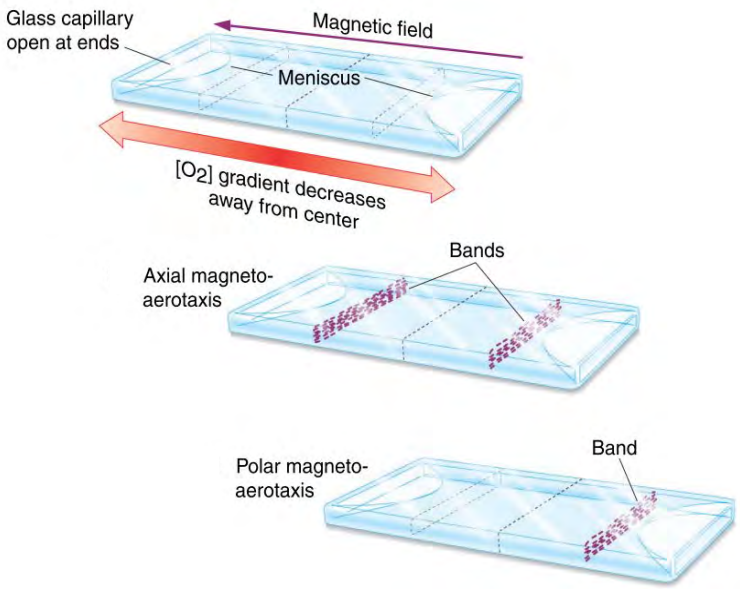

Figure.4: Difference of axial and polar magneto-aerotaxis. Schematic of aerotactic bands of magnetotactic bacteria in flat, glass, capillary tubes filled with reduced medium and open at both ends, placed in a magnetic field B. Bacteria with the axial magneto-aerotactic mechanism form bands at both ends of the tube. Northern hemisphere bacteria with the polar magneto-aerotactic mechanism form a band only at end of the tube for which B is antiparallel to the oxygen gradient. Southern hemisphere bacteria would form a band only at the other end of the tube for which B is parallel to the oxygen gradient (Frankel and Bazylinski, 2004).

3.1 Biochemical composition of magnetosomes and biomineralization of magnetosomes

Similar to eukaryotic organelles magnetosomes consists of a lipid bilayer membrane (MM) which has been studied in detailed only in strains of *Magnetospirillum*. It could be seen by TEM as vesicular structures that are empty or partially filled by tiny immature crystallites of magnetite in iron-starved or 'premagnetic' cells (Komeili et al., 2004). These magnetosomes membranes are intimately attached to the cytoplasmic membrane (CM) from which they seem to originate (Komeili et al, 2006) acting as a nanoreactor for magnetite synthesis. Isolated MM from *M.gryphiswaldense* were found to contain a series of phospholipids resembling the composition of CM composition; phosphatidylethanolamine and phosphatidylglycerol are the most abundant polar lipids, whereas ornithine amide lipid and an unidentified aminolipid are less abundant in the MM compared to the fraction of lipids from the outer and cytoplasmic membranes (Grunberg et al., 2004; Tanaka et al., 2006). Instead the protein subset of MM is highly specialized. The magnetosome sub proteome of *M.gryphiswaldense* has been described using a one-and two dimensional electrophoresis methods in combination with N-terminal and mass spectrometric sequencing techniques, reverse genetics and genomic data revealing the presence of at least 18 different bona-fide magnetosome membrane proteins. Similar studies confirmed that many magnetosome proteins are conserved between different magnetotactic bacteria. Magnetosome membrane proteins *in M. gryphiswaldense* and other MTB have been named either Mam (magnetosome membrane), Mms (magnetic particle membrane specific), Mtx (magnetotaxis), or Mme (magnetosome membrane) proteins and were assigned a letter in the order of their discovery or a number referring to their apparent molecular mass (e.g., MamA, Mms6). All magnetosome membrane proteins belong to characteristic protein families, which include TPR (tetratricopeptide repeat) proteins (MamA), CDF (cation diffusion facilitators) transporters (MamB and MamM), HtrA-like serine proteases (MamE, P, O), Actin-like proteins (MamK), generic transporters (MamH,N), and MTB-specific proteins with no homology to other proteins in nonmagnetic organisms (MamG, F, D, C, J, W, X, Y, Mms6, MmeA, MtxA) (Richter et al., 2007).

Most of these proteins participate to the biomineralization process including uptake, accumulation and precipitation of iron. Overall this biomineralization process is still poorly understood at molecular and biochemical level due to the absent of an appropriate laboratory model. In this contest the α-proteobacterium *M.gryphiswaldense* emerged as a an appropriate model for the investigation of magnetosome formation as it is genetically tractable (Schultheiss and Schüler, 2003), its genome is sequenced and it is easily cultivable by microaerobic mass cultivation (Heyen and Schüler, 2003).

The biomineralization process starts with the active uptake and transport of iron into the cell and into the magnetosomes vescicle. Genomic analysis and preliminary experimental data suggest that common constituents of the iron metabolism, such as uptake systems for ferrous and ferric iron, iron storage, iron reductases, as well as iron-regulatory elements, are present in all MTB, although their role for magnetite biomineralization is not fully understood (Richter et al., 2007). In *M.gryphiswaldense* different genes seems

to exhibit an important role for iron uptake. The first is *feoB1* which probably plays an accessory role in magnetite biomineralization and the second is the *fur*-like gene which deletion resulted in a dramatic inhibition of iron uptake and magnetosome formation (Qi et al., 2012). In magnetovibro strain MV-1 a major copper-containing periplasmic protein (ChpA ("copper handling protein") was found to be involved in iron uptake (Dubbels et al., 2004). This protein is part of a three components iron uptake system which resembles the copper-dependent high-affinity iron uptake system in *S. cerevisiae* including an iron permease and an Fe(II) oxidase. Homologous of this gene has been identified also in the genome of other magnetospirilla suggesting a similar pathway also for them (Dubbels et al., 2004).

Specific routes for iron uptake into the magnetosomes are likely to be used for accumulation of supersaturating quantities of iron into the magnetosomes. Previous genetic and biochemical studies suggested that the MagA protein plays a role in magnetosomal iron uptake in *M.magneticum.* More recently two different proteins indicated as MamB and MamM have been described in *M.gryphiswaldense* . Both MamB and MamM are members of the cation diffusion facilitator (CDF) family of metal transporters and they have greatest similarity to the CDF3 subfamily, which was postulated to comprise putative iron transporters suggesting a similar role for these two proteins also in magnetospirilla.

Once iron has been uptake the nucleation and growth of magnetic crystal can starts. In *M.magneticum* this second step has shown to be dependent on Mms6 protein which bearing a Leu-Gly-rich motive reminiscent to self-aggregating proteins of other biomineralization systems. This protein is tightly bound to iron-binding protein and had a striking effect on the morphology of growing magnetite crystals in vitro by facilitating the formation of uniform 30-nm-sized, single domain particles in solution (Arakaki et al., 2003; Prozorov et al., 2007). Even if its role for *in vitro* magnetic synthesis has been proven, no information is yet available about its role in magnetosomal magnetite synthesis in vivo. Other protein candidates involved in magnetic crystal nucleation are the two proteins MamN and MamT. MamN exhibits some similarity to H^+-translocating proteins, might mediate active H^+ efflux from the magnetosome compartment allowing that the solution within the magnetosome compartment could be sufficiently buffered to ensure that the solubility product of magnetite is always exceeded. The other protein MamT contains two putative c heme-binding sites and represent a redox-active protein which could be responsible for redox mediation of iron within the magnetosome compartment (Jogler and Schüler, 2006).

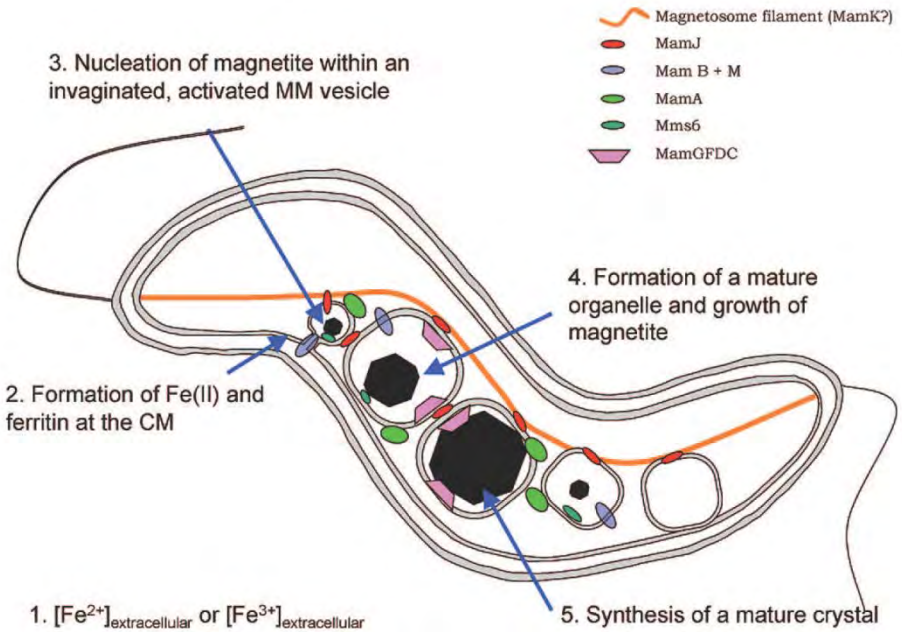

Figure.5 .Current model of the iron reaction pathway, and roles of the proteins that were so far shown to be necessary for magnetite biomineralization and chain formation in *M.gryphiswaldense* (Faivre and Schuler, 2008)

As previously described magnetosomes crystals are characterized by a précised shape like prismatic and bullet-, or hook-shaped. The molecular mechanisms responsible for this extremely precise structure are not yet understood. It has been demonstrated that environmental parameters such as oxygen concentration, rate of growth and iron uptakes may affects the habits of magnetic crystals (Heyen and Schüler, 2003). Moreover from the isolation of spontaneous *M.gryphiswaldense* mutants which produce aberrant or smaller particles it has been postulated that crystal shape are also under genetic control. In particular the four protein MamG, MamF, MamC and MamD were shown to control the size of magnetic crystals (Scheffel et al., 2008). These four proteins are encode by the MamGFDC operon and they could be considered part of the MTB-specific set of 28 ‘signature’ genes (Richter et al., 2007). Mutants lacking these four proteins showed the ability to synthesize magnetic crystal and to align in magnetic field but they produce crystal that have only 75 % of the wild-type size and that are less regular with respect to morphology and chain-like organization. Formation of wild-type-sized magnetite crystals could be gradually restored by the in trans complementation with one, two, or three genes of the mamGFDC operon, respectively, regardless of their combination, whereas the expression of all four genes resulted in crystals exceeding the wild-type size (Scheffel et al., 2008).

3.2 The assembly of magnetosome chain

In order to interact with the Earth magnetic field, magnetotactic bacteria evolved a strategy that allow to maximize its magnetic dipole arranging magnetic crystals in long chain resulting in a single magnetic dipole. Observing *Magnetospirillum* and other magnetotactic bacteria by transmission electron microscopy it is possible to see a long single linear chain, adjacent to cytoplasm membrane, apparently following the cell curvature in a helical manner. Recently using cryo-electron tomography on two strains *M.gryphiswaldense* and *M.magneticum* a network of filament 3-4 nm in thickness, traversing the cell adjacent to the citoplasmic membrane has been described (Komeili et al, 2006; Scheffel et al., 2006). This structure seems to be due to the action of two proteins MamJ and MamK. Cells of *M.magneticum* deleted for MamK lost their chain-like magnetosome structure and magnetosome were dispersed throughout the cell. Furthermore MamK fused to GFP protein showed a filament-like organization in vivo, appearing as a thin line inside cell (Komeili et al, 2006). The formation of filament-like structures seems to be an intrinsic property of MamK, because MamK of *M. magneticum* alone is sufficient to direct the synthesis of straight filament in *E. coli*. In addition to MamK , the acidic MamJ protein was identified in *M.gryphiswaldense* as implicated in the control of magnetosome chain assembly. The role for this protein has been elucidate trough the study of ΔMamJ mutant strain which still maintain the cytoskeleton network of magnetic chain but empty vesicles and immature crystals were scattered throughout the cytoplasm and detached from the filaments (Scheffel et al., 2006). Localization studies with GFP suggested that MamJ interacts with the magnetosome filament but is not required for its synthesis. A direct interaction between the putative filament-forming MamK protein and MamJ was experimentally confirmed by two-hybrid experiments (Scheffel and Schüler, 2007). One obvious model derived from these results is that the MamJ may connect magnetosomes to the cytoskeleton magnetosome filament composed of the MamK protein, which stabilizes the magnetosome chain and prevents it from collapsing.

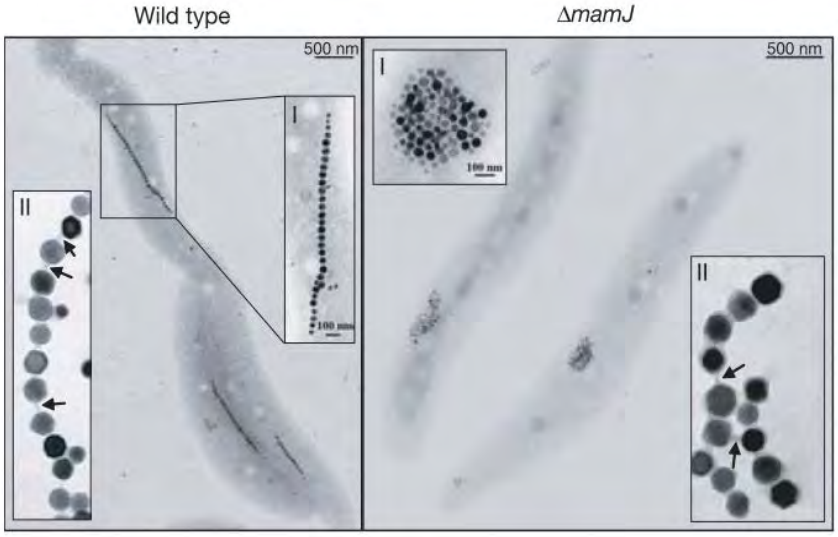

Figure 6. Transmission electron micrographs of wild-type and ΔmamJ cells. Insets show (I) magnification of magnetosome organization and (II) magnetosome membranes forming junctions (arrows) between isolated crystals (Scheffel et al., 2006)

4. Application of magnetosomes

Magnetic nanoparticles are of interest for a broad range of disciplines including nanosciences, material sciences and biotechnology. In this context magnetosomes purified from magnetotactic bacteria represent a new class of magnetic nanoparticles with unique characteristics: uniform sizes and shapes, high magnetic susceptibilities, low toxicity, good dispersibility, and a biocompatible surface trough the presence of magnetosomes membranes. Nowadays magnetosomes are investigated for their possible applications in a lot of biotechnological and biomedical fields. For instance magnetosomes have been investigated as a carrier in magnetic drug targeting (Sun et al., 2008). In addition a number of biotechnological applications have been reported such as procedures for DNA or RNA extraction (Yoza et al., 2003) or magnetosome-based immunoassays to detect antigens, environmental pollutants, hormones and toxic substances

Another potential application is the hyperthermal treatment of tumor because they have extremely high specific loss powers. This has been estimated by measuring magnetosome losses per cycles, which are defined as the magnetosome SAR (specific absorption rates) divided by the frequency of the applied magnetic field. The magnetosome losses per cycle has been estimated to increase with increasing magnetic field strength from 0.1 to 0.2 J/kg (joules per kilogram of iron contained in the heated magnetosomes) for a magnetic field strength of 6 mT , up to 0.5–1 J/kg for a magnetic field strength of 12 mT (Hergt et al., 2005; Timko et al., 2009; Dutz et al., 2007). These values are higher respect to those of SPION when the magnetic field is higher than 10 mT. The possibility for magnetosomes in hyperthermic treatment of tumors has been evaluated by Alphandery et al injecting suspensions containing either individual magnetosomes or chains of magnetosomes at a concentration of 10 mg/mL at the center of MDA-MB-231 breast tumors xeno-grafted under the skin of mice. The mice were then exposed to an alternating magnetic field of average field strength ~20 mT and frequency 198 kHz three times during 20 min. Repeating for 30 days this treatment tumors masses totally disappeared (Alphandéry et al, 2011).

References

Alphandéry, E., Faure, S., Seksek, O., Guyot, F., and Chebbi, I. (2011). Chains of Magnetosomes Extracted from AMB-1 Magnetotactic Bacteria for Application in Alternative Magnetic. ACS Nano: 6279–6296.

Arakaki, A., Webb, J., and Matsunaga, T. (2003). A novel protein tightly bound to bacterial magnetic particles in Magnetospirillum magneticum strain AMB-1. J. Biol. Chem. **278**: 8745–50.

Arash Komeili, Zhuo Li, Dianne K. Newman, G.J.J. (2006). Magnetosomes are cell membrane invaginations organized by the actin-like protein MamK. Science **311**: 242–246.

Bazylinski, D.A. and Blakemore, R.P. (1983). Nitrogen Fixation (Acetylene Reduction) in Aquaspirillum magnetotacticum. **9**: 305–308.

Bazylinski, D.A. and Frankel, R.B. (2004). MAGNETOSOME FORMATION IN PROKARYOTES. **2**.

Bazylinski D.A.; Frankel R.B.; Jannasch H.W. (1988). Anaerobic magnetite production by a marine, magnetotactic bacterium. Nature: 91–92.

Blakemore, R.P., Short, K.A., Bazylinski, D.A., and Frankel, R.B. (1985). Microaerobic Conditions Are Required for Magnetite Formation Within AquaspiriRum magnetotacticum. Geomicrobiol. J. **0**.

C.T. Lefèvre, F. Abreu, U. Lins, D.A.B. (2011). Metal Nanoparticles in Microbiology.: 75–102.

Davis, M.E., Chen, Z.G., and Shin, D.M. (2008). Nanoparticle therapeutics: an emerging treatment modality for cancer. Nat. Rev. Drug Discov. **7**: 771–82.

Dubbels, B.L., Dispirito, A.A., Morton, J.D., Semrau, J.D., Neto, J.N.E., and Bazylinski, D.A. (2004). Evidence for a copper-dependent iron transport system in the marine , magnetotactic bacterium.: 2931–2945.

Dutz, S., Hergt, R., Mürbe, J., Müller, R., Zeisberger, M., Andrä, W., Töpfer, J., and Bellemann, M.E. (2007). Hysteresis losses of magnetic nanoparticle powders in the single domain size range. J. Magn. Magn. Mater. **308**: 305–312.

Faivre, D. and Schu, D. (2008). Magnetotactic Bacteria and Magnetosomes.: 4875–4898.

Frankel, R.B., Bazylinski, D. a, Johnson, M.S., and Taylor, B.L. (1997). Magneto-aerotaxis in marine coccoid bacteria. Biophys. J. **73**: 994–1000.

Frankel, R.B. and Bazylinski, D.A. (2004). Magnetosome Mysteries. **70**: 176–183.

Frankel, R. B.; Blakemore, R.P. (1980). Navigational compass in magnetic bacteria. J. Magn. Magn. Mater.

Gould, P. (2004). Nanoparticles probe biosystems.Materials today.7.: 36–43.

Grunberg, K., Mu, E., Otto, A., Reszka, R., Linder, D., Kube, M., Reinhardt, R., and Schu, D. (2004). Biochemical and Proteomic Analysis of the Magnetosome Membrane in Magnetospirillum gryphiswaldense. **70**: 1040–1050.

Hergt, R., Hiergeist, R., Zeisberger, M., Schüler, D., Heyen, U., Hilger, I., and Kaiser, W. a. (2005). Magnetic properties of bacterial magnetosomes as potential diagnostic and therapeutic tools. J. Magn. Magn. Mater. **293**: 80–86.

Heyen, U. and Schüler, D. (2003). Growth and magnetosome formation by microaerophilic Magnetospirillum strains in an oxygen-controlled fermentor. Appl. Microbiol. Biotechnol. **61**: 536–44.

Jogler, C. and Schüler, D. (2006). Genetic Analysis of Magnetosome Biomineralization. Microbiol. Monogr.

Komeili, A., Vali, H., Beveridge, T.J., and Newman, D.K. (2004). Magnetosome vesicles are present before magnetite formation, and MamA is required for their activation. Proc. Natl. Acad. Sci. U. S. A. **101**: 3839–44.

Leslie-pelecky, D.L. and Rieke, R.D. (1996). Magnetic Properties of Nanostructured Materials. **4756**: 1770–1783.

Lins, U., Mccartney, M.R., and Farina, M. (2006). Crystal habits and magnetic microstructures of magnetosomes in coccoid magnetotactic bacteria. **78**: 463–474.

Prozorov, T., Mallapragada, S.K., Narasimhan, B., Wang, L., Palo, P., Nilsen-Hamilton, M., Williams, T.J., Bazylinski, D. a., Prozorov, R., and Canfield, P.C. (2007). Protein-Mediated Synthesis of Uniform Superparamagnetic Magnetite Nanocrystals. Adv. Funct. Mater. **17**: 951–957.

Qi, L., Li, J., Zhang, W., Liu, J., Rong, C., Li, Y., and Wu, L. (2012). Fur in Magnetospirillum gryphiswaldense influences magnetosomes formation and directly regulates the genes involved in iron and oxygen metabolism. PLoS One **7**: e29572.

R.P Blakemore; R.B Frankel; Kalmiin, A.J. (1980). South-seeking magnetotactic bacteria in the Southern Hemisphere. Nature: 4–5.

Richter, M., Kube, M., Bazylinski, D. a, Lombardot, T., Glöckner, F.O., Reinhardt, R., and Schüler, D. (2007). Comparative genome analysis of four magnetotactic bacteria reveals a complex set of group-specific genes implicated in magnetosome biomineralization and function. J. Bacteriol. **189**: 4899–910.

Riehemann, K., Schneider, S.W., Luger, T. a, Godin, B., Ferrari, M., and Fuchs, H. (2009). Nanomedicine--challenge and perspectives. Angew. Chem. Int. Ed. Engl. **48**: 872–97.

Roca, a G., Costo, R., Rebolledo, a F., Veintemillas-Verdaguer, S., Tartaj, P., González-Carreño, T., Morales, M.P., and Serna, C.J. (2009). Progress in the preparation of magnetic nanoparticles for applications in biomedicine. J. Phys. D. Appl. Phys. **42**: 224002.

Scheffel, A., Gärdes, A., Grünberg, K., Wanner, G., and Schüler, D. (2008). The major magnetosome proteins MamGFDC are not essential for magnetite biomineralization in Magnetospirillum gryphiswaldense but regulate the size of magnetosome crystals. J. Bacteriol. **190**: 377–86.

Scheffel, A., Gruska, M., Faivre, D., Linaroudis, A., Plitzko, J.M., and Schüler, D. (2006). An acidic protein aligns magnetosomes along a filamentous structure in magnetotactic bacteria. Nature **440**: 110–4.

Scheffel, A. and Schüler, D. (2007). The acidic repetitive domain of the Magnetospirillum gryphiswaldense MamJ protein displays hypervariability but is not required for magnetosome chain assembly. J. Bacteriol. **189**: 6437–46.

Schüler, D. (2008). Genetics and cell biology of magnetosome formation in magnetotactic bacteria. FEMS Microbiol. Rev. **32**: 654–72.

Schüler, D. and Baeuerlein, E. (1998). Dynamics of Iron Uptake and Fe 3 O 4 Biomineralization during Aerobic and Microaerobic Growth of Magnetospirillum gryphiswaldense Dynamics of Iron Uptake and Fe 3 O 4 Biomineralization during Aerobic and Microaerobic Growth of Magnetospirillum gryphiswald. J. Bacteriol.

Schultheiss, D. and Schüler, D. (2003). Development of a genetic system for Magnetospirillum gryphiswaldense. Arch. Microbiol. **179**: 89–94.

Sun, J.-B., Duan, J.-H., Dai, S.-L., Ren, J., Guo, L., Jiang, W., and Li, Y. (2008). Preparation and anti-tumor efficiency evaluation of doxorubicin-loaded bacterial magnetosomes: magnetic nanoparticles as drug carriers isolated from Magnetospirillum gryphiswaldense. Biotechnol. Bioeng. **101**: 1313–20.

Tanaka, M., Okamura, Y., Arakaki, A., Tanaka, T., Takeyama, H., and Matsunaga, T. (2006). Origin of magnetosome membrane: proteomic analysis of magnetosome membrane and comparison with cytoplasmic membrane. Proteomics **6**: 5234–47.

Timko, M. et al. (2009). Magnetic properties and heating effect in bacterial magnetic nanoparticles. J. Magn. Magn. Mater. **321**: 1521–1524.

Toshifumi Sakaguchi, A.A. and T.M. (2002). Desulfovibrio magneticus sp . nov ., a novel sulfate-reducing bacterium that produces intracellular single-domain-sized magnetite.: 215–221.

Yoza, B., Arakaki, A., Maruyama, K., Takeyama, H., and Matsunaga, T. (2003). Fully automated DNA extraction from blood using magnetic particles modified with a hyperbranched polyamidoamine dendrimer. J. Biosci. Bioeng. **95**: 21–6.

Chapter 1.A:

Characterization of Magnetic Nanoparticles from *Magnetospirillum gryphiswaldense* as potential theranostics tools

Characterization of Magnetic Nanoparticles from *Magnetospirillum gryphiswaldense* as potential theranostics tools

T. Orlando,[1, a), b)] S. Mannucci,[2, a)] E. Fantechi,[3] G. Conti,[2] S. Tambalo,[2] A. Busato,[2] C. Innocenti,[3] L. Ghin,[4] R. Bassi,[4] P. Arosio,[5] F. Orsini,[5] C. Sangregorio,[6] M. Corti,[1] M. F. Casula,[6] P. Marzola,[7] A. Lascialfari,[5] and A. Sbarbati[2]

[1]*Department of Physics and INSTM, Università degli Studi di Pavia, Pavia, I-27100, Italy*
[2]*Department of Neurological and Movement Science and INSTM, University of Verona, Verona, I-37134, Italy*
[3]*Department of Chemistry "Ugo Schiff" University of Florence and INSTM, Sesto Fiorentino (FI), I-50019, Italy*
[4]*Department of Biotechnology and INSTM, University of Verona, Verona, I-37134, Italy*
[5]*Department of Physics and INSTM, Università degli Studi di Milano, Milano, I-20133, Italy*
[6]*CNR-ICCOM and INSTM, Sesto Fiorentino (FI), I-50019, Italy*
[6]*Department of Chemical and Geological Science and INSTM, University of Cagliari, Monserrato (CA), I-09042, Italy*
[7]*Department of Computer Science and INSTM, University of Verona, Verona, I-37134, Italy*

Abstract

We investigated the theranostic properties of magnetosomes (MNs) extracted from magnetotactic bacteria, promising for nanomedicine applications. Besides a physico-chemical characterization, their potentiality as mediators for magnetic fluid hyperthermia and contrast agents for magnetic resonance imaging, both in vitro and in vivo, are here singled out. The MNs, constituted by magnetite nanocrystals arranged in chains, show a superparamagnetic behaviour and a clear evidence of Verwey transition, as signature of magnetite presence. The phospholipid membrane provides a good protection against oxidation and the MNs are stable over months. Using an alternate magnetic field, the specific absorption rate was measured, resulting among the highest reported in literature. The MRI contrast efficiency was evaluated by means of the acquisition of complete NMRD profiles. The transverse relaxivity resulted as high as the one of a former commercial contrast agent. The MNs were inoculated into an animal model of tumor and their presence was detected by magnetic resonance images even after two weeks from the injection in the tumor mass.

Introduction

Theranostics is an innovative method combining diagnosis and therapy which is expected to have a relevant impact in the fight against cancer. By eliminating the clinical multi-step procedures, theranostics could reduce the delays among diagnosis and therapy. The use of nanoparticles properly labeled to recognize tumor cells might allow the simultaneous imaging and the effective local treatment of diseases [1]. Among the different types of nanoparticles, iron oxide nanoparticles are considered to be promising candidates as effective tools for cancer theranostics due to their superparamagnetic behavior combined to their relatively low toxicity [2-4].

Over the last decade, several magnetic particles having a maghemite or magnetite core have been proposed for biomedical applications. They can be used as contrast agents for magnetic resonance imaging (MRI) [5], mediators for magnetic fluid hyperthermia (MFH) [6], and carriers for drug delivery [7]. Even if some of them have good performances in two or more of these tasks, none of them is, to our knowledge, at the clinical stage as theranostic agent.

In addition to synthetic iron oxide nanoparticles, the use of magnetosomes (MNs) in biomedicine has also been recently proposed [8]. These nanostructures, constituted by pure magnetite spherical particles arranged in chains and surrounded by a phospholipid membrane [9, 10], are naturally synthesized by magnetotactic bacteria under specific environmental conditions. Furthermore, MNs exhibit a great hyperthermic efficiency both in vitro and in vivo. For these reason, MNs were considered as thermotherapy agent.

In this work, we present the use of magnetosomes as theranostic tool for combined cancer detection by magnetic resonance imaging and treatment through magnetic fluid hyperthermia. The structural and magnetic properties, the hyperthermic efficiency and the relaxometry profiles of MNs extracted from *Magnetospirillum gryphiswaldense* bacteria have been investigated. In particular, we show that the MNs act as effective hyperthermia mediators under alternate field of amplitude 17 kA/m and frequency 183 kHz, and as MRI negative contrast agents at the clinical fields 0.2 T and 1.5 T both *in vitro* and *in vivo*. The MRI contrast efficiency has been established by collecting, for the first time to our knowledge, the complete NMR-dispersion profiles of longitudinal and transverse relaxivities.

Results

The structure and morphology of the MNs extracted from *Magnetospirillum Gryphiswaldense* was investigated by XRD and TEM. The X-ray diffraction pattern, reported in Figure 1a, can be ascribed to a single crystalline phase with a spinel stucture which is consistent with the occurrence of magnetite Fe_3O_4 phase (PDF card 19-629). However, it should be pointed out that the occurrence of the fully oxidized iron oxide spinel phase, i.e. maghemite, cannot be ruled out based only on diffraction data [16]. Peak broadening suggests the occurrence of a nanocrystalline phase, and in particular the average crystallite domain size as calculated from pattern profile analysis is 33 nm.

TEM investigation indicates the presence of cubic- and cubo-octahedral- shaped nanoparticles with a chain-like arrangement (Figure 1b). Comparison of the same area under bright and dark field mode (Fig 1c and d) confirms that the nanoparticles are nanocrystalline and, in particular, that the particles are single crystals.

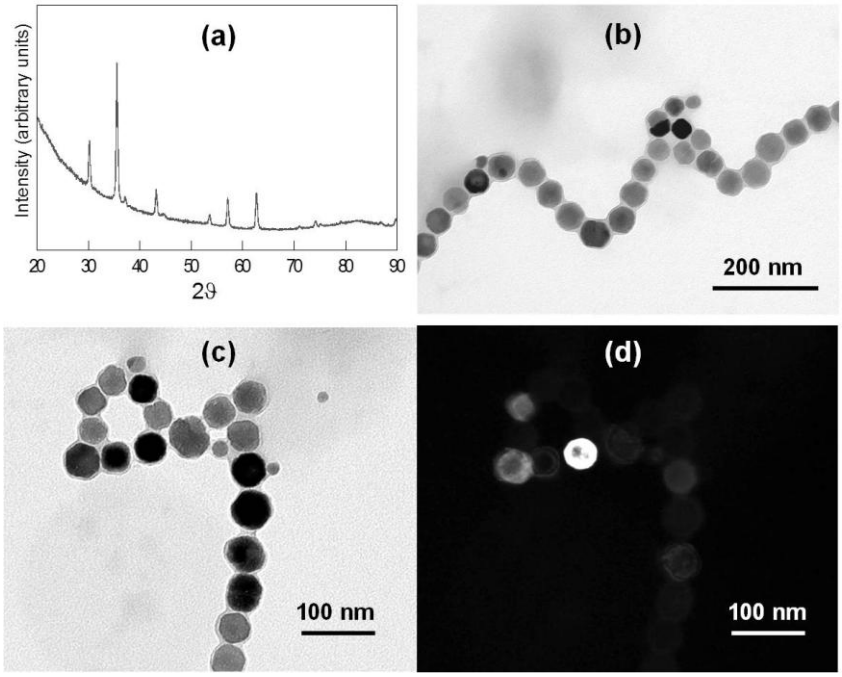

Figure 1 X-ray diffraction pattern (a) and representative Transmission electron microscopy image (b) MNs extracted from *Magnetospirillum gryphiswaldense*. A closer inspection of a magnetic nanoparticle chain as obtained by TEM under bright field (c) and dark field (d) imaging is also reported.
)

The field dependence of the magnetization is reported in Figure 2 both at 2.5 K and at 300 K. At low temperature, an open hysteresis loop is observed (see inset of Figure 2). The coercive field, $\mu_0 H_C$, is 42.8 mT, consistent with the literature values for nanosized iron oxides. The reduced remanent magnetization is $M_R = \frac{M_{0T}}{M_{5T}} = 0.45$, close to the one expected for a set of uniaxial nanoparticles whose axis is isotropically orientated (i.e. M_R=0.5). An open hysteresis loop with reduced coercivity ($\mu_0 H_C$ =2.1 mT) is observed also at 300 K (Figure 2). Both curves are well saturated at high fields, being the saturation magnetizations M_S = 139 and 126 $A \cdot m^2/kg_{Fe}$ at 2.5 and 300 K, respectively. Such values are very close to those of bulk magnetite (134 and 128 $A \cdot m^2/kg_{Fe}$ [17, 18], for low and room temperatures, respectively), confirming the high crystallinity of the sample.

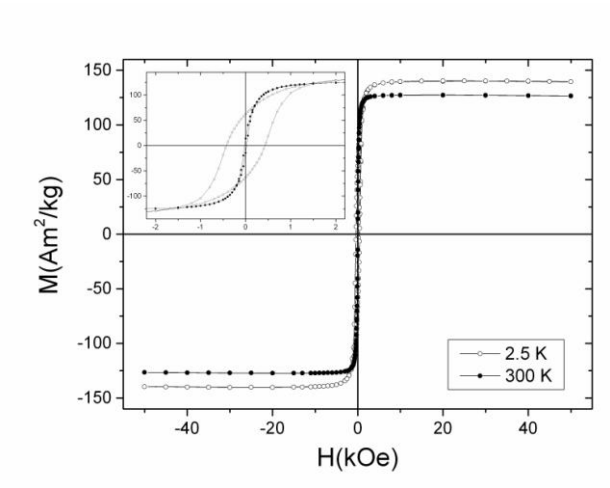

Figure 2 M vs. H curves of magnetosomes measured at 2.5 K (open circles) and 300 K (full circles). The magnification of both curves at low fields is reported in the inset.

Figure 3 shows the ZFC/FC magnetization curves for the MNs extracted from *Magnetospirillum gryphiswaldense*. A discontinuity in the curves acquired at different fields can be clearly observed around 105 K: this could be an evidence of the Verwey transition [19], a long range charge arrangement that occurs mainly in transition metal oxides and it is a signature for magnetite [20, 21]. This is confirmed by the fact that its position is independent from the applied external magnetic field (Figure 3a). The Verwey transition is generally not observed for small iron oxide NPs with mean size lower than a few tenths of nanometers. Indeed, they tend to rapidly oxidize due to their large surface to volume ratio and, for this reason, most of the time they are composed by a mixture of iron oxides (magnetite/maghemite). A so clear evidence of the Verwey transition confirms that the sample is composed by magnetite NPs with average crystalline size of the order of that observed in the TEM analysis size (42 ± 9 nm) [11]. Furthermore, the stability of the oxide phase was proved: indeed, as reported in Figure 3b, the Verwey transition is still clearly visible even after 3 months of storage. Most likely this is due to the phospholipid membrane that covers completely the magnetite crystals and prevents the contact with the air.

The blocking temperature T_B of the system, identifiable with the contact point between the ZFC curve and the FC one measured at low field, is above 300 K, as shown in the inset of Figure 3b. Considering the TEM average particle, T_B is expected to be much larger than the investigated temperature range [22].

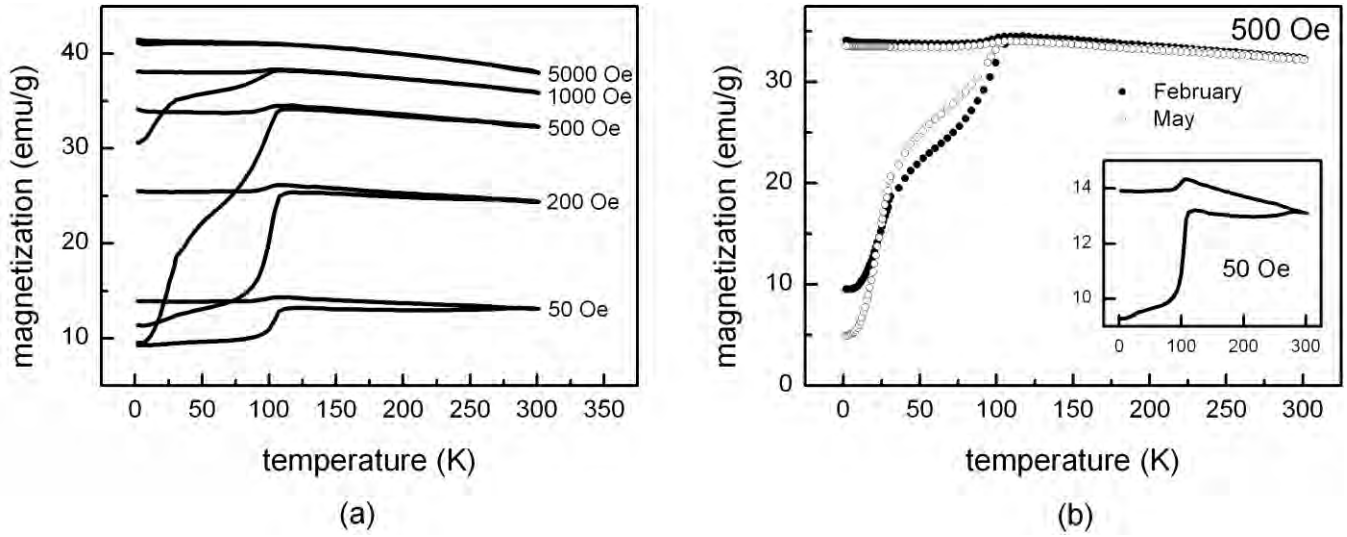

Figure 3 a) ZFC/FC curves collected at different magnetic fields for freeze-dried. b) ZFC/FC at 500 Oe collected for the same sample before and after a three months storage period at 4°C. The signature of the Vervey transition is still evident, proving the good quality of the phospholipid membrane as shelter. Inset: ZFC/FC curves at 50 Oe: from here the blocking temperature is estimated to be above 300 K.

The hyperthermic efficiency of extracted MNs was evaluated by recording the temperature kinetic curves of MNs dispersed in agarose gel and exposed to an alternate magnetic field of 17 kA/m and 183 kHz in amplitude and frequency, respectively. The concentration of the dispersion was 0.167 w/w of iron oxide. The kinetic curve, reported in Figure 4, shows that, despite the very low concentration of iron oxide, the temperature of the sample rises of about 5°C in 5 minutes of exposition to the alternate magnetic field. This corresponds to a specific absorption rate (SAR) of 482.7 ± 50.8 W/g per mass of iron, a value that is among the highest reported in the literature.

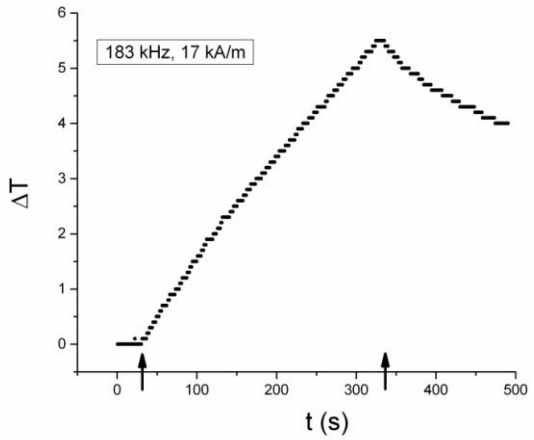

Figure 4 Temperature kinetics of the dispersion of MNs in agarose gel, exposed to an alternate magnetic field (17 kA/m, 183 kHz). The measurements were performed starting from body temperature (37 °C). The black arrows indicate the switch on and off of the magnetic field.

The NMR longitudinal and transverse relaxivity results as a function of frequency are displayed in Figure 5, in comparison to those of Endorem, a former commercial “negative” contrast agent. Although MNs are composed by superparamagnetic crystals, the behaviour of the longitudinal relaxivity r_1 as a function of frequency is different from the NMR profile typical of iron oxide nanoparticles, in which a low frequency plateau, a maximum around 10 MHz and a monotonic decrease of r_1 at high frequency can be seen. On the

contrary, MNs exhibit a monotonic decrease of r_1 as a function of frequency. This behaviour is independent from the dispersion matrix (water or agarose gel) and it is probably related to the MNs morphology and chain arrangement. For agarose dispersed MNs, the transverse relaxivity appears almost flat in the range of frequency 10-60 MHz. The quite low value is possibly due to the limited mobility of the protons in the MNs surrounding, which decreases the dephasing effect of the local magnetic field. On the other hand, the r_2 behaviour of MNs dispersed in water shows some frequency dependence. Remarkably, the r_2 values for MNs dispersed in water are higher than the ones of Endorem. As a consequence, MNs could be effectively used as negative contrast agent in magnetic resonance imaging.

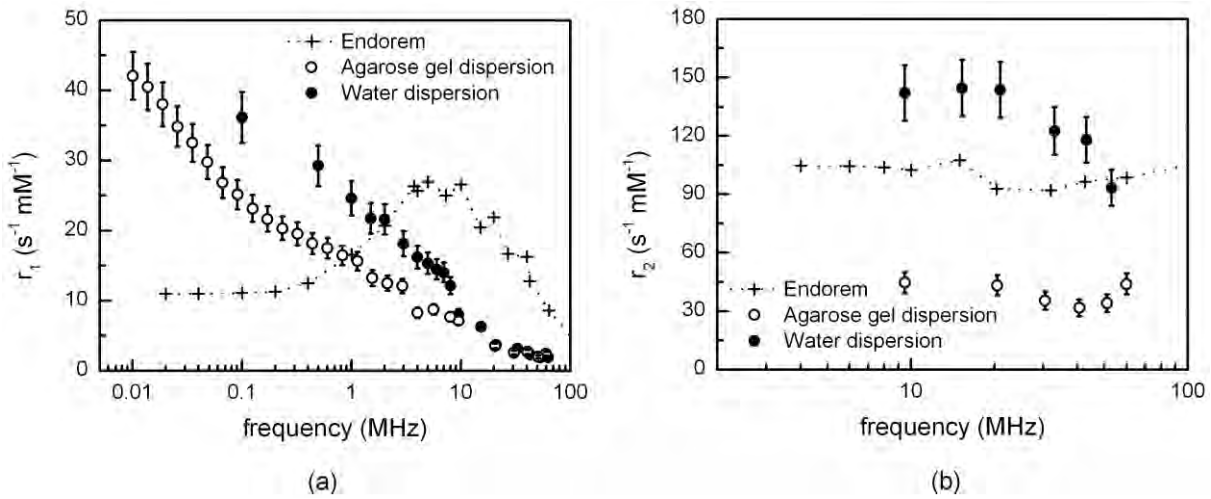

Figure 5 NMR dispersion profiles: (a) longitudinal relaxivity r 1 and (b) transverse relaxivity r 2 as a function of proton Larmor frequency for MNs dispersed in agarose gel (open circles) and in water (solid circles). The relaxometry values of a former commercial contrast agent, i.e. Endorem, are shown for comparison purpose.

The potential of MNs as MRI contrast agent was investigated *in vitro* and *in vivo* at 4.7 T, corresponding to the frequency ν = 200 MHz for the proton. Magnetic resonance images of agarose gel phantoms containing different amounts of MNs are reported in Figure 6a. As expected, the signal intensity clearly depends on the MNs concentration. Quantitative measurements of T_1 and T_2 values at different iron concentrations allowed the determination of longitudinal and transverse relaxivities, r_1 = 0.76 s^{-1} mM^{-1} and r_2 = 186 s^{-1} mM^{-1} respectively. For this field value, the transverse relaxivity of MNs in agarose gel is higher than the one of Endorem (r_2 = 94.8 $mM^{-1}s^{-1}$ mM^{-1}) [23] and comparable to other similar iron based contrast agents (e.g. Resovist, r_2 = 151.0 s^{-1} mM^{-1}) [24]. Furthermore, the value of r_2 at 200 MHz is greater than the one measured at 60 MHz; indeed, due to the large particle size, a raise of the r_2 value in the range 60-200 MHz cannot be excluded [25]. The observed high transverse relaxivity, as well as the high r_2/r_1 ratio, strongly confirms that the MNs could be efficient superparamagnetic contrast agents for MRI, also at higher fields.

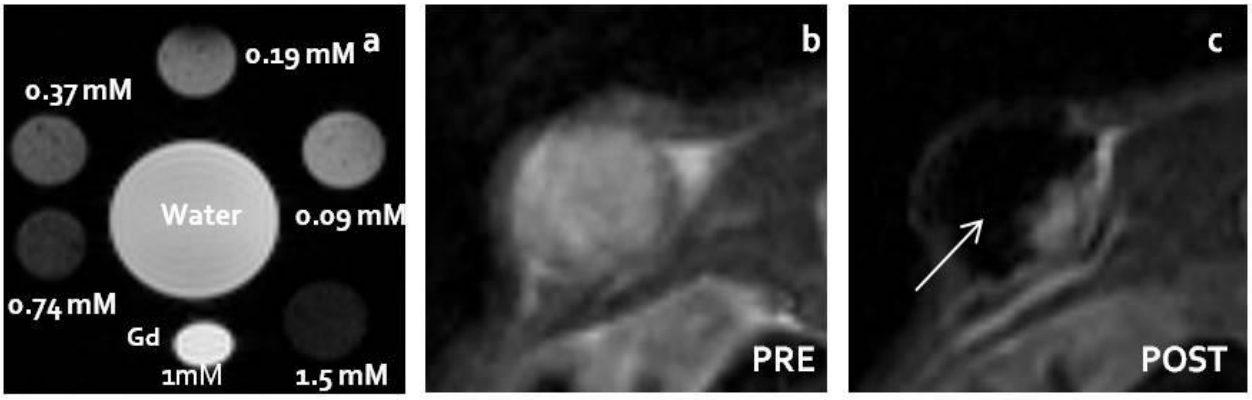

Figure 6 In vitro and in vivo contrast efficiency of MNs as MRI agents. (a) T 2 -weighted image of phantoms t different MNs concentrations (the values are reported in mM of iron). The iron content in our MNs samples determined by atomic absorption spectroscopy was 0.167 w/w. T 2 -weighted images of tumor tissue before (b) and 24 h after (c) MNs injection.

This was experimentally confirmed by the *in vivo* T_2-weighted images. Images of U87MG xenografted mice acquired before and after injection of 1 mg of MNs diluted in 200 µL of PBS into the tumor mass are shown in Figure 6b and c. Thanks to the high transverse relaxivity, the presence of MNs is well detectable as a dark region. Furthermore, we investigated the evolution of the signal as a function of the time (see Figure 7a-d): as one can see, the MNs remain detectable even after two weeks.

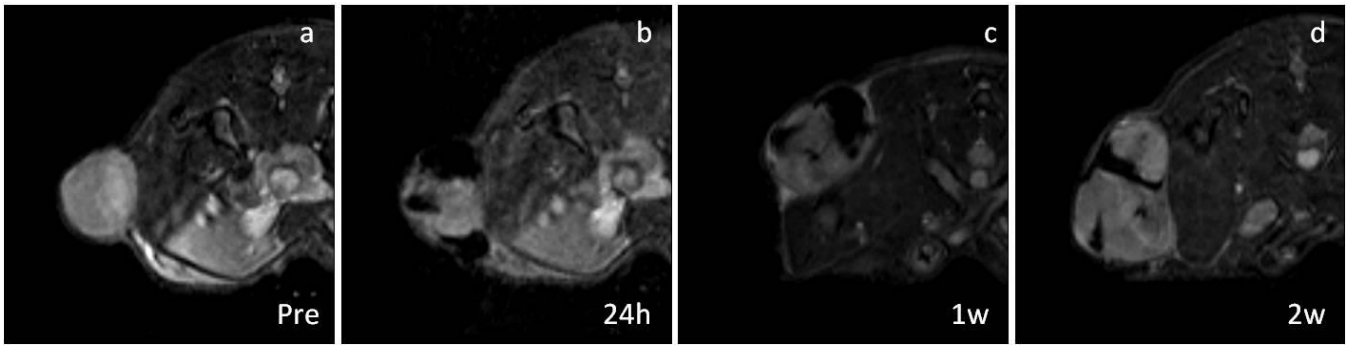

Figure 7 Time evolution of MNs signal in vivo. T 2 -weighted images of tumor (a) before the MNs injection, (b) 1 hour after, (c) 1 week after and (d) 2 weeks after the injection.

Discussion and conclusions

In this work several techniques have been used to characterize magnetosomes naturally produced by the magnetotactic bacteria *Magnetospirillum gryphiswaldence*. From structural analysis, we verified that their magnetic cores are composed by magnetite single crystals arranged in chains and coated with a phospholipid membrane. The oxide phase is stable over months thanks to the shielding effect of the membrane. This was confirmed by the magnetic measurements, which showed an evident and stable Verwey transition around 105 K. Due to the particles size, the blocking temperature is above 300 K.

The great potentiality of MNs as mediators for magnetic fluid hyperthermia was verified: the specific absorption rate (SAR) obtained after the application of an alternate magnetic field is 482.7 W/g, among the highest reported in literature. The NMRD profiles, acquired for MNs dispersed both in agarose gel and water, demonstrated good contrast efficiency as negative MRI contrast agents compared to Endorem, a former clinical contrast agent. An animal model of tumor was used for *in vivo* MRI tests. The high contrast efficiency allows to easily identify the region where the magnetosomes were injected, even after two weeks.

These results, together with the ones previously achieved [11], state how magnetosomes can represent a good platform to develop a multifunctional nanostructured material suitable for theranostics. Indeed, the possibility to combine the therapeutic effect of the released heat along with a higher contrast in MRI images is extremely interesting: this would allow monitoring the distribution of the particles in the tumor tissue and, at the same time, to have an immediate check of the hyperthermic treatment efficacy, through tumor volume measurements.

Materials and methods

Magnetospirillum gryphiswaldense culture and MNs purification

Magnetospirillum gryphiswaldense strain MSR-1, purchased from Deutsche Sammlung von Mikroorganismen und Zellkulturen GmbH (Germany), was cultured as described in Ref. 11. MNs were extracted and purified according to methods published by Grunberg [11, 12]. Briefly, *M. gryphiswaldense* (10 g) bacteria were suspended in 50 mL of 50 mM HEPES–4 mM EDTA (pH 7.4) and disrupted using French-press. Non lysated materials were removed by centrifugation at 680g for 5 min. The obtained lysate was passed through a magnetic separation column (MACS, MiltenyiBiotec) and finally MNs were eluted with 10 mM HEPES (pH 7.4) buffer. MNs were centrifuged at 280000 g for 12 h at 4°C and the obtained pellet was incubated with 10 mM HEPES for 16 h at 4°C to allow for solubilization. After purification, MNs were lyophilized and irradiated with □-rays. Iron content of MNs was determined by atomic absorption spectroscopy.

Chemical, Structural, and Morphological Characterization

The crystal structure of the MNs extracted from *Magnetospirillum gryphiswaldense* was studied by recording the XRD pattern within the range of 10°–90° (2ϑ) using Cu Kα radiation on a Panalytical Empyrean diffractometer equipped with a focusing mirror on the incident beam and an X'Celerator linear detector. The scans were acquired in Bragg–Brentano geometry with a graphite monochromator on the diffracted beam. The magnetosomes were deposited on a silicon low background sample holder and air dried prior to measurement collection. The average crystallite size was calculated by applying the Scherrer formula [13], from the peak full width at half maximum (FWHM) corrected for instrumental broadening as determined on a standard LaB_6 sample. Phase identification was performed according to the Powder Diffraction Files (PDF) crystallographic database [14].

Transmission electron microscopy (TEM) images were recorded on a Hitachi H-7000 Microscope, operating at 125 kV, equipped with a W thermionic electron source and with a AMT DVC (2048x2048 pixel) CCD Camera. Prior to observation, the samples were dropped on a carbon-coated copper grid and air-dried. Chemical composition was determined by inductively coupled plasma atomic emission spectrometry (ICP-AES) using a Varian Liberty 200 spectrophotometer. Typical solutions for the analysis of Fe content were prepared by dissolving about 0.5 mg of magnetosome powder in 10 mL of a 1:1 mixture of concentrated HNO_3/HCl and diluting up to 50 mL. Thermal gravimetry (TG) and differential thermal analysis (DTA) were carried out using a Mettler-Toledo TG/SDTA 851 in the range 25-1000 °C under oxygen flow (heating rate = 10 °C/min, flow rate = 50 mL/min).

The magnetic properties of extracted MNs were investigated using a Quantum Design MPMS SQUID magnetometer operating in the temperature range 2 K – 300 K with an applied field up to 5 Tesla.

Measurements were performed on dried powder samples hosted in a Teflon sample holder. The recorded data were normalized for the effective amount of iron obtained by ICP analysis and the magnetization values are reported in terms of emu/g of iron. Zero Field Cooled-Field Cooled (ZFC/FC) curves were obtained by measuring the temperature dependence of the magnetization after cooling the sample in presence (FC) or in absence (ZFC) of applied magnetic field.

Hyperthermic Characterization

The hyperthermic properties of the extracted MNs were investigated through calorimetric measurements. The experimental set-up, composed by a 6 kW Fives Celes® power supply, a water-cooled induction coil and a series of variable capacitors (420 nF - 4.8 nF), is able to produce an alternate magnetic field with variable frequency ν in the range of 50–400 kHz and with field amplitude up to 19.1 kA/m. The field parameters used in this work (183 kHz, 17.0 kA/m) were chosen in order to operate within the physiological limit, i.e. $H \cdot \nu < 5 \cdot 10^9$ $A \cdot m^{-1} s^{-1}$, beyond which living tissues damages have been observed [15]. A screw cap vial containing the sample dispersion (about 0.46 g of iron oxide, being the 0.017% of the total weight) in agarose gel at 0.25% w/w was placed in the middle of the induction coil. The polystyrene sample holder was placed in a glass container thermostatized by circulating ethylene glycol, in order to keep the system at 37°C. The temperature kinetics curve, i.e. temperature as a function of time, of the sample was recorded by an optical fiber thermometer connected to a digital temperature recorder (Fotemp®) during the whole exposition to alternate magnetic field. The specific absorption rate (*SAR*) value was evaluated using the formula $SAR = \left(\sum_i m_i C_{pi} \middle/ m_{Me}\right) \cdot \left(\Delta T / \Delta t\right)$, where ΔT is the temperature increase in the time interval Δt, m_{Me} is the total mass of metal, m_i is the mass of the i-species and C_{pi} is the corresponding specific heat. The sum is extended to all the species in the sample. The measurements were performed in non adiabatic conditions and the $\Delta T/\Delta t$ values were evaluated from the initial slope ($t \rightarrow 0$) of the temperature kinetic curves, considering a Δt much shorter than the time constant of the thermalization circuit. Due to the low concentration of agarose, the specific heat of the gel was assumed to be equal to the one of water.

Relaxivity measurements

Longitudinal and transverse nuclear relaxation times, T_1 and T_2 respectively, were measured in both aqueous solution and agarose gel dispersion (1% w/w) over a wide range of frequency (10 kHz - 60 MHz). The NMR signal detection and generation was obtained with a Stelar Smartracer fast-field-cycling relaxometer in the range 10 kHz - 10 MHz and with a Stelar Spinmaster spectrometer in the range 10 MHz - 60 MHz. Saturation Recovery and Carr Purcell Meiboom Gill (CPMG) pulse sequences were used for T_1 and T_2 measurements, respectively. In order to have a quantitative estimation of the efficiency as MRI contrast

agent, the nuclear relaxivities were calculated as follows: $r_i = \left(\frac{1}{T_{i,meas}} - \frac{1}{T_{i,matrix}} \right) \Big/ C_{[Fe]}$ where *i* = 1, 2, and $C_{[Fe]}$ is the molar concentration of iron ions.

Contrast agent efficiency

Longitudinal and transversal relaxivities were measured in agarose gel phantoms (0.25%) containing different amounts of MNs using a Bruker Tomograph (Bruker, Karlsruhe, Germany) equipped with a 4.7 T, 33 cm bore horizontal magnet (Oxford Ltd., Oxford, UK). T_2 values were measured by a Multi Slice Multi Echo (MSME) sequence with TR = 2000ms, TE= 5.5 ms, N echoes=16, FOV= 3.5x3.5 cm^2, MTX = 128/128, Slice Thickness = 2.00 mm, N slice=4. T_1 values were obtained by a Magnetization Recovery sequence (RARE VTR) with TR ranging between 110 and 12500 ms and TE_{eff}=9.5 ms.

For *in vivo* tests, nude homozygote male mice (Harlan Laboratories, Udine, Italy) were kept under standard environmental conditions (temperature, humidity, 12 h/12 h light/dark cycle, with water and food *ad libitum*) under veterinarian assistance. Animals handling and surgery were performed following a protocol approved by the Animal Care and Use Committee of the University of Verona (CIRSAL), and by the Italian Ministry of Health, in strict adherence to the European Communities Council (86/609/EEC) directives, minimizing the number of animals used and avoiding their suffering. For tumor implantation, human glioblastoma-astrocytoma i.e. epithelial-like cell line (U87MG) purchased by ATCC (Manassas, VA), were cultured in Eagle's Minimum Essential Medium (EMEM) with 10% of Fetal Bovine Serum (FBS), 1% of a mix of penicillin/streptomycin 1:1 and 1% of L-glutamine 200 mM, in 25 cm^2 plates and incubated at 37°C in humidified air with 5% CO2. Media and L-glutamine were purchased by Sigma-Aldrich (Italy), while serum and antibiotic mix were acquired by GIBCO, Life Technologies, USA. When at confluence, cells were treated with trypsin-EDTA 1% (GIBCO, Life Technologies, USA), harvested and centrifuged at 1200 rpm for 5 min. The supernatant was discarded and cells pellet was resuspended in 1 mL of complete medium, placed in 75 cm^2 plates and incubated at 37°C and 5% of CO2 until 80% confluence was detectable.

One million U87MG cells, resuspended in 200 µL of sterile PBS, were subcutaneously injected in the right flank of anesthetized mice. Thirty days after inoculation of tumor cells, mice were monitored by MRI to measure the tumor size; when tumor volume reached about 100 µL, 1 mg of MNs diluted in 100 µL of PBS were injected directly into the tumor mass using an intradermal needle (21G).

For *in vivo* imaging, animals were anesthetized by 1% isofluorane inhalation in a mixture of oxygen and nitrogen. Animals were placed in prone position over a heated bed and inserted into a 3.5 cm i.d. birdcage r.f. coil. T_2 and T_2* weighted images were acquired to detect the tumor and the presence of MNs. T_2 weighted images were acquired using a RARE 3D sequence with TR = 1200 ms, TE_{eff} = 47.5 ms, FOV=

5x2.5x2.5 cm^3, NEX = 1, MTX = 256/128/32, Slice Thickness = 0.78 mm. T_2* weighted images were acquired using a FLASH sequence with TR = 400 ms, TE = 4.4ms, flip angle = 10°, FOV = 5x2.5 cm, NEX = 2, MTX = 256/128, NSLICES = 8, Slice Thickness = 2 mm.

References

1. **Davis ME, Chen ZG, Shin DM**. Nanoparticle therapeutics: an emerging treatment modality for cancer. Nat. Rev. Drug Discov. 2008; 7: 771-782; doi: 10.1038/nrd2614
2. **Colombo M, Carregal-Romero S, Casula MF, Gutiérrez L, Morales MP, Böhm IB, Heverhagen JT, Prosperi D, Parak WJ**. Biological applications of magnetic nanoparticles. Chem. Soc. Rev. 2012; 41: 4306-4334. doi: 10.1039/c2cs15337h
3. **Pankhurst Q, Thanh N, Jones S, Dobson J**. Progress in applications of magnetic nanoparticles in biomedicine. J. Phys. D. Appl. Phys. 2009; 42: 224001. doi: 10.1088/0022-3727/42/22/224001
4. **Santhosh PB, Ulrih NP**. Multifunctional superparamagnetic iron oxide nanoparticles: Promising tools in cancer theranostics. Cancer Lett. 2013; 336: 8-17. doi:10.1016/j.canlet.2013.04.032
5. **Arosio P, Thévenot J, Orlando T, Orsini F, Corti M, Mariani M, Bordonali L, Innocenti C, Sangregorio C, Oliveira H, Lecommandoux S, Lascialfari A, Sandre O**. Hybrid iron oxide-copolymer micelles and vesicles as contrast agents for MRI: impact of the nanostructure on the relaxometric properties. J. Mater. Chem. B 2013; 1: 5317-5328. doi: 10.1039/c3tb00429e
6. **Lartigue L, Innocenti C, Kalaivani T, Awwad A, Sanchez Duque MDM, Guari Y, Larionova J, Guérin C, Montero JLG, Barragan-Montero V, Arosio P, Lascialfari A, Gatteschi D, Sangregorio C**. Water-dispersible sugar-coated iron oxide nanoparticles. An evaluation of their relaxometric and magnetic hyperthermia properties. J. Am. Chem. Soc. 2011; 133: 10459-10472. doi: 10.1021/ja111448t
7. **Sanson C, Diou O, Thévenot J, Ibarboure E, Soum A, Brulet A, Miraux S, Thiaudière E, Tan S, Brisson A, Dupuis V, Sandre P, Lecommandoux S**. Doxorubicin loaded magnetic polymersomes: theranostic nanocarriers for MR imaging and magneto chemotherapy. ACS Nano 2011; 5: 1122-1140. doi: 10.1021/nn102762f
8. **Alphandéry E, Faure S, Seksek O, Guyot F, Chebbi I**. Chains of magnetosomes extracted from AMB-1 magnetotactic bacteria for application in alternative magnetic field cancer therapy. ACS Nano 2011; 5: 6279-6296. doi: 10.1021/nn201290k
9. **Blakemore R**. Magnetotactic bacteria. Science 1975; 190: 377-379. doi: 10.1126/science.170679

10. **Yan L, Zhang S, Chen P, Liu H, Yin H, Li H**. Magnetotactic bacteria, magnetosomes and their application. Microbiol. Res. 2012; 167: 507-19. doi: 10.1016/j.micres.2012.04.002
11. **Mannucci S, Ghin L, Conti G, Tambalo S, Lascialfari A, Orlando T, Benati D, Bernardi P, Betterle N, Bassi R, Marzola P, Sbarbati A**. Magnetic Nanoparticles from Magnetospirillum gryphiswaldense Increase the Efficacy of Thermotherapy in a Model of Colon Carcinoma. PLoS One 2014; 9: e108959. doi: 10.1371/journal.pone.0108959
12. **Grunberg K, Muller EC, Otto A, Reszka R, Linder D, Kube M, Reinhardt R and Schuler D**. Biomedical and proteomic analysis of the MN membrane in Magnetospirillum gryphiswaldense. Appl. Environ Microbiol. 2004; 70: 1040-1050. doi: 10.1128/AEM.70.2.1040-1050.2004
13. **Klug HP, Alexander LE**. X-ray Diffraction Procedures. Wiley: New York, 1974.
14. ICDD International Centre for Diffraction Data, 1601 Park Lane, Swarthmore, USA.
15. **Hergt R, Dutz S**. Magnetic particle hyperthermia. Biophysical limitations of a visionary tumor therapy. J. Magn. Magn. Mater. 2007; 311: 187-192. doi: 10.1016/j.jmmm.2006.10.1156
16. **Corrias A, Mountjoy G, Loche D, Puntes V, Falqui A, Zanella M, Parak WJ, Casula MF**. Identifying spinel phases in nearly monodisperse iron oxide colloidal nanocrystal. J. Phys. Chem. C 2009; 113: 18667-18675. doi: 10.1021/jp9047677
17. **Schieber MM**. Iron oxides and their compounds. In Experimental Magnetochemistry, Wohlfarth, EP (ed). North-Holland Publishing Company: Amsterdam, 1967.
18. **Dunlop DJ, Özedmir Ö** . Rock Magnetism: Fundamental and Frontiers. Cambridge University Press: Cambridge, 2001.
19. **Prozorov R, Prozorov T, Mallapragada SK, Narasimhan B, Williams TJ, Bazylinski D** a. Magnetic irreversibility and the Verwey transition in nanocrystalline bacterial magnetite. Phys. Rev. B. Phys. 2007; 76: 054406. doi: 10.1103/PhysRevB.76.054406.
20. **Aragón R, Buttrey DJ, Shepherd JP, Honig JM**. Influence of nonstoichiometry on the Verwey transition. Phys. Rev. B 1985; 31: 430-436. doi: 10.1103/PhysRevB.31.430
21. **García J, Subías G**. The Verwey transition - a new perspective. J. Phys. Condens. Matter 2004; 16: R145-R178. doi: 10.1088/0953-8984/16/7/R01.
22. **Batlle X, Labarta A**. Finite-size effects in fine particles: magnetic and transport properties. J. Phys. D. Appl. Phys. 2002; 35: R15-R42. doi: 10.1088/0022-3727/35/6/201
23. **Masotti A, Pitta A, Ortaggi G, Corti M, Innocenti C, Lascialfari A, Marinone M, Marzola P, Daducci A, Sbarbati A, Micotti E, Orsini F, Poletti G, Sangregorio C**. Synthesis and

characterization of polyethylenimine-based iron oxide composites as novel contrast agents for MRI. Magn. Reson. Mater. Phys. 2009; 22: 77-87. doi: 10.1007/s10334-008-0147-x

24. **Wang Y-XJ**. Superparamagnetic iron oxide based MRI contrast agents: Current status of clinical application. Quant. Imaging Med. Surg. 2011; 1: 35-40. doi: 10.3978/j.issn.2223-4292.2011.08.03

25. **Roch A, Muller RN, Gillis P**. Theory of proton relaxation induced by superparamagnetic particles. J. Chem. Phys. 1999; 110: 5403-5411. doi: 10.1063/1.478435

Chapter 2.A

Magnetic Nanoparticles from *Magnetospirillum gryphiswaldense* Increase the Efficacy of Thermotherapy in a Model of Colon Carcinoma

OPEN ACCESS Freely available online

PLOS ONE

Magnetic Nanoparticles from *Magnetospirillum gryphiswaldense* Increase the Efficacy of Thermotherapy in a Model of Colon Carcinoma

Silvia Mannucci[1], Leonardo Ghin[2], Giamaica Conti[1], Stefano Tambalo[1,3], Alessandro Lascialfari[3,4,5], Tomas Orlando[3,4,5], Donatella Benati[1], Paolo Bernardi[1], Nico Betterle[2], Roberto Bassi[2], Pasquina Marzola[6], Andrea Sbarbati[1,3]*

1 Department of Neurological and Movement Sciences, Human Anatomy and Histology Section, University of Verona, Verona, Italy, **2** Department of Biotechnology, University of Verona, Verona, Italy, **3** Consorzio Interuniversitario Nazionale per la Scienza e Tecnologia dei Materiali (INSTM), Firenze, Italy, **4** Department of Physics, University of Milano, Milano, Italy, **5** Department of Physics, University of Pavia, Pavia, Italy, **6** Department of Computer Science, University of Verona, Verona, Italy

Abstract

Magnetic nanoparticles (MNPs) are capable of generate heating power under the influence of alternating magnetic fields (AMF); this behaviour recently opened new scenarios for advanced biomedical applications, mainly as new promising tumor therapies. In this paper we have tested magnetic nanoparticles called magnetosomes (MNs): a class of MNPs naturally produced by magnetotactic bacteria. We extracted MNs from *Magnetospirillum gryphiswaldense* strain MSR-1 and tested the interaction with cellular elements and anti-neoplastic activity both *in vitro* and *in vivo*, with the aim of developing new therapeutic approaches for neoplastic diseases. In *vitro* experiments performed on Human Colon Carcinoma HT-29 cell cultures demonstrated a strong uptake of MNs with no evident signs of cytotoxicity and revealed three phases in the interaction: adherence, transport and accumulation in Golgi vesicles. *In vivo* studies were performed on subcutaneous tumors in mice; in this model MNs are administered by direct injection in the tumor volume, then a protocol consisting of three exposures to an AMF rated at 187 kHz and 23kA/m is carried out on alternate days, over a week. Tumors were monitored by Magnetic Resonance Imaging (MRI) to obtain information about MNs distribution and possible tissue modifications induced by hyperthermia. Histological analysis showed fibrous and necrotic areas close to MNs injection sites in mice subjected to a complete thermotherapy protocol. These results, although concerning a specific tumor model, could be useful to further investigate the feasibility and efficacy of protocols based on MFH. Magnetic nanoparticles naturally produced and extracted from bacteria seem to be promising candidates for theranostic applications in cancer therapy.

Citation: Mannucci S, Ghin L, Conti G, Tambalo S, Lascialfari A, et al. (2014) Magnetic Nanoparticles from *Magnetospirillum gryphiswaldense* Increase the Efficacy of Thermotherapy in a Model of Colon Carcinoma. PLoS ONE 9(10): e108959. doi:10.1371/journal.pone.0108959

Editor: Bing Xu, Brandeis University, United States of America

Received February 5, 2014; **Accepted** September 5, 2014; **Published** October 7, 2014

Funding: The authors wish to thank AIRC for the financial support (project number: 11993 Area: targeted therapy, type of grant: IG). The financial support of Italian MIUR through project FIRB Riname RBAP114AMK is also acknowledged. The funders had no role in study design, data collection and analysis.

Competing Interests: The authors report that they have no conflicts of interest.

* Email: andrea.sbarbati@univr.it

Introduction

Thermotherapy represents an effective tool for the treatment of many types of tumor but it is strongly hampered by poor specificity of the induced lesion [1,2,3]. Several approaches have been proposed to improve the efficacy of the technique: one of them is based on intratumoral delivery of magnetic nanoparticles (MNPs) followed by application of alternating magnetic fields (AMF) to increase the local temperature of the tissue thus the effectiveness of the method [3,4,5]. This approach is called magnetic fluid hyperthermia (MFH).

In 1963, the Italian scientist Salvatore Bellini reported the first description of magnetotactic bacteria. This subtype of organisms naturally produces magnetic iron-oxide nanoparticles and uses them as a compass for geomagnetic navigation to search for optimal growth conditions [6,7]; those nanoparticles have been over time referred as magnetosomes (MNs). A more complete description of magnetotactic bacteria was later reported [8].

Recently, MNs have been proposed as active agents in hyperthermia for cancer therapy [9,10]; moreover, MNs extracted from magnetotactic bacteria [11,12] are considered with increasing interest as therapeutic and diagnostic agents mainly because of their physical properties. It has been reported that, for an applied AMF of frequency and strength kept below the tolerance threshold limit of about 200 kHz and 100 mT respectively, the specific absorption rate (SAR) of the chemically synthesized nanoparticles, currently used in magnetic thermotherapy, is several orders of magnitude lower than the one of the biologically synthesized magnetosomes [9,10-13]. Due to their magnetic properties, MNs also show high transversal relaxivity [14], a feature that makes these MNPs highly efficient contrast agents for magnetic resonance imaging (MRI).

The bacterial strain considered in the present investigation, *M. gryphiswaldense*, is able to internalize iron in ionic state from the environment and to synthesize iron oxide nanoparticles (size range 35-50 nm) of cubic-octahedral shape [15,16]. This biological

process is extremely repeatable with a very low variance in terms of size and shape of resulting nanoparticles.

As mentioned before, MNs isolated from magnetotactic bacteria develop a high heating effect when exposed to AMF. Preliminary studies prove the possibility of using these MNs as therapeutic agents when delivered in tumors [4,10].

However, data on the therapeutic effect and biological interaction of MNs with living tissues are still scarce, and their toxicity has not been definitively assessed [17]; moreover, ultrastructural studies on the localization of nanoparticles in the intracellular compartments are absent [16-18].

In the present study, the interaction of MNs extracted from M. *gryphiswaldense* with tumor cells was investigated by using Human Colon Carcinoma cells (HT-29). Hyperthermia treatment of colorectal cancer is of particular interest for potential clinical applications: for this purpose we used a protocol that include molecular biology, histology, electron microscopy analysis and magnetic resonance imaging.

The interaction of MNs with tumor cells and their therapeutic potential was also investigated *in vivo* in nude mice. In order to assess the potential usefulness of MNs in magnetic thermotherapy, we monitored, by MRI an experimental model of colon carcinoma before and after the treatment with thermotherapy.

Materials and Methods

In vivo experiments: experimental design and thermotherapy protocol

Twenty-two nude homozygote male mice (Harlan Laboratories, Udine, Italy) were maintained under standard environmental conditions (temperature, humidity, 12 h/12 h light/dark cycle, with water and food ad libitum) under veterinarian assistance. Animals handling and surgery were performed following a protocol approved by the Animal Care and Use Committee of the University of Verona (CIRSAL), and by the Italian Ministry of Health, in strict adherence to the European Communities Council (86/609/EEC) directives, minimizing the number of animals used and avoiding their suffering.

In a preliminary study on a limited number of animals, one million HT-29 cells, resuspended in 200 µl of sterile PBS, were subcutaneously injected in the right flank of anesthetized mice. Ten days after inoculation of tumor cells, mice were monitored by MRI to measure the tumor size: animals whose tumor volumes ranged between 0.4 and 0.5 cm^3 were injected with MNs. We observed that usually it was possible to inject a total volume of about 200 µl by using 3 to 4 separate punctures without relevant leakage of fluid from the tumor mass. These findings were then used to design the experimental protocol.

A population of n = 22 mice was divided in two groups: control and experimental. The control group (n = 12) was further divided in three subgroups: the first subgroup (n = 4) was administered with 1 mg of MNs diluted in 200 µl of PBS and did not receive AMF exposure. Administration of MNs was performed by direct injection into the tumor mass using an intradermal needle (21G). The second subgroup (n = 4) was exposed to AMF without MNs administration. The third subgroup (n = 4) did receive neither thermotherapy nor MNs administration.

The experimental group (n = 10) received 1 mg of MNs diluted in 200 µl of PBS and was exposed to AMF on day 0 (immediately after injection), 2 and 4. The AMF apparatus yield a magnetic field of intensity 23 kA/m (~29 mT) with a frequency of 187 kHz. These values are very close to those used in human application of hyperthermia [19]. Mice were placed on a custom made animal holder under isofluorane anesthesia 1.5% (Forane, Abbott) and exposed to AMF for 20 min. A digital IR camera (Flir I7, Flir Systems, Italy) was used by the operator to record maps of heating distribution in the tumor and surrounding tissues.

All the mice were monitored by MRI at three time points: 24 h, one week and two weeks after MNs administration. The first and second points were chosen to evaluate the physiological distribution of MNs and acute effects induced by MFH inside the neoplastic mass, respectively. The last point was useful to check whether some kinds of alterations do occur after the treatment. Animals were then sacrificed and tumors excised for histological analysis. Three mice died during the first steps of the treatment, probably due to an overdose of anesthetic. Mice were sacrificed by isofluorane overdose and successively by neck dislocation. These methods were performed in according to D.L. 4 March 2014 n°26 of the Italian Ministry of Health.

Magnetospirillum gryphiswaldense culture

M. gryphiswaldense MSR-1 (DSM6361) purchased from Deutsche Sammlung von Mikroorganismen und Zellkulturen GmbH (Germany) was cultured in specific growth medium (optimized during the present study) containing 0.1 g KH_2PO_4, 0.15 g $MgSO_4*7H_2O$, 2.38 g HEPES, 0.34 g $NaNO_3$, 0.1 g yeast extract, 3 g soy bean peptone, and 1 ml EDTA-chelated trace element mixture. The medium contained also 27 mM potassium l-lactate as carbon source and 100 µM of ferric citrate as iron source [20]. A single colony of MSR-1 from agar plates was transferred to a tube containing 10 ml of liquid medium and grown with 100 rpm shaking at 28°C for 24 h. This inoculum was grown by four escalating volume transfers at a ratio of 10% (v/v) before being used as inoculum in a 5 L screw cap bottle culture. Culture was maintained at 28°C and agitated at 100 rpm for 24 h.

Purification of MNs

The purification of MNs was performed according to the protocol proposed by Grunberg [20] as follows: 1) lyses of 10 g of *M. gryphiswaldense* dry weight with 50 ml of 50 mM HEPES 4 mM EDTA (pH 7.4) using French-press (1.26 Kbar); 2) centrifugation at 680 g for 5 min to remove non lysated materials; 3) magnetic separation with magnetic column (MACS, Miltenyi Biotec); 4) MNs were eluted with 10 mM HEPES (pH 7.4), positioned on a scaffold of sucrose (55% w/w in 10 mM HEPES), MNs were centrifuged at 280,000 g for 12 h at 4°C and the pellet was incubated with 10 mM HEPES for 16 h at 4°C to allow for solubilization. After purification, MNs were dried for 5 h using a lyophilizer, irradiated with γ-rays (56 Gy for 84 min) and finally stored at -20°C.

Transmission electron microscopy (TEM)

Whole mount bacteria of different samples of MNs, extracted and purified, were fixed with glutharaldehyde 2% in Sorensen buffer pH 7.4 for 2 h, post-fixed in 1% osmium tetroxide in aqueous solution for 2 h, dehydrated in graded concentrations of acetone. At the end of dehydrating process, samples were positioned in a multi-well grid for electron microscopy and observed using an EM10 electron microscope (Zeiss, Oberkocken, Germany).

Scanning electron microscopy (SEM)

Specimens were fixed with glutharaldehyde 2% in 0.1 M buffered phosphate, dehydrated in graded ethanol, critical point dried (CPD 030, Balzers, Vaduz, Liechtenstein), fixed to stubs with carbon-based adhesive, sputtered with carbon by MED 010 coater (Balzers), and examined with an XL30 ESEM scanning electron

microscope (FEI Company, Eindhoven, Netherlands) equipped for Energy Dispersion Analysis of X-Ray (EDAX).

Dynamic light scattering (DLS)

Hydrodynamic radius of MNs was determined from a batch of 0,5 mg resuspended in 5 ml of HEPES 10 mM, ultrasonicated for 10 min and filtered using a 450 nm filter. DLS data were obtained using a He-NE 633 nm wavelength laser with a goniometric set of 173° (Malvern Instrument LTD, UK), normalized to unity and reported in logarithmic scale.

Susceptibility measurements

Magnetic measurements were carried out on powders (total MNs weight = 3.6 mg) using a Quantum Design SQUID MPMS XL-7 magnetometer. The zero field-cooled and field-cooled (ZFC/FC) magnetization curves were obtained for different applied magnetic fields in the temperature range 2–300 K, while the field dependent magnetization measurements were recorded in the range of ±5 T at both 2 K and room temperature.

Thermal properties of MNs

A sample containing 6.7 mg of purified, sterilized and lyophilized MNs was exposed to an AMF (187 kHz, 23 KA/m [~29 mT]) for 24 min. The increment of temperature was measured by an infrared camera Flir i7 (Flir System Inc., Italy). MNs were then diluted in distilled water at concentration of: 3 mg/ml, 2 mg/ml, 1 mg/ml, 0.5 mg/ml and exposed to AMF using the same frequency and field strength. In order to estimate the iron content of our nanoparticles, 4 mg of extracted MNs were dispersed in a 1:3 mixture of H_2SO_4 and HNO_3 and digested using a microwave digestor. The preparation was analyzed by Atomic Adsorption Spectroscopy (AAS, Perkin-Elmer 1100B).

Cancer cells culture

Human Colon Carcinoma cells (HT-29) purchased by ATCC (Manassas, VA), were cultured in Dulbecco's Modified Eagle Medium (DMEM) with 10% of Fetal Bovine Serum (FBS) and 1% of a mix of penicillin/streptomycin 1:1, in 25 cm^2 plates and incubated at 37°C in humidified air with 5% CO_2. Medium, serum and antibiotic mix were purchased by GIBCO, Life Technologies, USA. When at confluence, cells were treated with trypsin-EDTA 1% (GIBCO, Life Technologies, USA), harvested and centrifuged at 1200 rpm for 5 min. The supernatant was discarded and cells pellet was resuspended in 1 ml of complete medium, placed in 75 cm^2 plates and incubated at 37°C and 5% of CO_2 until 80% confluence was detectable.

In vitro MTT test

The cytotoxicity of MNs versus HT-29 cells was assessed by the loss of cells viability using 3-(4,5-dimethylthiazol-2-yl)-2,5-diphenyltetrazolium bromide) (MTT) test. Cells were plated at a density of $8*10^3$ cells per well in 96-well plates and incubated at 37°C in a mixture of air and 5% CO_2. After 24 h, the medium was replaced with fresh medium containing 1, 0.5 and 0.2 mg/ml of sterilized MNs, respectively. After 6, 12 and 24 h of incubation, 10 µl of MTT solution (Sigma, Italy) was added to each well. Plates were then incubated for additional 4 h (37°C, 5% CO_2). After the incubation time, plates were removed from the incubator and formazan crystals formed by the living cells were dissolved in 100 µl of dimethyl sulfoxide (Sigma, Italy). The multiwell was placed into a microplate reader (CHROMATE 4300 Awareness Technology, USA) for the measurement of absorbance at 570 and 630 nm. Four measurements of optical density (OD) were recorded for each sample and cell viability (%) was calculated with the following equation: $CV\% = (OD_{sample}/OD_{control}) \cdot 100$.

In vitro assay of MNs-uptake in cancer cells

A plate containing $2*10^5$ cells was placed in specific glasses multiwell for optical microscopy (Falcon BD, Italy) with 1 ml of growth medium. Cells were incubated at 37°C in humidified air with 5% CO_2 for 24 h. The growth medium was then discarded and replaced with fresh medium added with MNs at different concentrations: 1 mg/ml, 0.5 mg/ml, 0.2 mg/ml. Cells were incubated as previously described for 6 h, 12 h and 24 h. At each time point, the growth medium was discarded and cells were washed with 1 ml of 1X sterile phosphate buffer saline (PBS, GIBCO, Life Technologies, USA). Cells were fixed with 1 ml of 4% buffered formalin (Bioptica, Italy) for 30 min at room temperature. Once formalin was discarded, cells were double stained: Prussian Blue to visualize MNs and Nuclear Fast Red (Bioptica, Italy) to visualize nuclei. HT-29 samples were observed at 10X, 20X and 40X optical magnification using an Olympus microscope (BX-URA2, Olympus optical, GMBH, Hamburg, Germany) equipped with Image ProPlus software (Media Cybernetics, Rockville, USA).

TEM of cells incubated with MNs

HT-29 cancer cells were plated on a 2.4 cm culture glass, positioned on the bottom of 3.5 cm Petri dishes and incubated at 37°C in humidified air with 5% of CO_2 in 3 ml of growth medium. After 24 h, cells were fixed with glutaraldehyde 2% in Sorensen buffer pH 7.4 for 2 h, then post-fixed in 1% osmium tetroxide (OsO_4) in aqueous solution for 2 h, and finally dehydrated in graded concentrations of acetone. At the end of dehydrating process, glasses were stained with lead citrate and observed using a XL30 ESEM scanning electron microscope (FEI Company, Eindhoven, Netherlands).

MRI

MR images were acquired in order to monitor the tumor growth at days 1, 7 and 14 both for control and experimental groups. MRI was performed using a Bruker tomograph operating at 4.7 T, equipped with an actively shielded gradient insert (Bruker, Germany) having a maximum gradient strength of 40 G/cm. Animals were placed prone in a heated bed and a 3.5 cm i.d. birdcage coil was used to acquire the MR signal. T_2 and T_2* weighted images were acquired to detect the tumor and the presence of MNs respectively. T_2weighted images were acquired using a RARE 3D sequence with TR = 1200 ms, TE_{eff} = 47.5 ms, FOV = 5×2.5×2.5 cm^3, NEX = 1, MTX = 256/128/32, Slice Thickness = 0.78 mm. T_2*weighted images were acquired using a FLASH gradient echo sequence with TR = 400 ms, TE = 4.4ms, flip angle = 10°, FOV = 5×2.5 cm, NEX = 2, MTX = 256/128, NSLICES = 8, Slice Thickness = 2 mm.

Histology

After the last MRI acquisition, animals were sacrificed and tumors were excised, washed with PBS 0.1 M and fixed with 10% buffered formalin for 4 h. Afterwards, samples were dehydrated with increasing concentration gradient of alcohol from 70% to 100% and then with xylene for final processing. Tissues were embedded in paraffin and sections of 5 µm were obtained and dried at 37°C for 24 h. Sections were stained with Prussian blue and Nuclear Fast Red (Bioptica) to visualize iron nanoparticles and nuclei respectively.

Results

Morphology and physical properties of MNs

TEM of whole-mount bacteria, observed by backscattered electron detector, showed that MNs are organized in long chains (**Figure 1a**) along the major axis of each bacterium. **Figure 1b and 1c** show TEM images of MNs extracted from M. *gryphiswaldense*. The cubic-octahedral structure of crystals (mean Feret's diameter of iron core $=42\pm9$ nm) and the surrounding membrane (see arrows in **Figure 1c**) are clearly visible. AAS reported an iron content 0.167 mg Fe/g of extracted MNs, EDAX spectrum showed the absence of any metal except iron (**Figure 1d**).

A temperature increment of about 10°C was obtained in lyophilized MNs sample (6.7 mg) upon application of AMF for 24 min (**Figure 2a**). The increment of temperature consistently decreased with the concentration of MNs diluted in distilled water. Such enhancement amounted to about 5°C for a sample containing 3 mg/ml of MNs, to about 3°C for the sample containing 2 mg/ml and to about 2°C for the sample containing 1 mg/ml of MNs. The less concentrated sample, with 0.5 mg/ml of MNs, gained an increment of 1°C (**Figure 2b**).

The magnetic measurements of MNs revealed, as expected, a single-domain superparamagnetic-like behaviour with almost closed hysteresis at room temperature (**Figure 3a**) and irreversibility effect in ZFC/FC curves. The saturation magnetization, Ms ~40 emu/g, is compatible with values commonly reported for magnetosomes [13] and iron oxide nanoparticles in general. From the ZFC curve maximum displayed at low applied magnetic field (**Figure 3b**), the superparamagnetic blocking temperature is estimated to be $T_B \sim 300$ K or higher. In addition, a discontinuity in the magnetization curves as a function of temperature can be clearly seen at around 110 K (**Figure 3b**). This is possibly an evidence of the Verwey transition, a long range charge rearrangement that occurs mainly in transition metal oxides; such transition is also a signature for the existence of magnetite phase [21].

DLS

The distribution of the mean hydrodynamic radius shows a peak centered at 225 nm; this value is in good agreement with other data obtained on magnetosomes [22,23]. A second peak, centered around 40 nm can be attributed to small single nanoparticles (**Figure 4**).

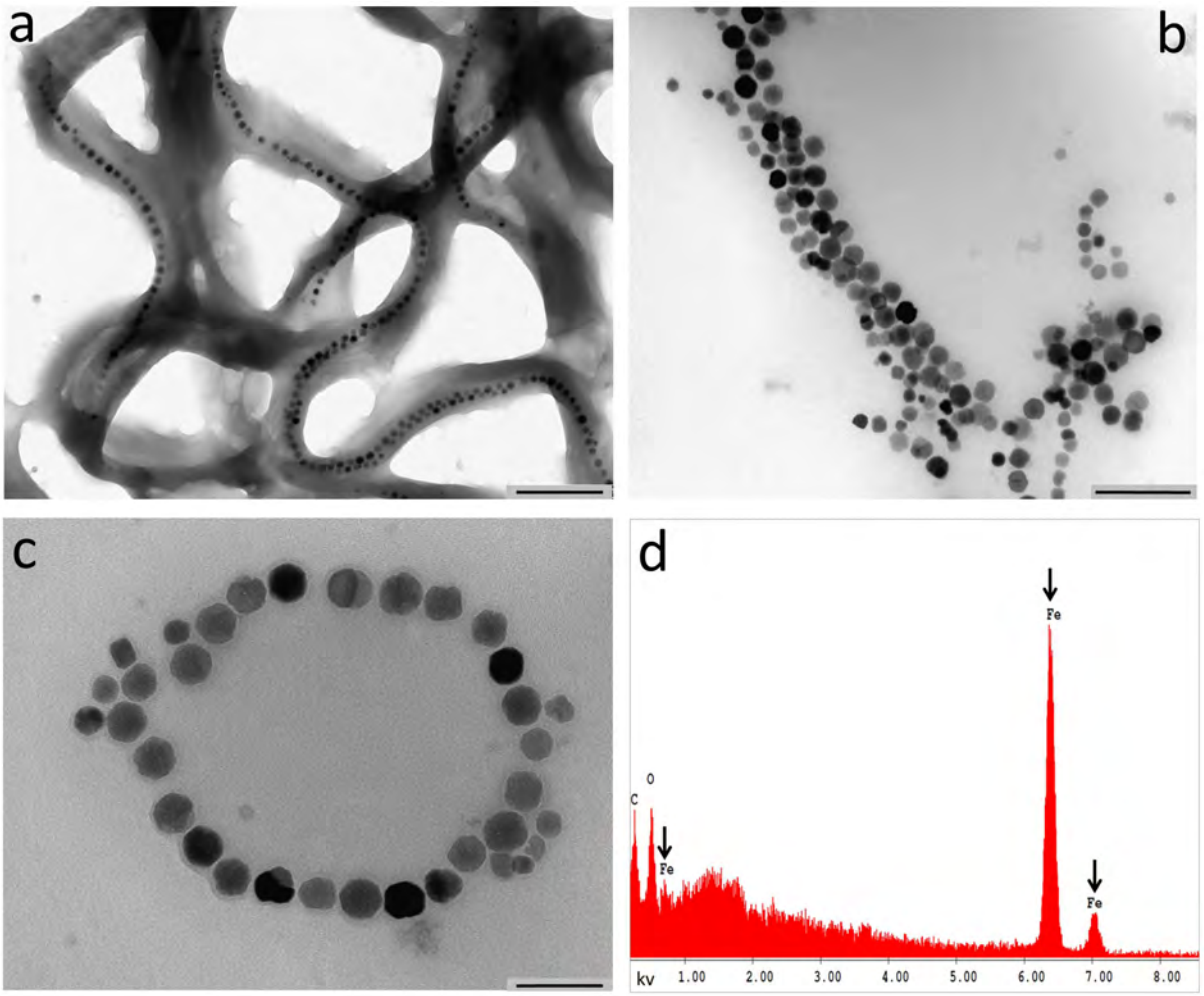

Figure 1. TEM of MNs. Panel a shows the organization of MNs in chains in the bacteria (scale bar, 500 nm). Panels b-c show that the typical conformation of chains is maintained after isolation of MNs. Scale bars: b>200 nm, c>100 nm. Panel d, X-ray microanalysis shows the iron content of the MNs.
doi:10.1371/journal.pone.0108959.g001

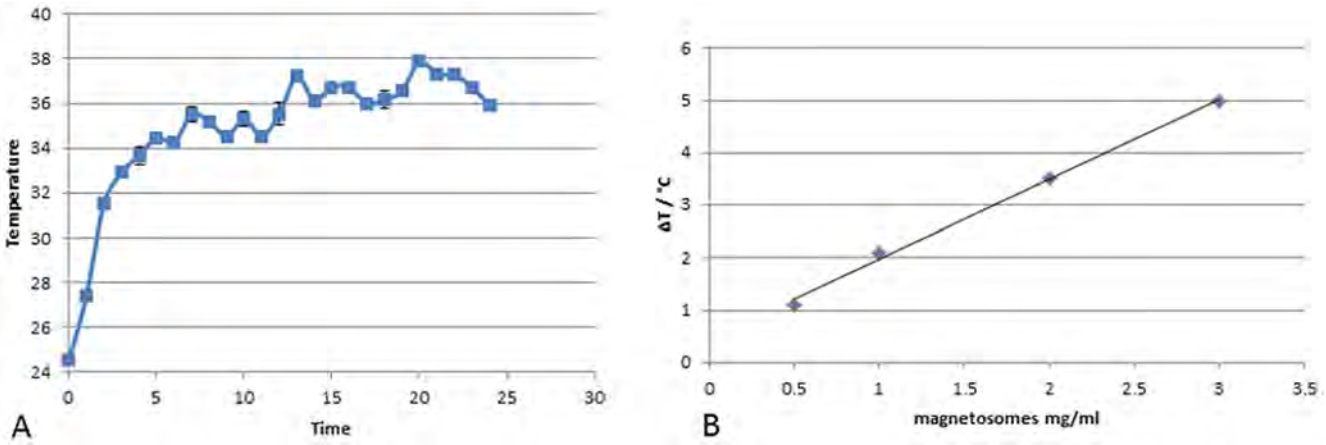

Figure 2. Thermal properties of MNs in alternate magnetic field. Variation of temperature of samples containing: (a) 6.7 mg of MNs lyophilized and (b) MNs diluted in distilled water at concentration of: 3 mg/ml, 2 mg/ml, 1 mg/ml, 0.5 mg/ml exposed to an AMF of 187 kHz (23kA/m) as a function of time, measured by infrared camera.
doi:10.1371/journal.pone.0108959.g002

In vitro uptake of MNs in HT-29 cancer cells

Prussian Blue staining demonstrated a strong uptake of iron nanoparticles by HT-29 cells as clearly depicted in **Figure 5**. MNs were detected primarily on the cell membrane although some were also visible within cytoplasm. The effect of varying MNs concentration in the culture medium and incubation time was investigated. Qualitative analysis of stained samples showed that, among the different concentrations tested (ranging from 0.2 to 1 mg/ml), the best condition for a good internalization was 0.2 mg/ml of MNs; the most effective time of incubation, with purified and sterilized MNs, was 24 h. Despite the high level of iron internalization, detectable changes of phenotype were not appreciable. (**Figure 5b-d**).

The internalization process of MNs was deeply investigated by TEM: representative images are reported in **Figure 6**. At least three kinds of interaction were found, likely corresponding to three different internalization steps. In the first step MNs were adherent to the cell membrane, with the formation of invaginations surrounding MNs chains (**Figure6 1b**). In the second step (**Figure 6 2b**), MNs were located into the cytoplasm, enclosed in vesicles. In the third step (**Figure 6 3b**), MNs were found into the Golgi apparatus and specifically into the innermost vesicles. In each of these steps, MNs were detectable as isolated particles, as small groups or short chains (**Figure 6 a,b**). MNs were found in vesicular formations similar to lysosomes presumably excreted from the Golgi apparatus. In some cases, these formations had a multi-vesicular aspect, while in others they appeared filled with material similar to multilamellar phospholipids. TEM images performed on HT-29 cancer cells showed the presence of chains of MNs in the cytoplasm, confirming the internalization process and the stability of the chain structure (**Figure 6c**).

SEM images did not show any appreciable alteration of the cellular surface in comparison to the controls (**Figure 6d**).

MTT test

MTT assay revealed that different amounts of sterilized MNs (1 mg/ml, 0.5 mg/ml, 0.2 mg/ml), when incubated for varying time periods with HT-29 cells, do not show statistically significant

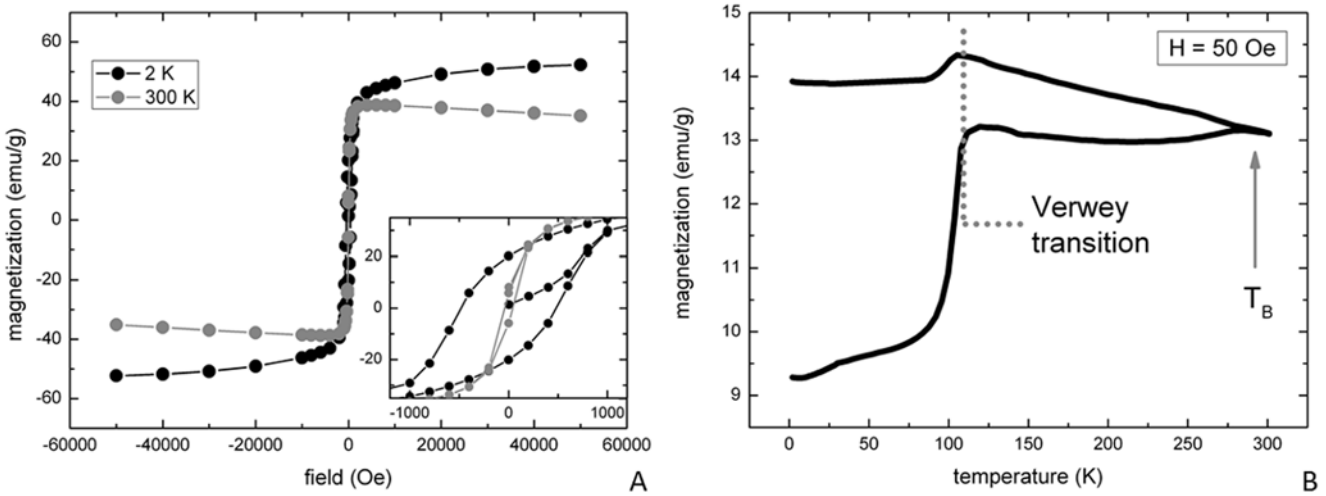

Figure 3. Susceptibility measurement. DC susceptibility measurements performed on a freeze-dried magnetosomes sample: (a) hysteresis loops at high (300 K) and low (2 K) temperature and (b) Zero Field-Cooled/Field-Cooled (ZFC/FC) curves collected at low field, H = 50 Oe.
doi:10.1371/journal.pone.0108959.g003

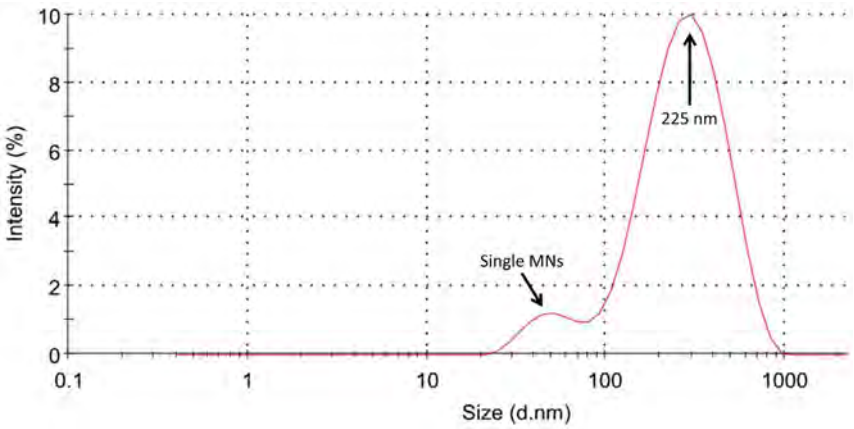

Figure 4. Dynamic Ligth Scattering. Scattered light intensity weighted magnetosomes size distribution in ultrasonicated and filtered HEPES solution; the two peaks centered at 225 nm and 40 nm are in good agreement with the size of chains of magnetosomes and single nanoparticles, respectively.
doi:10.1371/journal.pone.0108959.g004

negative effects (one way ANOVA, $p>0.05$) on cell viability at any dosage. The results are reported in **Figure 7**.

In vivo experiments

Thermal images were acquired in each mouse during the exposure to AMF by using an infrared camera. Temperature increments ranging between 2 and 3°C were observed in tumors treated with MNs. On the other side, negligible variations of thermal maps were recorded in tumors exposed to AMF that did not receive MNs injection.

MR images were acquired to monitor the development of tumor mass before and after hyperthermia treatment: as reported in **Figure 8**, several regions of strong signal drop are clearly visible. In T_2-weighted images, most of the neoplastic parenchyma was iso-intense. In the first subgroup of control group (**Figure 8A a-d, white stars**), the injection of MNs was clearly detectable and MRI showed areas of signal drop due to the presence of iron in the injection site. No other relevant changes were detectable in the signal intensity of the tumor parenchyma. This strong, negative enhancement, common to iron-based nanoparticles [24,25], sets the basis for potential application of MNs as negative contrast agents in MRI. This feature has relevance in the possible translation of these methods to the clinics for theranostics applications. Mice in the second subgroup of control group (**Figure 8B i-m**) showed moderate increase of signal intensity in small regions of the tumor, probably due to edema associated to necrosis caused by fast tumor growth. In the third subgroup of the control group (**Figure 8B n**), tumor appeared as a well defined mass with sharp boundaries, located in subcutaneous tissue (see arrow). Furthermore, a thin hyperintense layer was detectable at

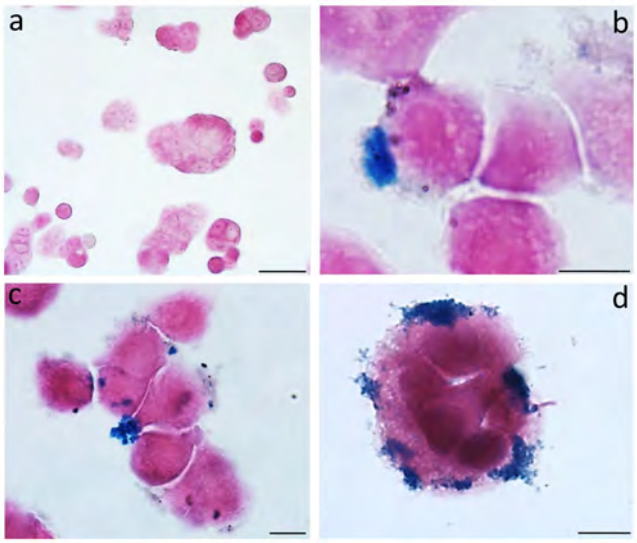

Figure 5. Cancer cell culture. The figure shows the untreated cells (a) and MNs-treated cells (b-d) observed after 24 h. Prussian Blue evidences the iron depots. Enlargement: a>50 μm, b>10 μm, c> 10 μm and d>10 μm.
doi:10.1371/journal.pone.0108959.g005

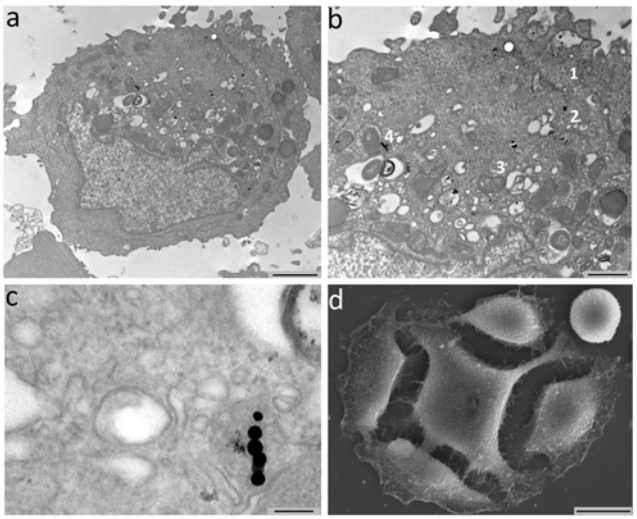

Figure 6. TEM shows the internalization of chains of MNs in HT-29 cancer cells. The chains that have penetrated in the cells are composed by 6-10 units of MNs and are positioned near the nucleus (Panel a). In Panel b, MNs are visible at cell membrane (arrows) or in the Golgi complex. Panel c shows the localization of the MNs in cytoplasmic vacuoles at high enlargement (Scale bars, a 2 μm, b 1 μm, c 120 nm, d 10 μm). Panel d shows a representative SEM image of HT-29 cancer cell (0.2 mg/ml MNs 12 h); no appreciable alterations of the surface are visible when compared to controls.
doi:10.1371/journal.pone.0108959.g006

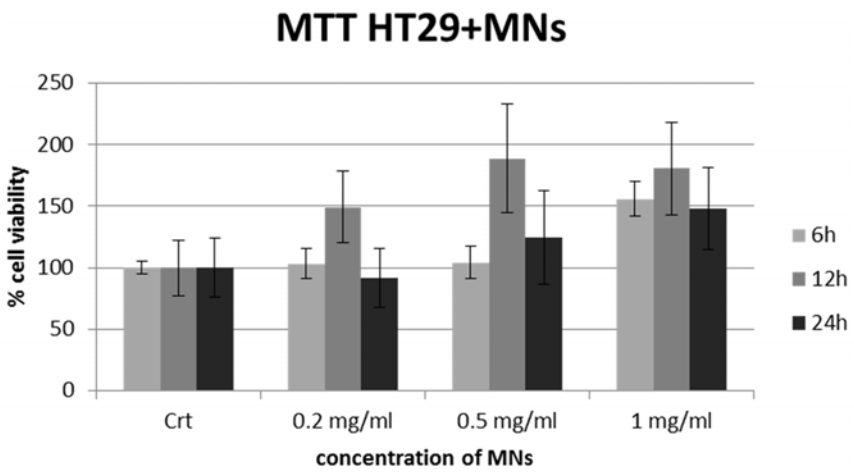

Figure 7. MTT assay on HT-29 cells after uptake with MNs. MTT assay shows a negligible cytotoxic effect of MNs: percent viability of cells incubated with MNs is expressed relevant to control cells.
doi:10.1371/journal.pone.0108959.g007

the edges of the tumor (**Figure 8B n**). Areas of high intensity were detectable and attributable to edema. In the central portion of the tumor, areas of low signal intensity, that could be identified as necrotic or hemorrhagic sites, were observable (see arrow). In the experimental group (**Figure 8A e-h**), tumors appeared as non-homogeneous masses characterized by regions of moderate loss of signal (probably corresponding to necrosis, see arrows), while areas with a higher loss of signal represent regions of MNs diffusion (white stars in **Figure 8A g, h**). Compared to the control group (third subgroup, **Figure 8B n**), there was an increment of both the edematous (hyperintense) and necrotic/hemorrhagic (hypointense) components. In some cases, these degenerative aspects were prominent in correspondence to the injection site.

MR images performed after a complete thermotherapy protocol (**Figure 8Ag**), did not show significant differences in signal intensity when compared to images acquired 24 h after MNs injection (white stars, **Figure 8A f**).

Histology

Histological examinations contributed in elucidating the effect of different treatments. Sections obtained from tumors treated with MNs and thermotherapy showed clear evidence of edematous and necrotic phenomena that were not evident in corresponding sections extracted from the control group (**Figure 9 A-C**). The injection site of MNs was clearly visible (white star, **Figure 9A**) and is characterized by degenerating unclustered cells intruded by extracellular matrix. Evidences of necrosis and fibrosis, induced by temperature enhancement, were significantly spread and detectable also in regions away from the site of injection (white star, **Figure 9C**). Tumors treated only with MNs (first subgroup, **Figure 9 D-F**) did not show appreciable differences compared to those of the second subgroup; in these tumors the site of injection was highlighted by histochemical staining. Iron nanoparticles marked with Prussian Blue staining were detected in subcutaneous areas and within the tumor mainly along the connective tissue septa or in perivascular locations. There, elongated cellular elements showing a marked uptake of MNs were present and possibly identifiable as macrophages (**Figure 9, D-F**). Tumors belonging to the third subgroup (**Figure 9, L-N**) were characterized by the presence of a thin connective capsule surrounded by a layer of adipose tissue, with some connective branches infiltrating the neoplastic mass. Tumor tissue showed the typical features of epithelial tumors: a solid mass with a high nucleo-cytoplasmatic ratio arranged in nests. Isolated areas of edema, necrosis or hemorrhage were visible usually in the central portion of the histological sample. Tumors of the second subgroup did not shown marked differences compared to those of the third subgroup with the exception of a moderate increase in edematous or necrotic components (**Figure 9, G-I**).

Concerning the persistence of the MNs, histological examinations performed two weeks after administration revealed the presence of MNPs next to the injection site, with spots also detectable in the surrounding parenchyma.

Discussion

A renewed interest in biomedical applications of MNPs has increased considerably over the past years, with MNs attracting widespread attention because of their prospective medical applications either as contrast agents for MRI, as heating mediators for cancer therapy by intracellular hyperthermia or as drug delivery carrier [14,26,27,28]. The efficiency of MNs as heating mediators is strongly dependent on the interaction with cells and the capability to cross the phospholipid membrane [29].

Recent studies on cancer proposed a new potential role of MNs as ''theranostics'' agents. The therapeutic efficacy of MNPs on mouse mammary carcinoma, glioblastoma, and prostate cancer demonstrated the feasibility and efficacy of this heating method, as well as a very low clearance rate of these nanoparticles from tumors, allowing for longitudinal treatment following a single magnetic fluid injection [3,30]. MNPs have been used in clinical trials with prostate cancer [4] and glioblastoma multiforme [2]. Although these studies proved that thermotherapy of tumors using MNPs can be safely applied, studies on the biological interaction between cells and MNPs are still poor.

The aim of this study was to analyze the interaction, both *in vitro* and *in vivo*, of tumor cells with MNs extracted from a strain of magnetotactic bacteria. Among different strains, we chose *M. gryphiswaldense* for its availability and lack of knowledge about its biological interaction with cells. TEM images on bacteria and isolated nanoparticles confirmed the cubic-octahedric shape and the organization in chains; DLS data, obtained on an homogeneous solution, showed the presence of clusters of about five elements along with a small number of single MNs. Some researches focused on chains length suggesting a relation between

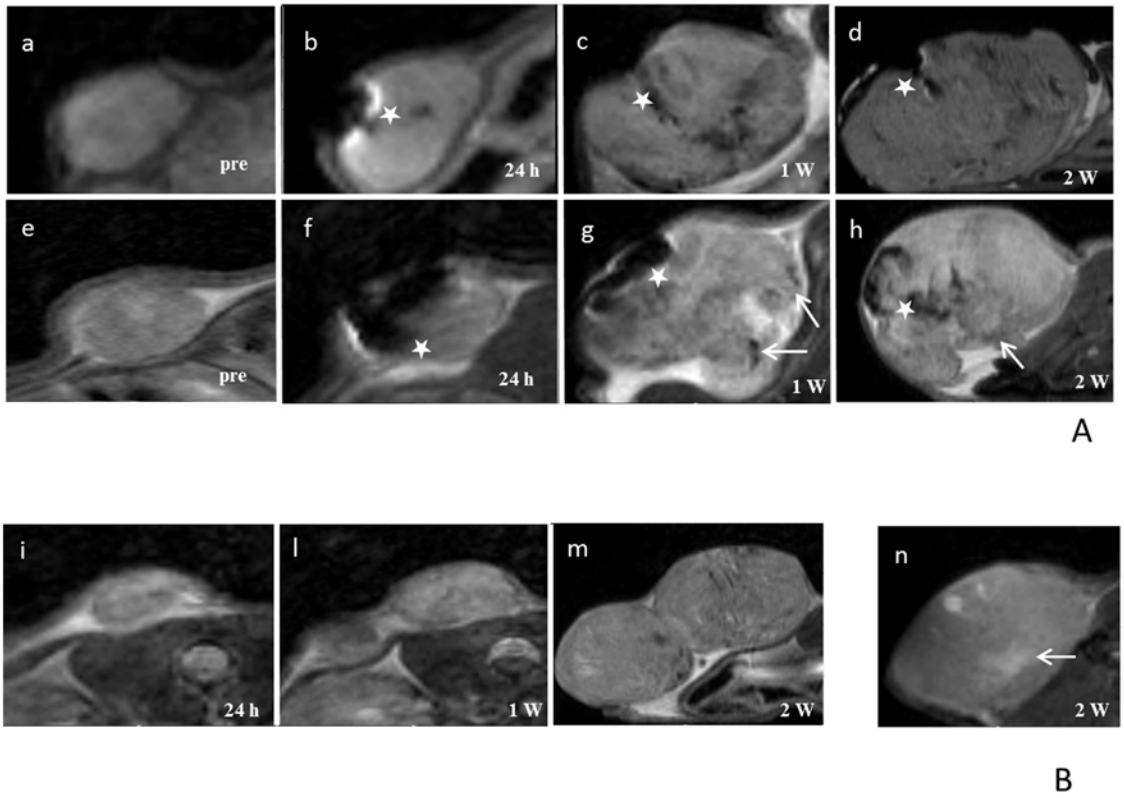

Figure 8. MR Images of representative animals. A) MRI Upper line: animal treated with MNs injection; images acquired before MNs injection (a), 24 h (b), one week (c) and two weeks (d) after MNs injection. Second line: animal treated with MNs injection with AMF; images acquired before MNs injection (e), 24 h (f), one week (g) and two weeks (h) after MNs injection. Magnetosomes are injected in tumor mass and MRI allows the detection of injection sites (white stars). B) animal treated with AMF; images acquired before 24 h (i), one week (l) and two weeks (m) after treatment. Control animal not treated with MNs and AMF; images acquired after two weeks (n).
doi:10.1371/journal.pone.0108959.g008

this parameter and the thermal properties of MNs. Our findings on ultrastructural analysis show that even though MNs extracted from bacteria are actually organized in chains of several elements as previously reported [10], they enter the intracellular space as single nanoparticles or as short chains.

Due to intrinsic limitations of standard histology, the interaction between MNs and tumor cells was investigated at a higher spatial resolution by electron microscopy. TEM images suggested a determined multistep pathway of MNs internalization. After adhesion to the phospholipid membrane, MNs were enclosed in vesicles, carried near the Golgi apparatus and finally included in vesicles that resemble a double layered membrane.

It is well known the high sensitivity of tumor cells to thermal variation. Temperatures ranging between 42 and 47°C degrees cause degenerative processes in neoplastic cells [25]. We tested thermal properties of MNs from *M. gryphiswaldense* included in a tumor mass with a protocol based on hyperthermia induced by an AMF and the reaction of the xenograft neoplasm was observed by MRI and histology. Contrary to what previously reported [9], in none of the animals belonging to the experimental group a complete remission of the tumor after the treatment was obtained. The lower AMF strength and frequency (~29 mT vs. 40 mT, 187 kHz vs. 183 kHz) as well as intrinsic magnetic properties of MSR-1 MNs, could be hypothesized as sources of differences against the results described in the literature.

However, we showed a local effect of MNs within tumors, with evidences of tissue necrosis both by histology and MRI (**Figures 8-9**). Furthermore, longitudinal MRI data demonstrated that MNs spread from the injection site through the surrounding tissue (**Figure 8A g, h**).

The physiological conditions for MNs migration still need to be clarified; a possible scenario involves the combination of passive transport mediated by reticuloendothelial system and active transport, mediated by macrophages. These processes resemble the transport pathways for conventional iron oxide nanoparticles, as described in [31].

The proposed experimental design, that involves both *in vitro* and *in vivo* examination, allows for non invasive follow up of the lesions at different time points. In addition, our results demonstrate that clinical MRI could be included in protocols based on theranostic employment of MNs: both the injection site and the necrotic areas of the tumor can be detected at once in a single MRI session. Theranostic is a combination of diagnostics and therapy and our data confirms that MNs exhibit some core characteristics of the so called "theranostic agents".

Our results do not match data available in the literature; it has to be noticed that different parameters used for hyperthermia, as well as different strain of magnetotactic bacteria used to obtain MNs and a different tumor model, are all features that could lead to some inconsistencies with previous discoveries. Future efforts will focus on the optimization of experimental conditions: initial tumor volume and MNs administration among others, to obtain a more homogeneous distribution of nanoparticles and improve the therapeutic effect of MFH based on MNs.

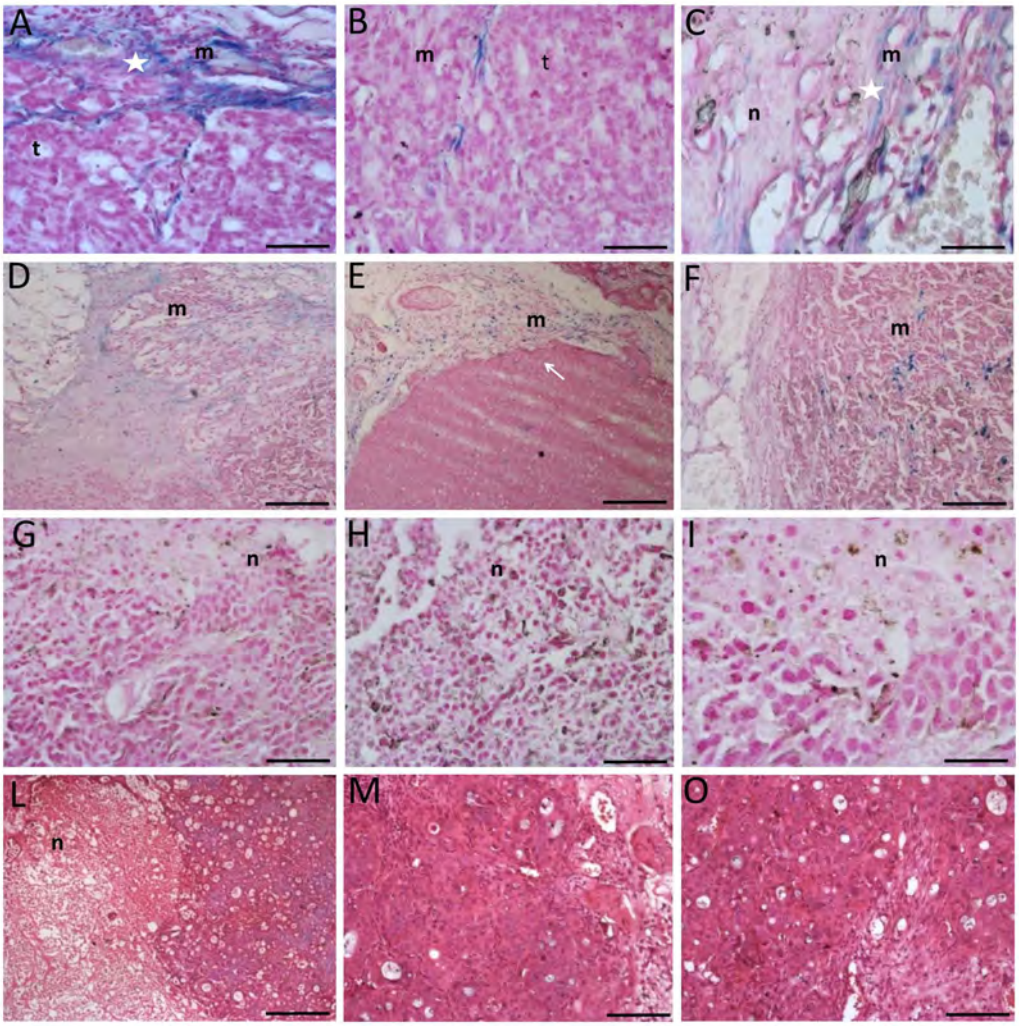

Figure 9. Histological analysis of tumors. In the Panel A-C histology of tumor of the experimental group is showed. Injection site is showed in Panel A while in Panel B the living tumor area is illustrated. In the Panel C injured tumor area is showed. In Panel E-F histology of first subgroup of the control group is presented. In Panel G-I histology of second subgroup of the control group is presented and in the Panel L-N is showed the third subgroup of the control group. The presence of MNs depots is detectable in injection sites (A). MNs are capable to migrate and spread in tumor tissue causing the formation of fibrotic and necrotic areas (B, C). Scale bars, A-C 60 μm, D-E 300 μm, F and G 120 μm, H-I 60 μm, I 300 μm, M 120 μm, N 60 μm. Legend: m = MNs, n = necrosis and t = tumor.
doi:10.1371/journal.pone.0108959.g009

Conclusions

This study reports a multimodal approach to assess biological properties of MNPs extracted from magnetotactic bacteria. A clearly detectable increase of temperature has been recorded by exposing MNs to an AMF. In addition, the temperature increase showed a good linear relation when measured in samples with increasing concentrations of MNs. When investigated *in vivo* by MRI, chains of our MNs are easily detectable if injected directly in the living tissue due to their iron content. This suggests a possible use of these nanoparticles as negative contrast agent or magnetic tracer. This behavior is useful to localize a bolus of MNs injected in a tumor mass: we were able to visualize the site of injection and follow the physiological distribution of nanoparticles within the tumor over time by MR imaging. Moreover, the same modality allows to record the effect of AMF exposures on tumors at different time points. Although we did not observe a reduction of tumor mass, areas of fibrosis and necrosis were visible at microscopic level.

Multimodal approach is a valuable strategy to characterize several aspects of MNs. Many more efforts are needed to further understand key aspects of their interactions with living systems [32,33,34], both healthy or not, but these results enforce the hypothesis of a potential, minimally invasive, therapeutic application of nanoparticles-based hyperthermia.

Author Contributions

Conceived and designed the experiments: AS PM RB AL. Performed the experiments: SM GC ST. Analyzed the data: SM GC ST LG TO DB PB NB. Contributed reagents/materials/analysis tools: LG NB RB PM TO ST SM GC. Wrote the paper: SM ST AS.

References

1. Johannsen M, Gneveckow U, Thiesen B, Taymoorian K, Hee Cho C, et al. (2007) Thermotherapy of prostate cancer using magnetic nanoparticles: flesibility, imaging, and three-dimensional temperature distribution. J Eur Uro 52: 1653–1662.
2. Maier-Hauff K, Nestler D, Niehoff H, Wust P, Thiesen B, et al. (2011) Efficacy and safety of intratumoral thermotherapy using magnetic iron-oxide nanoparticles combined with external beam radiotherapy on patients with recurrent glioblastoma multiforme. J Neurooncol 103: 317–324.
3. Jordan A, Scholz R, Maier-Hauff K, van Landeghem FK, Waldoefner N, et al. (2006) The effect of thermotherapy using magnetic nanoparticles on rat malignant glioma. J Neurooncol 78: 7–14.
4. Johannsen M, Gneveckow U, Thiesen B, Taymoorian K, Cho CH, et al. (2007) Thermotherapy of prostate cancer using magnetic nanoparticles: feasibility, imaging, and three-dimensional temperature distribution. Eur Urol. 52(6):1653–61.
5. Wust P, Hildebrandt B, Sreenivasa G, Rau B, Gellermann J, et al. (2002) Hyperthermia in combined treatment of cancer. Review. Lancet Oncol 3(8):487–97.
6. Bellini S (1963a) Su di un particolare comportamento di batteri d'acqua dolce (On a unique behavior of freshwater bacteria). Institute of Microbiology, University of Pavia, Italy.
7. Bellini S (1963b) Ulteriori studi sui "batteri magnetosensibili" (Further studies on magnetosensitive bacteria). Institute of Microbiology, University of Pavia, Italy.
8. Blakmore R (1975) Magnetotactic bacteria Science 190(4212):377–9
9. Alphandery E, Guyot F, Chebbi I (2012) Preparation of chains of MN, isolated from Magnetospirillum magneticum strain AMB-1 magnetotactic bacteria, yielding efficient treatment of tumor using magnetic hyperthermia. Int J Pharm 434: 444–452.
10. Alphandery E, Faure S, Seksek O, Guyot F, Chebbi I (2011) Chains of MN extracted from AMB-1 magnetotactic bacteria for application in alternative magnetic field cancer therapy. ACS Nano 23;5(8):6279–96.
11. Lee N, Kim H, Choi SH, Park M, Kim D, et al. (2011) MN-like ferrimagnetic iron oxide nanocubes for highly sensitive MRI of single cells and transplanted pancreatic islet. Proc Natl Acad Sci U S A 108–2662
12. Hartung A, Lisy MR, Herrmann KH, Hilger I, Schuler D, et al. (2007) Labeling of macrophages using bacterial MN and their characterization by magnetic resonance imaging. Journal of Magnetism and Magnetic Materials 311: 454–459
13. Hergt R, Hiergeist R, et al (2005) Magnetic properties of bacterial MN as potential diagnostic and therapeutic tools. Journal of Magnetism and Magnetic Materials 293: 80–86
14. Lisy MR, Hartung A, Lang C, Schüler D, Richter W, et al. (2007) Fluorescent bacterial magnetic nanoparticles as bimodal contrast agents. Invest Radiol 42(4):235–41.
15. Zeytuni N, Offer T, Davidov G, Zarivach R (2012) Crystallization and preliminary crystallographic analysis of the C-terminal domain of MamM, a magnetosome-associated protein from Magnetospirillum gryphiswaldense MSR-1. Acta Crystallogr Sect F Struct Biol Cryst Commun 68 (Pt 8):927–30.
16. Greene SE, Komeili A (2012) Biogenesis and subcellular organization of the MN organelles of magnetotactic bacteria. Curr Opin Cell Biol 24: 490–495
17. Xiang L, Wei J, Jianbo S, Guili W, Feng G, et al. (2007) Purified and sterilized MN from Magnetospirillum gryphiswaldense MSR-1 were not toxic to mouse fibroblasts in vitro. Lett Appl Microbiol 45: 75–81
18. Zeytumi N, Offer T, Davidov G, Zarivach R (2012) Crystallization and preliminary crystallographic analysis of the C-terminal domain of MamM, a MN-associated protein from Magnetospirillum gryphiswaldense MSR-1. Acta Crystallogr Sect F Struct Biol Cryst Commun 68: 927–930
19. Mustafa T, Zhang Y, Watanabe F, Karmakar A, Asar MP, et al. (2013) Iron oxide nanoparticles-based radio-frequency thermotherapy for human breast adenocarcinoma cancer cell. Biomater Sci 1, 870–880.
20. Grünberg K, Müller EC, Otto A, Reszka R, Linder D, et al. (2004) Biochemical and proteomic analysis of the MN membrane in Magnetospirillum gryphiswaldense. Appl Environ Microbiol.;70(2):1040–50
21. Senn MS, Wright JP, Attfield JP (2012) Charge order and three-site distortions in the Verwey structure of magnetite. Nature 481: 173–176.
22. Gojzewski H, Makowski M, Hashim A, Kopcansky P, Tomori Z, et al. (2012). Magnetosomes on surface: an imaging study approach. Scanning Vol. 34, 159–169.
23. Timko M, Dzarova A, Kovac J, Skumiel A, Jozefczak A, et al. (2009) Magnetic properties and heating effect in bacterial magnetic nanoparticles. Journal of Magnetism and Magnetic Materials, 321: 10 1521–1524.
24. Masotti A, Pitta A, Ortaggi G, Corti M, Innocenti C, et al. (2009) Synthesis and characterization of polyethylenimine-based iron oxide composites as novel contrast agents for MRI. MAGMA 22(2):77–87.
25. Valero E, Tambalo S, Marzola P, Ortega-Muñoz M, López-Jaramillo FJ, et al. (2011) Magnetic nanoparticles-templated assembly of protein subunits: a new platform for carbohydrate-based MRI nanoprobes. J Am Chem Soc. 133(13):4889–95.
26. Ito A, Shinkai M, Honda H, Kobayashi T (2005) Medical application of functionalized magnetic nanoparticles. J Biosci Bioeng 100(1):1–11.
27. Hilger I, Hiergeist R, Hergt R, Winnefeld K, Schubert H, et al. (2002) Thermal ablation of tumors using magnetic nanoparticles: an in vivo feasibility study. Invest Radiol. 37(10):580–6.
28. Won J, Kim M, Yi YW, Kim YH, Jung N, et al. (2005) A magnetic nanoprobe technology for detecting molecular interactions in live cells. Science. 309(5731):121–5.
29. Wilhelm C, Fortin JP, Gazeau F (2007) Tumour cell toxicity of intracellular hyperthermia mediated by magnetic nanoparticles. J Nanosci Nanotechnol. 7(8):2933–7.
30. Jordan A, Scholz R, Wust P, Fähling H, Krause J, et al. (1997) Effects of magnetic fluid hyperthermia (MFH) on C3H mammary carcinoma in vivo. Int J Hyperthermia. (6):587–605.27.
31. Saokar A, Braschi M, Harisinghani MG (2006) Lymphotrophic nanoparticle enchanced MR imaging (LNMRI) for lymph node imaging. Abdom imaging 31(6):660–7
32. Pan Y, Du X, Zhao F, Xu B (2012) Magnetic nanoparticles for the manipulation of proteins and cells. Chem Soc Rev 41(7): 2912–42.
33. Shin J, Lee KM, Lee JH, Lee J, Cha M (2014) Magnetic manipulation of bacterial magnetic nanoparticle-loaded neurospheres. Integr Biol (Camb) 6(5):532–9.
34. Liu F, Mu J, Bhattacharjya S, Yeow EK, Xing B (2014) Peptide-perylene diimide functionalized magnetic nano-platforms for fluorescence turn-on detection and clearance of bacterial lipopolysaccharides. Chem Commun; 50(47):6200–3.

Chapter 3.A:

Inhibition of tumor growth in a xenograft model of glioblastoma treated with MSR-1 Magnetosomes and Alternating Magnetic Field

Inhibition of tumor growth in a xenograft model of glioblastoma treated with MSR-1 Magnetosomes and Alternating Magnetic Field

Silvia Mannucci[1,2], Stefano Tambalo[2,3*], Giamaica Conti[2], Leonardo Ghin[4], Alessio Milanese, Anna Carboncino[2], Elena Nicolato[2], Maria Rosaria Marinozzi[2]*

Donatella Benati[2], Roberto Bassi[4], Pasquina Marzola[1], Andrea Sbarbati[2,3]

1. Department of Computer Science, University of Verona, 37134 Verona, Italy,

2. Department of Neurological and Movement Sciences, Human Anatomy and Histology Section, University of Verona, Strada Le Grazie 8 I-37134, Verona, Italy.

3. Consorzio INSTM, Via G. Giusti 9, I-50121 Firenze, Italy.

4. Department of Biotechnology, University of Verona, Strada Le Grazie 15, I-37134, Verona, Italy.

Abstract

Glioblastoma multiforme (GBM) is the most common and the most aggressive malignant primary brain tumor in humans. Current treatments include surgery, radiation therapy and chemiotherapy, sometimes supplemented with novel therapies but despite recent advances, survival of patients remains poor. Magnetic Fluid Hyperthermia (MFH) involves the use of iron-based magnetic nanoparticles inserted into the tumor mass to selectively heat malignant tissues. Recently, some clinical trials and experimental MFH treatments with synthetic magnetic nanoparticles have been conducted by some research units in humans.

In a previous work we have tested the hyperthermic properties both *in vitro* and *in vivo* of magnetosomes (MNs), magnetic nanoparticles naturally produced by magnetotactic bacteria: aim of this paper was to develop a protocol for MFH based on magnetosomes and test their therapeutic potential on a xenograft murine model of GBM. Subjects treated with MNs were exposed three times in a week for 20 minutes to an alternating magnetic field (AMF) with strenght of 29 mT and frequency of 110 kHz. MR imaging was used to map the distribution of nanoparticles and the efficacy of the treatment by measuring tumor volumes. Alterations of MR signal in tumor tissues that were visible at imaging were then confirmed by histology and a sensible inhibition of the tumor growth was finally observed in animals exposed to AMF who received MNs, compared to controls.

The superparamagnetic behaviour of MNs enable their visualization within the tissues by MRI; moreover they can be used as thermal energy source when exposed to alternating magnetic fields. Our results suggest that magnetosomes could be effectively considered as theranostic agents candidates for hyperthermia treatments based on iron oxide nanoparticles.

Introduction

Glioblastoma multiforme (GBM) is the most frequent and malignant type of glioma, with a mean survival of less than 15 months despite the advances in diagnosis and treatments now available [1, 2]. Novel therapeutic agents and approaches to increase the survival rates, and eventually cure this type of disease, are highly needed.

In oncology, the term hyperthermia refers to the treatment of malignant diseases by administering heat in various ways. The process of rising body temperature, either locally or globally for medical purposes, is usually applied as an adjunct to an already established treatment modality (radiotherapy and chemotherapy). Temperatures in the range of 40–46°C are aspired to trigger cancer cells apoptosis by temperature driven alterations in molecular pathways, although some restraints are to be considered: local temperatures should be maintained under 44°C to avoid damage to tissues surrounding the target while the whole body temperature should remain under 42°C, which is the upper limit compatible with life [3, 4]. Conventional thermotherapy procedures use different energy sources for the generation of heat within the tissue: radiofrequency waves, ultrasound and electric or magnetic fields [5, 6]. The cellular effect of thermal energy deposition is very complicated. Briefly, hyperthermia may kill or weaken tumor cells and is controlled to limit effects on healthy cells. Tumor cells are characterized by a disorganized and compact vascular structure which negatively impacts on tissue perfusion. This reduces their capabilities to efficiently dissipate heat induced by energy transfer and is proven that intense heating will cause denaturation of proteins and other biochemical consequences (slowed cell division, altered molecular pathways, inhibited synthesis of proteins) that ultimately lead to cell apoptosis [7]. On the other hand, healthy tissues around tumor can more easily maintain temperature in the physiological range and compensate for mild heating stress therefore minimizing the effects of hyperthermia [3].

A new nanotechnology based thermotherapy also referred to as magnetic fluid hyperthermia (MFH), represent a further development in the area and is currently under testing in some clinical and preclinical trials [6, 8, 9]. The thermal energy is delivered to the target region by superparamagnetic iron oxide nanoparticles exposed to an alternating magnetic field; when MNPs are injected in the tumor and an alternating magnetic field is applied, the tumor temperature rises and results in thermal ablation of tumor cells [10].

Recent studies report that MNPs such as magnetite, hematite and maghemite are the most frequently investigated nanoparticles for biomedical applications because of their biocompatibility [11]. We have developed a murine model of subcutaneous glioblastoma injecting U87MG cancer cells, and treating the animals with magnetosomes (MNs): magnetite nanoparticles that are naturally produced by magnetotactic bacteria [12, 13, 14]. These magnetic agents, extracted from *Magnetospirillum gryphiswaldense,* are largely described in the literature and are well characterized in terms of magnetic properties, interactions with living tissues and thermal efficiency when subjected to alternating magnetic field [15, 16, 17]. Our previous

findings [16] suggested a possible application of MFH protocols based on magnetosomes; the aim of this work is to further investigate the biocompatibility of MNs on cancer cell cultures and quantitatively evaluate the outcome of intratumoral heating therapy in a xenograft model of glioblastoma.

Results

Cellular assay to determine uptake of MNs by U87MG cancer cells

Magnetotactic bacteria observed by backscattered electron detector (Figure1A), showed the cubo-octahedral structure of included MNs crystals and their organization in chains (Figure1B), as reported by Mannucci et al. [16]

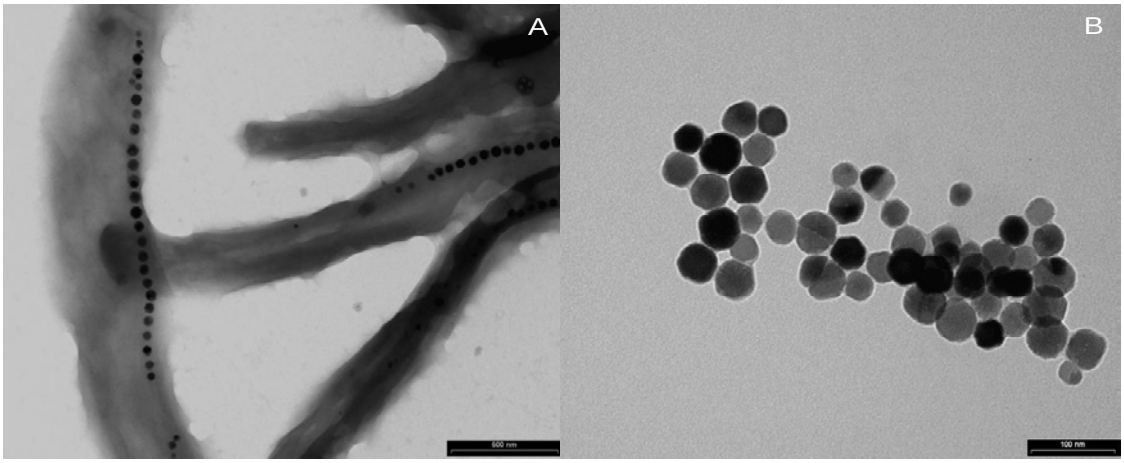

Figure 1: **TEM of MNs.** A) TEM of whole-mount of bacteria (scale bar, 500 nm). B) MNs after isolation of *M. gryphiswaldense.*

Figure2 shows the uptake of iron nanoparticles by U87MG cancer cells. MNs are distributed on the cellular membrane, within the cytoplasm and near the nucleus. The effect of varying MNs concentration in the culture medium and incubation time was investigated. Qualitative analysis of stained samples showed that the best condition for a good internalization was 0.2 mg/ml of MNs; the most effective time of incubation, with purified and sterilized MNs, was 24 h.

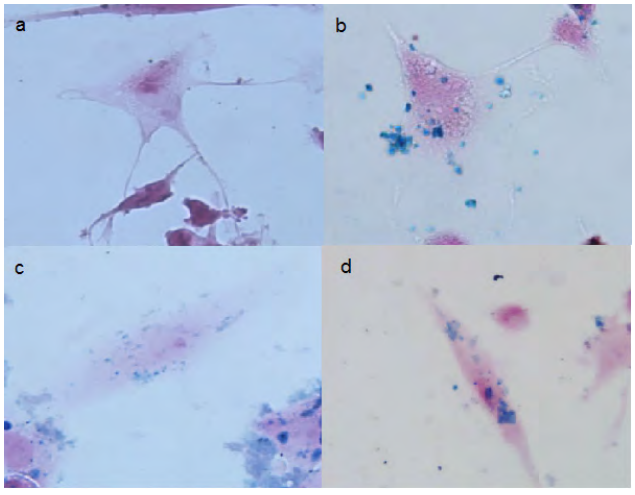

Figure 2: Cellular uptake a) untreated cells, b) MNs-treated cells (b-d) after 24 h. Prussian Blue evidence the iron depots.

Transmission Electron Microscopy was used to investigate the homing of MNs. Representative TEM images are reported in Figure3: chains of MNs are bound on the internal surface of small vesicles inside the cytoplasm and close to the nucleus.

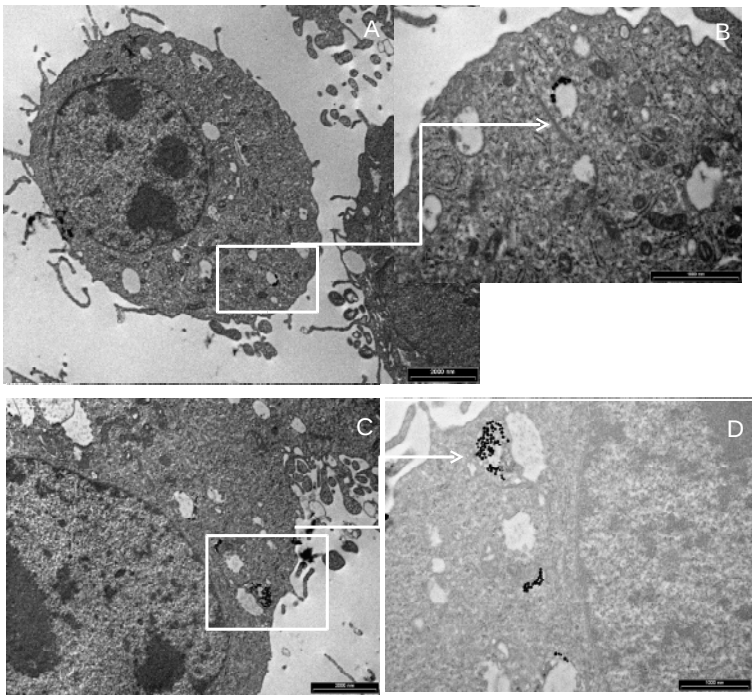

Figure 3: TEM of the internalization of MNs with U87MG cells. In panel a-d, MNs are visible in cytoplasm vacuoles.

MTT test

MTT assay revealed that different amounts of sterilized MNs (1 mg/ml, 0.5 mg/ml, 0.2 mg/ml), when incubated for varying time periods with U87MG cells, show a moderate though negligible negative effects on cell viability at the lower investigated dosages. The results are reported in Figure 4.

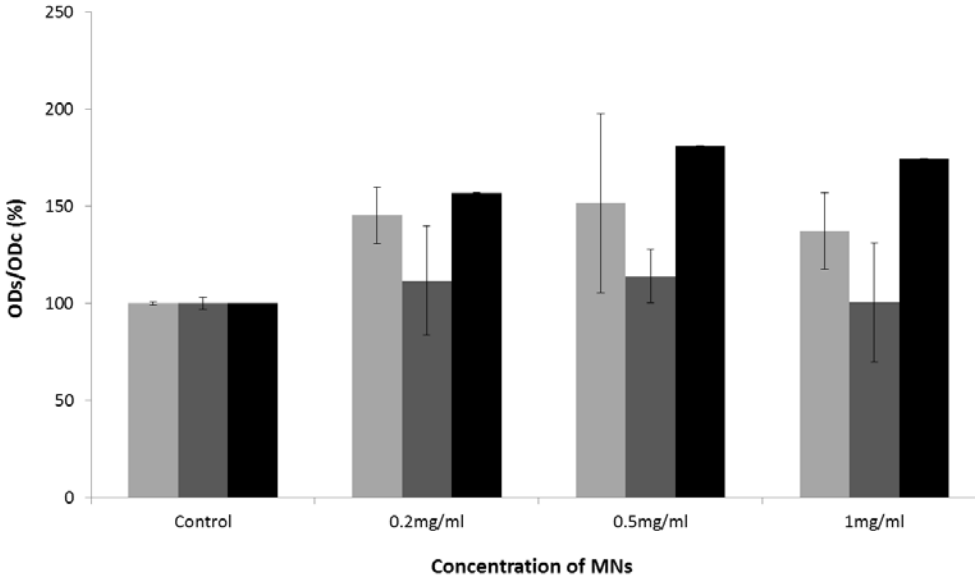

Figure 4: MTT assay on U87 MG cells after with MNs. MTT assay shows a negligible cytotoxic effect of MNs: percent viability of cells incubated with MNs is expressed relevant to control cells.

In vivo experiments

Temperature variations in animals treated with AMF were measured during the exposure both with thermal IR camera and optical fiber probes. Figure 5A is a thermal map acquired while the animal was placed inside the coil; the increased temperature of the tumor is clearly visible on the right flank as indicated by the arrow. Two ROIs on the thermal maps were placed by the operator to calculate differential temperature between body and tumor immediately after the treatment (Figure 5B). Despite the reliability of the measure, it was not possible to record thermal maps for all subjects: some major issues as anatomical localization of the tumor and subsequent positioning of the animal inside the coil did prevent the tumor mass to be visible through the viewfinder of the camera. Temperature variations were sampled by optical probes every 10s for the whole exposure time and recorded for later processing. Figure 5C shows ΔT expressed as mean ± sem for the two channels, tumor (red) and body (blue), as a function of time. Decrease in body temperature is due to the inner temperature of the induction coil and anesthetics, which induce mild hypothermia. A moderate heating of the tumor mass is visible and the difference with the measured body temperature becomes statistically significant after about 8 minutes of exposure, as reported in Figure 5D, which shows the associated 1–*p* value of the t-test. When tumors were treated only with AMF, without MNs, intratumoral temperature increase was not detectable.

A

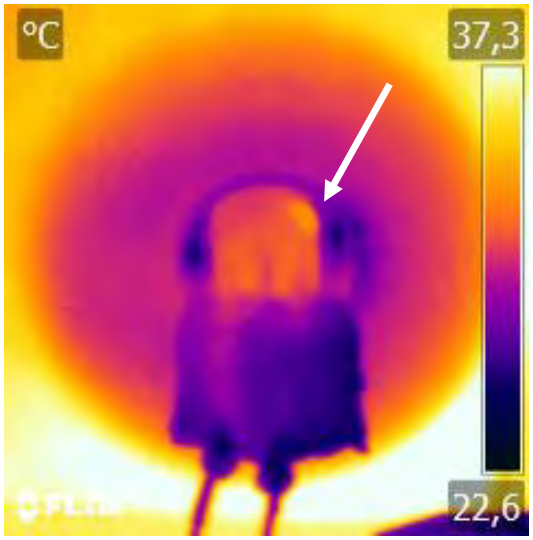

B

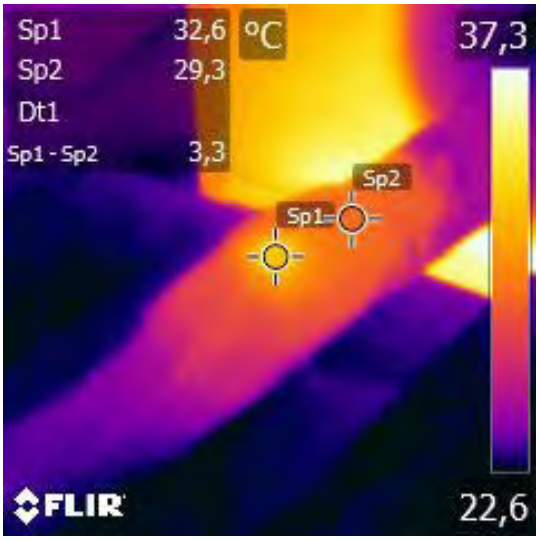

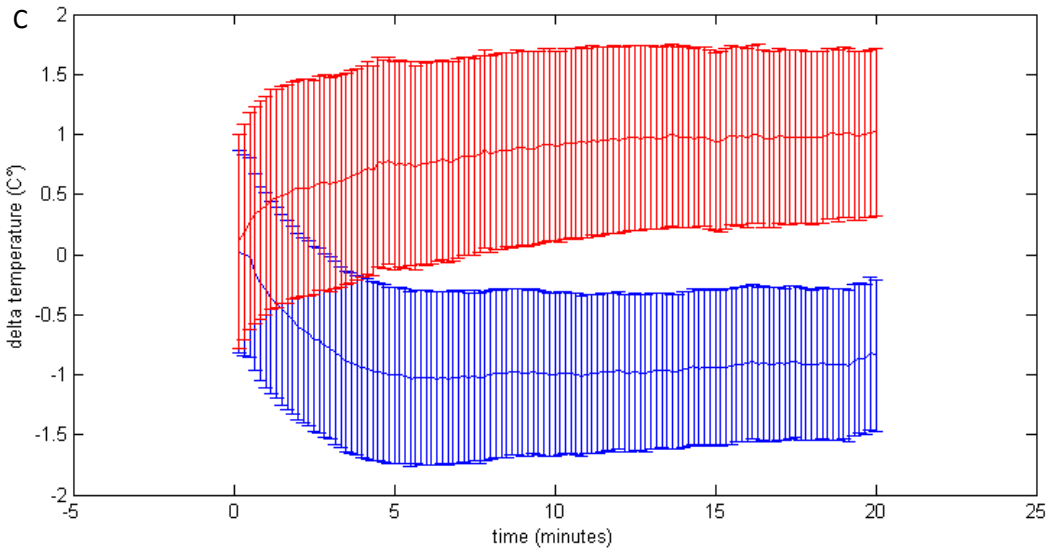

Figure 5: Analysis of temperature within tumor mass. Panel a show the thermal map acquired with the animal placed inside the coil. Panel b Two ROIs on the thermal maps of temperature between body and tumor immediately after the treatment. Panel c shows ΔT expressed as mean ± sem for the two channels, tumor (red) and body (blue) as a function of time. Panel d are the measure of body temperature becomes statistically significant after about 8 minutes of exposure, (1 – p value of the t-test).

Volumetric T_2w MRI images were obtained for each subject both for experimental and control groups. A first set of images was necessary to assess the initial volume of the tumor and lately used as reference to estimate the growth rate. Immediately after the administration of MNs, but prior to hyperthermia treatment, a second set of images was acquired to localize MNs and saline bolus within the tumor masses for group M and S, respectively. An additional set of images was acquired immediately after the treatment (1w) and one week later (2w) to evaluate efficacy of the therapy and estimate the final volume of tumors. For each experimental group, representative MR images of the development of U87MG tumors are reported in Figure 6. The first row (Figure 6a-b) shows the tumor before and after the injection of MNs. Panel c shows the almost complete remission of the tumor after MFH treatment, with only a thin layer of malignant tissue still visible. This effect was reported for two subjects in group HT, while the remaining showed only minor signs of tissue damage at macroscopic level. Panel d exhibit an evident progression of the disease with the presence of new neoplastic tissue one week after the last exposure. The middle row (Figure 6e-h) shows the progression of tumor in group M. These mice did not receive any MFH treatment. MNs inside the tumor mass two weeks after the administration are clearly detectable by MRI as dark spots, as indicated by the arrow. The bottom row (Figure 6i-n) report the growth of tumors for group S, administered with saline only. At 2w time point the MR signal of the mass is inhomogeneous, with signs of tissue degeneration marked by moderate areas of hyperintensity.

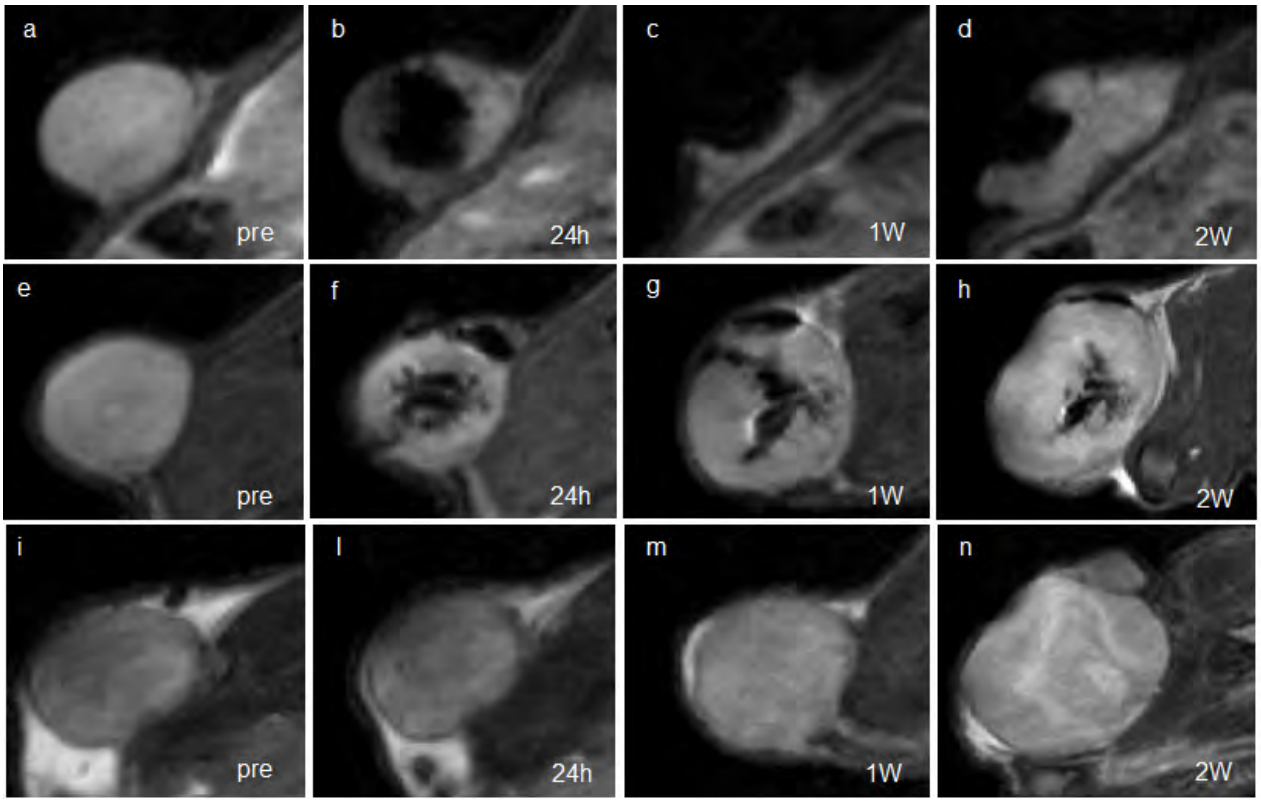

Figure 6: MR images of representative animals. Upper line: animal treated with MNs injection with AMF; images acquired before MNs injection (a), 24 h (b), one week (c), two weeks (d) after MNs injection. Second line: animal treated with MNs injection; images acquired before MNs injection (e), 24 h (f), one week (g), two weeks (h) after MNs injection. Third line: animal treated with saline injection; images acquired before saline injection (e), 24 h (f), one week (g), two weeks (h) after saline injection.

Tumor size for the three experimental groups as a function of time is reported in Figure 7. Values expressed as percentage of the initial size, measured before administration of magnetosomes or saline, for each subject. Data were then grouped and reported as Mean±SEM. At the first time point, upon completion of MFH therapy, the growth rate of group HT is reduced when compared to control groups, with values ranging from 161±23%, 314±33% and 300±36% for groups HT, M and S. One week later, at time point 2w, a similar trend was observed, with 371±58% (HT), 602±106% (M), 626±124% (S). Statistical significance was tested among the three groups by one way ANOVA: average growth rate for group HT is significantly different from both M and S at 1w ($p < 0.01$), while no differences were found between the two control groups: MNs injection alone showed a similar growth of the tumors compared to the untreated ones. At the second time point (2w) these differences are not statistically significant.

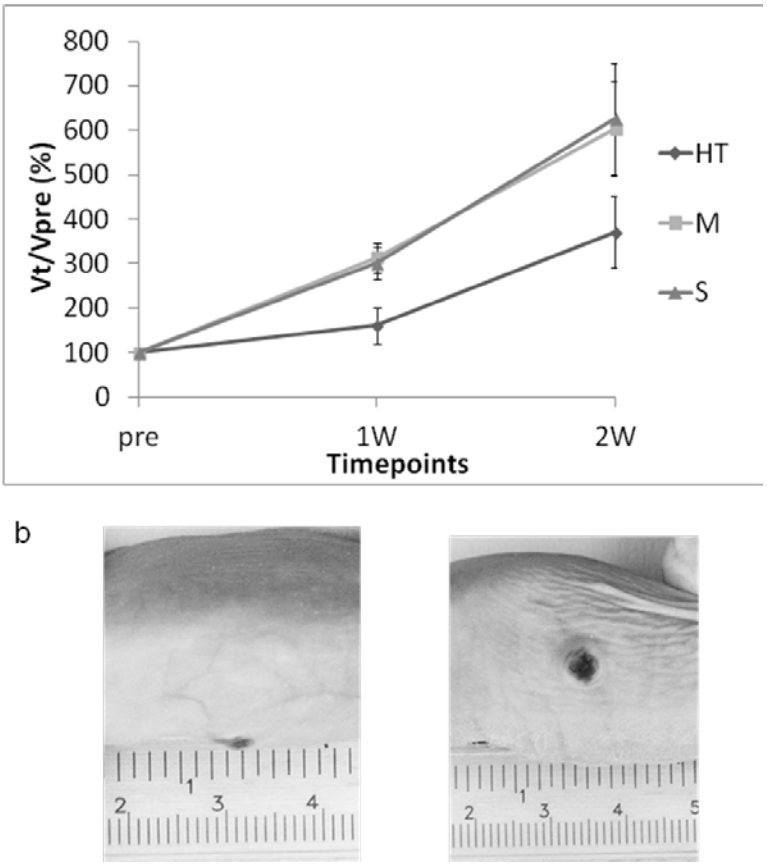

Figure 7: Effects of magnetic fluid hyperthermia with MNs and AMF. (a) Repeated application of AMF over a week on xenograft U87MG tumors led to a marked reduction of volume increase in group HT compared to untreated ones (1w, $p<0.01$). One week after the last exposure (2w), growth rates are not statistically different among the experimental groups. (b) Tumor tissue damage caused by thermal energy release of MNs under AMF. Tumor was almost completely disappeared, with eschars and tissue loss localized and limited to tumor tissue loaded with iron nanoparticles. No signs of damages to the surrounding healthy tissue were detected.

Histological evaluation of tumor mass

Upon completion of the last MRI acquisition on day 14, animals were sacrificed for histological processing of the tumor masses. Slices were stained with Prussian Blue and Nuclear Fast Red to label iron cores and nuclei of cells: blue staining was found exclusively in tumors injected with MNs, as expected.

Histology of group HT showed areas of high concentration of MNs, corresponding to the multiple injections sites, that were clearly identified by blue staining. Necrosis is visible in different portions of tumor slices and is characterized by a paucity of cells and the presence of thin collagen fibers that substitute dead tissue. Moreover, the presence of nanoparticles depots within the edges of necrotic lesions, could be an evidence of the effectiveness of hyperthermic treatment associated to the administration of MNs (Figure 8 a-b).

Histological sections of tumors treated with magnetosomes but not exposed to AMF (group M, Figure 8 c-d) show that MNs are evenly distributed across the whole mass. Nanoparticles were found next to injection's sites, with an almost homogeneous distribution also in the parenchyma, indicating the good diffusion through the capillaries. No evident signs of cytotoxic effects were detected.

Tumors treated with sterile saline solution (group S, Figure 8 e-f) exhibit little to none modifications in the parenchyma, with a good preservation of cellular morphology. Spontaneous necrosis phenomena occurred in the deeper portion of the mass due to a reduction of capillary density in those areas.

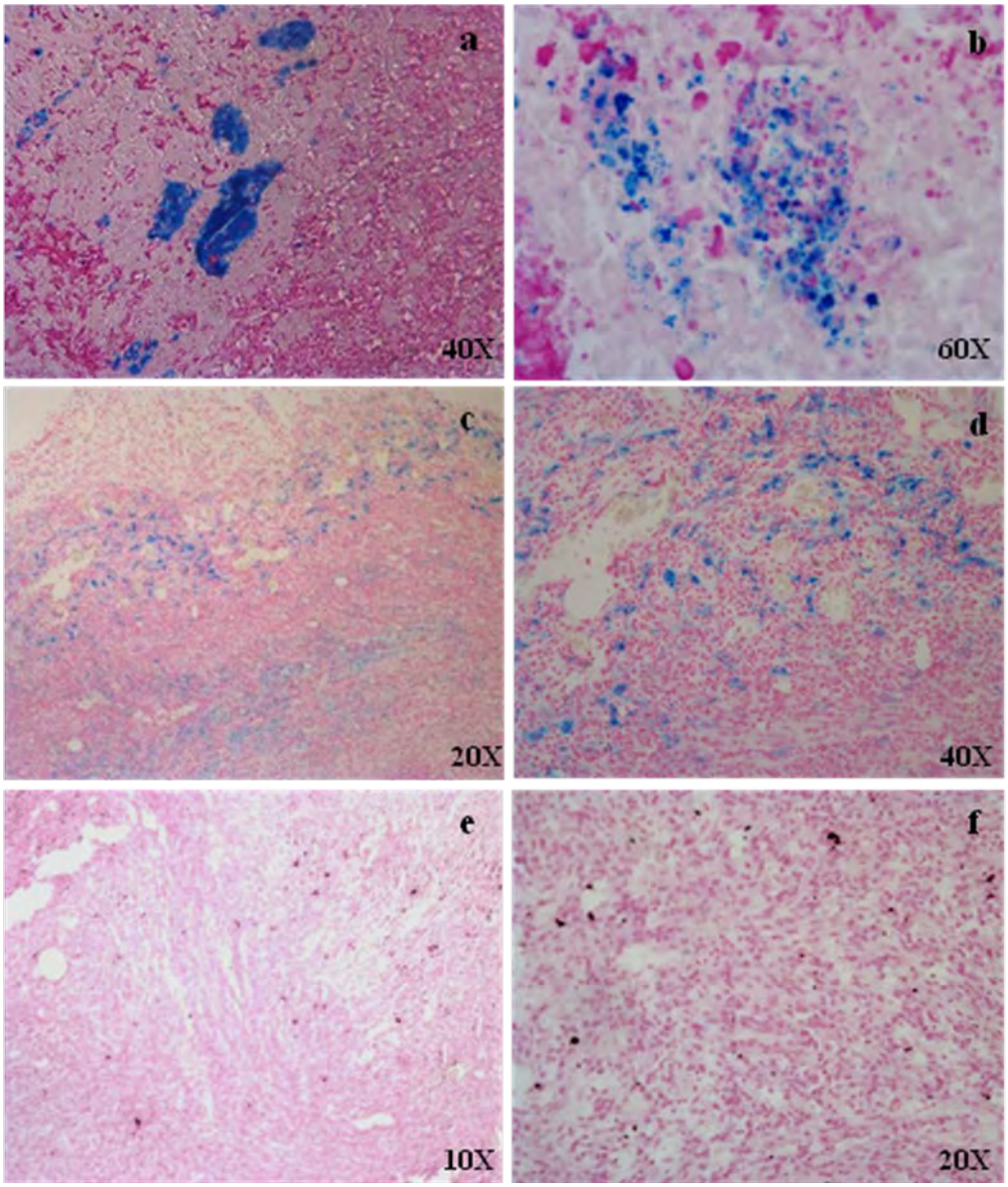

Figure 8: **Histological analysis of tumors**. In the Panel a-b histology of tumor of the experimental group is showed. Injection site is showed in Panel a while in Panel b the living tumor area is illustrated. In Panel c-d histology of group M is presented. In Panel e-f histology of group S is presented and in the Panel L-N is showed the third subgroup of the control group. MNs are capable to migrate and spread in tumor tissue causing the formation of fibrotic and necrotic areas (a, b). Scale bars, a-b, c-d, e and f,

Discussion

Iron Oxide Magnetic Nanoparticles (MNP) are known to generate heat due to molecular vibration under AMF [9]. Magnetic fluid hyperthermia is a fairly new concept that finds its applications in the treatment of different types of cancers previously loaded with MNP and exposed to an AMF. The key mechanism of this treatment is based on intracellular heat stress resulting in activation of many cellular degradation processes including protein degeneration, reduced perfusion and changes in pH among others, that ultimately lead to apoptosis [20, 21]. In a previous work we tested the theranostic properties of MNs on xenograft tumor models [16]; in this paper we have further developed the protocol and demonstrated in vivo the inhibition of the tumor growth in a murine model of glioblastoma multiforme. The proposed method is minimally invasive and the efficacy of the treatment and progression of the disease can be monitored at once within a standard MRI session. MNs are equally effective both for therapy, as heating mediators, and for MR imaging as negative contrast agents : these properties can qualify MNs extracted from magnetotactic bacteria as theranostic agents. These nanoparticles, delivered by intratumoral injection, remained within the tumor for the whole period of observation with no evidence of migration to other organs or tissues: this allows for repeatable and highly specific treatments while minimizing unwanted side effects. Thermal maps of animals exposed to AMF and treated with MNs show a well defined area of increased temperature corresponding to the entire volume of the tumor, while the heat distribution of body temperature apart from tumor remain homogeneous for the entire duration of the treatment; heating spots might lead to cancer cell death within a certain distance from the MNs, an effect that could compensate for the non homogeneous distribution of MNs in the tumor mass. The hyperthermic temperature gained by MNs in the tumor was lower compared to values commonly reported in the literature for MFH [22, 23] although similar findings were referred also by other groups [24]. Despite the elevate SAR value measured for lyophilized samples of MNs [17], the heating potential could be reduced when MNs are included in a living tissue [25, 26]: biological structures as cellular membranes and vesicles could lead to immobilization of the nanoparticles, with subsequent partial inhibition of heating mechanisms [27]. Heating power emanated by MNs however resulted in a marked inhibition of growing in tumors who received MFH treatment compared to control groups, who were not exposed to the magnetic field. This indicates that the therapeutic effect is caused by the heat released by MNs and not by their solely presence inside the neoplastic mass, which showed tumor volumes overlapping between control groups. We have also recorded the progressive disappearance of the tumor in two mice during the treatment, with mild signs of burn on the skin and more severe effects in the core portion of tumor, caused by thermal energy release; only minor signs of tissue damage were visible at the rim of the xenograft implant. Similar effects in the surrounding tissues were completely absent. One week after the treatment we observed a recovery in the growth rate. It can be hypothesized that active cancer cells survived on the outer regions of the lesion, where some residual malignant tissue was still present as pointed out by MRI images. This

incomplete remission of the tumor mass could find an explanation in the route of administration: even if carefully fractionated, intratumoral injections could not lead to uniform distribution of nanoparticles within the mass. Elevated interstitial pressure combined with irregularities in the circulating blood flow are among the main issues that prevents the homogeneous redistribution of MNs and their subsequent uptake by cancer cells [28]. Taking this into account, our findings show that even with an inhomogeneous distribution of magnetic materials, MFH based on magnetosomes lead to a distinct reduction in tumor growing with significant therapeutic effects.

Conclusion

Magnetic Fluid Hyperthermia based on naturally synthetized magnetic nanoparticles extracted from magnetotactic bacteria, lead to an effective reduction in the growth rate of xenograft tumors in treated animals. Our work demonstrated that notable therapeutic effects can be achieved with temperature increase much lower than values commonly reported in the literature and strongly depends on the simultaneous application of both MNs and AMF. The solely presence of magnetosomes inside the tumor mass do not elicit any cytotoxic response and do not lead to significant effects on tumor volumes. For the whole duration of the experiment we did not record any evidence of degeneration or alterations in the distribution of nanoparticles: their marked parenchymal stability over time suggests that repeated hyperthermia treatments after a single administration of magnetic material are feasible. Improvement to the proposed protocol could include an optimization of AMF and exposure times to increase the heating power of magnetosomes. The development of biosensors to target U87MG cancer cells would also be desirable: an highly specific delivery of magnetosomes would improve the uptake of magnetic material and thus the clinical outcome of therapies. Our future perspective is the application of this protocol to ortotopic models of glioblastoma to gain insights toward clinical translation of iron oxide-based MFH.

Materials and methods

Production and extraction of MNs

Magnetosomes were extracted and purificated from MSR-1 culture according to the protocol proposed by Grunberg et al. [18] and detailed in Mannucci et al. [16]. After purification, MNs were dried for 5 h using a lyophilizer, irradiated with γ-rays (56 Gy for 84 min) and finally stored at -20°C.

Cancer cells culture

Human glioblastoma-astrocytoma, epithelial-like cell line (U87MG, purchased by ATCC Manassas, VA), was cultured in Eagle's Minimum Essential Medium (EMEM) with 10% of Fetal Bovine Serum (FBS), 1% of a mix of penicillin/streptomycin 1:1 and 1% of L-glutamine 200 mM, in 25 cm^2 plates and incubated at 37°C in humidified air with 5% CO_2. Medium and L-glutamine were purchased by Sigma-Aldrich (Italy), while serum and antibiotic mix were acquired by GIBCO Life Technologies (USA). When at confluence, cells were treated with trypsin-EDTA 1% (GIBCO Life Technologies, USA), harvested and centrifuged at 1200 rpm for 5 min. The supernatant was discarded and cells pellet was resuspended in 1 ml of complete medium, placed in 75 cm^2 plates and incubated at 37°C and 5% of CO_2 until 80% confluence was detectable.

MNs-uptake in cancer cells

The internalization of MNs into U87MG cells was determined using a Prussian blue staining for iron. $2X10^5$ cells were seeded in specific glasses multiwell for optical microscopy (Falcon BD, Italy) with 1 ml of growth medium. Cells were incubated at 37°C in humidified air with 5% CO_2 for 24 h. Different concentrations of MNs (1 mg/ml, 0.5 mg/ml, 0.2 mg/ml) were added to the wells and incubated as previously described for 6 h, 12 h and 24 h. At each time point, the growth medium was discarded and cells were washed with 1 ml of 1X sterile phosphate buffer saline (PBS, GIBCO, Life Technologies, USA). Cells were fixed with 1 ml of 4% buffered formalin (Bioptica, Italy) for 30 min at room temperature. Once formalin was discarded, samples were double stained: Prussian Blue to visualize MNs and Nuclear Fast Red (Bioptica, Italy) to visualize nuclei. U87MG cells were observed at 10X, 20X and 40X optical magnification using an Olympus microscope (BX-URA2, Olympus optical, GMBH, Hamburg, Germany) equipped with Image ProPlus software (Media Cybernetics, Rockville, USA).

TEM of cells incubated with MNs

U87MG cancer cells were plated on a 2.4 cm culture glass, positioned on the bottom of 3.5 cm Petri dishes and incubated at 37°C in humidified air with 5% of CO_2 in 3 ml of growth medium. After 24 h, cells were fixed with glutaraldehyde 2% in Sorensen buffer pH 7.4 for 2 h, then post-fixed in 1% osmium tetroxide (OsO_4) in aqueous solution for 2 h, and finally dehydrated in graded concentrations of acetone. At

the end of dehydrating process, glasses were stained with lead citrate and observed using a XL30 ESEM scanning electron microscope (FEI Company, Eindhoven, Netherlands).

Cell viability

Cell viability was checked by MTT assay. Cells were plated at a density of 5000 cells per well in 96-well plates and incubated at 37°C in a mixture of air and 5% CO_2. After 24 h, the medium was replaced with fresh medium containing 1, 0.5 and 0.2 mg/ml of sterilized MNs, respectively. After 6, 12 and 24 h of incubation, 100 µl of MTT (5 mg/ml) (Sigma, Italy) were added to each well and incubated for additional 4 h (37°C, 5% CO_2). After the incubation time, plates were removed from the incubator and formazan crystals resulting from plasma membrane electron transport in viable cell were dissolved in 100 µl of DMSO (Sigma, Italy). The multiwell was placed into a monochromator (ChroMate Awareness Technology) for the measurement of absorbance at 570 and 630 nm. Four measurements of optical density (OD) were recorded for each sample and cell viability (%) was calculated with the following equation: CV%= (ODsample/ODcontrol) 100.

In vivo experiments: experimental design and thermotherapy protocol

Thirty-two nude homozygote male mice (Harlan Laboratories, Udine, Italy) were maintained under standard environmental conditions (temperature, humidity, 12 h/12 h light/dark cycle, with water and food ad libitum) under veterinarian assistance. Animals handling and surgery were performed according to protocols approved by the Animal Care and Use Committee of the University of Verona (CIRSAL), and by the Italian Ministry of Health, in strict adherence to the European Communities Council (86/609/EEC) directives, minimizing the number of animals used and avoiding their suffering.

One million U87MG cells resuspended in 200 µl of sterile PBS were subcutaneously injected in the right flank of anesthetized mice. Size of the tumor mass was measured on alternate days with a handheld caliper, and the gross volume was calculated as (D*d^2)*100 [19]. When tumor volume reached 100 µl (about 30±5 days after the injection) tumors were measured also by MRI to check the effective size of the mass: at this point, animals were divided in two main groups. The control group (n=20) was further divided in two subgroups: n=10 subjects were administered with 100 µl of saline (Group S); the remaining n=10 animals (Group M) received 1.5 mg of MNs diluted in 100 µl of PBS by direct injection into the tumor mass, using an intradermal needle (21G). Both these groups were not exposed to AMF.

The experimental group (n=12, Group HT) received 1.5 mg of MNs diluted in 100 µl of PBS and was exposed to AMF on day 0 (immediately after injection), 2 and 4. The AMF apparatus (Magnetherm, NanoTherics UK) yield a magnetic field of intensity 23 kA/m (≅29 mT) and frequency of 110 kHz. These

values are very close to those used in human application of hyperthermia [8]. Mice were placed on a custom animal holder under isofluorane anesthesia 1.5% (Forane, Abbott) and exposed to AMF for 20 minutes. A digital IR camera (Flir I7, Flir Systems, Italy) was used by the operator to take snapshots of heating distribution in the tumor and surrounding tissues. In addition to the thermal camera, a multichannel thermometer equipped with optical fibers probes (FOTEMP4, Optocon AG, Germany) was used to assess temperature variation within the tumor and the body. Probes were placed by a non-metallic catheter inside the tumor mass and under the skin of the contralateral flank of the mouse; temperature was continuously recorded during AMF exposures.

All the mice were monitored by MRI at three time points: 24 h, one week and two weeks after MNs administration. The first and second time points were chosen to evaluate the physiological distribution of MNs and acute effects induced by MFH inside the neoplastic mass, respectively. The last point was useful to check whether some kinds of alterations do occur in the tumor and in the surrounding tissues after the treatment. Mice were sacrificed by isofluorane overdose and successively by neck dislocation and tumors excised for histological analysis. These methods were performed in according to D.L. 4 March 2014 n°26 of the Italian Ministry of Health.

MRI

MR images were acquired to monitor the tumor growth at days 0, 7 and 14 both for control and experimental groups. MRI was performed using a Bruker tomograph operating at 4.7 T, equipped with an actively shielded gradient insert (Bruker, Germany) having a maximum gradient
strength of 40 G/cm. Animals were placed prone in a heated bed and a 3.5 cm i.d. birdcage coil was used to acquire the MR signal. T_2 and T_2* weighted images were acquired to detect the tumor and the presence of MNs respectively, with the following parameters: T_2 w RARE 3D sequence with TR = 1200 ms, TE_{eff} = 47.5 ms, FOV= 5x2.5x2.5 cm^3, NEX = 1, MTX = 256/128/32, Slice Thickness = 0.78 mm; T_2*weighted FLASH gradient echo sequence with TR = 400 ms, TE = 4.4ms, flip angle = 10°, FOV = 5x2.5 cm, NEX = 2, MTX = 256/128, NSLICES = 8, Slice Thickness = 2 mm.

MR Image processing

To estimate the volume of tumors, MR images were processed with custom software coded in MATLAB. The tumor area was selected manually by entering a series of points and extracting the polygon represented by this set of points. This polygon was then segmented into three parts: the magnetosomes, the tumour and the background. The portion of the polygon that contains magnetosomes was then extracted via Otsu's thresholding, in order to minimize the intraclass variance on the histogram of the two sets of values created by the thresholding.

Histology

After the last MRI acquisition, animals were sacrificed and tumors were excised, washed with PBS 0.1 M and fixed with 10% buffered formalin for 4 h. Afterwards, samples were dehydrated with increasing concentration gradient of alcohol from 70% to 100% and then with xylene for final processing. Tissues were embedded in paraffin and sections of 5 μm were obtained and dried at 37°C for 24 h. Sections were stained with Prussian blue and Nuclear Fast Red (Bioptica) to visualize iron nanoparticles and nuclei respectively.

References:

1. Brandes AA, Tosoni A, Franceschi E, et al. Glioblastoma in adults. Crit Rev Oncol Hematol. 2008; 67(2):139-152
2. Wen PY, Kesari S. Malignant gliomas in adults. N Engl J Med. 2008; 359(5):492-50
3. Hegyi G, Szigeti GP, Szasz A. Hypethermia versus Oncothermia: Cellular effects in complementary cancer therapy. Evid Based Complement Alternat Med 2013; 672873
4. Cavaliere R, Ciocatto EC, Giovanella BC, et al. Selective heat sensitivity of cancer cells. Biochemical and clinical studies. Cancer. 1967 20(9):1351-81
5. Wust P, Hildebrandt B, Creenivasa G, et al. Hyperthermia in combined treatment of cancer. Lancet Oncol 2002(3):487-497
6. Jordan A, Scholz R, Maier-Hauff K, et al. The effect of thermotherapy using magnetic nanoparticles on rat malignant glioma. J Neurooncol. 2006;78(1):7-14.
7. Hildebrandt B, Wust P, Ahlers O, et al. The cellular and molecular basis of hyperthermia. Crit Rev Oncol Hematol. 2002 43(1):33-56
8. Jordan A, Maier-Hauff K. Magnetic nanoparticles for intracranial thermotherapy. J Nanosci Nanotechnol. 2007;7(12):4604-6.
9. Maier-Hauff K, Rothe R, Scholz R, et al. Intracranial thermotherapy using magnetic nanoparticles combined with external beam radiotherapy: results of a feasibility study on patients with glioblastoma multiforme. J Neurooncol. 2007;81(1):53-60.
10. Ito A, Shinkai M, Honda H, et al. Medical application of functionalized magnetic nanoparticles. J Biosci Bioeng. 2005;100(1):1-11
11. Faraji M, Yamini Y, Rezaee M. Magnetic nanoparticles: synthesis, stabilization, functionalization, characterization, and applications. J Iran Chem Soc. 2010;7(1):1-37
12. Bellini, S.,. 1963a Su di un particolare comportamento di batteri d'acqua dolce (On a unique behavior of freshwater bacteria). Institute of Microbiology, University of Pavia, Italy.
13. Bellini, S., 1963b. Ulteriori studi sui "batteri magnetosensibili" (Further studies on magnetosensitive bacteria). Institute of Microbiology, University of Pavia, Italy.

14. Blakmore R. Magnetotactic bacteria Science (1975) 190(4212):377-9
15. Alphandery E, Faure S, Seksek O, et al. Chains of MN extracted from AMB-1 magnetotactic bacteria for application in alternative magnetic field cancer therapy. ACS Nano 2011 23;5(8):6279-96.
16. Mannucci S, Ghin L, Conti G, et al. Magnetic nanoparticles from Magnetospirillum gryphiswaldense increase the efficacy of thermotherapy in a model of colon carcinoma. PloS One 2014; 9(10)
17. Orlando T, Mannucci S, Fantechi E, et al. Characterization of Magnetic Nanoparticles from Magnetospirillum Gryphiswaldense as potential theranostics tools. Submitted
18. Grünberg K, Müller EC, Otto A, et al. Biochemical and proteomic analysis of the MN membrane in Magnetospirillum gryphiswaldense. Appl Environ Microbiol.; 2004 70(2):1040-50
19. Marzola P, Ramponi S, Nicolato E, et al. Effect of tamoxifen in an experimental model of breast tumor studied by dynamic contrast-enhanced magnetic resonance imaging and different contrast agents. Invest Radiol. 2005; 40(7):421-9.
20. Laszlo A. The effects of hyperthermia on mammalian cell structure and function. Cell Prolif. 1992; 25(2):59-87
21. Kregel KC. Heat shock proteins: modifying factors in physiological stress responses and acquired thermotolerance. J Appl Physiol 2002; 92(5):2177-86
22. Jordan A, Scholz R, Wust P, et al. Effects of magnetic fluid hyperthermia (MFH) on C3H mammary carcinoma in vivo. Int J Hyperthermia. 1997 (6):587-605.27.
23. Johannsen M, Thiesen B, Jordan A, et al. Magnetic fluid hyperthermia (MFH)reduces prostate cancer growth in the orthotopic dunning R3327 rat model. Prostate. 2005 1;64(3):283-92.
24. Kossatz S, Ludwig R, Dähring H, et al. High therapeutic efficiency of magnetic hyperthermia in xenograft models achieved with moderate temperature dosages in the tumor area. Pharm Res. 2014; 31(12):3274-88
25. Dutz S, Kettering M, Hilger I, et al. Magnetic multicore nanoparticles for hyperthermia-influence of particle immobilization in tumour tissue on magnetic properties. Nanotechnology. 2011; 22(26):265102
26. Richter H, Kettering M, Wiekhorst F, et al. Magnetorelaxometry for localization and quantification of magnetic nanoparticles for thermal ablation studies. Phys Med Biol. 2010; 55(3):623-33
27. Kallumadil M, Tada M, Nakagawa T, et al. Suitability of commercial colloids for magnetic hyperthermia J Magn Magn Mater 2009 321(21) 3650-3651.
28. Nichols JW, Bae YH. Odyssey of a cancer nanoparticle: from injection site to site of action. Nano Today. 2012; 7(6):606-618.
29. Benoit MR, Mayer D, Barak Y, et al. Visualizing implanted tumors in mice with magnetic resonance imaging using magnetotactic bacteria. Clin Cancer Res. 2009 15(16):5170-7

Section B

Heterologous expression of *Physcomitrella patens* LHCSR1 protein in *Nicotiana* plants

Introduction of section B

1.Photosynthesis: the equation of life

The evolution of oxygenic photosynthetic process changed drastically our planet. The ancient atmosphere was composed by different gases as methane, carbon dioxide and nitrogen. 2.4 Gya with the onset of photosynthetic organism O_2 progressively accumulated and the redox balance of earth changed. Anoxic organisms were forced to adapt to oxygen or to retreat anaerobic niches and the Earthlandscape's of dominant color became green. Oxygen accumulation was due to a reaction by which organisms use energy from sun and electrons from water, to reduce carbon dioxide into organic compound, generating O_2 as secondary product. This reaction can be expressed by the following equation, which can be called "the equation of life":

$$2n\ CO_2 + 2n\ H_2O + \text{photons} \rightarrow 2(CH_2O)_n + 2n\ O_2$$

To perform this apparently simple reaction cyanobacterium, algae and plants need a complex set of biochemical reactions and molecular machinery. The entire biochemical can be divided into two parts: the light reactions and the dark ones. In the light-dependant steps, energy from light is converted into chemical energy, in the form of ATP and NADPH, while in the dark phase the enzyme RuBisCo uses CO_2 from atmosphere and newly formed NADPH to release three-carbon sugars.

1.1 Inside the organization of chloroplast: the factory of photosynthesis.

The chloroplast is the organelle of photosynthesis, it is the descendant of an ancestral cyanobacteria which started endosymbiosis with eukaryotic cells (~1-1,5 biillion of year ago) (Keeling, 2010). In land plants, it is a lens-shaped organelle with a diameter of ~5µm and a width of 2,5 µm; it possess circular genome of ~120-160 kb in size carrying 100 protein-coding genes which covers only a little part of the ~2000-3000 proteins found in the plastid. All the others chloroplast proteins are encoded in the nucleus and imported after cytosol expression (Timmis et al., 2004). Looking at the organization of choloroplast it is possible to distinguish two envelope membranes which encompass an aqueous matrix called **stroma** and an internal membrane called **thylakoids**. In the stroma compartment it is possible to find carbon fixation circle enzymes, starch globuli, plastoglobuli and circular DNA. Thylakoids, on the other hand, create a continuous 3-D membrane network that contains the thylakoids lumen. This membrane network can be further divided into two different domains: the stacked one called **grana** interconnected by pairs of **stroma lamellae** membrane (Fig.1) (Staehelin, 2003). The assembly of chloroplast complexes is complex and sophisticated, necessitating the coordination of two genomes. Import of proteins from the cytosol require they include a N-terminal targeting transit peptide, which engage a translocation machinery localized at the chloloroplast bilayer membrane. The translocation process is mediated by multiprotein complexes termed TOC (Translocon at the Outer envelope membrane of Chloroplasts) and TIC (Translocon at the Inner envelope membrane of Chloroplasts) (Li and Chiu, 2010).

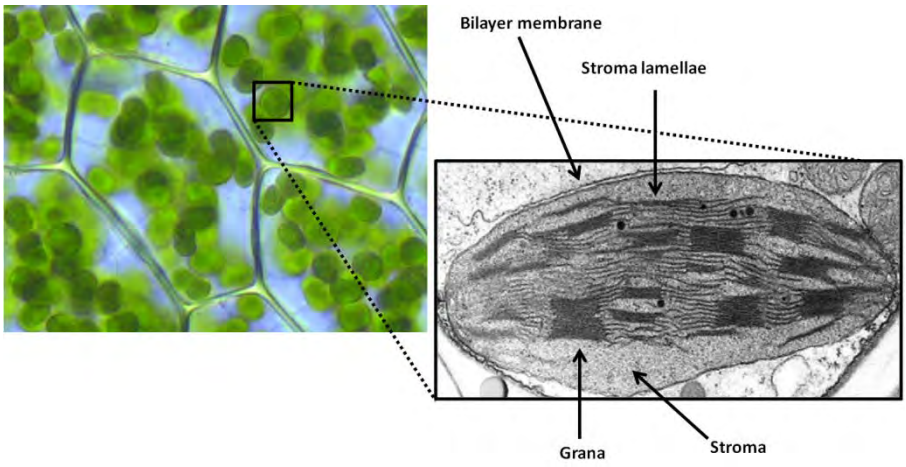

Figure.1. Chloroplast organization. Chloroplast appears as a green disc inside plant cells (righ panel). A transmission microscopy image (TEM) of chloroplast reveal the inside organization in grana and stroma membrane

.1.2 The light phase: capture of light and its transformation into chemical energy in form of ATP and NAPH

The light-dependant reaction is the first step of photosynthesis, a process that occurs in thylakoid membranes and involves a proteic machinery able to catch energy from sun and convert it into chemical energy. Four major membrane supercomplexes catalyze light energy conversion: Photosystem II (PSII), Cytochrome b6/f, Photosystem I (PSI) and ATP synthase (Fig.2).

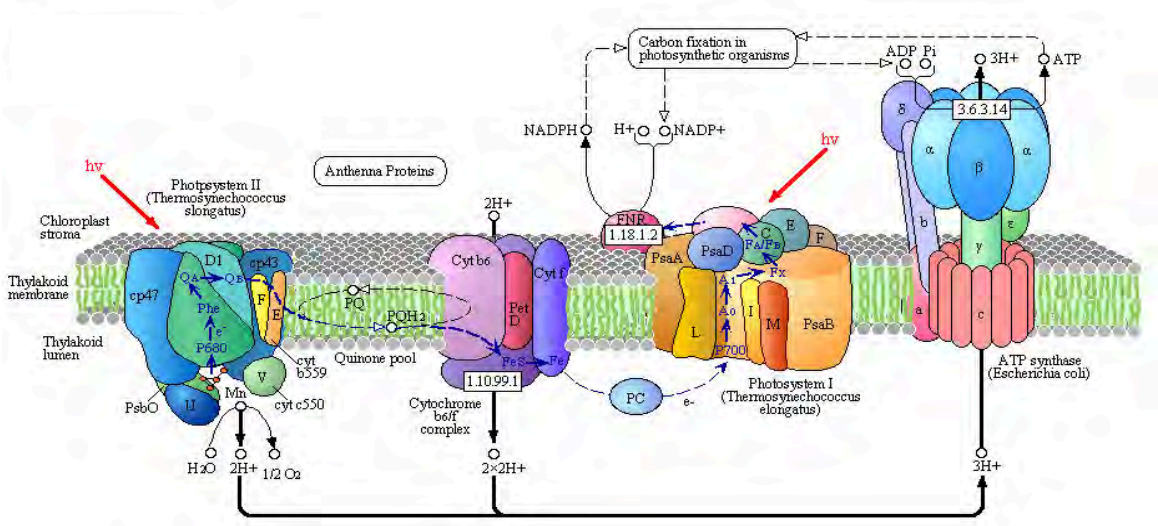

Figure.2 Light phase reaction. The principal "actors" in light phase are represented as cartoons in this picture. Starting from the left : photosystem II (PSII), cytochrome b6/f (Cyt b6/f), photosystem I (PSI) and ATP synthase. (image from http://employees.csbsju.edu/hjakubowski/classes/ch331/oxphos/olphotsynthesis.html)

These complexes are not homogeneously distributed in thylakoid membranes as shown by Freeze-fracture electron microscopy which evidences a lateral heterogeneity between stroma membrane and grana partition ; PSII is located in grana partitions while PSI and ATP synthase are located in stroma-exposed membranes. Cyt b6/f, instead, was found both in grana and in stroma membranes. These complexes work together catalyzing conversion of light energy (photons) into chemical energy (ATP and NADPH). PSI and PSII could be considered the main actors. They each include a central core containing the

reaction center which is surrounded by light harvesting proteins (LHC) constituting the “antenna” moiety. Both photosytems bind pigments which harvest light and transfer excitation energy to the reaction centers (RC). The two photosystems act in series, as described in the so called Z-scheme. (Fig.3)

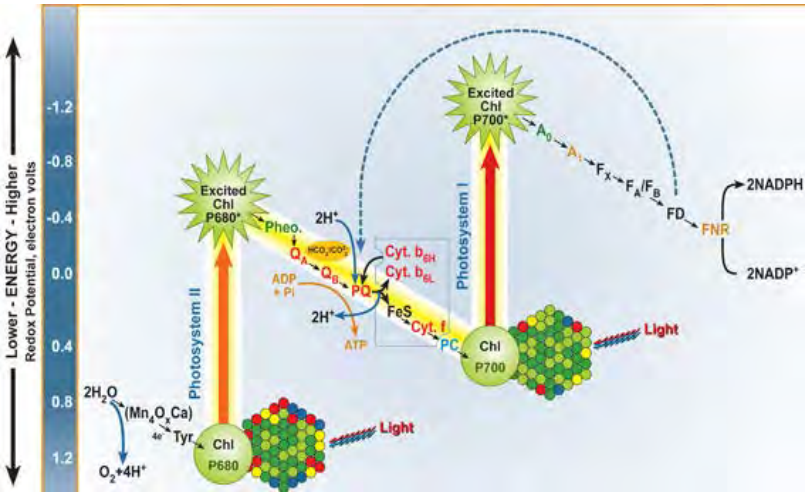

Figure.3. The Z-scheme of electron transport in photosynthesis. Cofactors involved in electron translocation between H_2O and $NADP^+$ and their redox potential are indicated in this scheme. (image from http://www.life.illinois.edu/govindjee/Z-Scheme.html)

Pigments absorb light within the visible region and this energy is transferred between individual pigments of the light-harvesting antennae in an ordered way, a physical process called Föster transfer. This mechanism is an energetically down-hill process: energy is transferred from Chl b (λ=647 nm) to Chl a (λ=663 nm). Excitons are then transferred among Chl a until they reach the primary electron donor which are P680 or P700. P680 is the PSII primary electron donor, localized in the PSII-RC, able to release an electron from pheophytin acceptor (Pheo) towards the stromal side of the thylakoid membrane where it is donated to monovalent quinonic acceptor (Q_A) and then to divalent plastoquinone molecule (PQ). Receiving a second electron from P680, plastoquinone takes two protons from the stroma and form plastoquinol (PQH_2) which is able to diffuse in the membrane and be oxydized the Cyt b6/f complex. The positive charge of $P680^+$ is neutralized by electron taken from a water molecule leading the formation of O_2 and release of protons in the inner thylakoid lumen which generate an acidification of the lumen. Electrons are then transferred from Cyt b6/f to a small copper-containing protein, plastocyanin, while two protons are released into the inner thylakoid space.

As in PSII, in PSI a special pair of Chls is present in the reaction center, the P700 primary electron donor, which upon excitation releases an electron that reduce ferredoxin (FD). Electrons from two molecules of reduced ferredoxin are used by $NADP^+$ oxidoredutase (FNR) to convert NAD^+ to NADPH which is released in the stroma. The oxidized $P700^+$ is reduced by electrons that come from PSII via photosynthetic electron transport chain. Both PSI and PSII are extraordinary efficient machines, indeed the quantum yield of PSI is 0,93.0 while PSII has a somehow lower efficiency (quantum yield 0,83). The charge separation in PSI and PSII, together with the electron transfer through the Cyt-b6/f and cyclic electron transport, leads to the formation of an electrochemical potential gradient, between the stromal and the

lumenal side of the membrane, which powers ATP synthesis by the ATPase, the fourth protein complex. The ATPase enzyme could be considered a molecular engine driven by the proton motive force: It is a multimeric complex with both stromal and transmembrane regions, known as CF 1 and CF 0. Proton transport through CF 0 is coupled to ATP synthesis/hydrolysis in the β-subunits of CF 1. CF 0 is composed of four subunits I, II, III and IV (in a probable stoichiometry of 1:1:14:1; the 14 III subunits form a ring-like structure). The whole CF 0 -CF 1 complex acts as a rotary proton-driven motor, in which it is possible to distinguish stationary subunits: I, II, IV, α,β and δ, and rotary subunits like III,ε and γ.

1.3 The dark phase: using ATP and NAPH to produce carbohydrates

The chemical free energy (ATP and NAPH) produced in the light phase are used in a cyclic series of reaction, known as Calvin-Benson cycle, to reduced atmospheric CO_2 molecules to carbohydrates. One molecule of gluteraldehyde-3 phosphate (GAP) is generated from 3 molecule of CO_2 reduced, regenerating ribulose-5 phosphate (Ru5P) to preserve cyclic character of the process. The all process can be summarized by the following reactions:

$$\mathbf{3\ CO_2 + 3\ Ru5P + 9\ ATP + 6\ NADPH \rightarrow 6\ GAP + 9\ ADP + 6\ NADP^+ + 8\ P_i}$$

$$\mathbf{5\ GAP \rightarrow 3\ Ru5P}$$

2. Light harvesting pigments

During evolution three types of pigments has been selected for photosynthetic process: chlorophylls (Chls), carotenoids (Cars) and phycobilins. These pigments are responsible for light absorption, charge separation and energy transfer toward the reaction centre in both photosystems.

2.1 Chlorophylls

The biosynthesis of chlorophylls takes place in the chloroplast and involves a series of 17 enzymes. All the process can be divide into four main steps: (1) synthesis of 5-aminolevulonic acid (ALA), precursor of Chl and eme (2) formation of a pyrrole ring porphobilinogen from the condensation reaction of two molecules of ALA and assembly of four pyrroles leading to the synthesis of the first closed tetrapyrrole having inversion of ring D, i.e., uroporphyrinogen III; (3) synthesis of protoporphyrin IX via several decarboxylation and oxygenation reactions, and (4) insertion of Mg2+ to the protoporphyrin IX (PPIX) moiety steering it to the Mg-branch of tetrapyrrole synthesis leading to the formation of Chl (Tripathy, 2012) Five different type of Chl can be found in photosynthetic organism differing in their substitutions: the most abundant are Chl a and Chl b but it is possible to find also Chl d present in red algae and cyanobacteria and Chl f described in cyanobacteria only (Chen et al., 2010; Larkum et al.).(Fig.4)

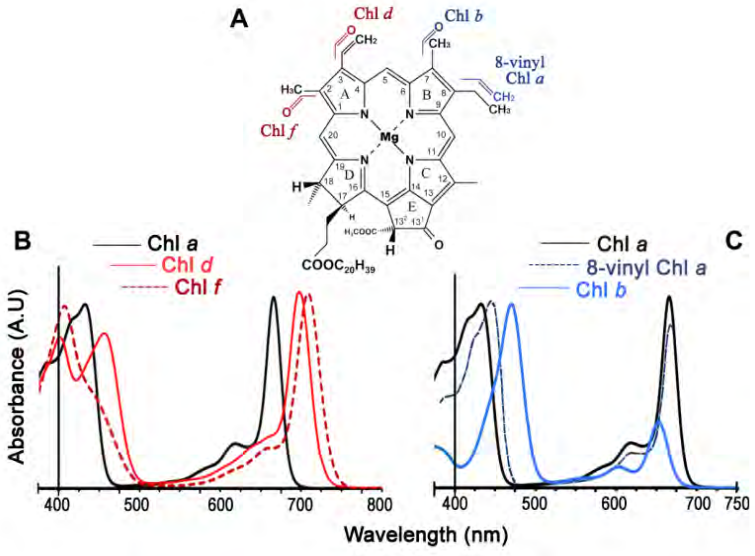

Figure .4. Chemical structure of chlorophylls and their absorption spectra in 100% methanol. (A) Chemical structure of chlorophyll *a* and the structural differences of other chlorophylls from chlorophyll *a*. The carbon atoms are numbered using IUPAC system. (B) Absorption spectra of red-shifted chlorophylls, chlorophylls *d* and *f*, compared with chlorophyll *a*. (C) Absorption spectra of chlorophyll *b* and 8-vinyl chlorophyll *a* compared with chlorophyll *a*. *(image adapted from http://plantsinaction.science.uq.edu.au/book/export/html/166)*

The two different types of Chls present in vascular plants differ for the substituent in the second pyrrole ring: a methyl for Chl a and an aldehyde for Chl b. The presence of conjugated double bonds in Chls is responsible for the light absorption in visible region, in particular the absorption spectra of Chl a and Chl b do not overlap thus increasing the efficiency of light-harvesting. Chl a is characterized by two strong absorbtion bands, located in the blu-violet and in the red region of the spectrum. The first band is the "Soret" band, corresponding to transition to higher state, has a maximum at 430 nm. The Qy transition band, instead, is the red-most band with a maximum at 670 nm and correspond to the transition of an electron from S_0 to S_1. Chl b spectrum differs from that of Chl a for the two bands being closer together: the Soret band is located at 460 nm while the red band at 630 nm. The absorption of Chls in red and blu/violet light confers a green colors to plants. Chls in plant cells are present like pigments bound to protein due to the presence of the Mg atoms at the center of porphyrin ring which is able to bound nucleophilic amino acid residue like hystidine (Liu et al. 2004.). Chls are indispensable for the proper folding of some photosynthetic proteins such as the LHC proteins.

2.2 Carotenoids

Carotenoids are synthesized in a wide variety of photosynthetic organisms (plants, algae) and non photosynthetic (some fungi and bacteria) organisms. In plants and algae carotenoids play two crucial roles in photosynthetic process: they absorb light energy for photosynthetic process and are involved in photoprotection mechanisms (Moore et al 1982). Carotenoids are poly-isoprenoid compounds containing a C_{40} hydrocarbon backbone that includes between 3 and 15 conjugated double bounds. The number of double bounds determines the spectral absorbtion range of carotenoids from 400 to 500 nm (Armstrong and Hearstt, 1996). So far, over 750 carotenoid structures are known and divided into two classes: non-oxygenated molecules designated as carotenes and oxygenated carotenoids referred to as xanthophylls. In

photosynthetic organism carotenoids synthesis happens in the plastids like chloroplast where carotenogenic proteins encoded by nuclear genes are post-translationally processed. The carotenoids biosynthesis starts from the condensation of 8 isopentenil diphospate (IPP) molecules that produce phytoene which undergone several reduction steps to produce lycopene. Subsequently lycopene can follow two different pathways: one leads to the formations of β-carotene, that is the substrate for the synthesis of Zeaxanthin (Zea), Violaxanthin (Vio) and Neoxanthin (Neo) while the other leads to the formation of α-carotene for the biosynthesis of lutein (Lut). (Fig.5)

The double bonds present in carotenoids are responsible for their photochemical properties. Light absorbed by Cars induce the transfer of electron from the ground state (S_0) to the second excited singlet state (S_2), this dipole-dipole allowed transition is responsible of the characteristic absorption spectrum. These absorption of Cars contribute to increase the light harvesting capacity of Chl-binding proteins in the blue spectral region. Clearly, maximizing light harvesting efficiency implies that Cars are in close proximity and properly positioned with respect to Chls in light harvesting complexes of photosystems. Thus, the majority of carotenoids of the thylakoid membrane are bound to specific binding sites in pigment-protein complexes, where the protein scaffold determines both the distance and orientation with respect to Chl molecules in the same complex. Actually in case of the LHC family the binding of xanthophylls to protein is necessary for the proper protein folding and for their activity in photoprotection (Niyogi et al., 1997; Dall'Osto et al., 2006). Cars are differentially distributed among photosynthetic complexes: β-carotene binds to Core moieties of both photosystem I (PSI) and II (PSII), whereas xanthophylls are both accessory pigments and structural elements of light-harvesting complexes (LHCS) in antenna moieties. In both cases the binding between Cars and photosynthetic protein complex is non-covalent , probably involving hydrophobic interactions (Gastaldelli et al., 2003). Besides the carotenoids importance in protein structural stabilization and light absorption, carotenoids are involved in protection from photo-oxidative damage (Havaux and Niyogi, 1999). Indeed, Cars are important antioxidant in the thylakoid membrane and are involved in dissipation of excited states of Chls in overexcitation conditions. In particular each carotenoid species plays a distict and complementary role in photosynthetic organism. Lutein, the most abundant carotenoid in photosynthetic apparatus, has been found to be the exclusive ligand for the conserved binding site L1 in all light-harvesting complexes where it is involved in quenching of harmful ^{3} Chl* states and scavenging of ROS produced by the reaction of ^{3}Chl* with molecular oxygen. Neoxanthin is present in light harvesting system, accounting for the 15% of total carotenoids. Its major binding site is N1 in LHCII (Liu et al., 2004) besides it binds also the two monomeric antennae LHCB4 and LHCB5 protruding with their allene groups which acts in superoxide scavenging. β-carotene is a component of both PSI and PSII reaction centre core complexes where it act in scavenging of $^1O_2$ generated by the triplet state of the primary electron donor in isolated PSII core complexes (Telfer et al., 1994).

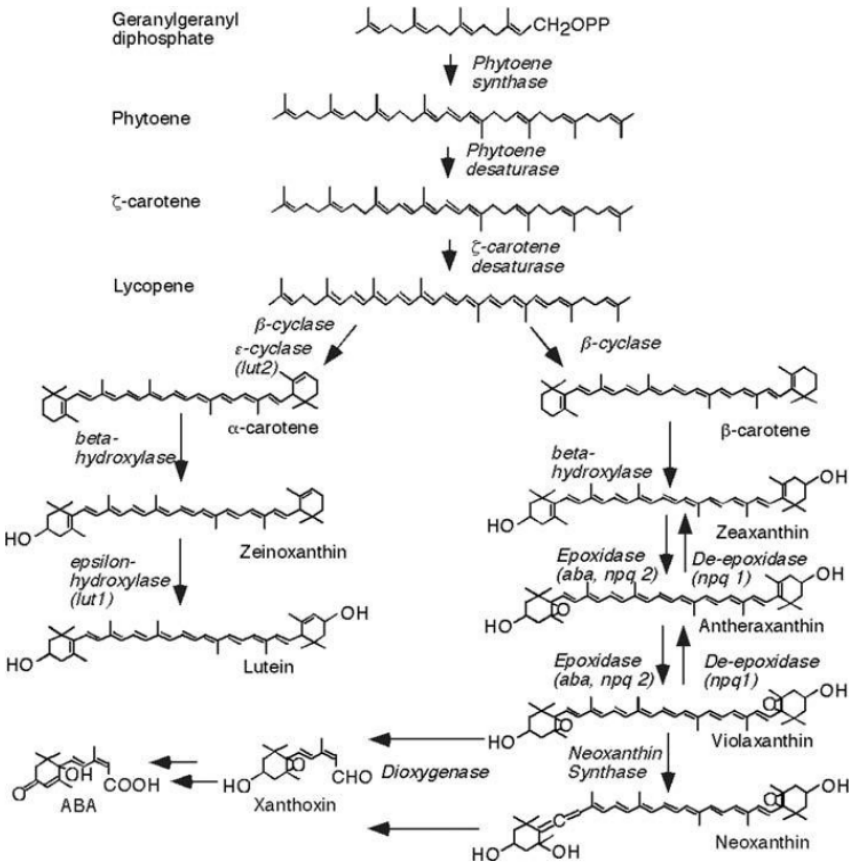

Figure.5. Biosynthetic pathway of carotenoids in vascular plants, with enzymes involved**.**

2.3 Xanthophyll's cycle carotenoids

The composition of carotenoids in thylakoids undergoes changes during acclimation to light intensity changes due to the operation of xanthophylls cycle. The xanthophyll's cycle involves the three xanthophylls Viola, Anthera and Zea, and consists in a light-dependent, reversible de-epoxidation of Viola to Zea via the intermediate Anthera. The de-epoxidation of Violaxanthin is catalyzed by the enzyme Violaxanthin de-epoxidase (VDE) which is activated by light-driven proton translocation across the thylakoid membrane exceeds the dissipation rate of the proton gradient by ATPase, leading to a decrease in pH in thethylakoid lumen. VDE enzyme is present and inactive in soluble form while after activation it associate with the thylakoid membrane binding Violaxanthin (Morosinotto et al., 2003). At neutral pH the protein is monomeric with a typical lipocalin folding but when pH decreases the protein dimerizes assuming conformation that allows for ligand binding (Arnoux et al., 2009). Upon return to light-limiting conditions of photosynthesis zeaxanthin is converted back to Viola by a stromal enzyme: zeaxanthin epoxidase (ZEP).

Under excess light conditions zeaxanthin is involved in several photoprotection mechanisms: scavenging of ROS , down regulation of ^{3}Chl* (Dall'Osto et al., 2012) and up-regulation of NPQ (Niyogi et al., 1998)

3.The actors of light harvesting: photosystems I and II

The light-driven electron transfer reactions are catalyzed by two photosystem complexes PSI and PSII. The core complex, widely conserved during evolution, is composed by the product of the genes called psa and psb respectively for PSI and PSII, encoded by nuclear and chloroplast genomes. The core complex binds exclusively Chl a and carotenes. On the other hand the antenna system is more variable among photosynthetic organism. In land plants and algae it is encoded by the nuclear gene family LHC. The LHC proteins are three helicx membrane proteins able to bind different type of pigments like Chl a, Chl b and xanthophylls (Green et al 1996). PSI antennae are named LHCa while PSII antennae are called LHCb.

3.1 Photosystem I

Photosystem I is a multiprotein complex which reduced ferredoxin and oxidized plastocyanin. It could be considered a remarkable nano-photoelectric machine that operates with a quantum yield close to 1.0. It emerged as a homodimeric structure containing several chlorophyll molecules over 3.5 billion years ago, and has optimized its photoelectric properties ever since (Amunts and Nelson, 2008).The first PSI solved structure was that of cyanobacterium *T.elongatus* at 2.5 Å. This model contains 12 protein subunits and 127 cofactors (96 Chl, 22 carotenoids, 2 phylloquinones, 3 Fe_3S_3 clusters and 4 lipid) (Jordan et al., 2001). In crystal and in vivo PSI is a trimer with a diameter of 210 Å and a maximum height of 96 Å. Also information on plants PSI comes from X-ray solved structure complex at 4.4 Å reveals a different structure respect to cynobacteria one. Indeed it is a monomer containing 16 protein subunits, 167 Chl, 2 phylloquinones and 3 Fe_3S_3 clusters (Ben-shem et al., 2003). It is composed by a core complex composed by 14 different polypeptides named PsaA-PsaP and a membrane-associated antennae complex (LHC) which capture light and guide it to the reaction centre. The central part of the core complex is made of two proteins PsaA and PsaB which form a heterodimer consisting of 22 transmembrane helices, which harbors most of cofactors of the transport electron chain. The heterodimer also coordinates 80 Chls which act as intrinsic light-harvesting complex. The stromal subunit of PsaC carriers the two terminal iron-sulfur clusters and it participates with PsaD and PsaE in the docking of ferredoxin. PsaF is necessary for the binding of plastocyanin and for providing excitation energy transfer from LHCI to the core complex. (Boekema et al., 2001). PsaG is an anchor for LHCI binding while PsaJ should be considered important for assembly and stability of PSI (Hansson et al., 2007). The other proteins PsaH, PsaI, PsaL and PsaO interact with LHCI during state transition and PsaH prevents trimer formation (Zhang and Scheller, 2004; Ben-shem et al., 2003).Finally the role of PsaP is not yet completely understood (Khrouchtchova et al., 2005).

The LHCI antennae system is composed of four gene products (Lhca1-Lhca4) assembled into two dimers (LHCA1-LHCA4 and LHCA2-LHCA3) arranged in a half-moon shaped belt around the reaction center. (Ben-shem et al., 2003). Each LHC polypeptides has three transmembrane α-helices and coordinates Chl a and Chl b .Some species, such as *A.thaliana*, besides LHCa1-4 genes have also two homologous genes

encoding LHCA5 and LHCA6 protein (Jansson, 1999). LHCA5 accumulates to sub-stechiometric amounts respect to PSI, it can from homodimers and seems to associate to native PSI at LHCA2 and LHCA3 and PSI core at the LHCA1/4 binding site (Lucinski et al., 2006). LHCA6 protein, instead is expressed at a very low level, its function is not yet completely understood but, recently, the LHCA6 polypeptide has been described as necessary together with LHCA5 for the formation of the full-size NAD(P)H dehydrogenase-PSI supercomplex formation (NDH-PSI supercomplex)(Peng and Shikanai, 2011).

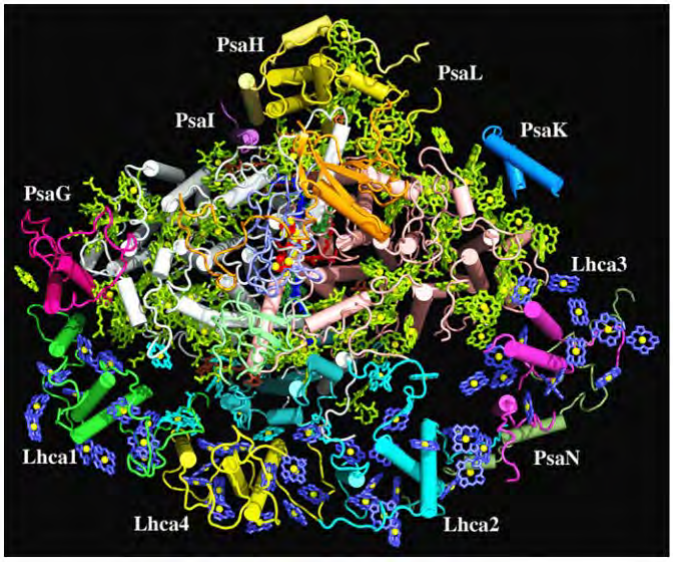

Figure. 6. The overall structure of a plant photosystem I. View from the stroma. Each individual of 17 protein subunits is coloured differently. Chlorophylls of the RC complex are shown in green, chlorophylls of the LHCI complex in blue and gap chlorophylls in cyan. The Fe 4 S 4 clusters are shown as spheres (Fe in red, S in yellow), phylloquinones in blue and carotenes in red, Mg atoms in yellow. (Amunts and Nelson, 2008)

3.2 Photosystems II

The photosystem II (PSII) is a multiproteic complex operating a reaction indispensable for aerobic life on Earth: it is able to split water into protons and molecular oxygen reducing a plastoquinone. All these processes start in the PSII reaction center where a special pair of Chls called P680 undergoes light-induced charge separation traslocating an electron to pheophytin molecules then to plastoquinone A (Q_A) and subsequently to plastoquinone B (Q_B).

The functional PSII core complex is located in the grana membrane as a dimer associated with the peripheral antennae complex. The PSII dimeric core complex of higher plants, algae and cyanobacteria seem to be structurally very similar (Nield and Barber, 2006). Recently the structure of cyanobacteria PSII has been solved providing information on protein subunits and cofactors arrangement. Every PSII monomers binds 19 protein subunits, 35 Chls, two pheophytins, 11 β-carotene, more than 20 lipids, two plastoquinones, two haem irons, one non-haem iron, four manganese atoms, three or four calcium atoms (one of which is in the Mn_4Ca cluster), three Cl_2 ions (two of which are in the vicinity of the Mn_4Ca cluster), one bicarbonate ion and more than 15 detergents in a monomer. Within each PSII monomer, more than 1,300 water molecules were found, yielding a total of 2,795 water molecules in the dimer (Umena et al., 2011). The PSII core complex consists of two transmembrane proteins D1 and D2 containing the reaction centre P680 and all the cofactors of the electron transport chain. Each side of D1 and D2 proteins are

flanked by Chl-binding protein CP43 and CP47. These symmetrically major subunits are surrounded by a number of low molecular weight transmembrane proteins. Attached to the luminal side of PSII are the Oxygen-evolving complex proteins (OEC) which in higher plants and green algae consist of the PsbO, PsbP and PsbQ subunits (Nield and Barber, 2006).

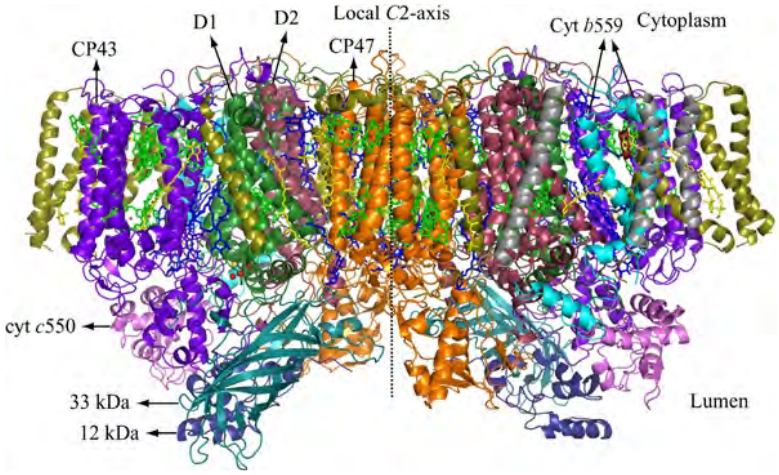

Figure.7. 3-D structure of Photosystem II core complex from cyanobacterium *T.elongatus*. View of PSII dimer perpendicular to the membrane . Protein are represented with different colours. Starting from the external protein it is possible to identify CP43 (violet), D1 (green), D2 (purple), CP47 (orange))(Umena et al., 2011)

The PSII peripheral antenna system is composed of two different classes of light harvesting complex: the **trimeric major light-harvesting complexes** of PSII and the **monomeric (or minor) antennae**.

The LHCII trimers are heterotrimers composed by LHCB1, LHCB2 and LHCB3 subunits present in non equimolar ratios, LHCB1 indeed is more abundant respect to the other two polypeptides (Caffarri et al., 2004). In the trimer complex each LHCII monomer is composed of 3 transmembrane α-helices. Both the N-terminal and the C-terminal peptides are exposed respectively to the stroma and to the lumen side. Each monomer bind 14 Chls and 4 xanthophylls. Two helices, named A and C, participate to Chl binding because they possess a characteristic 'LHC motif' in which a Glu from one LHC motif binds a Chl a molecule via a salt bridge to the Arg of the other: this characteristic of chlorophyll stabilized the two central helices. Chlorophylls are coordinated to the polypeptide chain trough their central Mg^{2+} atom, one facing the luminal side and one the stroma side of the thylakoid membranes. LHC binds also xanthophylls; it is possible to find 2 luteins, 1 neoxanthin and 1 violaxanthin Cycle pigments (Liu et al 2004.). Luteins are bound in the hook-like extension at the stromal end of transmembrane helix 4 by the characteristics DPLG sequence. Thanks to their cross-brace construction the two luteins stabilized the LCHII complex. Neoxanthin binding site has been identified in the lumenal loop; the epoxycyclohexane ring OH group is bound with an hydrogen group with Tyr 112 while the cyclohexane ring at the stromal side protruding in the lipid bilayer (Hobe et al., 2006). The Violaxanthin Cycle pigment is bound in the so called V1 site, a hydrophobic pocket at the interface monomer-monomer formed by several Chls, hydrophobic residues and the phosphatidyl glycerol (PG) (Caffarri et al. 2001). As its name indicates, LHCII plays a role in light

harvesting for PSII transferring light energy to the reaction center where primary photochemistry takes place.

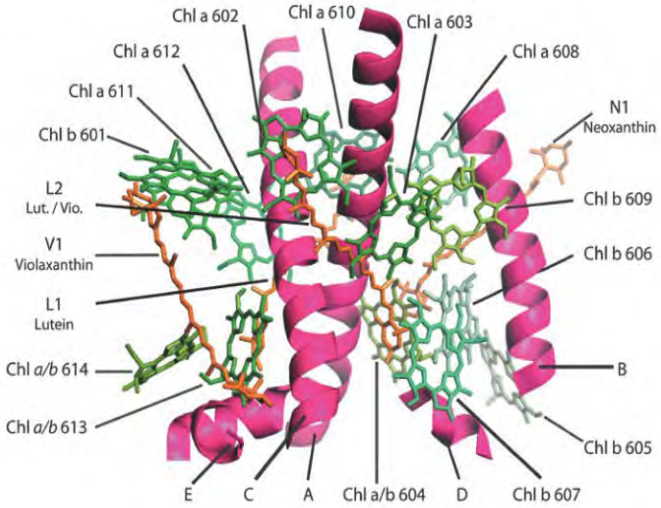

Figure.8. Molecular model of LHCII monomer. Chlorophyll and xanthophyll chromophores bound to different binding sites are represented. The model has been drawn based on the crystal structures of LHCII trimer. Pink, polypeptide; green, chlorophylls; orange, carotenoids; blue, lipids. (Ballottari et al., 2012)

The minor antennae consist of three proteins: **LHCB4** (CP29), **LHCB5** (CP26) and **LHCB6** (CP24). These three proteins are monomeric subunits present in one copy per PSII, responsible for binding 10% of the total Chls and 20% of the Violaxanthin in all supercomplex. Minor antennae plays an important role in thermal dissipation of excess energy as well as in energy transfer to the reaction center (DeBianchi et al. 2010). Two monomeric antennae LHCB4 and LHCB5 and their respective orthologous have been found in all classes of green plants (Koziol et al., 2007). Instead, the LHCB6 orthologous has not been found in green algae and it seem to be associated to a land environment since it is first found in the moss *P.patens* and the maintained in green plants.

The **LHCB4** (CP29) protein structure has been recently solved at 2.8 Å resolution (Pan et al., 2011), it is characterized by three membrane-spanning helical regions connected by both stroma and lumen-exposed loops and the two amphipathic helices exposed on the thylakoid lumen surface. LHCB4 possess 13 Chl-binding sites: eight for Chl a, four for Chl b and one promiscuous for Chl a and Chl b at site 610. Also xanthophyll pigments are present in crystallized structure: Neoxanthin, Violaxanthin and Lutein. LHCB4 is very similar to LHCII monomer except for Chl-binding site which only partially corresponds to LHCII one. In particular Chl 605 and Chl 601 of LHCII are absent in Lhcb4, while Chl 615 has no counterpart in LHCII. This Chl 615 binds glyceraldehyde-3-phosphate (G3P), which bridges this chlorophyll to Chl 612 and Chl 611. Additional differences between LHCB4 and LHCII regarding the absence of V1 site in LHCB4 and the localization of the xanthophylls cycle pigment violaxanthin in the inner site L2, which is instead occupied by lutein in LHCII. This characteristic seems to be crucial for transition of this protein between two different conformational state regulating light harvesting vs energy dissipation (Wehner et al., 2006). LHCB4 is normally located in PSII complex between the outmost LHCII protein and the inner CP43 antenna, a position that ensures a good energy flow toward the reaction center (Caffarri et al., 2009). Under high light

conditions LHCB4 adopts different conformations in order to photoprotect PSII system from excess light. The pigment cluster Viola (Zea)–a603–a609 may dissipate excess energy through a charge-transfer mechanism (Ahn et al, 2008). Alternatively, another pigment cluster, a615–a611–a612–Lut, may quenches the Chl excited states in a way similar to what Lut620–a611–a612 does in LHCI (Mozzo et al., 2008).
Furthermore LHCB4 under stress conditions in higher plants is phosphorylated at threonine or serine residues (Hansson and Vener, 2003). LHCB4 reversible phosphorylation is mainly involved in photoinhibition recovery (Bergantino et al, 1995) and in state transition (Tokutsu et al, 2009). Moreover, the mechanistic connection of LHCB4 phosphorylation in rice and Non-photochemical quenching has been recently described (Betterle et al., 2014) elucidating a photoprotective role for LHCB4 phosphorylation in reducing singlet oxygen production and enhancing excess energy dissipation.

LHCB5 (CP26) is a 26 kDa protein of LHC family. It binds nine chlorophylls and two xanthophylls (Croce et al., 2002). Data on the protein refolded in vitro with pigments suggests that lutein has a primary role in the folding and stability of the complex, whereas violaxanthin and zeaxanthin have a negative effect on folding yield and stability, respectively (Ballottari et al., 2009). Biochemical analysis showed that LHCB5 is involved in the slowly activated NPQ component qI (Dall'Osto et al, 2005).

LHCB6 (CP24) is the most recent member of LHC family evolved after the splitting between land plants and algae (Koziol et al., 2007). It is the smallest one due to the absence of the amphipathic helix at the C-terminus. The *in vitro* reconstitution of this protein shown that it bind 10 Chl molecule and two Xanthophyll (Pagano et al 1998). *A.thaliana* mutants lacking LHCB6 show an altered PSII with reduced ability in photoprotection due to the inefficient energy transfer from LHCII to reaction center (Kovács et al., 2006). It has been proposed that LHCB6 with other antenna proteins is the site for the formation of the zeaxanthin-radical cation (Avenson et al., 2008). Furthermore in vivo and in vitro experiments have showed that LHCB6 protein, upon activation of the xanthophyll cycle, accumulates zeaxanthin into inner binding sites faster and to a larger extent than any other pigment–protein complex. By comparative analysis of LHCB6 complexes binding violaxanthin or zeaxanthin, it has been demonstrated that zeaxanthin not only down-regulates chlorophyll singlet excited states, but also increases the efficiency of chlorophyll triplet quenching, with consequent reduction of singlet oxygen production and significant enhancement of photo-stability (Betterle et al., 2010).

3.3 PSII supercomplex

A variable number of peripheral antennae can associate with dimeric PSII core complex to form the so called PSII-LHCII supercomplex. These supercomplexes can be easily recognized using transmission electron microscopy (TEM) by their peculiar rectangular shape after mild detergent solubilization of grana membrane. The supermolecular organization of *A.thaliana* PSII-LHCII is now available at 12 Å of resolution. This supercomplex contains a dimeric core (C2), two LHCII trimers (trimer S) strongly bound to the complex

on the side of CP43 and CP26 and two more trimers, moderately bound in contact with CP24 and CP29 (trimer M). This complex is known as $C_2S_2M_2$ (Dekker and Boekema, 2005) (Fig). The S-LHCII trimer is composed by the Lhcb1 and Lhcb2 gene products while the M-LHCII trimer consists of Lhcb2 and Lhcb3 gene products. In spinach besides S and M trimers another type of trimer loosely bound and so called L trimer has been described. Recent studies suggest that these L-LHCII trimers can move between PSII and PSI balancing the excitation level of two photosystems during fluctuations in light intensity (Galka et al., 2012; Yakushevska et al., 2001). Supercomplexes can be associated to each other forming megacomplex, for example in spinach three types of megacomplex have been observed while in *Arabidopsis* a fourth type has been found

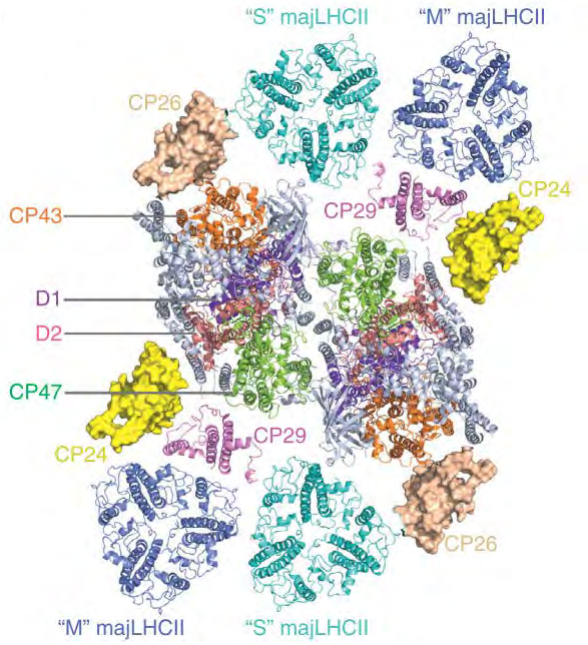

Figure.9. Models of PSII–LHCII and PSI–LHCII supercomplexes showing the relative position of light-harvesting complexes in respect to the core complexes. A structural model of $C_2S_2M_2$-type PSII–LHCII supercomplex. Subunits D1, D2, CP43 and CP47 of PSII core are coloured in purple, salmon, orange and green, respectively. 'S'-, 'M'-type of majLHCII trimers and the minor antenna CP29 are shown as cyan, blue and magenta ribbons. (Pan et al., 2013)

Recently it has been shown that it is possible to separate homogeneous preparation of PSII-LHCII with increasing antennae size (Caffarri et al., 2009). By comparing WT supercomplexes obtained by this procedure to those from Lhcb-deficient genotypes it has been possible to determine the importance of individual subunits in supramolecular organization. LHCB3 and CP24 KO lines completely lack the largest supercomplexes (C_2S_2M and $C_2S_2M_2$) and the small pentameric complex LHCII/CP29/CP24. The complete absence suggests that LHCB3 and CP24 are necessary for the association of M trimers to PSII complex. Also for CP26 ko mutants it has not been possible to detect high molecular weight supercomplexes of and also the amount of smallest complex is reduced (C_2S, C_2M, C_2S_2 and C_2SM) (Dekker and Boekema, 2005).

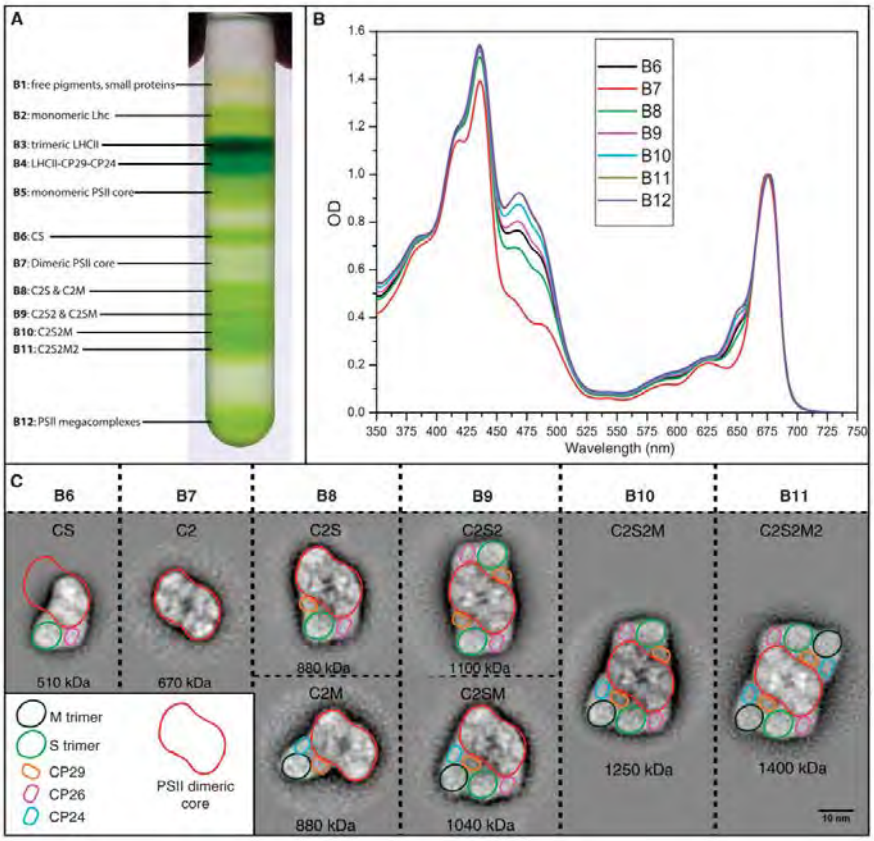

Figure.11. Isolation and characterization of the PSII supercomplexes. (A) Sucrose gradient of solubilized membranes, showing 12 green bands. The content of each band is indicated on the basis of earlier work (Caffarri et al, 2001) (B1–B5) and this work (B6–B12). (B) Absorption spectra of bands 6–12. The spectra are normalized to the maximum in the red region. B11 and B12 are almost superimposed. The Chls b content, which is proportional to the antenna content, is deducible from the intensity of the bands at 470 and 650nm. (C) EM analysis of the supercomplexes. The projections obtained for bands 6–12 are shown. B6 contains a newly identified supercomplex formed by a monomeric core, one LHCII S trimer and the minor antenna CP26. Contours representing the different complexes are superimposed. Also note that the position of the M trimer in the absence of trimer S (C2M in B8) is different. C, core; S, LHCII trimer strongly bound; M, LHCII trimer moderately bound (see text). The molecular weight of each particle, calculated on the basis of the protein content as determined by EM and SDS–PAGE, is also reported.

4. Photoinibition and photoprotective mechanisms

Light in excess can damage the photosynthetic apparatus. Indeed when the absorbed energy exceeds the rate of its use in photochemistry, the formation of oxygen reactive species (ROS) occurs which is responsible for the so-called photoinhibition process. This consists into damage of photosynthetic apparatus and a decrease in the rate of photosynthesis. Normally, light absorbed by chlorophyll or carotenoids is rapidly (<ps time scale) transferred to the excitation energy of the reaction center. Upon photon absorption, Chl is promoted from its ground state to its singlet excited state ^{1}Chl* with a lifetime of ns . This excited state relaxes back to the ground state by several concurrent pathways. Excitation energy can be quenched by (i) photochemical reactions, (ii) it can relax by emitting light as fluorescence or finally

(iii) can de-excite by internal conversion thus into heat (Fig 12). A fourth decay pathway consists into ISC (inter system crossing) to triplet state (^{3}Chl*). ISC is a slow process and therefore its rate becomes relevant only when the life time of ^{1}Chl*increase, which, in turn, depends of the saturation of photochemical reactions. Triplet chlorophyll is characterized by a long life time (~ms time scale) and it can react with triplet oxygen ($^3O_2$*) leading to convertion into singlet oxygen ($^1O_2$*) a highly toxic/dangerous/unstable ROS (Fig.)

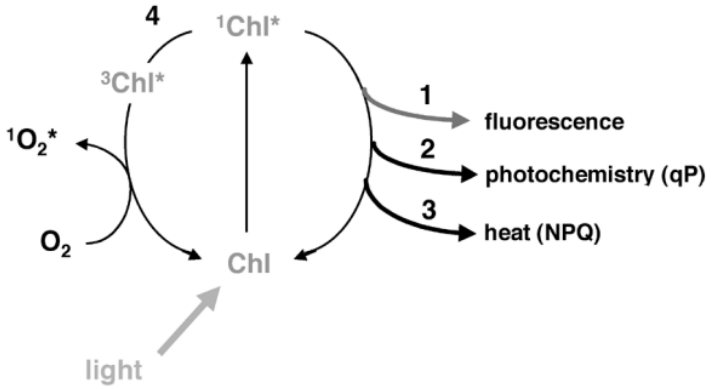

Figure.12. Fates of excited Chl. When Chl absorbs light it is excited from its ground state to its singlet excited state, 1 Chl*. From there it has several ways to relax back to the ground state. It can relax by emitting light, seen as fluorescence (1). Its excitation can be used to fuel photosynthetic reactions (2), or it can de-excite by dissipating heat (3); both of these mechanisms reduce the amount of fluorescence. They are therefore referred to as qP and NPQ of Chl fluorescence. Last, 1 Chl* can, by intersystem crossing, produce 3 Chl* (4), which in turn is able to produce $^1O_2$*, a very reactive oxygen species (Adapted from Muller et al.,

During evolution plants evolved different strategies in order to prevent ROS formation and photoinibition. These strategies can be divided into three different classes on the basis of their being constitutive (a) or beng activated in either short (b) or long (c) time-scale. A-type mechanism consists into triplet quenching and ROS scavenging reactions catalyzed by carotenes and xanthophylls in both core complexes and antenna systems. B-type mechanisms consists into prompt activation of quenching mechanisms dissipating energy as heat. Subsequently, C-type mechanisms lead to plant acclimation through regulation of gene expression in order to adapt their structure and/or metabolism to long-term stress conditions.

A special case is the fast response called Non photochemical quenching (NPQ) reaction which allows for the thermal dissipation of excess absorbed energy and can be monitored as a light-dependent quenching of leaf chlorophyll fluorescence. NPQ can be divided into different components according to their relaxation kinetics upon return of quenched plants in darkness as well as based on their response to different inhibitors.The fastest NPQ is triggered by the building of a excessive pH gradient across the thylakoid membrane and is called **qE**(energy quenching). Another component of NPQ is the slow component **qI** (inhibitory quenching) which relaxes with an half-time > 20 min. This component, attributed to photoinhibition in early reports, is due to the D1 re-synthesis . A third component, called **qT**, is attributed to the state transition. More recent results showed that Zeaxanthin accumulation and its binding to LHC modulate the amplitude of the intermediate kinetic component of NPQ relaxation, thus renamed as **qZ**

(Dall'Osto, 2005). An additional kinetic component is not a real quenching but rather avoidance of absorption (phenomenologically both appears as a decrease in fluorescence) depends on movement of chloroplasts in plants cells which cluster away from direct excess light . This component called **qM** has been described using KO line lacking blue light photoreceptors phototropins (phot2 mutant) in *A. thaliana* antennae, demonstrating that the intermediate phase of NPQ kinetics strongly depends on the chloroplast avoidance movement (Cazzaniga et al., 2013).

According to the topics of this thesis attention will be focus on qE components, elucidating its way of action and the major structural components involved its triggering.

qE is dependent on a signal transduction pathway which involves activation of xanthophylls cycle and sensing by antennae protein subunits of PSII of a low intrathylakoid pH. Lumen acidification activates Violaxanthin de-epoxidase (VDE) to convert violaxanthin to zeaxanthin in the so-called xanthophyll cycle (Gilmore and Yamamoto, 1992). VDE is a monomeric, soluble, inactive, protein at pH >6.0 but dimerses and associates to the thylakoid membrane where its substrate is located upon upon acidification (Morosinotto et al., 2002)(Arnoux et al., 2009). The central role of VDE and Zea for NPQ is clearly demonstrated by qE is decreased by 70% respect to WT in the *A. thaliana* mutants *npq1* which lacks VDE enzyme and is unable to convert Vio to Zea, (Niyogi et al., 1998). The primary role of Zea in inducing qE is also confirmed by the phenotype of *npq2* mutants, in which the zeaxanthin epoxidation is blocked, leading an accumulation of Zea even in the dark-adapted plants. These show a more rapid saturation of qE respect to WT (Niyogi et al., 1998). It is important to note that in these mutants a residual component of qE is activated independently on the presence of a functional xanthophyll cycle due to xanthophyll species bound to Lhcb proteins in the dark. This component is lutein as shown by the *lut2npq1* mutants which lack both Zea and Lut and has a null NPQ-phenotype (Niyogi et al., 2001). These evidences regarding mutants in Lutein or Zeaxanthin clearly suggest a determinant role of both xanthophylls for qE activation.

Besides the presence of VDE and xanthophylls molecule the qE activation is also due to the presence of two specific LHC proteins, PSBS for plants and LHCSR for algae. The following section will discuss their function in NPQ activation.

4.1 PSBS protein and qE induction in plants

PSBS protein was discovered as a 22 kDa protein in PSII preparations (Funk et al., 1995). Its role has been hidden until the isolation by video imaging of chlorophyll fluorescence of *A.thaliana* mutants defective in qE which was called *npq4*. This mutant lacked qE but has got a normal xanthophylls cycle, its mutation was mapped on chromosome 1 like a total deletion of *PSBS* gene codifying for the LHC protein PSBS (Li et al. 2000). PSBS protein differs from other LHC proteins for having four transmembrane helices and because it does not bind pigments (Dominici et al., 2002). The typical characteristic of this protein is the presence of two lumen-exposed glutamate residues, Glu^{122} and Glu^{226}, able to bind to *N,N*'-

Dicyclohexylcarbodiimide (DCCD). Site direct mutagenesis of these two aminoacids to non-protonatable ones, i.e E122Q and E226Q, decreased by 50% both qE and DCCD binding capacity , whereas the double mutant has a null-phenotype like *npq4* (Li et al. 2000). These data suggest that the protonation of these two residues in excess light is necessary for qE and that PSBS acts as a pH sensor. Considering the role of PSBS in triggering qE we can infer that the level of qE should be related to the level of PSBS per PSII. Indeed molecular and genetic analysis reveals that there is a psbs gene dosage effects on qE indeed increasing PSBS expression confers a higher qE capacity (Li et al., 2002; Hieber et al., 2004) with a saturation 5 times more respect to the WT level in *A.thaliana* plants. From this saturation data it is possible to conclude that there are a maximum number of functional binding sites for PSBS per PSII.

Even if PSBS has been isolated in PSII preparation it precise localization is not yet completely understood. Early biochemical studies showed that PSBS could be co-immunoprecipitated with the non pigmented 33 kDa and 22 kDa subunits of the oxygen-evolving complex of PSII suggesting an association with the PSII reaction centre (Ljungberg et al., 1986). Subsequently, selective PSBS extraction allowed the disruption of interaction between the peripheral LHCII and the reaction center suggesting a localization of PSBS at the interface between these two complexes (Li et al. 2000). Recently it has been shown that PSBS is not a component of purified C_2S_2 complex (Nield and Barber, 2006) and cannot be accommodated in $C_2S_2M_2$ supercomplex (Dekker and Boekema, 2005) so it is possible to suggest a peripheral localization of PSBS even if it has not yet experimentally confirmed. Using immunoprecipitation technique, It has also shown that PSBS interacts with many photosynthetic complex like CP29, component of LHCII, PSI and Cyt-b6f, suggesting a mobile behavior of PSBS in thylakoids membrane (Teardo et al., 2007). Two aggregation states have been reported: monomer and dimer. The dimer to monomer transition was suggested to be triggered by decreasing by pH or by high light, suggesting the monomeric form is active in NPQ kinetics. Furthermore, these two forms might also have a distinct localization in thylakoids: indeed, the dimeric form co-fractionated with PSII reaction center while the monomeric one was associated with LHC fraction (Bergantino et al., 2003).

As described above PSBS is able to sense the transmembrane pH through the protonation of two luminal glutamic acid residues, protonated PSBS is so able to activate a Lutein/Zeaxanthin dependant quenching process in LHCB proteins (Bonente et al., 2008a). Nevertheless, the mode of interaction is still obscure (fig). In one proposal, PSBS would promote LHCII aggregation, whereas the level of quenching is regulated by de-epoxidation state of the site V1 (Kiss et al., 2008). A second hypothesis is based on the two different forms of PSBS suggesting that the dimer to monomer transition might uncover the Zeaxanthin-binding site on the PSBS surface so PSBS monomer could transiently bind Zeaxanthin and bring this pigment in close contact with either LHCII or minor LHCB forming a Chl-Zea heterodimer(Bergantino et al., 2003). A third hypothesis is based on the observation that treatment that prevents dissociation of a pentameric complex, including LHCB4 and LHCB6, together with a LHCII trimer also blocks NPQ. Thus the

unquenched conformation of LHCB proteins is stabilized by their inclusion in this large complex, while its dissociation by PSBS would allow transition to the quenching state, also promoted by Zea binding. Thus the unquenched conformation of LHCB proteins is stabilized by their inclusion in this large complex, while its dissociation by PSBS would allow transition to the quenching state, also promoted by Zea binding (Betterle et al., 2009).

4.2 LHCSR protein and qE induction in algae

Although genes encoding PSBS have been identified in the genomes of green algae, the corresponding polypeptides have never been detected (Koziol et al. 2007; Bonente et al. 2008b) suggesting that algae rely on different proteins for NPQ activation. In *Chlamydomonas reinhardtii*, NPQ activation depend on a Lhc-like protein called LHCSR (Light harvesting complex stress-related, or Li818) (Peers et al., 2009). Indeed *C. reinhardtii* mutants depleted in Lhcsr gene (npq4 showed a qE-deficient phenotype and also a reduced fitness in variable light conditions, demonstrating that Introduction of LHCSR is required for survival in a dynamic light environment. LHCSR-dependent NPQ mechanism is likely widespread among algae, as it has been recently demonstrated to be involved in NPQ also in some diatoms (Bailleul et al., 2010)

Biochemical analysis of reconstituted LHCSR from *C. reinhardtii* showed that this protein function as a pH-sensitive site for quenching of excitation energy. LHCSR is Chla/b and xanthophyll-binding protein with a high Chla/b ratio. It binds seven Chls per polypeptide, two binding sites with strong affinity for Lutein and Violaxanthin, probably L1 and L2, and no binding site for Neoxanthin. LHCSR also binds Zeaxanthin in the V1 site. LHCSR accumulating in high light, is a strong quencher of Chl excited states, exhibiting a very fast fluorescence decay, with lifetimes below 100 ps, capable of dissipating excitation energy from neighbor antenna proteins (Bonente et al., 2011). Recently it has been demonstrated that the C-terminus domain, rich in acidic residues, of *C.reinhardtii* LHCSR acts as a luminal pH sensor domain driving NPQ response(Liguori et al., 2013).

LHCSR regulates energy dissipation by establish reversible interaction with others LHCB proteins, in particular LHCBM1, induced by low lumenal pH through protonatable DCCD-binding sites (Bonente et al., 2011; Tokutsu and Minagawa, 2013). A four step model for qE induction in *C.reinhardtii* has been proposed. according to which the first step is the accumulation of LHCSR protein in high light condition following by the binding of LHCSR to the periphery of PSII-LCHII supercomplex in the membrane. Finally, LHCSR is protonated upon lumen acidification directly modifies the antenna conformation within the supercomplex to form a quenching center (Tokutsu and Minagawa, 2013). This model is confirmed by fluorescence lifetime measurement on PSII supercomplex containing LHCSR3 which exhibited a long fluorescence

lifetime at a neutral pH (7.5) by single-photon counting analysis, but a significantly shorter lifetime at pH 5.5, which mimics the acidified lumen of the thylakoid membranes.

5. Physcomitrella patens: a new model organism to study the evolution of photosynthesis regulation

5.1 Physcomitrella patens as an evolutionary key intermediate in evolution of land plants

The moss *Physcomitrella patens* has recently emerged as a powerful genetically tractable model plant system providing a unique opportunity to study plant evolution. Mosses belong to bryophyte group which also includes liverworts and hornworts; together, these groups comprise some 15000-20000 species originated 500 million of years ago (Sanderson et al. 2004). Evolutionary studies support the monophyletic origin of land plants and indicate that bryophytes may form a sister clade with tracheophytes (Kenrick and Crane, 1997). During the Paleozoic era bryophyte first colonized terrestrial environment evolving strategies that made them able to adapt to the low CO_2 levels and high UV-B radiation. These processes can be partially reconstituted by analyzing the *P.patens* genome, sequenced in 2008. Indeed, through a direct comparison with plant and algae genomes it is possible to reconstitute genome evolution that occurred in colonization of land. It is possible to conclude that last common ancestor of land plants during evolution lost genes associated with aquatic environments (e.g., flagellar components for gametic motility); lost dynein-mediated transport; gained signaling capacities, such as those for auxin, ABA, cytokinin, and more complex photoreception; gained tolerance for abiotic stresses, such as drought, radiation, and extremes of temperature; gained more elaborate transport capabilities; and had an overall increase in gene family complexity (Rensing et al., 2008).

In common with ferns and seed plants, mosses show alternation of generations: a haploid phase that produces gametes (the gametophyte generation) and a diploid phase that produces haploid spores by meiosis (the sporophyte generation). *P.patens* life cyle is dominated by gametophyte generation which comprises by chloronemal and caulonemal cells which develop by apical growth and cell division of apical and subapical cells (Fig.). Chloronemal cells are densely packed with large chloroplasts while caulonemal cells contain fewer, less well developed chloroplasts. Caulonemal filaments are responsible for bud productions which represent a three dimensional shoot development: the second gamethophyte stage, called gametophores or leafy shoot. At the top of a single gametophore, both male (antheridia) and female (archegonia) sexual organs form. In the antheridia the flagellate sperm are produced which swim to fertilize the egg cell within an archegonium (Cove, 2005; Prigge and Bezanilla, 2010) (fig)

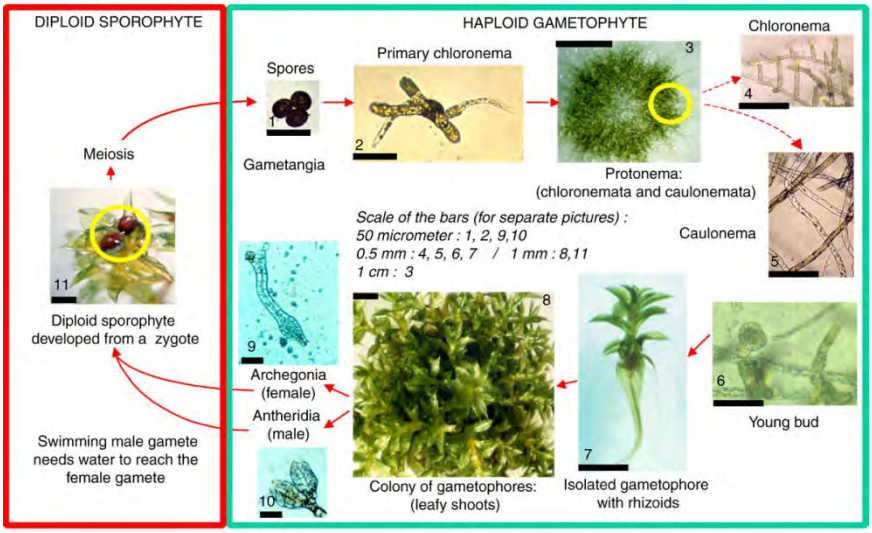

Figure.13. *P.patens* life cycle. (1) Spores, (2) light-dependent spore germination generating primary chloronemata,(3) 15-d-old protonemal colony, (4) branching chloronema, (5) caulonema cells characterized by an oblique cell wall and a small number of chloroplasts, (6) filamentous two-dimensional structure switches to three dimensions with the appearance of young bud, (7) young bud developing to form the leafy shoot of the gametophore, (8) a fully developed moss leafy gametophyte (4 weeks old), (9) an archegonium (female structure) dissected out from a gametophore, (10) two antheridia (male structures) dissected out from a gametophore. P. patens being a monoecious species both structures are present on the same plant and appears after a cold treatment (15°C for 3 weeks), (11) after fertilization by swimming spermatozoids (under water), the egg cell develops into a small diploid sporophyte and within its capsule meiosis occurs leading to spore formation (approximately 5,000 spores per capsule (Schaefer and Zry, 2001)

P. patens is an ephemeral, developing in early summer, generally from overwintered spores. It grows beside lakes, rivers, and ditches on soil that has been exposed by falling water levels, and on damp open ground in fields . Temperatures below 18°C are required to induce gametogenesis, and short day lengths enhance gametangia induction .Isolates are now available from a number of European, Japanese, and North American location. (Cove, 2005).

5.2 Advantages of using *P. patens* as model organism

As mentioned, *P.patens* is evolutionary an intermediate between algae and vascular plants. It shares many biological features with them, in terms of gene conservation, physiology and development (Rensing et al., 2008). Since now it has been used as a model organism to study plant development and plant evolution taking advantages of its peculiar physiologically and genetic characteristics. *P.patens* life cyle is dominated by the haploid gametophyte, this facilitates genetic analysis in fact, in haploids recessive loss of function traits can be observed directly without further backcrossing to obtain homozygous diploids (Schaefer and Zry, 2001).This is directly opposite to the life cycle of higher plants, where the diploid is dominant. *P.patens* could be considered a unique model for plant functional genomics approaches because

of the highly efficient homologous recombination in its DNA genome which can be used for the generation of knock-out (KO) plants depleted in specific proteins, or the gene replacement with a mutated one to study proteins function. Genetic transformation techniques for *P.patens* takes advantages of poly-ethylene glycol (PEG)-mediated transformation (Schaefer et al. 1991). Futhermore, *P.patens* genome was sequenced in 2008 giving a resource for phylogenetic inferences about gene function and for experimental analysis of plant processes through this plant ' s unique facility for reverse genetics (Rensing et al., 2008)

P. patens grow photo-autotrophic in a simple medium of inorganic salts under relatively low light conditions between 6 and 70 µE. A temperature of about 25°C is optimal for growth, although growth rates are only slightly lower at 20°C. Small pieces of either gametophytic or sporophytic tissue regenerate to produce protonemal tissues in 5-7 days. Protonemal tissue can be disrupted mechanically with a tissue homogenizer, and the resulting tissue fragments can be used as an inoculum for further culture (Cove, 2005)

5.3 P. patens as a useful tool for study of the photosynthetic and photoprotective mechanism.

The evolutionary intermediate position of *P.patens* respect to algae and plants offers the possibility to understand the evolution of photosynthetic organisms. In general, mosse's photosynthetic apparatus is similar to tat of green algae and vascular plants, with the presence of Chls a and b, carotene and xanthophylls and LHC for light harvesting (Alboresi et al., 2008). Mosses usually live in shade habitats and so they are characterized by a shade-adapted photosynthetic apparatus with a Chl a/b ratio of about 1-2.5 depending of the species. It is important to consider also the simpler leaf morphology, one-cell thick and so they are not able to respond to different light by modifying leaf thickness. Furthermore, they lack stomata and they can only get water and CO_2 directly through diffusion. Consistently they are characterized by a higher CO_2 compensation point than tracheophytes can exploit the high CO_2 concentration near the soil due to decomposition.

Looking in depth the photosynthetic apparatus, it is possible to identify interesting peculiarities (Alboresi et al., 2008). A functional core of antennae proteins conserved with the whole green lineage (LHCA1, LHCA2, LHCA3, LHCB4, LHCB5) has been identified. Orthologs of other antenna proteins such as LHCB3 and LHCB6 have not been identify suggesting a possible role for these two proteins in terrestrial adaptation of land plants. Moreover in *P.patens* has been described a new LHC protein, called LHCB9. This protein, very similar to LHCB antennas, was attributed to PSII antennae system suggesting a possible role for this red-shifted antennae protein either in optimization of light use efficiency or in photoprotection in the specific environmental conditions (Alboresi et al., 2011). Information on PSI and PSII composition in *P.patens* are still scarce. It is known that PSI subunits are characterized by a large number of isoforms. Considering that *P.patens* underwent all genome duplication 45 million of year ago, leading to a wealth of multiple gene (Rensing et al., 2008) it is possible to speculate that the high number of isoform was retained

and specialized to fine-tune the structure and function of PSI during different development stages or stress conditions. In particular, PSI retains the cyanobacteria PsaM subunits and also contains the plant specific PsaG,-H and –O. However a PsaN homologue has not been identified and the sequence protein of PsaF could be considered an example of that *P.patens* retains a more ancient version of protein compared of higher plants (Busch et al., 2013). Also the PSI-LHCI complex seems different from the plant counterpart. Based on native gel analysis it has been proposed that *P.patens* PSI-LHCI is smaller than in plants (Alboresi et al., 2008). More recent analysis has better clarified that two different population of PSI supercomplex can be described. The larger particles, presented in the majority, represent a PSI with four Lhca proteins at the PsaF/PsaJ side of the PSI core(Busch et al., 2013), opening the question of which Lhca protein replace Lhca4 in the complex, as has been shown that *Physcomitrella* doesn't have an Lhca4 homologues (Alboresi et al., 2008). Hence, one of the Lhca1–Lhca3 isoforms has to occupy the Lhca4 position in order to form the half-moon-shaped LHCI complex.

As described above land colonization required an improvement in photoprotection mechanisms. This was confirmed by sequence analysis which revealed the presence of both LHCSR and PSBS in *P.patens* genome (Alboresi et al., 2008) demonstrating that it is the first organism in which both proteins have been shown to be present and active in triggering NPQ. Two LHCSR isoforms exist in *P. patens*, called LHCSR1 and LHCSR2. They share 91% sequence identity. LHCSR1 encodes for the largest fraction of LHCSR pool and its deletion causes the strongest effect on NPQ amplitude, whereas lhcsr2 KO has a NPQ phenotype closer to that of WT (Alboresi et al., 2010). Recently the activity of LHCSR1 has been clarified starting from VDE mutants for which it has been demonstrated that the effect of zeaxanthin on LHCSR-dependent NPQ is stronger. A search for the basis of the high zeaxanthin dependence of NPQ led to the identification of a new zeaxanthin binding site in the LHCSR protein upon its isolation in the form of native chlorophyll a/b – xanthophyll binding protein demonstrating that LHCSR protein binds zeaxanthin upon excess light stress (Pinnola et al., 2013). Moreover the specific role for these PSBS and LHCSR proteins was analyzed by generating *P. patens* genotypes such as psbs KO, lhcsr KO, psbs lhcsr KO and genotypes differing in PSBS and LHCSR content (OE) (Alboresi et al., 2010; Gerotto et al., 2012). Analyzing mutants for PSBS or LHCSR polypeptides it was possible to identify a decreased NPQ phenotype, implying that both LHCSR and PSBS are active in triggering this photoprotection mechanism and their NPQ activities are independent one from each other. Even if mutual interactions cannot be excluded, PSBS and LHCSR1 act additively in triggering NPQ (Alboresi et al., 2010). All these data taken together suggest that *P.patens* retains the LHCSR-dependant NPQ mechanism found in *Clamydomonas* and evolved an additionally mechanism based on PSBS protein. Moreover modulation of PSBS or LHCSR content was found to be correlated with NPQ amplitude indicating that *P.patens* can modulates its response to excess light by altering the accumulation of one or both of these proteins (Gerotto et al., 2012).

6. General biology of *N.tabacum* and *N.benthamiana*

The genus *Nicotiana* includes 76 species of mainly tropical and subtropical distribution from four continents, with the majority occurring in South America and Australia. Although the base haploid chromosome number is considered to be 12, amphiploidy is common in the genus, with many extant species (or their recent successors) featuring in the reticulate evolution of the allopolyploids. Haploid chromosome numbers range from 9 and 10 to 24 and even 32 in some collections of *N.suaveolens* and there is a great variation in chromosome and genome size

Among the genus *Nicotiana* the allotetraploid plant *Nicotiana tabacum* is one of the most widely cultivated non-food crops worldwide and is grown in ~120 countries. *N. tabacum* is a amphidiploids which is thought to be created from two progenitors. As a species, *N. tabacum* (2n = 4n= 48) evolved through the interspecific hybridization of the ancestors of *Nicotiana sylvestris* (2n=24, maternal donor) and *Nicotiana tomentosiformis* (2n = 24, paternal donor) about 200,000 years ago (Leitch et al., 2008). *N.tabacum* is a perennial plant but it is cultivated as annual. Plants are stout, thick-stemmed herbs or single-stemmed shrubs with large oily hairy leaves that expand directly from the stem (*sessile*, no petioles) or have broadly winged petioles. Tubular flowers are nearly regular with the petals spreading at right angles to the broadly inflated tube (*salverform*). Flowers are usually pinkish, but ranging from white to red; the flowering is *diurnal* (day opening). It could be considered a useful plant species for studying fundamental biological process (Sierro et al., 2014) expecially as a model for plant disease susceptibility, which it shares with other Solanaceae plants including potato, tomato and pepper. Instead diseases affecting tobacco include the tobacco mosaic virus (TMV), the tobacco vein mottling virus (TVMV), the tobacco etch virus (TEV), and the potato virus Y (PVY).

Nicotiana benthamiana is another plant in Nicotiana genus highly studied as experimental host in plant virology due mainly to the large number of diverse plant viruses that can successfully infect it. *N.benthamiana* is distributed widely and occupies seasonally arid habitats that are unfavorable to other native species of Nicotiana. Indeed it has a broad, somewhat discontinuous distribution from extreme Western Australia east to western Queens-land, with a single documented collection from northern South Australia. The herbaceous plant is found amongst rocks on hills and cliffs throughout the northern regions of Australia. Variable in height and habit, the species may be erect and up to 1.5 metres or sprawling out no taller than 200 millimetres. The flowers are white.

N. benthamiana is susceptible to a wide variety of plant-pathogenic agents (such as bacteria, oomycetes, fungi, and so on), making this species a cornerstone of host–pathogen research, particularly in the context of innate immunity and defence signalling. Moreover, because it can be genetically transformed and regenerated with good efficiency and is amenable to facile methods for virus-induced gene silencing or transient protein expression, *N. benthamiana* is rapidly gaining popularity in plant biology, particularly in

studies requiring protein localization, interaction, or plant-based systems for protein expression and purification (Goodin et al., 2008).

6.1 Stable and transient expression of heterologugus proteins in *N.tabacum* and *N.benthamiana*

In the past decade plants has emerged as a convenient useful system for large-scale production of recombinants proteins and it nowadays used for expression of antibodies, vaccines, human blood products, hormones and growth factors. For these products plants offer a lot of practical and safety advantages respect traditional systems based on microbial or animal cells, or transgenic animals. It is estimated that recombinant proteins can be produced in plants at 2–10% of the cost of microbial fermentation systems and at 0.1% of the cost of mammalian cell cultures, although this depends on the product yield (Giddings, 2001).. Plant platforms can be divided into two main categories, based respectively on stable and transient expression of target recombinant protein.

Stable expression plant platforms are generally based on stable heterologous gene transfer to the plant nuclear genome. This transformation is achieved using two different technologies: particles bombardments or *Agrobacterium*-mediated transformation. Indeed the soil pathogen *A.tumefaciens* provides a common system for transformation of dicots species, it has the natural occurring plasmid (Ti plasmid) which has the ability to integrate its T-DNA and transform host cell (Escobar and Dandekar, 2003). A portion of T-DNA can be replaced by gene of interest without affecting its transformation ability representing the basic concept in *Agrobacterium*-mediated transformation. To achieve high yields, expression-construct design must optimize all stages of gene expression. For high-level transcription, the two most important elements are the promoter and the polyadenylation site, which are often derived from the 19S and 35S transcripts of the cauliflower mosaic virus (CaMV) (Ma et al., 2003). Promoters that allow the expression of a transgene in a particular environmental, developmental or tissue-specific manner might also be useful. Among plants historically Tobacco has been established as a model system for stable molecular farming and it is the most used system for the production of recombinant pharmaceuticals proteins. The main advantages in using tobacco include the mature technology for gene transfer and expression, the high biomass yield, the potential for rapid scale-up owing to prolific seed production, and the availability of large-scale infrastructure for processing.

Although stable plant transformation is now a routine in many species, it has a major disadvantage in terms of production time-scales, which is being addressed by the development of alternative plant production technologies based on protein transient expression. Transient expression systems can e divided in two groups: systems based on agroinfiltration with conventional vectors and systems based on plant viral vectors (Gleba et al., 2007). For transient expression *Nicotiana.benthamiana* is the most used host because this specie is amenable to facile agro-infiltration and it is susceptible to a wide variety of plant viruses (Goodin et al., 2008). *N. benthamiana agrobacterium*-mediated transient expression exploits the facts that

infiltration of the intercellular spaces in plant leaves with a suspension of the bacterium (i.e. agroinfiltration) via syringe or vacuum, can result in mobilization of T-DNA into the nuclei of a large proportion of the cells so exposed. An optimization of transgene transformation could be easy because many constructs can be tested in parallel, using different versions of the same basic gene, different promoters or different leader or organelle targeting sequence (Rybicki, 2010). Another strategy for transient expression includes the use of plants viruses which are more easily to manipulate and assure a high yield of product. Several viruses have been extensively developed for vaccine production, including tobacco mosaic virus (TMV), potato virus X (PVX) and cowpea mosaic virus (CPMV). These viral vectors are functional viruses that express, in addition to all genes of the wild-type virus, the coding sequence of a protein of interest: recombinant viral particles replicate in infected tissue and move systemically, producing the target heterologous protein in addition to the viral proteins.

Even if as previously described these two systems nowadays are primarily used for efficient and convenient expression of recombinant biomedical proteins, plants systems are rapidly gaining popularity in plant biology, particularly in studies requiring protein localisation, interaction, or plant-based systems for protein expression and purification. For example it has been reported the possibility of *N.tabacum* transformation with β-carotene ketolase gene from the alga *H.pluvialis* showing the possibility of astaxanthin accumulation in chromoplast-containing tissue of the nectary that normally synthesizes β-carotene and xanthophylls (Mann et al., 2000). Others applications includes the tobacco chloroplast transformation in order to engineering photosynthesis, introducing heterologous Rubisco subunits in order to increase the carbon fixation (John Andrews and Whitney, 2003; Bock and Khan, 2004) or to optimize production of recombinant hemicellulases in transplastomic tobacco, developing a set of cassettes that incorporate elements known to facilitate protein expression in chloroplasts and examined expression and accumulation of a bacterial xylanase XynA (Kolotilin et al., 2013).

Other application until not exploited could regard the expression in a high yield of proteins involved in photosynthetic process. This is one of the major aims of this thesis, showing the possibility of heterologous LHC proteins over-expression in order to purify correctly folded proteins for biochemical and spectroscopic analysis. Until now the properties of different LHC proteins have been studied in detail using in vitro reconstitution allowing the production of complexes giving us information about the properties of individual pigments and their role in light harvesting and photoprotection. However only few LHCs proteins have been purified from thylakoids in their native state without losing cofactors or some pigments. For example CP24,CP26 and CP29 has been certainly purified in several steps using high detergent concentration but this lead to loss of pigments (Ruban et al., 1999; Pascal et al., 1999). For example crystal structure of CP29 shown biochemical and spectroscopic properties different from that of the starting material and of all other CP29 preparations found in literature (Feng et al., 2013; Croce et al., 1996; Pascal et al., 1999; Pan et al., 2011). Also for CP24 data regarding its properties are not completely coherent, CP24

purified from plants coordinates only few chlorophylls while complex reconstituted in vitro binds 10 chlorophylls and 2 carotenoids (Dainese and Bassi, 1991; Pagano, 1998). To get the most reliable information about the properties of the complexes in their native state, it is thus necessary to purify them to homogeneity from plants using a very mild purification procedure. For this reason in this thesis has been exploited the possibility of overcome limitations in expression and purification procedure using stable and transient expression in *N.tabacum* and *N.benthamiana*.

The LHCSR1 from *P.patens* has been chosen as candidate for heterelogous expression in these two systems. Indeed this protein until now escaped purification and biochemical or spectroscopic characterization because it is present in a very low quantity in *P.patens* thylakoid membrane even if its fundamental role in Non-photochemical quenching (Alboresi et al., 2010). Furthermore previous work shown that *P.patens* mutans overexpressing LHCSR1 are not able to accumulate a high level of LHCSR1 due probably to an unidentified mechanism of post-translational regulation active for this protein (Gerotto et al., 2012). The heterologous expression of this protein in foreign systems could represent a good solution to overcome problems of proteins accumulations allowing its purification and biochemical characterisation.

References

Ahn, T.K. (2008). Architecture of a charge-transfer state regulating light harvesting in a plant antenna protein. Science (80-.).

Alboresi, A., Caffarri, S., Nogue, F., Bassi, R., and Morosinotto, T. (2008). In silico and biochemical analysis of Physcomitrella patens photosynthetic antenna: identification of subunits which evolved upon land adaptation. PLoS One **3**: e2033.

Alboresi, A., Gerotto, C., Cazzaniga, S., Bassi, R., and Morosinotto, T. (2011). A red-shifted antenna protein associated with photosystem II in Physcomitrella patens. J. Biol. Chem. **286**: 28978–87.

Alboresi, A., Gerotto, C., Giacometti, G.M., Bassi, R., and Morosinotto, T. (2010). Physcomitrella patens mutants affected on heat dissipation clarify the evolution of photoprotection mechanisms upon land colonization. Proc. Natl. Acad. Sci. U. S. A.

Amunts, A. and Nelson, N. (2008). Functional organization of a plant Photosystem I: evolution of a highly efficient photochemical machine. Plant Physiol. Biochem. **46**: 228–37.

Anderson, M.I.J.S., Horne, J.E.L.T., and Ikstro, N.I.W. (2004). Molecular evidence of plant divercence time . **91**: 1656–1665.

Armstrong, G.A. and Hearstt, J.E. (1996). Serial review carotenoids 2. **10**.

Arnoux, P., Morosinotto, T., Saga, G., Bassi, R., and Pignol, D. (2009). A structural basis for the pH-dependent xanthophyll cycle in Arabidopsis thaliana. Plant Cell **21**: 2036–44.

Avenson, T.J., Tae, K.A., Zigmantas, D., Niyogi, K.K., Li, Z., Ballottari, M., Bassi, R., and Fleming, G.R. (2008). Zeaxanthin radical cation formation in minor light-harvesting complexes of higher plant antenna. J. Biol. Chem. **283**: 3550–3558.

Bailleul, B., Rogato, A., Martino, A. De, Coesel, S., Cardol, P., and Bowler, C. (2010). An atypical member of the light-harvesting complex stress-related protein family modulates diatom responses to light.

Ballottari, M., Girardon, J., Dall'osto, L., and Bassi, R. (2012). Evolution and functional properties of photosystem II light harvesting complexes in eukaryotes. Biochim. Biophys. Acta **1817**: 143–57.

Ballottari, M., Mozzo, M., Croce, R., Morosinotto, T., and Bassi, R. (2009). Occupancy and functional architecture of the pigment binding sites of photosystem II antenna complex Lhcb5. J. Biol. Chem. **284**: 8103–13.

Ben-shem, A., Frolow, F., and Nelson, N. (2003). Crystal structure of plant photosystem I. Nature **426**: 2–7.

Bergantino, E. et al (1995). A post-translational modification of the photosystem II subunit CP29 protects maize from cold stress.

Bergantino, E., Segalla, A., Brunetta, A., Teardo, E., Rigoni, F., Giacometti, G.M., and Szabò, I. (2003). Light- and pH-dependent structural changes in the PsbS subunit of photosystem II. Proc. Natl. Acad. Sci. U. S. A. **100**: 15265–70.

Betterle, N., Ballottari, M., Baginsky, S., and Bassi, R. (2014). High light-dependent phosphorylation of Photosystem II inner antenna CP29 in monocots is STN7-independent and enhances Non Photochemical Quenching. Plant Physiol.

Betterle, N., Ballottari, M., Hienerwadel, R., Dall'Osto, L., and Bassi, R. (2010). Dynamics of zeaxanthin binding to the photosystem II monomeric antenna protein Lhcb6 (CP24) and modulation of its photoprotection properties. Arch. Biochem. Biophys. **504**: 67–77.

Betterle, N., Ballottari, M., Zorzan, S., de Bianchi, S., Cazzaniga, S., Dall'osto, L., Morosinotto, T., and Bassi, R. (2009). Light-induced dissociation of an antenna hetero-oligomer is needed for non-photochemical quenching induction. J. Biol. Chem. **284**: 15255–66.

Bianchi, S. De, Ballottari, M., Osto, L.D., and Bassi, R. (2010). Regulation of plant light harvesting by thermal dissipation of excess energy. Biochem. Soc. Trans.: 1–10.

Bock, R. and Khan, M.S. (2004). Taming plastids for a green future. Trends Biotechnol. **22**: 311–8.

Boekema, E.J., Jensen, P.E., Schlodder, E., van Breemen, J.F.L., van Roon, H., Scheller, H.V., and Dekker, J.P. (2001). Green Plant Photosystem I Binds Light-Harvesting Complex I on One Side of the Complex †. Biochemistry **40**: 1029–1036.

Bonente, G., Ballottari, M., Truong, T.B., Morosinotto, T., Ahn, T.K., Fleming, G.R., Niyogi, K.K., and Bassi, R. (2011). Analysis of LhcSR3, a protein essential for feedback de-excitation in the green alga Chlamydomonas reinhardtii. PLoS Biol. **9**: e1000577.

Bonente, G., Howes, B.D., Caffarri, S., Smulevich, G., and Bassi, R. (2008a). Interactions between the photosystem II subunit PsbS and xanthophylls studied in vivo and in vitro. J. Biol. Chem. **283**: 8434–45.

Bonente, G., Passarini, F., Cazzaniga, S., Mancone, C., Buia, M.C., Tripodi, M., Bassi, R., and Caffarri, S. (2008b). The occurrence of the psbS gene product in Chlamydomonas reinhardtii and in other photosynthetic organisms and its correlation with energy quenching. Photochem. Photobiol. **84**: 1359–70.

Busch, A., Petersen, J., Webber-Birungi, M.T., Powikrowska, M., Lassen, L.M.M., Naumann-Busch, B., Nielsen, A.Z., Ye, J., Boekema, E.J., Jensen, O.N., Lunde, C., and Jensen, P.E. (2013). Composition and structure of photosystem I in the moss Physcomitrella patens. J. Exp. Bot. **64**: 2689–99.

Caffarri, S., Croce, R., Cattivelli, L., and Bassi, R. (2004). A look within LHCII: differential analysis of the Lhcb1-3 complexes building the major trimeric antenna complex of higher-plant photosynthesis. Biochemistry **43**: 9467–76.

Caffarri, S., Kouril, R., Kereïche, S., Boekema, E.J., and Croce, R. (2009). Functional architecture of higher plant photosystem II supercomplexes. EMBO J. **28**: 3052–63.

Cazzaniga, S., Dall' Osto, L., Kong, S.-G., Wada, M., and Bassi, R. (2013). Interaction between avoidance of photon absorption, excess energy dissipation and zeaxanthin synthesis against photooxidative stress in Arabidopsis. Plant J. **76**: 568–79.

Chen, M., Schliep, M., Willows, R.D., Cai, Z.-L., Neilan, B. a, and Scheer, H. (2010). A red-shifted chlorophyll. Science **329**: 1318–9.

Cove, D. (2005). The moss Physcomitrella patens. Annu. Rev. Genet. **39**: 339–58.

Croce, R., Breton, J., and Bassi, R. (1996). Conformational Changes Induced by Phosphorylation in the CP29 Subunit of. Biochemistry **2960**: 11142–11148.

Croce, R., Canino, G., Ros, F., and Bassi, R. (2002). Chromophore Organization in the Higher-Plant Photosystem II Antenna Protein CP26. Biochemistry **41**: 7334–7343.

Dainese, P. and Bassi, R. (1991). System and Aggregation State of the Component Chlorophyll u / b.: 8136–8142.

Dall'Osto, L., Holt, N.E., Kaligotla, S., Fuciman, M., Cazzaniga, S., Carbonera, D., Frank, H. a, Alric, J., and Bassi, R. (2012). Zeaxanthin protects plant photosynthesis by modulating chlorophyll triplet yield in specific light-harvesting antenna subunits. J. Biol. Chem. **287**: 41820–34.

Dall'Osto, L., Lico, C., Alric, J., Giuliano, G., Havaux, M., and Bassi, R. (2006). Lutein is needed for efficient chlorophyll triplet quenching in the major LHCII antenna complex of higher plants and effective photoprotection in vivo under strong light. BMC Plant Biol. **6**: 32.

Dall'Osto, L.C. (2005). A Mechanism of Nonphotochemical Energy Dissipation , Independent from PsbS , Revealed by a Conformational Change in the Antenna Protein CP26. **17**: 1217–1232.

Dekker, J.P. and Boekema, E.J. (2005). Supramolecular organization of thylakoid membrane proteins in green plants. Biochim. Biophys. Acta **1706**: 12–39.

Dominici, P., Caffarri, S., Armenante, F., Ceoldo, S., Crimi, M., and Bassi, R. (2002). Biochemical properties of the PsbS subunit of photosystem II either purified from chloroplast or recombinant. J. Biol. Chem. **277**: 22750–8.

Escobar, M. a and Dandekar, A.M. (2003). Agrobacterium tumefaciens as an agent of disease. Trends Plant Sci. **8**: 380–6.

Feng, X., Kell, A., Pieper, J., and Jankowiak, R. (2013). Modeling of optical spectra of the light-harvesting CP29 antenna complex of photosystem II--part II. J. Phys. Chem. B **117**: 6593–602.

Funk, C., Adamska, I., Green, B.R., Andersson, B., and Renger, G. (1995). The nuclear-encoded chlorophyll-binding photosystem II-S protein is stable in the absence of pigments. J. Biol. Chem. **270**: 30141–30147.

Galka, P., Santabarbara, S., Khuong, T.T.H., Degand, H., Morsomme, P., Jennings, R.C., Boekema, E.J., and Caffarri, S. (2012). Functional analyses of the plant photosystem I-light-harvesting complex II supercomplex reveal that light-harvesting complex II loosely bound to photosystem II is a very efficient antenna for photosystem I in state II. Plant Cell **24**: 2963–78.

Gastaldelli, M., Canino, G., Croce, R., and Bassi, R. (2003). Xanthophyll binding sites of the CP29 (Lhcb4) subunit of higher plant photosystem II investigated by domain swapping and mutation analysis. J. Biol. Chem. **278**: 19190–8.

Genet, M.G., Schaefer, D., Zryd, P., Cove, J., and October, U.K.R. (1991). Physcomitrella patens 1.: 418–424.

Gerotto, C., Alboresi, A., Giacometti, G.M., Bassi, R., and Morosinotto, T. (2012). Coexistence of plant and algal energy dissipation mechanisms in the moss Physcomitrella patens. New Phytol.: 763–773.

Giddings, G. (2001). Transgenic plants as protein factories. Curr. Opin. Biotechnol. **12**: 450–454.

Gilmore, A.M. and Yamamoto, H.Y. (1992). Dark induction of zeaxanthin-dependent nonphotochemical fluorescence quenching mediated by ATP. Proc. Natl. Acad. Sci. U. S. A. **89**: 1899–1903.

Gleba, Y., Klimyuk, V., and Marillonnet, S. (2007). Viral vectors for the expression of proteins in plants. Curr. Opin. Biotechnol. **18**: 134–41.

Goodin, M.M., Zaitlin, D., Naidu, R. a, and Lommel, S. a (2008). Nicotiana benthamiana: its history and future as a model for plant-pathogen interactions. Mol. Plant. Microbe. Interact. **21**: 1015–26.

Green, B.R. and Vt, C. (1996). CHLOROPHYLL-CAROTENOID PROTEINS OF OXYGENIC PHOTOSYNTHESIS.

Grunberg, K., Mu, E., Otto, A., Reszka, R., Linder, D., Kube, M., Reinhardt, R., and Schu, D. (2004). Biochemical and Proteomic Analysis of the Magnetosome Membrane in Magnetospirillum gryphiswaldense. **70**: 1040–1050.

Hansson, A., Amann, K., Zygadlo, A., Meurer, J., Scheller, H. V, and Jensen, P.E. (2007). Knock-out of the chloroplast-encoded PSI-J subunit of photosystem I in Nicotiana tabacum. FEBS J. **274**: 1734–46.

Hansson, M. and Vener, A. V (2003). Identification of Three Previously Unknown in Vivo Protein Phosphorylation Sites in Thylakoid Membranes of Arabidopsis thaliana *.: 550–559.

Havaux, M. and Niyogi, K.K. (1999). The violaxanthin cycle protects plants from photooxidative damage by more than one mechanism. Proc. Natl. Acad. Sci. U. S. A. **96**: 8762–7.

Hieber, A.D., Kawabata, O., and Yamamoto, H.Y. (2004). Significance of the Lipid Phase in the Dynamics and Functions of the Xanthophyll Cycle as Revealed by PsbS Overexpression in Tobacco and In-vitro De-epoxidation in Monogalactosyldiacylglycerol Micelles. **45**: 92–102.

Hobe, S., Trostmann, I., Raunser, S., and Paulsen, H. (2006). Assembly of the major light-harvesting chlorophyll-a/b complex: Thermodynamics and kinetics of neoxanthin binding. J. Biol. Chem. **281**: 25156–66.

Jansson, S. (1999). A guide to the Lhc genes and their relatives in Arabidopsis. Trends Plant Sci. **4**: 236–240.

John Andrews, T. and Whitney, S.M. (2003). Manipulating ribulose bisphosphate carboxylase/oxygenase in the chloroplasts of higher plants. Arch. Biochem. Biophys. **414**: 159–169.

Jordan, P., Fromme, P., Witt, H.T., Klukas, O., Saenger, W., and Krauû, N. (2001). Three-dimensional structure of cyanobacterial photosystem I Ê resolution at 2 . 5 A. **411**: 909–917.

Keeling, P.J. (2010). The endosymbiotic origin, diversification and fate of plastids. Philos. Trans. R. Soc. Lond. B. Biol. Sci. **365**: 729–48.

Kenrick, P. and Crane, P.R. (1997). The origin and early evolution of plants on land.: 33–39.

Khrouchtchova, A., Hansson, M., Paakkarinen, V., Vainonen, J.P., Zhang, S., Jensen, P.E., Scheller, H.V., Vener, A. V, Aro, E.-M., and Haldrup, A. (2005). A previously found thylakoid membrane protein of 14kDa (TMP14) is a novel subunit of plant photosystem I and is designated PSI-P. FEBS Lett. **579**: 4808–12.

Kiss, A.Z., Ruban, A. V, and Horton, P. (2008). The PsbS protein controls the organization of the photosystem II antenna in higher plant thylakoid membranes. J. Biol. Chem. **283**: 3972–8.

Kolotilin, I., Kaldis, A., Pereira, E.O., Laberge, S., and Menassa, R. (2013). Optimization of transplastomic production of hemicellulases in tobacco: effects of expression cassette configuration and tobacco cultivar used as production platform on recombinant protein yields. Biotechnol. Biofuels **6**: 65.

Kovács, L., Damkjaer, J., Kereïche, S., Ilioaia, C., Ruban, A. V, Boekema, E.J., Jansson, S., and Horton, P. (2006). Lack of the light-harvesting complex CP24 affects the structure and function of the grana membranes of higher plant chloroplasts. Plant Cell **18**: 3106–20.

Koziol, A.G., Borza, T., Ishida, K.-I., Keeling, P., Lee, R.W., and Durnford, D.G. (2007). Tracing the evolution of the light-harvesting antennae in chlorophyll a/b-containing organisms. Plant Physiol. **143**: 1802–16.

Larkum, A.W.D., Douglas, S.E., and Raven, J.A. Photosynthesis in Algae Edited by.

Leitch, I.J., Hanson, L., Lim, K.Y., Kovarik, a, Chase, M.W., Clarkson, J.J., and Leitch, a R. (2008). The ups and downs of genome size evolution in polyploid species of Nicotiana (Solanaceae). Ann. Bot. **101**: 805–14.

Li, H. and Chiu, C.-C. (2010). Protein transport into chloroplasts. Annu. Rev. Plant Biol. **61**: 157–80.

Li, X.-P., Gilmore, A.M., and Niyogi, K.K. (2002). Molecular and global time-resolved analysis of a psbS gene dosage effect on pH- and xanthophyll cycle-dependent nonphotochemical quenching in photosystem II. J. Biol. Chem. **277**: 33590–7.

Liguori, N., Roy, L.M., Opacic, M., and Croce, R. (2013). Regulation of Light Harvesting in the Green Alga Chlamydomonas reinhardtii : The C - Terminus of LHCSR Is the Knob of a Dimmer Switch.

Liu, Z., Yan, H., Wang, K., Kuang, T., Zhang, J., Gui, L., An, X., and Chang, W. (2004). Crystal structure of spinach major light- ˚ resolution harvesting complex at 2 . 72 A. Nature: 287–292.

Ljungberg, U., Akerlund, H.-E., and Andersson, B. (1986). Isolation and characterization of the 10-kDa and 22-kDa polypeptides of higher plant photosystem 2. Eur. J. Biochem. **158**: 477–482.

Lucinski, R., Schmid, V.H.R., Jansson, S., and Klimmek, F. (2006). Lhca5 interaction with plant photosystem I. FEBS Lett. **580**: 6485–8.

Ma, J.K.-C., Drake, P.M.W., and Christou, P. (2003). The production of recombinant pharmaceutical proteins in plants. Nat. Rev. Genet. **4**: 794–805.

Mann, V., Harker, M., Pecker, I., and Hirschberg, J. (2000). Metabolic engineering of astaxanthin production in tobacco flowers. **18**.

Morosinotto, T., Baronio, R., and Bassi, R. (2002). Dynamics of chromophore binding to Lhc proteins in vivo and in vitro during operation of the xanthophyll cycle. J. Biol. Chem. **277**: 36913–20.

Morosinotto, T., Caffarri, S., Dall, L., and Bassi, R. (2003). Mechanistic aspects of the xanthophyll dynamics in higher plant thylakoids.: 347–354.

Mozzo, M., Passarini, F., Bassi, R., Amerongen, H. Van, and Croce, R. (2008). Biochimica et Biophysica Acta Photoprotection in higher plants : The putative quenching site is conserved in all outer light-harvesting complexes of Photosystem II. **1777**: 1263–1267.

Muller, P., Li, X., and Niyogi, K.K. (2001). Update on Photosynthesis Non-Photochemical Quenching . A Response to Excess Light Energy 1. Plant Physiol. **125**: 1558–1566.

Nield, J. and Barber, J. (2006). Refinement of the structural model for the Photosystem II supercomplex of higher plants. Biochim. Biophys. Acta **1757**: 353–61.

Niyogi, K.K., Björkman, O., and Grossman, a R. (1997). The roles of specific xanthophylls in photoprotection. Proc. Natl. Acad. Sci. U. S. A. **94**: 14162–7.

Niyogi, K.K., Grossman, A.R., and Björkman, O. (1998). Arabidopsis Mutants Define a Central Role for the Xanthophyll Cycle in the Regulation of Photosynthetic Energy Conversion. **10**: 1121–1134.

Niyogi, K.K., Shih, C., Chow, W.S., Pogson, B.J., and Dellapenna, D. (2001). Photoprotection in a zeaxanthin- and lutein-deficient double mutant of Arabidopsis.: 139–145.

Pagano, a. (1998). In Vitro Reconstitution of the Recombinant Photosystem II Light-harvesting Complex CP24 and Its Spectroscopic Characterization. J. Biol. Chem. **273**: 17154–17165.

Pan, X., Li, M., Wan, T., Wang, L., Jia, C., Hou, Z., Zhao, X., Zhang, J., and Chang, W. (2011). Structural insights into energy regulation of light-harvesting complex CP29 from spinach. Nat. Struct. Mol. Biol. **18**: 309–15.

Pan, X., Liu, Z., Li, M., and Chang, W. (2013). Architecture and function of plant light-harvesting complexes II. Curr. Opin. Struct. Biol. **23**: 515–25.

Pascal, A., Gradinaru, C., Wacker, U., Peterman, E., Calkoen, F., Irrgang, K.-D., Horton, P., Renger, G., van Grondelle, R., Robert, B., and van Amerongen, H. (1999). Spectroscopic characterization of the spinach Lhcb4 protein (CP29), a minor light-harvesting complex of photosystem II. Eur. J. Biochem. **262**: 817–823.

Peers, G., Truong, T.B., Ostendorf, E., Busch, A., Elrad, D., Grossman, A.R., Hippler, M., and Niyogi, K.K. (2009). An ancient light-harvesting protein is critical for the regulation of algal photosynthesis. Nature **462**: 518–21.

Peng, L. and Shikanai, T. (2011). Supercomplex formation with photosystem I is required for the stabilization of the chloroplast NADH dehydrogenase-like complex in Arabidopsis. Plant Physiol. **155**: 1629–39.

Pinnola, A., Dall'Osto, L., Gerotto, C., Morosinotto, T., Bassi, R., and Alboresi, A. (2013). Zeaxanthin binds to light-harvesting complex stress-related protein to enhance nonphotochemical quenching in Physcomitrella patens. Plant Cell **25**: 3519–34.

Prigge, M.J. and Bezanilla, M. (2010). Evolutionary crossroads in developmental biology: Physcomitrella patens. Development **137**: 3535–43.

Rensing, S. a et al. (2008). The Physcomitrella genome reveals evolutionary insights into the conquest of land by plants. Science **319**: 64–9.

Ruban, a. V., Lee, P.J., Wentworth, M., Young, a. J., and Horton, P. (1999). Determination of the Stoichiometry and Strength of Binding of Xanthophylls to the Photosystem II Light Harvesting Complexes. J. Biol. Chem. **274**: 10458–10465.

Rybicki, E.P. (2010). Plant-made vaccines for humans and animals. Plant Biotechnol. J. **8**: 620–37.

Schaefer, D.G. and Zry, J. (2001). The Moss Physcomitrella patens , Now and Then. **127**: 1430–1438.

Sierro, N., Battey, J.N.D., Ouadi, S., Bakaher, N., Bovet, L., Willig, A., Goepfert, S., Peitsch, M.C., and Ivanov, N. V (2014). The tobacco genome sequence and its comparison with those of tomato and potato. Nat. Commun. **5**: 3833.

Staehelin, L.A. (2003). Chloroplast structure: from chlorophyll granules to supra-molecular architecture of thylakoid membranes. Photosynth. Res. **76**: 185–96.

Teardo, E., de Laureto, P.P., Bergantino, E., Dalla Vecchia, F., Rigoni, F., Szabò, I., and Giacometti, G.M. (2007). Evidences for interaction of PsbS with photosynthetic complexes in maize thylakoids. Biochim. Biophys. Acta **1767**: 703–11.

Telfer, A., Dhami, S., Bishop, S.M., Phillips, D., and Barber, J. (1994). p-Carotene Quenches Singlet Oxygen Formed by Isolated Photosystem I1 Reaction.: 14469–14474.

Timmis, J.N., Ayliffe, M. a, Huang, C.Y., and Martin, W. (2004). Endosymbiotic gene transfer: organelle genomes forge eukaryotic chromosomes. Nat. Rev. Genet. **5**: 123–35.

Tokutsu, R. (2009). CP29 , a Monomeric Light-harvesting Complex II Protein , Is Essential for State Transitions in Chlamydomonas reinhardtii * □.

Tokutsu, R. and Minagawa, J. (2013). Energy-dissipative supercomplex of photosystem II associated with LHCSR3 in Chlamydomonas reinhardtii. Proc. Natl. Acad. Sci. U. S. A. **110**: 10016–21.

Tripathy, B.C. (2012). Photosynthesis J.J. Eaton-Rye, B.C. Tripathy, and T.D. Sharkey, eds (Springer Netherlands: Dordrecht).

Umena, Y., Kawakami, K., Shen, J.-R., and Kamiya, N. (2011). Crystal structure of oxygen-evolving photosystem II at a resolution of 1.9 Å. Nature **473**: 55–60.

Wehner, A., Grasses, T., and Jahns, P. (2006). De-epoxidation of violaxanthin in the minor antenna proteins of photosystem II, LHCB4, LHCB5, and LHCB6. J. Biol. Chem. **281**: 21924–33.

Xiao-Ping Li, C., Grossman, A.R., Rosenquist, M., Jansson, S., Niyogi, K.K., Li, X., and Bjo, O. (2000). A pigment-binding protein essential for regulation of photosynthetic light harvesting. Nature **403**: 391–395.

Yakushevska, A.E., Ruban, A. V, Jensen, P.E., Roon, H. Van, Niyogi, K.K., Scheller, H. V, Dekker, J.P., and Boekema, E.J. (2001). CHAPTER 5 Supermolecular organization of photosystem II and its associated light-harvesting antenna in the wild-type and npq4 mutant of Arabidopsis thaliana.: 1–4.

Zhang, S. and Scheller, H.V. (2004). Light-harvesting complex II binds to several small subunits of photosystem I. J. Biol. Chem. **279**: 3180–7.

Chapter 1.B:

Transient and stable expression of *P.patens* LHCSR1 in *Nicotiana benthamiana* and *Nicotiana tabacum:* a heterologous expression system for a membrane bound pigment-binding protein.

Transient and stable expression of *P.patens* LHCSR1 in *Nicotiana benthamiana* and *Nicotiana tabacum:* a heterologous expression system for a membrane bound pigment-binding protein.

Introduction

Sunlight provides energy for photosynthetic organisms which harvest photons through complex antenna systems which transfer excitation energy to the photosynthetic reaction centres, where photochemical events that drive oxygenic photosynthesis start (Green and Durnford, 1996). In green algae and plants antenna complexes belong to Light harvesting complex (LHC) superfamily: chlorophyll/xanthophyll binding proteins associated to Photosystem I (PSI) or Photosystem II (PSII). According to their ability in pigments binding LHC proteins can be divided into the Chl a/b-binding proteins of land plants and green algae, the Chl a-binding proteins of the red algae, and the Chl a/c-binding proteins of the chromalveolates (Koziol et al., 2007). All LHC proteins contain three membrane-spanning helices sharing a 'LHC-motif': a highly hydrophobic sequence of 22 amino acids with three invariant charged amino acids – glutamic acid (Glu) and arginine (Arg), as well as a few highly conserved glycine (Gly) residues (Jansson, 1999). Although these considerable amino acid identity/similarity in specific domains, LHCs are diverse in sequences, likely of importance for tuning to specific functions. Indeed, besides their crucial role in absorption of light, LHC proteins play other important roles: they dissipate energy absorbed in excess by Non-photochemical quenching (NPQ) (Horton et al., 1996), they compensate unbalance in excitation of PSI vs PS II by the mechanism of state1-state2 transitions (Bellafiore et al., 2005; Kargul and Barber, 2008) and are crucial for determining the structural organization of the thylakoid membrane, through their involvement in grana stacking, which, in turn define the lateral heterogeneity of the thylakoid membrane (Kovács et al., 2006; Standfuss et al., 2005).

The isolation of LHC proteins from each other is problematic due to their similar physic–chemical properties and molecular mass as well for their hydrophobic nature that makes them extractable only with detergent (Ballottari et al., 2012). Until now only few LHC have been purified from thylakoids in their native state; the large majority of them have proven difficult to isolate with all cofactors. For example the minor antenna complexes of higher plants (CP29, CP26 and CP24) were purified in several steps using high detergent concentrations but leading to loss of pigments (Dainese and Bassi, 1991; Ruban et al., 1999). A different strategy for obtaining pigment-protein complex is *in vitro* reconstitution of recombinant apoproteins expressed in bacteria. Indeed, LHC apoproteins have the property of spontaneously folding *in vitro* upon addition of chlorophylls and carotenoids (Paulsen et al., 1993; Giuffra et al., 1996; Pagano et al., 1998). Even if this system was largely used for studying LHC protein the Chl a/b ratio of the recombinant

complex strongly depends on the Chl a/b ratio of the reconstitution mix (Sandonà et al., 1998) suggesting that this system might advise imprecise pigment composition. Moreover, it has been impossible to crystallize recombinant LHC proteins refolded *in vitro* (Bassi.R , personal communication).

As an alternative strategy, we consider here the over-expression of LHC proteins in organisms endowed with all co-factors needed for folding of LHC proteins, namely chlorophyll a, chlorophyll b and the xanthophylls lutein, violaxanthin, neoxanthin. By this strategy we expect that the recombinant protein will undergo the same translocation and membrane integration events as constitutive LHC proteins and yield a product in "native state". Within this strategy two different solutions could be applied in order to improve recombinant LHC accumulation and recovery: expression of LHC protein in plants depleted for LHC gene or expression of LHC in heterelogous plant host.

LHCSRs proteins founded in green algae and mosses, but absent in lycopods and seed plants (Peers et al., 2009; Alboresi et al., 2010) are involved in photoprotection mechanisms and belong to sub-family of LHC protein called stress-induced LHC-like proteins (Andersson et al., 2003; Engelken et al., 2010).
The two main studied proteins of this group are the algae protein LHCSR3 from *Chlamydomonas reinharditii* and the moss LHCSR1 from *Physcomitrella patens*. *In vitro* reconstitution of LHCSR3 demonstrated that it acts both like a pH-sensitive activator of excitation energy quenching by being a quencher *per se* due to its capacity of activating a chlorophyll-carotenoid charge transfer mechanism (Bonente et al., 2011a). Moreover, it has recently been shown that LHCSR1 quenching activity is strongly dependant on Zeaxanthin (Pinnola et al., 2013) but few information is available on biochemical and spectroscopic characteristics of *P.patens* LHCSR1 protein.

In this work the heterelogous expression of *P.patens* LHCSR1 protein has been realized in *N.tabacum* and *N.benthamiana plants* leading to the isolation this protein in its native form of chlorophyll a/b–xanthophyll-binding complex, in thylakoids membrane and accumulated in a monomeric form. Finally the correlation of NPQ activity with the abundance of LHCSR1 in *N.tabacum* was demonstrated.

Results

Physcomitrella patens LHCSR1 is expressed in *Nicotiana* plants

The full length cDNA of *LHCSR1 encoding* sequence was introduced in the binary gateway vector pK7WG2 under the control of the constitutive promoter CaMV 35S. The resulting vector named pK7WG2.Lhcsr1 was used for transient and stable transformation respectively of *N.benthamiana* and *N.tabacum* (Fig.1A). Five or six weeks-old *N.benthamiana* plants have been used for transient transformation by agroinfiltrating 5 leaves per plant with a syringe. First of all protein accumulation was been evaluated in a time-course collecting leaf discs for 7 days post-agroinfiltration (dpa). Total proteins

were extracted from each disc in a denaturing buffer. An equal volume of protein extract was loaded on an SDS-PAGE, transferred to a PVDF membrane and detected with a specific homemade anti-PpLHCSR1 polyclonal antibody (Fig. 1B). The immunodected bands were then quantified by densitometric analysis with GelPro Analyzer software (Media Cybernetics, Rockville, MD, USA). LHCSR1 was not detectable at 1 dpa, suggesting that *N.benthamiana* leaves need more than 24 hours to synthesize good amounts of LHCSR1. A significant increase of LHCSR1 was detectable at 2 dpa and 3 dpa while protein accumulation peaked at 4 dpa, suggesting that the fourth day could be chosen for leaf collection in order to ensure the higher accumulation level of recombinant LHCSR1 protein.

N. tabacum cv petit Havana transgenic plants were generated by Agrobacterium-mediated transformation. The presence of protein in transgenic plants was checked by immunoblot analysis on total leaves extracts identifying transgenic plants with a wide range of LHCSR1 accumulation. The best productive plants were then chosen for the following analysis (data not shown).

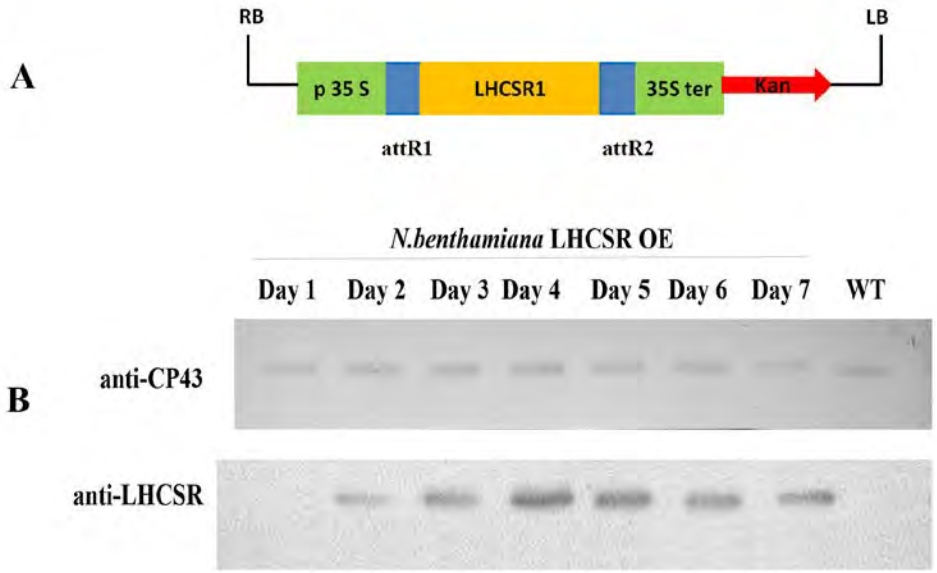

Fig 1.: (A) The Lhcsr1 sequence cloned in pK7WG2 gateway vector. **(B)** Time course of recombinant protein accumulation. Disc leaves collected every day for 7 day post agroinfiltration were ground in LB buffer (Tris pH 6,8, 10% glycerol, 2% SDS and 3% β-mercaptoethanol) separated by SDS-PAGE, transferred on a PVDF membrane and analyzed using anti-LHCSR1 antibody. *N.benthamiana* system accumulates mature LHCSR1 at the fourth day post agroinfiltration. Western blot against CP43 is also shown as loading control.

LHCSR1 is expressed in thylakoid membranes as a mature monomeric LHC protein.

Once the possibility to express LHCSR1 in the two systems was assessed, the presence of the recombinant protein in thylakoid membranes was checked. Indeed for structure-function studies LHCSR1 needs first of all to be expressed as a mature protein, to be processed and correctly assembled with pigments within thylakoid membranes. Then, even if expressed in a heterologous system, it should be able to play its function of pH-sensitive NPQ trigger .

To this aim an equal quantity of thylakoid membrane proteins (on a Chl basis) was compared to thylakoids purified from *P.patens* protonemata as a reference. As reported in Fig. 2A, the signal detected by anti-LHSCR1 antibody was at the same apparent molecular weight for the three organisms, suggesting that *N.benthamiana* and *N.tabacum* express a mature LHCSR1 protein processed like the native one at 24 kDa, consistent with Chloro P predictions.

The expression yield of LHSCR1 in these two systems was determined by immuno-titration. The intensity of the immune-reaction for LHCSR1 was quantified by densitometric analysis using GelPro Analyzer software, normalized for protein content and compared to immunodetected band of recombinant *P.p* LHCSR1 protein expressed in *E.coli* and reconstituted in-vitro with pigments. Every ug of *N.benthamiana* thylkoids (on Chl basis) accumulated 0,13 ug of LHCSR1 protein while *N.tabacum* accumulates 0,03 ug of LHCSR1 per ug of thylakoids (on Chl basis) (Fig.2C).

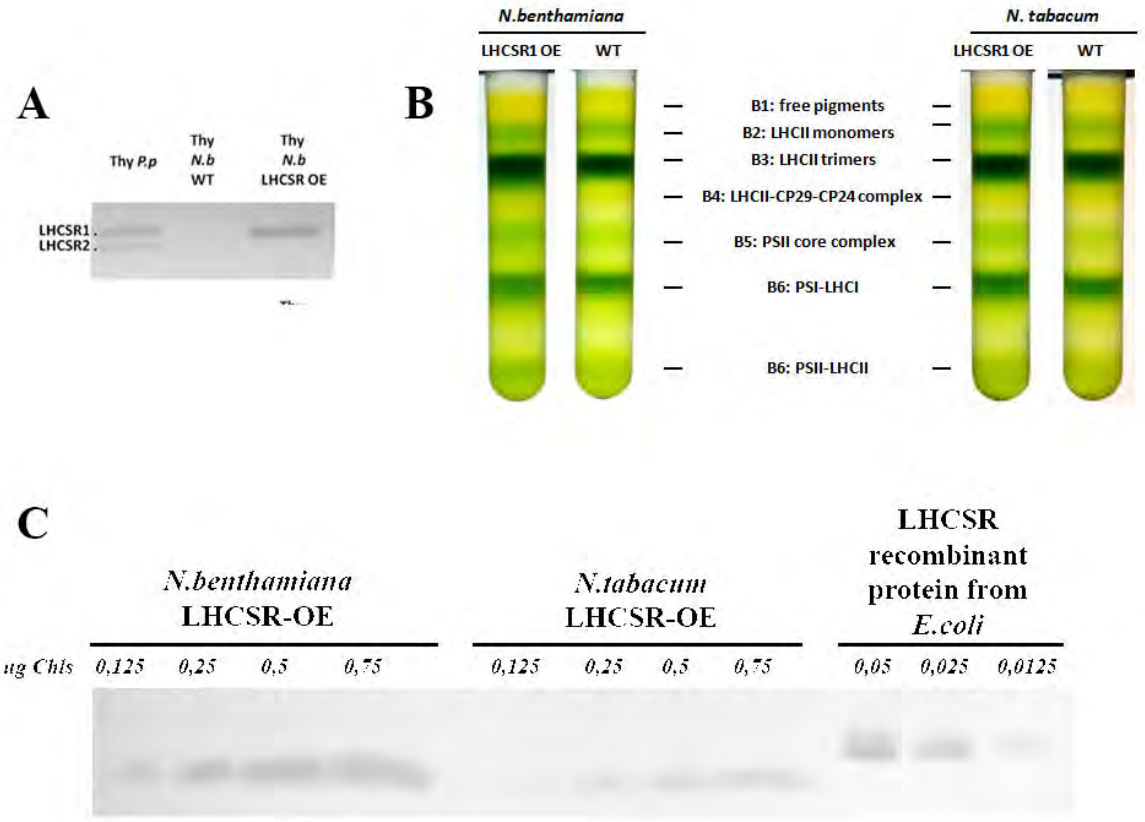

Fig 2.: (A) Immunoblot with α-LHCSR1 antibody had shown a signal in *N.benthamiana (N.b)* thyalkoids and *N.tabacum (N.t)* expressing LHCSR1 at the same molecular weight of *P.patens* thylakoids. Two bands were present *in P.patens* thyalkoids because it possesses two different isoforms of LHCSR called LHCSR1 and LHCSR2. No signal was detectable in *N.benthamiana* and N.tabacum WT thylakoids. **(B)** Sucrose gradient of thylakoid solubilized with 0,8 % α-DM. The separation pattern was the same for *N.benthamiana and N.tabacum* LHCSR1 expressing thylakoids respect to WT ones. **(C)** Immunotitration analysis for LHCSR1 expression in *N.benthamiana* and *N.tabacum*. Different concentrations of thylakoids (on Chl basis) were compared to different concentration (on Chl basis) of LHCSR1 recombinant protein from *E.coli* reconstituted in vitro with pigments. Bands detected with anti-LHCSR1 antibody were analyzed by densitometric analysis using Gel Pro software.

Since LHCSR1 was expressed in thylakoid membranes of *Nicotiana*, we tested if it was accumulated as a multimeric complex or as a monomeric LHC pigment-protein, as previously shown for *P.patens* LHCSR1 (Pinnola et al., 2013). Thylakoids were solubilized with the mild detergent α-DM and loaded onto a sucrose gradient, which was centrifuged at 40.000xg for 22h. The separation pattern consisting of 7 bands was very similar for both *N.benthamiana or N.tabacum* LHCSR1 over-expressors and WT plants. Bands collected from the gradient were analyzed by spectrophotometry and SDS-PAGE to identify their pigment-protein content and polypeptide composition. Starting from the top of the gradient it is possible to recognize: free pigments (B1), LHCII monomers (B2), LHCII trimers (B3), LHCII-CP29-CP24 complex (B4), PSII core complex (B5), PSI-LHCI (B6) and PSII-LHCII supercomplex (B7) (Fig.2B).

A spectroscopic analysis revealed that free pigments and LHCII monomers fractions from *N.benthamiana* and *N.tabacum* LHCSR1 thylakoids were characterized by Qy absorption peak red-shifted to 679 nm versus 672 nm of WT counterpart (not shown), suggesting the presence of LHCSR1 protein in these fractions. SDS-PAGE analysis confirmed that a band of 24 kDa was present in the free pigments and LHCII monomeric region obtained from LHCSR1 plants and was absent in samples from WT (Fig.3A). Immunoblotting analysis using α-LHCSR1 antibody reveals that these bands effectively correspond to LHCSR1 protein, confirming the localization of LHCSR1 as monomers in thylakoids membranes (Fig.3B). Moreover SDS-PAGE and immunoblotting analysis of other fractions do not shown difference respect to WT ones confirming that all LHCSR1 migrates as monomer in sucrose gradient.

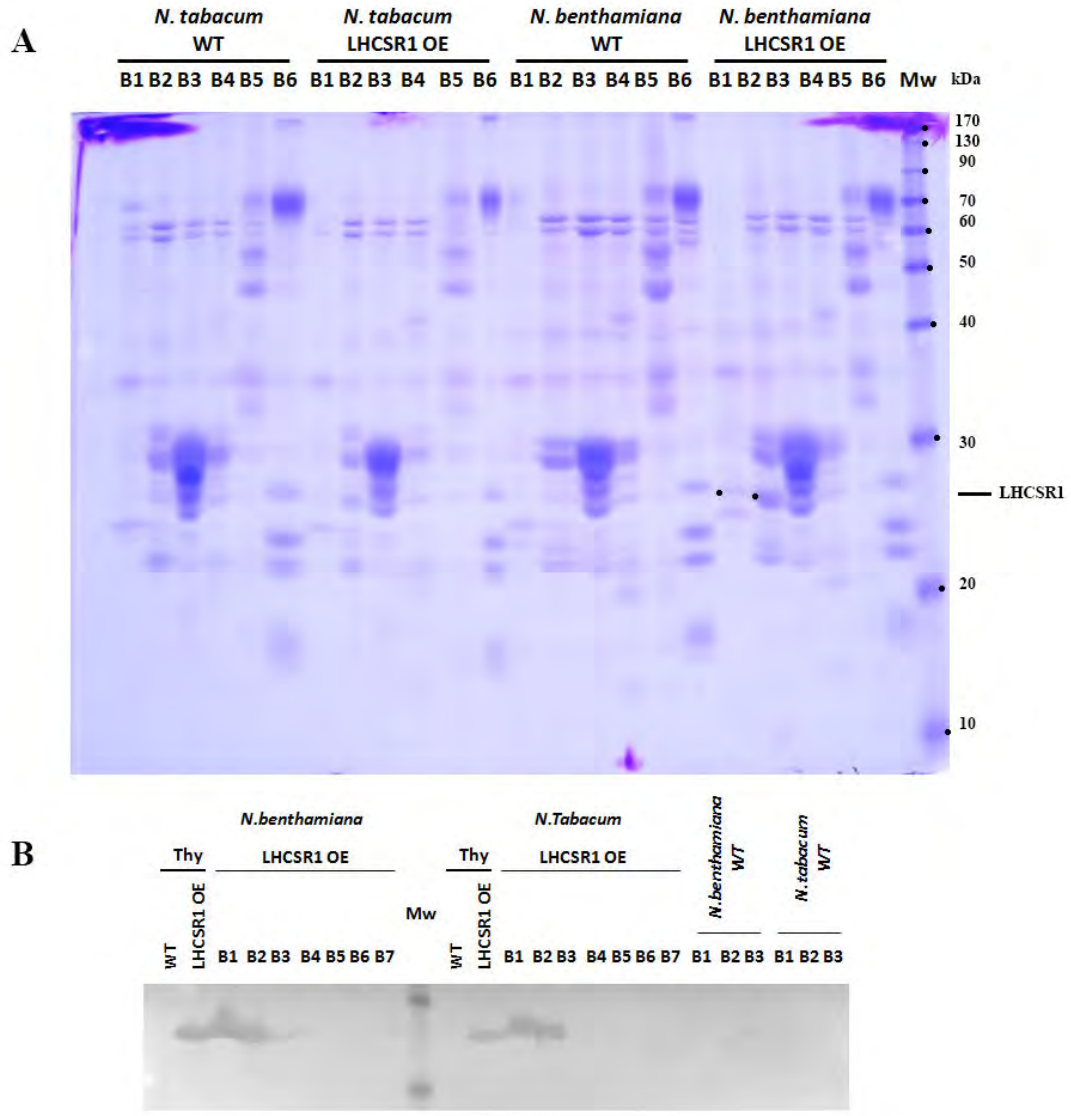

Fig.3: (A) SDS-PAGE stained with Comassie blue of bands collected from sucrose gradient An equal volume (30 ul) of each band collected from sucrose gradient was loaded. A polypeptide corresponding to LHCSR1 molecular weight, underline in red, was clearly visible in band 1 (B1) and band 2 (B2) (respectively corresponding to free pigments and monomers). **(B)** Western blot analysis on the bands collected from sucrose gradient. A clear signal could be recorded in band 1 and 2 confirming that the polypeptide observed in SDS-PAGE was actually LHCSR1. Thylakoids (Thy) from WT plants were loaded as a control excluding that the signal observed in transformed plants could be due to a not specific reaction. Polypeptides from band 1-band 2-band 3 from WT thylakoids has been loaded as negative control.

Isolation of LHCSR1 using Deriphat-PAGE gel system

Next we tried to verify whether the protein formed pigment-binding complexes. To this aim, a non-denaturating Deriphat-PAGE was applied to fractionate low molecular mass proteins with high-resolution in order to attempt to the separation of LHCSR1 protein from the resident *Nicotiana* LHC proteins. For both expression systems, it was possible to observe a green band migrating below LHCII monomers from

thylakoids of LHCSR1 expressing plants which was absent in the corresponding WT lane (Fig.4), consistent with the localization of LHCSR1 in the upper bands of the sucrose gradient.

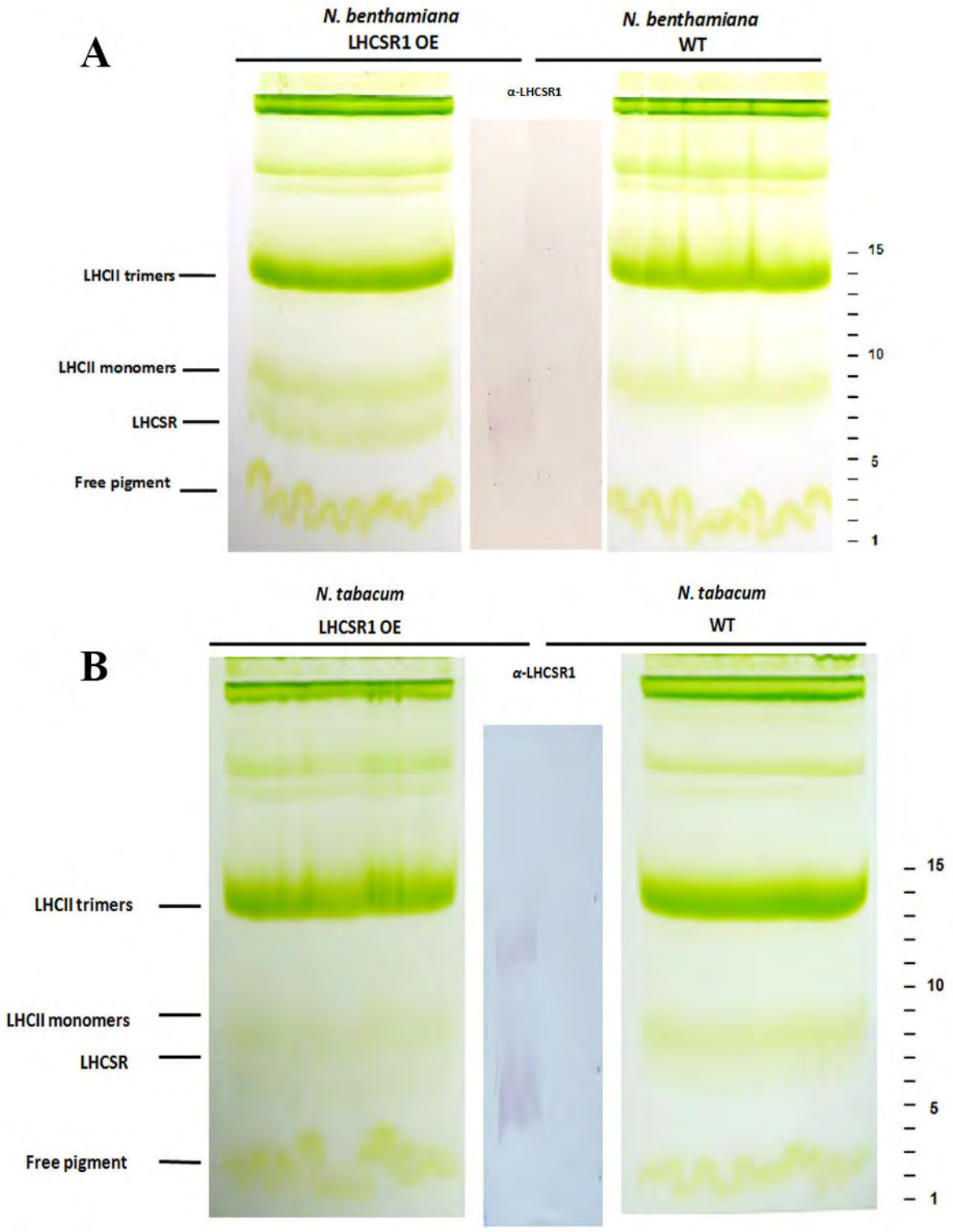

Fig.4. Non-denaturing gel electrophoresis of pigment-binding complexes from thylakoids of wild-type (WT) and LHCSR1 expressing plants after solubilization with 0.8% α-DM. The stacking gel contained 3.5% (w/v) acrylamide, and the resolving gel contained 7% (w/v) acrylamide (48:1.5 acrylamide/bis-acrylamide). Different pigment-binding complexes, identified from their mobility, are indicated on the left. The central part of the gel was transferred on a PVDF membrane for immunoblotting analysis using an antibody raised against LHCSR. The image of the membrane is superposed on the picture of the green gel. The position of gel slices

excised from the non denaturing gel is shown on the right side. In figure A is reported the Deriphat gel on *N.benthamiana* while in B is reported the *N.tabacum* one. It is interesting to note as in *N.tabacum* sample it is possible to identified a reaction against LHCSR1 also just below the LHCII trimers, suggesting the possibility of a dimeric form for LHCSR1.

In order to confirm that this band corresponds to LHCSR1 protein the middle lane of the gel including both WT and OE LHCSR samples was excised and blotted on a PVDF membrane from which the presence of the LHCSR1 protein was confirmed with an anti-LHCSR1 antibody. A clear reaction was detectable at the apparent molecular weight corresponding to the low molecular weight green band, suggesting that Non denaturating Deriphat-PAGE is effective in separating LHCSR1 from LHCII monomers.

This Deriphat-PAGE was also used to detect the distribution of LHCSR1 in thylakoid complexes: the 20-100 kDa molecular mass range was cut into thin slices and proteins were eluted using a Hepes 10 mM pH=7,8 buffer solution containing 0,03% α-DM. The eluate from each slice was characterized by absorption spectroscopy, SDS-PAGE/immunoblotting and HPLC analysis. The slices corresponding to the green band previously described as containing LHCSR1 protein showed an absorption spectrum of with a Qy absorption peaks red-shifted to 678,8 nm (Fig. 5) and closely resembling the *C. reinhardtii* recombinant LHCSR3 spectrum as obtained from the apoprotein reconstituted *in vitro* with pigments (Bonente et al., 2011a).

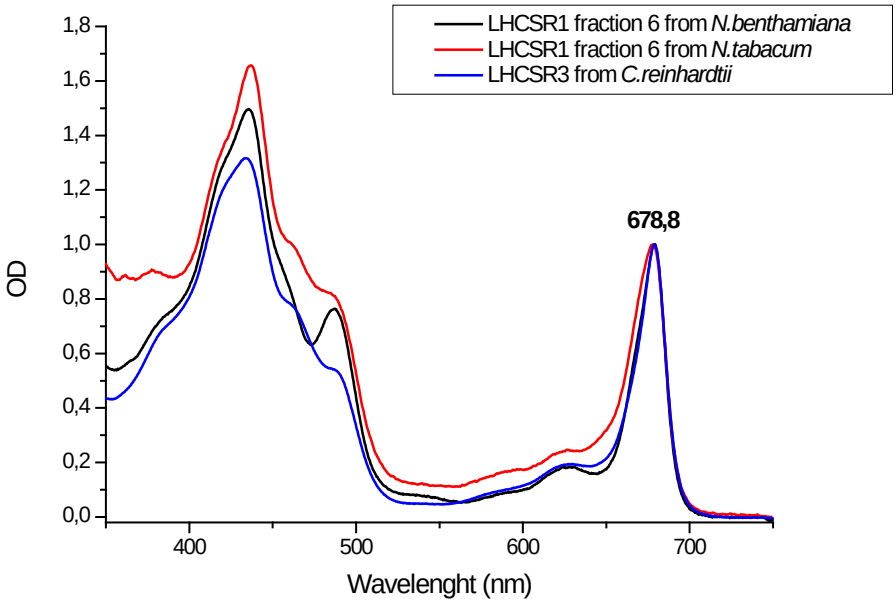

Figure5.: Absorption spectra of slices eluted from deriphat gel. Fraction 6 from *N.tabacum* (red line) or *N.benthamiana* (black line) corresponding to slices previously detected as containing LHCSR1. *N.benthamiana* fraction shown a strong red-shifted peaks (678,8) which matches with red-shifted peaks of *C. reinhardtii* LHCSR3 reconstituted in vitro with pigments (blue line).

SDS-PAGE analysis confirmed that the slices number 5 and 6 from *N.benthamiana* and *N.tabacum*, corresponding to the green band observed in the Deriphat-PAGE, were strongly enriched in a polypeptide of an apparent molecular weight of 23 kDa which is absent in WT counterpart gel slices (Fig. 6). Moreover, no other contaminant polypeptides were detectable in these fractions suggesting that Deriphat-PAGE could

be considered a good system for LHCSR1 isolation in a small scale. Also in this case the identity of the bands in fractions 5 and 6 as LHCSR1 was confirmed with an anti-LHCSR1 antibody (Fig. 6). Furthermore, consistently with immunoblot analysis on Deriphat-PAGE, it was possible to detect a reaction in fractions corresponding to migration of LHCII monomer as well as trimers, suggesting LHCSR1 could be also present as dimeric form in *Nicotiana* thylakoid membranes as previously reported for PSBS in plants (Bergantino et al., 2003). Moreover HPLC analysis on eluted slices showed that fractions enriched in LHCSR1 protein is characterized by a very high Chl a/b ratio, suggesting that LHCSR1 is able to bind chlorophyll b in low amount as previously reported also for LHCSR3 and other LHC proteins (Bone nte et al., 2011b; Morosinotto et al., 2002)..

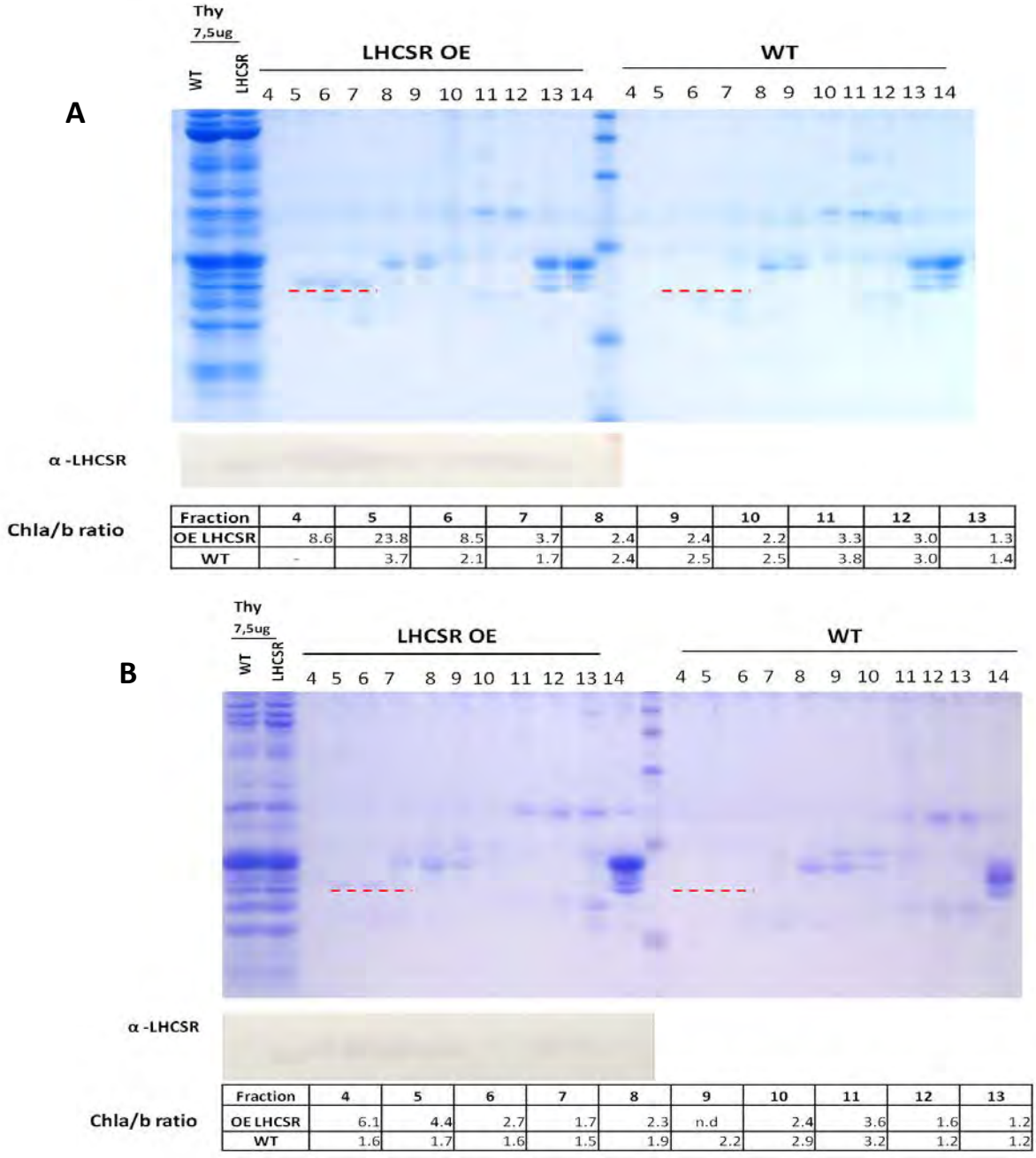

Chla/b ratio	Fraction	4	5	6	7	8	9	10	11	12	13
	OE LHCSR	8.6	23.8	8.5	3.7	2.4	2.4	2.2	3.3	3.0	1.3
	WT	-	3.7	2.1	1.7	2.4	2.5	2.5	3.8	3.0	1.4

Chla/b ratio	Fraction	4	5	6	7	8	9	10	11	12	13
	OE LHCSR	6.1	4.4	2.7	1.7	2.3	n.d	2.4	3.6	1.6	1.2
	WT	1.6	1.7	1.6	1.5	1.9	2.2	2.9	3.2	1.2	1.2

Fig 6. SDS-PAGE analysis of slices eluted from the gel. The resolving gel contained 15%(w/v) acryllamide plus 6 M urea Leammly gel was used to analyzed slices polypeptide compositions. An equal amount of volume per each slide was loaded in the gel.

N.benthamiana sample are reported in figure A while in figure B are presented from *N.tabacum*. For both expression systems in fractions 5 and 6 it is possible to observe a polypeptide of 25 kDa (red dashed line) absent in WT slices. No polypeptides contaminants are present in slices enriched of LHCSR1. Western-blot on reveals that fraction 5 and 6 are effectively enriched in LHCSR1 even if a signal corresponding to LHCSR1 could be detected also in slices in between LHCII monomer and trimer suggesting the presence of a dimeric form for LHCSR1. Under each gel is reported the Chl a/b ratio of fraction from 4 to 13 from each gel. Fractions containing LHCSR are characterized by a higher Chla/b respect to WT ones.

Information on cromophore organization within pigment-proteins can be obtained by circular dicroism (CD). CD spectra of proteins eluted from the gel slices containing LHCSR1 has features similar to those reported for LHC proteins, with signal in the Qy region at 680 nm (-) and 663 nm(+) (Fig.7). Interestingly, the amplitude of CD spectra in Qy region is strong respect to that of recombinant CP29, upon normalization at the same protein molar concentration, suggesting an enhanced level of excitonic interactions between Chl a chromophores (Georgakopoulou et al., 2007) in LHCSR1. In the Soret region, the spectrum was characterized by a strong broad negative signal at 464 nm, associated to excitonic interactions between xanthophyll and chlorophyll b molecules. The strong optical activity here reported for LHCSR1 is a clear indication of a stable protein complex binding Chl and xanthophyll chromophores indeed free pigments in detergent solution or not specifically bound to protein have a very low amplitude in CD signal , with a single positive component in Qy region (Giuffra et al., 1996)

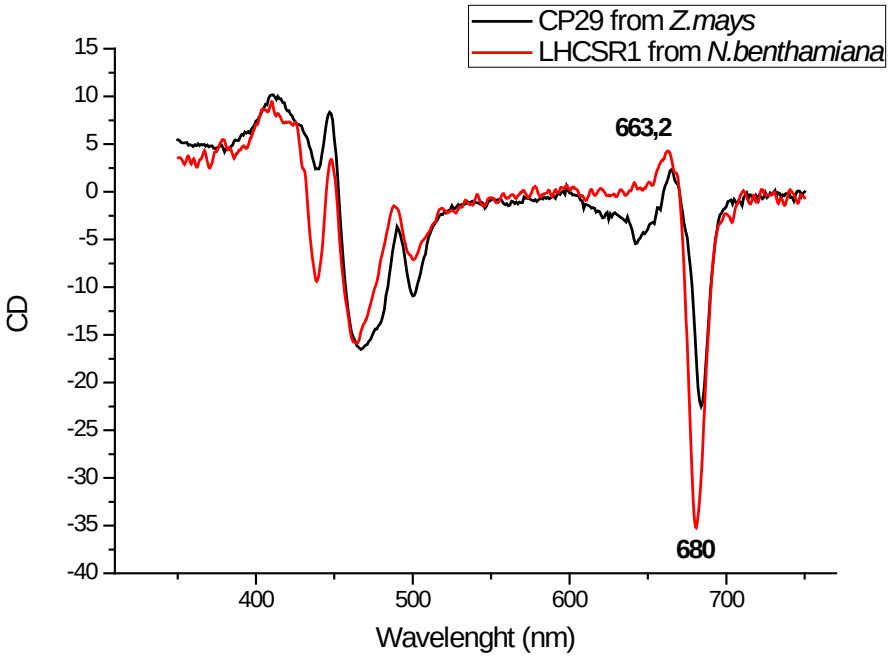

Figure.7 : CD spectrum in visible light of LHCSR1 eluted from gel (red line) here compared to CP29 CD spectrum. LHCSR1 Qy Chl major peaks are shown.

Pigment composition of isolated LHCSR1 protein depoxidated versus non depoxidated one

Considering that *P.patens* LHCSR1 protein binds zeaxanthin upon excess light and that this binding controls the amplitude of LHCSR-dependent NPQ (Pinnola et al., 2013), we proceeded to test whether the recombinant LHCSR1 produced in *N.benthamiana* was able to bind zeaxanthin as an indication that LHCSR1 protein assume a native conformation and is active in recombinant expression systems. For *in vitro* de-epoxidation, thylakoids were incubated at pH 5.2 in presence of ascorbate to induce Violaxanthin De-epoxidase activity (Gilmore and Yamamoto, 1992; Arnoux et al., 2009). Thyalkoids de-epoxidated and non

de-epoxidated *in vitro* by incubation at pH 5.2 in the presence of ascorbate as substrate for VDE, were loaded onto the same non-denaturating deriphat gel described above and LHCSR1 slices eluted from the gel were loaded at the top of sucrose density gradient (60 000 rpm for 10 h) to separate LHCSR1 protein from free pigments possibly present in the sample and not bound to the protein (Fig.8). LHCSR1 separated from free pigments was so collected upon sucrose gradient ultracentrifugation, analyzed by absorption spectroscopy and SDS-PAGE and upon extraction with 80% acetone, subjected to High-performance liquid chromatography (HPLC). Comparing the absorption spectra of de-epoxidated *vs* non de-epoxidated LHCSR1 preparation from sucrose gradient we could observe a positive signal at 504 nm which corresponded to Zeaxantin absorption, thus confirming that de-epoxidation occurred *in vitro* and the protein exchanged xanthophylls. SDS-PAGE analysis showed a single Coomassie stained band at 24 kDa suggesting that LHCSR1 was purified without contaminants.

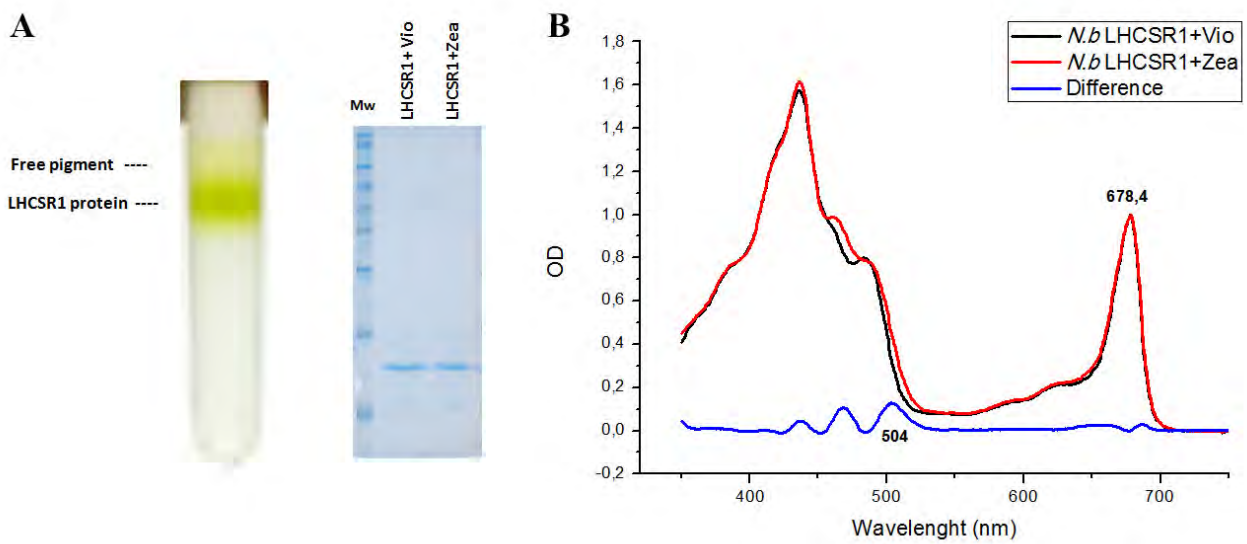

Fig.8. Thyalkoids were subjected to in vitro de-epoxidation in presence of ascorbate and then were run on a Deriphat non denaturating gel. Fraction corresponding to LHCSR1 was eluted from the gel and loaded at the top of a sucrose gradient. After 10 h of running at 60'000 g two different fractions can be detected in the sucrose gradient: the upper one corresponding to free pigments and the lower one corresponding to LHCSR1. This fraction was loaded on a SDS-PAGE gel for checking the absence of contaminants. **B** The difference of LHCSR1 protein (black line) and LHCSR1 de-epoxidated (red line) absorption spectra revealed the presence of a peaks at 504 nm corresponding to Violaxantin . This means that deeepoxidation works.

HPLC analysis of the pigment extract showed LHCSR1 bound mainly Chl a , lutein, violaxanthin, antheraxanthin, zeaxanthin but not neoxanthin and Chl b was present in traces (Table 1). As report from sequence alignment (Fig.9) Chl binding residues are conserved in both LHSCR1 from *P.patens* and LHCSR3 from *C.reinharditii* . Based on a similar chlorophyll composition of CrLHCSR3 and PpLHCSR1, and an observed a Chl/Car ratio of 2,6 obtained from HPLC analysis and a chlorophyll polypeptide ratio of 7-8 Chls (Bonente et al., 2011a) three xanthophyll binding sites are proposed for *P.patens* LHCSR1, one for lutein and two for xanthophyll's cycle pigments: violaxanthin/antheraxanthin/zeaxanthin. Furthermore, de-epoxidation index obtained after acidic incubation was very high (0,56) indicating that LHCSR1 underwent

high level of violaxanthin to zeaxanthin exchange following de-epoxidation by VDE, in fact far higher than any other LHCb antenna component previously studied (Morosinotto et al. 2003, Jahns et al. 2007). All these data together suggest that *P.patens* LHCR1 expressed in *N.benthamiana* is correctly folded and able to exchange violaxanthin for zeaxanthin upon lumen acidification.

Sample	Chl (a+b) Norm	chl a	chl b	neo	vio	anthera	lute	zea	beta	chl a/chl b	Depox index
LHCSR1 Ctrl	100	82,7	17,3	0	27,5	0,49	28,4	0	0	4,7	0,0
LHCSR1 Depox	100	80,2	19,8	0	11,8	4,3	18,5	14,7	0	4,1	0,54

Table 1. Pigments composition of purified LHCSR1 protein was analyzed by HPLC. Carotenoid content (mol) is normalized to chlorophylls a+b (100 mol). Vio, violaxanthin; Ant, antheraxanthin; Zea,zeaxanthin. Deepoxidation index (DEP) is calculated as follows: (0.5 * A+Z)/(A+Z+V).

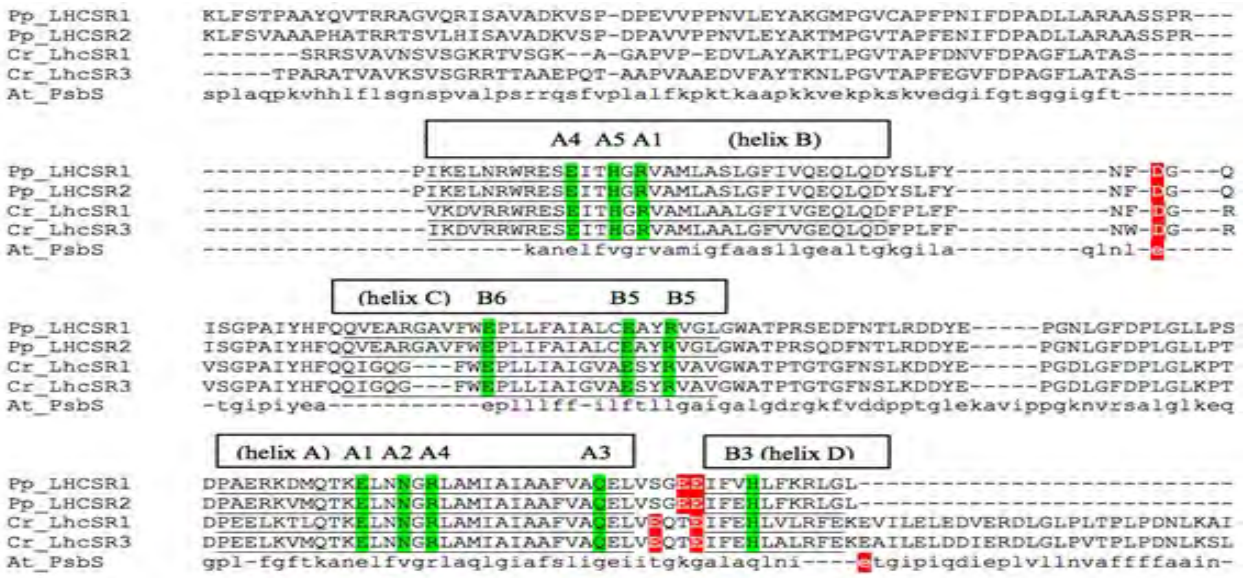

Fig. 9. Sequence alignment of LHCSR1/2 from *P.patens*, LHCSR1/3 from *C.reinharditii* and PSBS from *A.thaliana***.** Chl-coordinating residues (green line) and dicyclohexylcarbodiimide (DCCD)–binding glutamate residues (red line) are conserved between all LHCSR proteins. Pp, P.patens, Cr, C.reinharditii, At, A.thaliana.

Correlation between LHCSR1 accumulation and NPQ kinetics

We further proceeded to verifying if LHSCR1 protein was able to catalyze NPQ in the heterologous systems. Leaves from *N.tabacum* plants expressing LHCSR1 at different levels were analysed for their NPQ kinetics as compared to WT ones lacking LHCSR. It should be appreciated that WT tobacco does perform NPQ by the activity of PSBS. We therefore expect a background NPQ activity and an increased NPQ in plants overexpressing LHCSR if the protein is active. In addition it must be considered that *P.patens* produces Zea

faster and to higher level than *Nicotiana*, making it possible that Zea is limiting for NPQ activation (Pinnola et al. 2013). Consistent with the characteristics of the heterologous system, NPQ activity measured upon illumination of dark-adapted plants was somehow lower in WT respect to OE LHCSR. However, upon further illumination OE LHCSR plants performed better than WT and the difference was larger upon a further cycle of illumination. Furthermore as reported in figure 11D a positive correlation between the level of LHCSR as determined by immunoblotting and NPQ activity could be identified. Based on this correlation we conclude that PpLHCSR1 expressed in *N.tabacum* is active in NPQ.

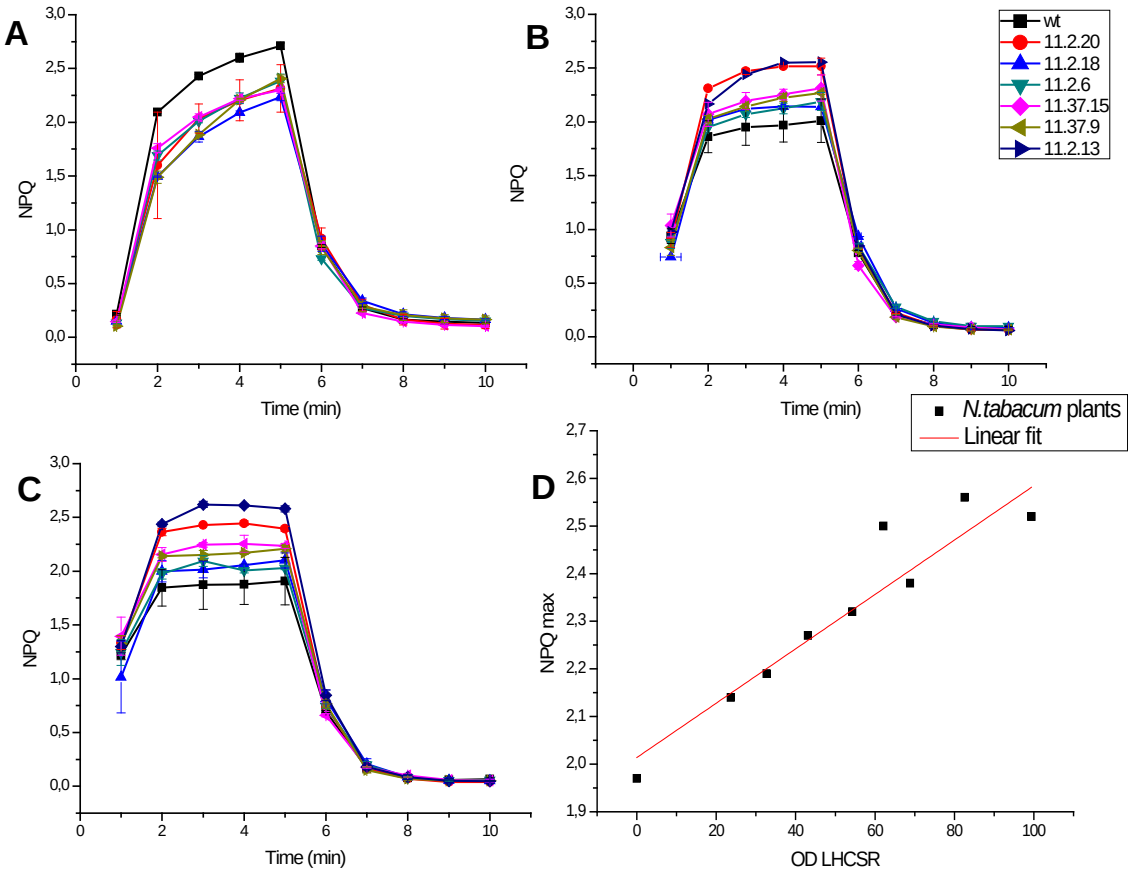

Figure 10. NPQ kinetics measurements of *N.tabacum* plants. *N.tabacum* plants expressing different level of LHCSR1 are compared to WT plant (black). Different cycle of strong illumination are represented. **A**, first cycle. **B**, second cycle. **C**, third cycle. Data are presented as a mean ± SD (n ≥ 3). **(D)** Positive correlation between NPQ of *N.tabacum* plants and LHCSR accumulation. Equation of linear fitting f(x)=0,0057x+2,01, R^2=0,9.

Discussion

The moss *P.patens*, is an evolutionary intermediate between plants and algae, as both PSBS and LHCSR cooperatively catalyzes a strong NPQ activity (Alboresi et al., 2010; Gerotto et al., 2012). Moreover in *P.patens* Zeaxanthin has a strong control on LHCSR-dependent NPQ (Pinnola et al., 2013). Until now the biochemical properties of LHCSR have so far been inferred from recombinant proteins refolded *in vitro* due to the difficulty of purification from natural sources in sufficient amount for its full characterization. Here we have reported the purification of LHCSR1 expression upon either stable or transient heterologous expression in *N.tabacum* and *N. benthamiana* respectively.

The first strategy adopted was transient expression of *P.patens* LHCSR1 in *N.benthamiana* as this option is faster to be implemented and is commonly used to screen different constructs before moving to higher throughput expression systems (Rycke and Kapila, 1997). Secondary stable expression in *N.tabacum* has been developed. Indeed *N.tabacum* expression system has been and will continue to be a major crop for molecular farming and offers several practical advantages over other crops. It produces significant leaf biomass, reaches high protein accumulation and it is a non-food crop with highly-efficient genetic transformation/regeneration (Tremblay et al., 2010). According to our porpoise both these two systems contains all the chromophores needed for LHCSR protein folding and can be easily treated with high light *in vivo* or by *in vitro* acidification of thylakoid preparations to obtain the Zeaxanthin binding form which has tenfold increased NPQ activity. Comparing these two systems the yield of the LHCSR1 recombinant protein from stable transformed transgenic tobacco plants was 1/10 respect to the transient expression system. However that gap will be decreased when stably transformed plants, presently at the T2 generation, will reach homozygosis upon further rounds of selfing.

The heterologous protein expressed was correctly addressed to thylakoid membranes and processed to an apparent MW identical to that observed in SDS-PAGE of moss thylakoids strongly suggesting a correct targeting and processing of the pre-protein encoded by the construct. Further characterization focused on the formation of a pigment binding complex, its pigment composition and spectroscopic properties. Non-denaturing Deriphat-PAGE was previously applied as a fast method for purification of LHCSR proteins from *P.patens* owing to the higher mobility in this type of gels respect to other non-recombinant monomeric LHCBs. Consistently, LHSCR1 was isolated by elution from gel of the fast-running monomeric band. The properties of the pigment-protein obtained were similar to recombinant CrLHCSR3 refolded *in vitro* (Bonente et al, 2011) and to LHCSR isolated from *P.patens*. (Pinnola et al 2013) including the high Chl a/b ratio, the lack of neoxanthin, a red-shifted Qy absorption peak at approx 679 nm and a strong optical activity of the negative Qy band as observed in the CD spectra. It is interesting to note that the CD spectrum did not contain negative features at 640-650 nm typical of Chl b, thus suggesting this

pigment, a conserved component of all LHC proteins so far described (Ballottari et al. 2011), is not a genuine component of the complex. Thus LHCSR1 proteins are likely not to bind Chl b at all suggesting that it is the only member of the LHC superfamily so far reported binding Chl a only. However, isolation of PpLHCSR1 completely lacking Chl b must await further work.

LHCSR1 is activated by zeaxanthin binding and therefore the study of structural and spectroscopic properties of LHCSR1 in order to understand changes associated to the activation of quenching processes will greatly benefit for the comparison between Violaxanthin- and Zeaxanthin- binding forms of LHCSR1. Here, we have shown that it is possible to isolate LHCSR1 in both forms by simply incubating leaves in the dark to favour epoxidation of incubating thylakoids in acidic pH + ascorbate to favour de-epoxidation. The protein obtained in the two conditions has, respectively, violaxanthin or zeaxanthin bound with a high de-epoxidation level, far above that reported for other LHC proteins (Morosinotto et al. 2002, Jahns et al. 2007). The accumulation of Zeaxanthin increased upon repeated treatment with HL (Fig.10) together with NPQ activity in OE LHCSR1 plants, not in WT. This result clearly shows that recombinant LHCSR1 is zea-activated in *Nicotiana* as previously shown in mosses (Pinnola et al. 2013).

We conclude that heterologous expression of LHCSR1 in *Nicotiana* yields an active protein which has properties similar, if not identical to those of LHCSR1 in *P.patens* that will be useful for structural and functional studies on the mechanisms of NPQ. Further studies are needed in order to understand the reasons for the lower specific NPQ activity in *Nicotiana* vs *Physcomitrella*. Likely the localization of the protein is the stroma membranes of thylakoids which is rich in LHCII in mosses but not in plants (Pinnola et al. PhD thesis, 2014) thus allowing for quenching of a small fraction of highly fluorescent LHCII in plants.

Moreover recombinant LHCSR1 appears to be highly enriched in zeaxanthin as demonstrated by the high de-epoxidation index (0,56), a level very similar to that previously described for LHCs monomer from *P.patens* enriched in LHCSR1. Zeaxanthin has been showed to be fundamental for LHCSR1 activity in *P.patens* (Pinnola et al., 2013) , so the ability of recombinant LHCSR1 in zeaxanthin binding could be considered an indication of its good folding as active protein .

The activity of protein has been evaluated measuring NPQ kinetics of expressing plants respect to WT ones. On one hand the transient *N.benthamiana* expression system cannot be used for monitoring LHCSR1 activity. Indeed it has been reported that *A.tumefaciens* infection induce a strong down-regulation of effective photosystem II quantum yield (Berger et al., 2007). On the other hand in *N.tabacum* stable expression was instead possible to measure an LHCSR1 –dependant NPQ activity. According to previously published data (Pinnola et al., 2013) also in *N.tabacum* plants LHCSR1 activity is strongly related to zeaxanthin accumulation. Indeed an increased in NPQ quenching was measured repeating cycle of strong

illumination that induce zeaxanthin accumulation. Moreover the NPQ activity has been demonstrated to be directly correlated with LHCSR1 accumulation as showing by plants expressing different levels of LHCSR1.

Conclusion

In this work it has been shown for the first time that *N.benthamiana* and *N.tabacum* emerged so as a good choice for studying heterologous LHC-like proteins like P.patens LHCSR1. These systems are indeed able to express LHCSR1 as mature LHC monomer in thylakoid membrane. Using a Deriphat-PAGE system it has been realized the first isolation of native LHCSR1 protein. Spectral properties of native LHCSR1 fit those previously reported for recombinant *C. reinhardtii* (Bonente et al., 2011) and CD spectra confirm that LHCSR1 isolated is correctly well folded with pigments. LHCSR1 pigment composition has been described indicating that LHCSR1 is characterized for a strong Chl a/b ratio and for no binding of neoxanthin. Furthermore in vitro de-epoxidation confirm that LHCSR1 is able to bind zeaxanthin, as previously reported (Pinnola et al., 2013). Finally the positive correlation of LHCSR1 accumulation and NPQ maximum reported for *N.tabacum* plants suggest that the protein is fully able to induce NPQ.

Materials and methods

Construction of plant expression vector

Genomic *P.patens* protonemal DNA has been extracted (Allen et al., 2007) and used as a template to construct the pENTR™/D-TOPO based vector. Lhcsr1 gene was amplified using the following primers: the forward primer 5'-CACCCTCGCTCTGCAACTTTCCTTT-3' and the reverse primer 5'-GGGGACCACTTTGTACAAGAAAGCTGGGTCGACTGCGAATCAATCAGAA-3'. The pENTR.LHCSR1 vector obtained was used for LR recombination reactions with the GATEWAY destination vector pK7WG2, generating the final vector pK7WG2.LHCSR1.

N.tabacum plants transformation

Tobacco (*Nicotiana tabacum* cv Petit Havana SR1) leaf discs were transformed with pK7WG2-based constructs as described (Horsch et al., 1986) . Kanamycin-resistant transgenic lines were selected and tested by western blot analysis using home-made polyclonal anti-*P.p*LHCSR1 antibody.

Agroinfiltration of *N.benthamiana* leaves

The vector pK7WG2.LHCSR1 was transformed in *A.tumefaciens* strain which was used for agroinfiltration. Bacterial suspension in infiltration buffer (10 mM MES, 10 mM $MgCl_2$, 100 µM acetosyringone , pH 5,6) was use for syringe infiltration of 5-6 weeks-old N.benthamiana plants, 5 leaves were infiltrated for each plants. The recombinant protein time-course accumulation of LHCSR1 protein has been estimated by immunoblotting on total protein extract starting from disc of infected leaves collected for 7 days after agroinfiltration and frozen in liquid nitrogen immediately after harvesting. Discs were all grinded directly in Loading Buffer (LB; Tris pH 6,8, 10% glycerol, 2% SDS and 3% β-mercaptoethanol) just before SDS-PAGE analysis.

Thylakoids extraction and Pigment Binding Complex purification

Thylakoids were purified from *N.tabacum* and *N.benthamiana* leaves following a protocol for seed plants with minor modifications. Leaves were harvested and homogenized in extraction buffer (0.5% milk powder, 0.4 M NaCl, 0.02 M Tricine-KOH, pH 7.8, and 0.005M e -aminocaproic acid, 0.001 phenyl-methylsulfonyl fl uoride and 0.001 benzamidine as protease inhibitors). After filtration, samples were precipitated by centrifugation at 1500g for 15 min at 4°C and then resuspended in hypotonic buffer (0.15 M NaCl, 0.005 M $MgCl_2$, 0.02 M Tricine-KOH, pH 7.8, and protease inhibitor). After centrifugation for 10 min at 10,000g at 4°C, thylakoids were resuspended in a buffer containing 0.4 M sorbitol, 0.015 M NaCl, 0.005 M $MgCl_2$, and 0.01 M HEPES-KOH, pH 7.5. All this procedure was done in the dark at 4°C. Finally, thylakoids were either used directly or frozen in liquid nitrogen and stored at – 80°C until use.

For separation of pigment binding complex 500 µg of thylakoid membranes were washed with 5 mM EDTA and resuspended at a final concentration of 1 mg/ml in 10 mM Hepes, pH 7,5. Samples were then solubilised at a final concentration of 0,5 mg/ml adding 1,6% α-DM and 10 mM Hepes, pH 7,5 and vortexing for 1 min. After 10 min of ice incubation, thylakoids membranes were centrifuged at 15.000 g for 10 min to eliminate not solubilised materials. Fractionation occurred upon by ultracentrifugation on a 0,1 to 1 M sucrose gradient containing 0,03 α-DM and 10 mM Hepes, pH 7,5 (22 hours at 40,000xg at 4°C). The green bands were harvested using a syringe needle connected to a peristaltic pump.

Deriphat page

Non-denaturating Deriphat-PAGE was performed according to previously protocol applying minor modification. The stacking gel contained 3.5% (w/v) acrylamide (38:1 acrylamide/bis-acryl-amide) and the resolving gel contained 7% (w/v) acrylamide. Thylakoids concentrated at 1 mg/mL of chlorophyll were solubilized with 0.8% a –DM. 500 ug of chlorophylls were loaded in each lane comparing LHCSR1 over-expressing plants to the corresponding WT.

Absorption spectroscopy

Samples collected from the sucrose gradients were analyzed by SLM-Aminco DW-2000 spectrophotometer at room temperature collecting absorption measurements. Spectra were collected in the same way also for native chlorophyll binding complexes after extraction from the acrylamide gel by grinding the slices in a buffer containing 10 mM HEPES, pH 7.5, and 0.03% a –DM.

SDS-PAGE and immunoblotting analysis

SDS-PAGE analyses were performed as described by Laemmli (1970) An acrylamide/bis-acrylamide ratio of 75: 1 and a total concentration of acrylamide of 4.5 and 15% was used respectively, for stacking and running gel. Urea (6 M) was also added into the running gel. Polypeptides, following SDS-PAGE, were transferred onto an Immobilon PVDF membrane (Millipore) using a Mini Trans-Blot cell (Bio-Rad) and detected by home-made polyclonal antibodies.

Pigment analysis

Pigments were extracted and then separated and quantified by HPLC as previously described (Gilmore and Yamamoto, 1991).

NPQ measurements

In vivo chlorophyll fluorescence of *N.tabacum* leaves WT and LHSCR1 expressing lines was measured at room temperature on Fluorcam imaging fluorometers (Photon system instrument) , with saturating light at 4000 µmol $m^{-2}s^{-1}$ and actinic light at 900 µmol $m^{-2}s^{-1}$. Before measurements, plants were dark-adapted for

40 min at room temperature. Parameters Fv /Fm and NPQ were calculated as (Fm – Fo)/Fm and (Fm –Fm ')/Fm' (Demmig-Adams et al., 1996). Data are presented as means ± SD of at least three independent experiments.

References

Alboresi, A., Gerotto, C., Giacometti, G.M., Bassi, R., and Morosinotto, T. (2010). Physcomitrella patens mutants affected on heat dissipation clarify the evolution of photoprotection mechanisms upon land colonization. Proc. Natl. Acad. Sci. U. S. A.

Allen, G.C., Flores-vergara, M.A., Krasnyanski, S., Kumar, S., and Thompson, W.F. (2007). A modified protocol for rapid DNA isolation from plant tissues using cetyltrimethylammonium bromide. **1**: 2320–2326.

Andersson, U., Heddad, M., and Adamska, I. (2003). Light stress-induced one-helix protein of the chlorophyll a/b-binding family associated with photosystem I. Plant Physiol. **132**: 811–820.

Arnoux, P., Morosinotto, T., Saga, G., Bassi, R., and Pignol, D. (2009). A structural basis for the pH-dependent xanthophyll cycle in Arabidopsis thaliana. Plant Cell **21**: 2036–44.

Ballottari, M., Girardon, J., Dall'osto, L., and Bassi, R. (2012). Evolution and functional properties of photosystem II light harvesting complexes in eukaryotes. Biochim. Biophys. Acta **1817**: 143–57.

Bellafiore, S., Barneche, F., Peltier, G., and Rochaix, J.-D. (2005). State transitions and light adaptation require chloroplast thylakoid protein kinase STN7. Nature **433**: 892–895.

Bergantino, E., Segalla, A., Brunetta, A., Teardo, E., Rigoni, F., Giacometti, G.M., and Szabò, I. (2003). Light- and pH-dependent structural changes in the PsbS subunit of photosystem II. Proc. Natl. Acad. Sci. U. S. A. **100**: 15265–70.

Berger, S., Sinha, A.K., and Roitsch, T. (2007). Plant physiology meets phytopathology: plant primary metabolism and plant-pathogen interactions. J. Exp. Bot. **58**: 4019–26.

Bonente, G., Ballottari, M., Truong, T.B., Morosinotto, T., Ahn, T.K., Fleming, G.R., Niyogi, K.K., and Bassi, R. (2011a). Analysis of LhcSR3, a protein essential for feedback de-excitation in the green alga Chlamydomonas reinhardtii. PLoS Biol. **9**: e1000577.

Bonente, G., Ballottari, M., Truong, T.B., Morosinotto, T., Ahn, T.K., Fleming, G.R., Niyogi, K.K., and Bassi, R. (2011b). Analysis of LhcSR3, a protein essential for feedback de-excitation in the green alga Chlamydomonas reinhardtii. PLoS Biol. **9**: e1000577.

Dainese, P. and Bassi, R. (1991). System and Aggregation State of the Component Chlorophyll u / b.: 8136–8142.

Engelken, J., Brinkmann, H., and Adamska, I. (2010). Taxonomic distribution and origins of the extended LHC (light-harvesting complex) antenna protein superfamily. BMC Evol. Biol. **10**: 233.

Georgakopoulou, S., van der Zwan, G., Bassi, R., van Grondelle, R., van Amerongen, H., and Croce, R. (2007). Understanding the changes in the circular dichroism of light harvesting complex II upon varying its pigment composition and organization. Biochemistry **46**: 4745–54.

Gerotto, C., Alboresi, A., Giacometti, G.M., Bassi, R., and Morosinotto, T. (2012). Coexistence of plant and algal energy dissipation mechanisms in the moss Physcomitrella patens. New Phytol.: 763–773.

Gilmore, A.M. and Yamamoto, H.Y. (1992). Dark induction of zeaxanthin-dependent nonphotochemical fluorescence quenching mediated by ATP. Proc. Natl. Acad. Sci. U. S. A. **89**: 1899–1903.

Gilmore, A.M. and Yamamoto, H.Y. (1991). Zeaxanthin Formation and Energy-Dependent Fluorescence Quenching in Pea Chloroplasts under Artificially Mediated Linear and Cyclic Electron Transport1.: 635–643.

Giuffra, E., Cugini, D., Croce, R., Bassi, R., Verona, U., and Mm, S. (1996). Reconstitution and pigment-binding properties of recombinant CP29. Eur. J. Biochem. **120**: 112–120.

Green, B.R. and Durnford, D.G. (1996). the Chlorophyll-Carotenoid Proteins of Oxygenic Photosynthesis. Annu. Rev. Plant Physiol. Plant Mol. Biol. **47**: 685–714.

Horsch, R.B., Klee, H.J., Stachelt, S., Winanst, S.C., Nestert, E.W., Rogers, S.G., and Fraley, R.T. (1986). Analysis of Agrobacterium tumefaciens virulence mutants in leaf discs. Proc. Natl. Acad. Sci. U. S. A. **83**: 2571–2575.

Horton, P., Ruban, a. V., and Walters, R.G. (1996). Regulation of Light Harvesting in Green Plants. Annu. Rev. Plant Physiol. Plant Mol. Biol. **47**: 655–684.

Jansson, S. (1999). A guide to the Lhc genes and their relatives in Arabidopsis. Trends Plant Sci. **4**: 236–240.

Kargul, J. and Barber, J. (2008). Photosynthetic acclimation: Structural reorganisation of light harvesting antenna - Role of redox-dependent phosphorylation of major and minor chlorophyll a/b binding proteins. FEBS J. **275**: 1056–1068.

Kovács, L., Damkjaer, J., Kereïche, S., Ilioaia, C., Ruban, A. V, Boekema, E.J., Jansson, S., and Horton, P. (2006). Lack of the light-harvesting complex CP24 affects the structure and function of the grana membranes of higher plant chloroplasts. Plant Cell **18**: 3106–20.

Koziol, A.G., Borza, T., Ishida, K.-I., Keeling, P., Lee, R.W., and Durnford, D.G. (2007). Tracing the evolution of the light-harvesting antennae in chlorophyll a/b-containing organisms. Plant Physiol. **143**: 1802–16.

Morosinotto, T., Baronio, R., and Bassi, R. (2002). Dynamics of chromophore binding to Lhc proteins in vivo and in vitro during operation of the xanthophyll cycle. J. Biol. Chem. **277**: 36913–20.

Pagano, A., Cinque, G., and Bassi, R. (1998). In Vitro Reconstitution of the Recombinant Photosystem II Light-harvesting Complex CP24 and Its Spectroscopic Characterization *. **273**: 17154–17165.

Paulsen, H., Finkenzeller, B., and Kühlein, N. (1993). Pigments induce folding of light-harvesting chlorophyll a/b-binding protein. Eur. J. Biochem. **215**: 809–816.

Peers, G., Truong, T.B., Ostendorf, E., Busch, A., Elrad, D., Grossman, A.R., Hippler, M., and Niyogi, K.K. (2009). An ancient light-harvesting protein is critical for the regulation of algal photosynthesis. Nature **462**: 518–21.

Pinnola, A., Dall'Osto, L., Gerotto, C., Morosinotto, T., Bassi, R., and Alboresi, A. (2013). Zeaxanthin binds to light-harvesting complex stress-related protein to enhance nonphotochemical quenching in Physcomitrella patens. Plant Cell **25**: 3519–34.

Ruban, a. V., Lee, P.J., Wentworth, M., Young, a. J., and Horton, P. (1999). Determination of the Stoichiometry and Strength of Binding of Xanthophylls to the Photosystem II Light Harvesting Complexes. J. Biol. Chem. **274**: 10458–10465.

Rycke, R. De and Kapila, J. (1997). An agrobacterium-mediated transient gene expression intact leaves system for. **122**.

Sandonà, D., Croce, R., Pagano, A., Crimi, M., and Bassi, R. (1998). Higher plants light harvesting proteins. Structure and function as revealed by mutation analysis of either protein or chromophore moieties. Biochim. Biophys. Acta - Bioenerg. **1365**: 207–214.

Standfuss, J., Terwisscha van Scheltinga, A.C., Lamborghini, M., and Kühlbrandt, W. (2005). Mechanisms of photoprotection and nonphotochemical quenching in pea light-harvesting complex at 2.5 A resolution. EMBO J. **24**: 919–928.

Tremblay, R., Wang, D., Jevnikar, A.M., and Ma, S. (2010). Tobacco, a highly efficient green bioreactor for production of therapeutic proteins. Biotechnol. Adv. **28**: 214–21.

Chapter 2.B:

Purification of *Physcomitrella patens* Light harvesting stress-related protein 1 (LHCSR1) using *Nicotiana benthamiana* expression system

Purification of *Physcomitrella patens* Light harvesting stress-related protein 1 (LHCSR1) using *Nicotiana benthamiana* expression system

Introduction

Light energy is collected to fuel photosynthesis through an antennae system composed by proteins belonging to the Light Harvesting Complex (LHC) multigene superfamily (Jansson, 1999). These membrane-embedded pigment-binding proteins are organized around Photosystem I (PSI) or Photosystem II (PSII) and they transfer absorbed light energy to the core for charge separation. Beside their crucial role in light-harvesting, LHC proteins possess different functions such as for example photoprotection from excess light. In fact, they are active in dissipating excess absorbed light by Non-photochemical quenching (NPQ) of chlorophyll a fluorescence, a key mechanism regulating the amount of excitation energy directed to the reaction center (Horton, 2012; Ruban et al., 2007), they participate to state transition balancing energy between PSII and PSI (Bellafiore et al., 2005; Kargul and Barber, 2008) and finally some LHC of PSII participate also to structure of thylakoid membranes as they are involved in stacking of grana thylakoids (Kovács et al., 2006; Standfuss et al., 2005). LHC proteins are structurally very similar indeed they contain three membrane-spanning helices, of which, helix one and three are highly conserved. LHC proteins share a 'generic LHC motif': a highly hydrophobic sequence of about 22 amino acids with three invariant charged amino acids – glutamic acid (Glu) and arginine (Arg), as well as a few highly conserved glycine (Gly) residues (Kühlbrandt et al., 1994).

LHC proteins share also some common physic–chemical features and molecular mass making the isolation of pure isoforms problematic (Ballottari et al., 2012), even more difficult considering that LHC are membrane proteins which can be extracted from surface only using detergents. Until now only a few LHC protein have been purified from thylakoid membranes maintaining their native state. It is the case of minor antennae proteins CP24, CP26 and CP29 which has been extracted from thylakoid membranes using high detergent concentration but loosing pigments which play a crucial role in light absorption, charge separation and energy transfer toward the reaction centre(Ruban et al., 1999; Dainese and Bassi, 1991; Caffarri et al., 2001)

A strategy largely adopted to overcome the purification problems includes the possibility to express LHC protein as apoproteins in *E.coli* and then reconstitute them *in vitro* with pigments (Paulsen et al., 1993; Giuffra et al., 1996; Pagano et al., 1998). Even if this system is largely used for studying LHC protein the Chl a/b ratio of the recombinant complex strongly depends on the Chl a/b ratio of the reconstitution mix (Sandonà et al., 1998), suggesting that this system might yield into misevaluation of pigment composition and therefore needs to be integrated by information about the complexes in their native state in order to drive conclusion at fine structural level.

A valuable solution is represented by the expression of LHC proteins in eukaryotic systems naturally endowed with pathways for the biosynthesis of the chromophores (Chlorophyll a, Chlorophyll b, xanthophylls) essential for the folding of pigment-binding photosynthetic proteins. This is the case of chimeric LHCII expressed in *Nicotiana tabacum* plants for which has been demonstrated the possibility of its purification in native state (Flachmann and Kühlbrandt, 1996) although at very low yield. The choice of *Nicotiana* has the advantage of well optimized protocols for its transformation available in a fast growing plant obtaining good amounts of biomass. Furthermore, the purification of recombinant proteins can be facilitated by the additions of tags as recently shown for CP24 over-expressed in *A.thaliana* (Passarini et al., 2014).

A similar strategy was adopted in this work for the heterologous expression of light harvesting stress related protein 1 (LHCSR1) from *Physcomitrella patens* taking advantage of the transient expression system *Nicotiana benthamiana*.

LHCSRs are LHC-like proteins that form a subgroup of LHC proteins involved in NPQ activation present in green algae and mosses, but absent in lycopods and seed plants (Peers et al., 2009; Alboresi et al., 2010). In particular LHCSR proteins participate to harmless thermal dissipation of excess absorbed light energy, a process called Non-photochemical quenching (NPQ) (Niyogi, 2000). NPQ is a very fast phenomenon due to two components energy quenching (qE) and inhibitory quenching (qI). The qE component depends on lumen acidification and develops within seconds upon light increasing (Demmig-Adams, 1996). Indeed the slower component qI is due to photosystem II (PSII) photoinhibition but also the accumulation of zeaxanthin (Dall'Osto, 2005). The contribution due to zeaxanthin accumulation and in particular to its binding to light-harvesting complex (LHC) proteins, has been recently defined as qZ.

The involvement of LHCSR proteins in qE was described for the first time by the isolation of *lhcsr3* mutant of *Chlamydomonas reinharditii* (Peers et al., 2009; Alboresi et al., 2010)and later *lhcsr1* and *lhcsr2* in the *Physcomitrella patens* (Peers et al., 2009; Alboresi et al., 2010). *In vitro* reconstitution of LHCSR3 demonstrated that it acts both like a pH-sensitive activator of qE and also as quencher *per se* by a chlorophyll-carotenoid charge-transfer mechanisms in *C. reinharditii* (Bonente et al., 2011a) while recently it has been shown that LHCSR1 quenching activity is strongly dependant on Zeaxanthin in *P. patens* (Pinnola et al., 2013). However, information on *P. patens* LHCSR1 structural, biochemical and spectroscopic properties is very limited.

P. patens LHSCR1 has been successfully expressed in *N. benthamiana* expression system, purified in its native form from thylakoid membranes through a 6x histidine tail and then characterized.

Results

Expression of *Physcomitrella patens* LHCSR1 in *Nicotiana benthamiana*

The full length cDNA of *LHCSR1* sequence was amplified in frame with the coding sequence of six histidines at the 3' and introduced in the binary gateway vector pK7WG2 under the control of the constitutive promoter CaMV 35S. The vector named pK7WG2.Lhcsr1-HisTag was used for transient transformation of *N.benthamiana* (Fig.1A).

Five-six week-old *N.benthamiana* plants have been used for agroinfiltrating 5 leaves per plant by a syringe. First of all, protein accumulation has been daily evaluated in a time-course collecting leaf discs for 7 days post-agroinfiltration (dpa). Total proteins were extracted from each disc in a denaturing buffer. An equal volume of protein extract was loaded on an SDS-PAGE and analysed by western blotting with a specific homemade anti-PpLHCSR1 polyclonal antibody (Fig. 1B). LHCSR1 bands were not visible at 1 dpa, suggesting that *N.benthamiana* leaves need more than 24 hours to synthesize detectable amounts of LHCSR1. A significant increase of LHCSR1 was detectable at 2 dpa and 3 dpa and its accumulation peaked at 4 dpa, suggesting that the fourth day could be chosen for leaf collection in order to assure the higher accumulation of recombinant LHCSR1 protein.

Once we had verified that LHCSR1 *P. patens* protein was expressed in *N. benthamiana* leaves, its import and accumulation in thylakoid membranes was also evaluated. Thylakoids were prepared from *N.benthamiana* infected leaves. The presence of the recombinant protein was confirmed by western blotting using an equal amount of *P.patens* thylakoid membranes (on a Chl basis) as reference (Fig. 1C). Two bands corresponding to LHCSR1 and LHCSR2 were resolved in *P. patens* thylakoids while no signal was detectable in *N. benthamiana* wild type thylakoids. Nuclear encoded thylakoid proteins are addressed to thylakoid membranes by a transit peptide at the N-terminus. The transit is cleaved to give rise to a chloroplast mature protein. As reported in figure 1.C, LHCSR-HT is expressed in thylakoid membranes at a lightly higher apparent molecular weight as compared to LHCSR1 from *P.patens*. This difference in molecular weight can be attributed to a mature LHCSR1 with the presence of six histidine tail.

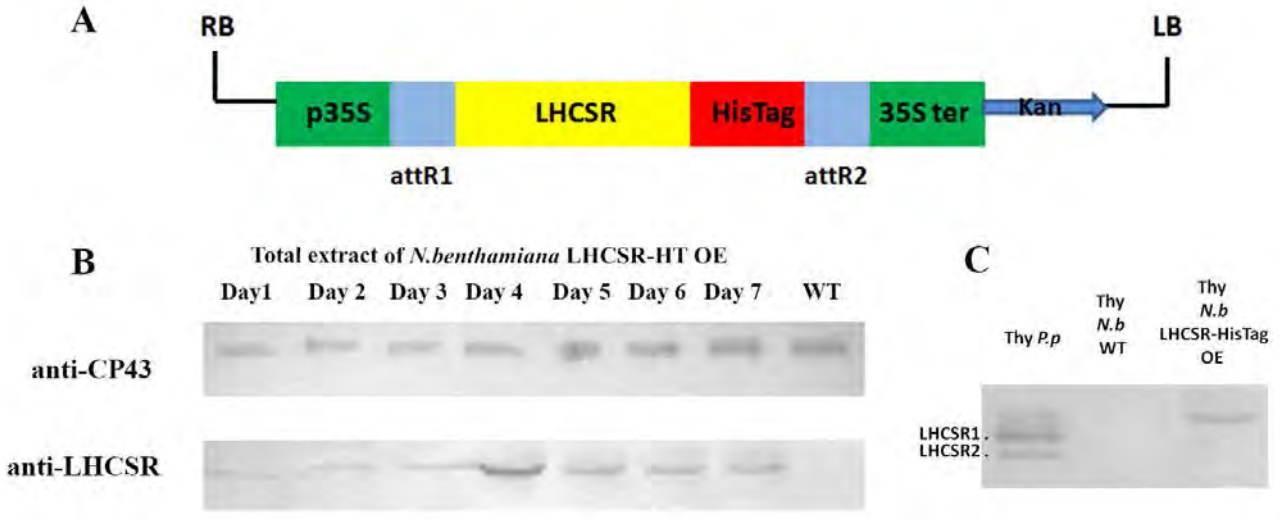

Figure.1. (A) Simplified scheme of pK7WG2.Lhcsr1-HisTag gateway construct. RB: right border, p35s: 35s promoter, attR1 and attR2: sequence for recombinant process, LHCSR: sequence coding for LHSCR protein, HisTag: sequence coding for 6-histidine tail. **(B)** Time course of recombinant protein accumulation in *N.benthamiana*. Disc leaves collected every day for 7 days post agroinfiltration were ground in LB buffer and analyzed by western blotting using anti-LHCSR1 antibody. Anti-CP43 is shown as loading control. Accumulation of LHCSR1 protein is clearly visible at the fourth day post agro-infiltration **(C)** Immunoblot analysis of thylakoid proteins with α-LHCSR1 antibody. P. p. stands for *Physcomitrella patens*. N. b. WT stands for *N. benthamiana* wild-type and LHCSR-His Tag OE stands for plants transformed with pK7WG2.Lhcsr1-HisTag. LHCSR1 and LHCSR2 of *P. patens* are indicated on the right side of the panel

Aggregation state of LHCSR1 in *N.benthamiana* thylakoids

LHC complexes can be isolated as single pigment-binding protein or as multimeric complex. Pigment-protein complexes after solubilization with 0,8% α-DM were separated by native electrophoresis as shown in figure 2. The band with highest mobility contains free pigments while the slower migrating bands represent pigment-protein complexes with high complexity. By comparing thylakoids from *N.benthamiana* WT and LHCSR1-HT plants by immoblotting analysis with the anti-LHCSR antibody, a single reactive band was detected, migrating just below the band corresponding to monomeric LHC proteins. LHCSR1 is correctly expressed in *N.benthamiana* thylakoids as monomeric protein as previously reported for LHCSR1 in *P.patens* (Pinnola et al., 2013).

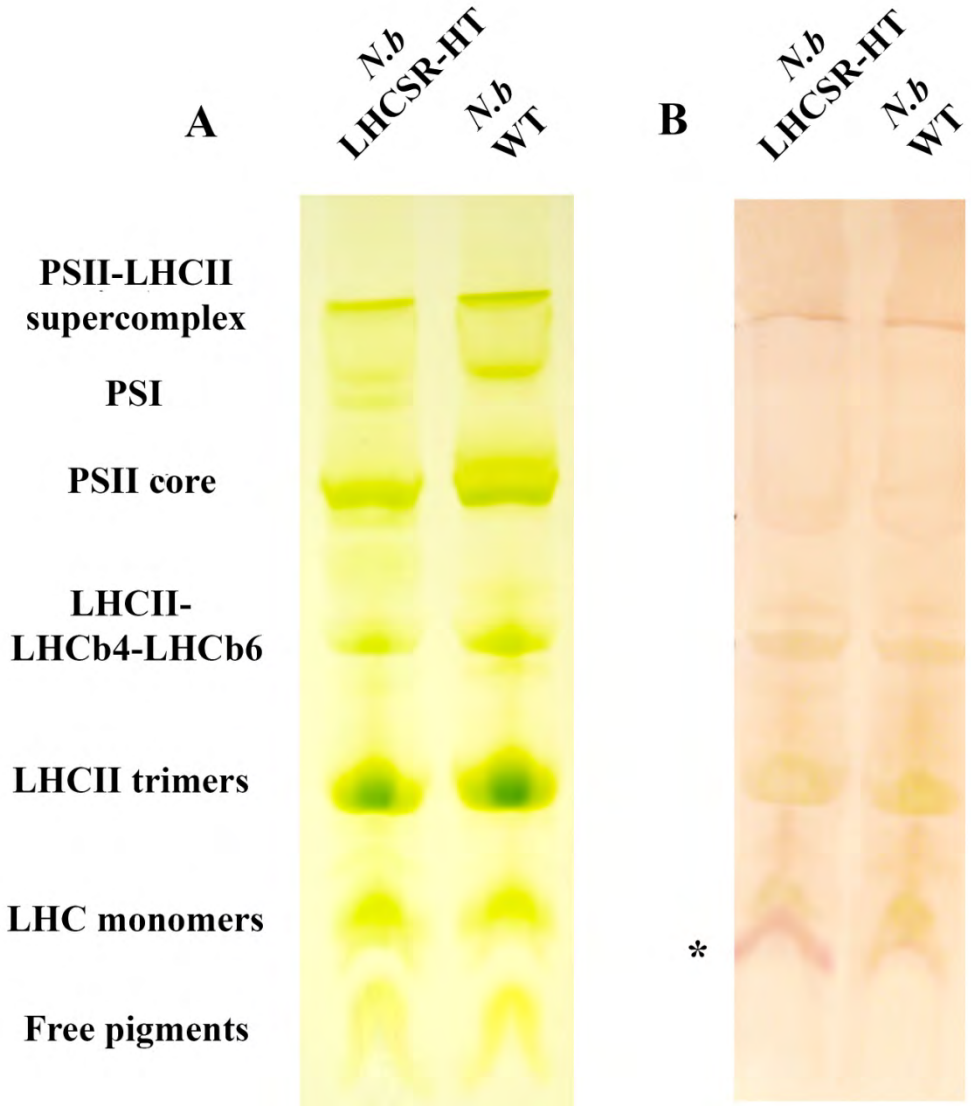

Figure.2. (A) Native Deriphat-PAGE electrophoresis of *N.benthamiana* WT and LHCSR1-HT thylakoids. Chlorophylls (60 ug) were loaded for each sample **(B)** Non-denaturating gel was transferred on a PVDF membrane for immunoblotting analysis using an antibody raised against LHCSR. Immuno-reacting band (asterisks) specific to LHCSR-HT appeared at the level of monomeric antenna proteins molecular weight.

Purification of LHCSR1 from thylakoid membranes

Thyalkoid membranes from 4-days agroinfiltated *N.b.* leaves were solubilised with 1% of β-DM at a chlorophyll concentration of 1mg/ml and loaded onto a Ni-affinity column. LHCSR1 was eluted from the column using different increasing concentration of Imidazole (10-25-50 and 250 mM). Fraction from different washing steps were loaded onto a SDS-PAGE gel and stained with Coomassie blue and analyzed for LHCSR1 content by western blotting. As shown by SDS-PAGE stained with Coomassie blue (Fig .3A) samples eluted with 50 and 250 mM of imidazole are enriched in a polypeptide migrating at an apparent molecular weight of 29 kDa. Sample eluted with 50 mM still contained some high-molecular weight contaminants polypeptides while sample eluted with 250 mM Imidazole a single band corresponding to the

apparent molecular weight of LHCSR1 could be detected. The same fractions stained with Coomassie blue were also analyzed by immunoblotting with a monoclonal anti-Histidine antibody. A strong reaction was clearly visible in sample eluted with 50 mM and 250 mM of Imidazole at the same molecular weight of the signal obtained for thylakoids used as reference. In fractions corresponding to flow trough no signal corresponding to LHCSR1 could be detected suggesting that all LHCSR1 proteins remained strong bound to the column and that could be purified by different imidazole steps.

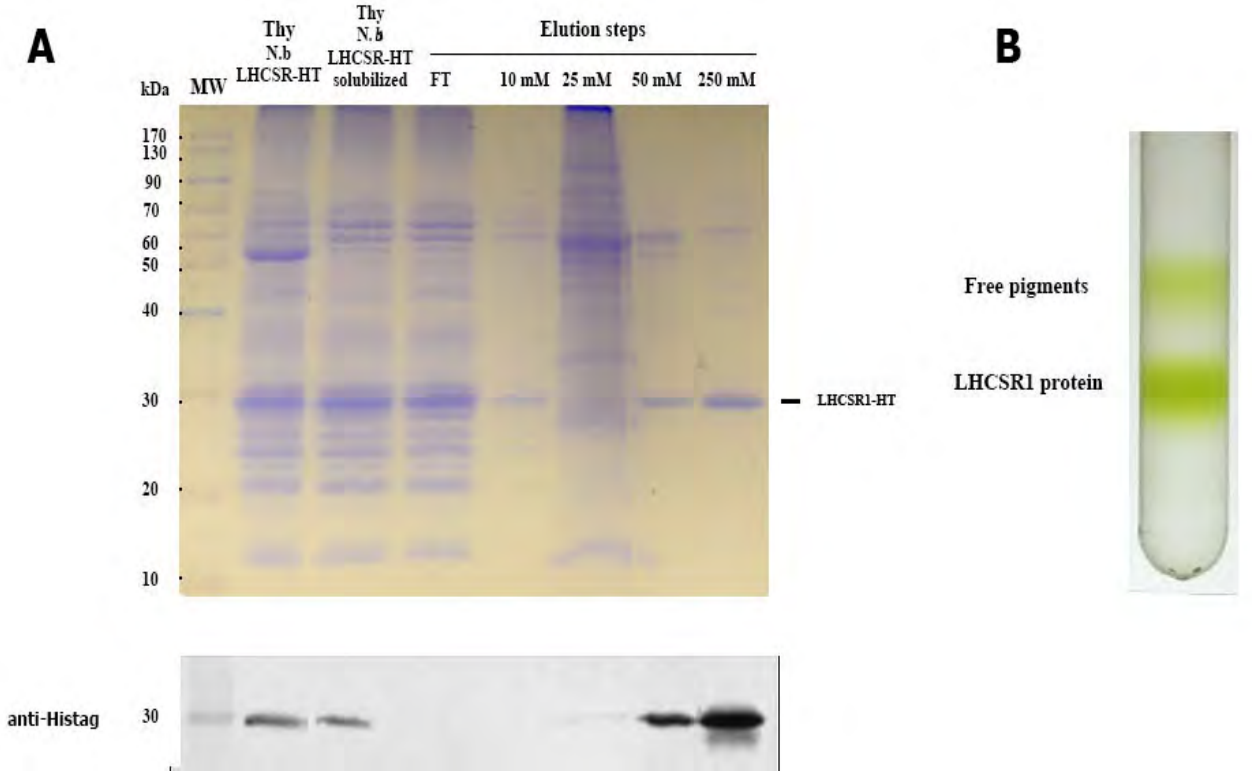

Figure.3. (A) SDS-PAGE and Western blot of of sample purified from Ni-affinity column. 5 ug (on Chl basis) of each elution steps was loaded showing the presence of a band at an apparent molecular weight of 26 kDa in fractions corresponding to 50 and 250 mM Imidazole. Fraction eluted with 250 mM imidazole is affected by a very low quantity of contaminants suggesting that purification protocols worked. The western blot analysis of the same sample is reported below the SDS-PAGE image. Starting from left Thy N.b LHCSR-HT: 3 ug of thylakoids of *N.benthamiana* expressing LHCSR-HT; Thy N.b.LHCSR-HT solubilised: the same thylakoids after solubilisation; FT: materials that did not bound to the column; 10-25-50-250 mM: different concentration of imidazole used for LHCSR-HT elution. Immunoblotting using monoclonal antibody against Histidine tail confirmed that LHSCR1 is correctly eluted with 250 mM of Imidazole. **(B)** Sucrose gradient of sample eluted with 250 mM imidazole. Two bands are clearly present, the upper one corresponding to free pigments and the lower one due to LHCSR1 migration

Light absorption properties of LHCSR1

Fractions containing LHCSR1 proteins were then loaded onto a sucrose gradient and centrifuged at 60.000xg for 20h. The separation pattern consisting of two different bands: an-upper one corresponding to free pigments and a lower one putatively corresponding to LHCSR1 protein (Fig.3B). Fraction collected from sucrose gradient was used for studying its light absorption properties.

The absorption spectrum of LHCSR1 compared to *C.reinharditii* LHCSR3 apoprotein reconstituted *in vitro* with pigments (Bonente et al., 2011a) showed a Qy transition peak red-shifted to 679 nm (Fig.4A). This peak is strongly shifted with respect to the 670-nm peak of the free Chl a in detergent solution, and even more red-shifted than any PSII antenna protein. Information on cromophore organization within pigment-protein can be obtained by circular dicroism (CD). The LHCSR1 CD spectra has features previously reported for native and recombinant LHCb proteins, with signal in the Qy region at 680 nm (-) and 660 nm (+) (Fig.4B). Interestingly, the amplitude of CD spectra in Qy region is strong respect to that of recombinant CP29, upon normalization at the same protein molar concentration, suggesting an enhanced level of excitonic interaction between Chl a chromophores in LHCSR1 (Georgakopoulou et al., 2007). Moreover, the LHCSR1 CD spectrum is also characterized by the absence of signal at 646 nm (-) due to Chl b contribution, suggesting that LHCSR1 binds a low number of Chl b molecules. This was confirmed by comparing the signal at 464 nm which is associated to excitonic interactions between xanthophyll and chlorophyll b molecules. In LHCSR1 this signal is present but not so strong broad negative as CP29 one. The strong optical activity here reported for LHCSR1 is also a clear indication of a stable protein complex with Chl and xanthophyll chromophores. Indeed free pigment in detergent solution or not specifically bound to protein have a very low amplitude in CD spectra, with a single positive component in Qy region (Giuffra et al., 1996).

The Fluorescence emission spectra (Fig.3C) were characterized by a 684 nm peak, independently of exciting Chl a (440 nm), Chl b (475 nm) or xanthophylls (500 nm), implying efficient energy transfer between pigments suggesting that LHCSR1 purified from *N.benthamiana* form stable complex with Chl a, Chl b and xanthophylls.

.

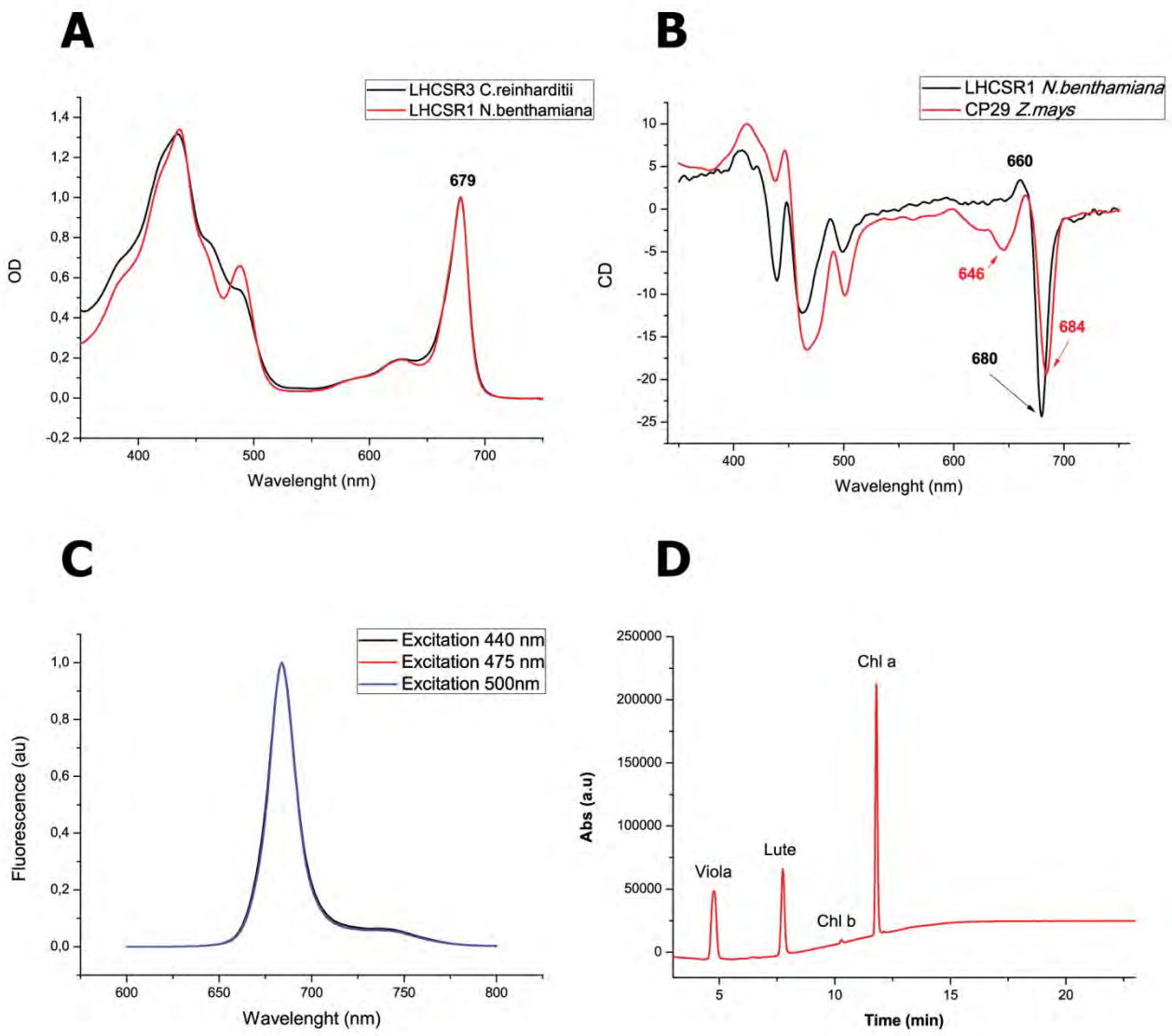

Figure.4. (A) Absorption spectrum of LHCSR1 collected from the sucrose gradient (red line). LHCSR1 spectra resembling spectrum of LHCSR3 from *C.reinharditii* reconstituted in vitro with pigments (black line). Both of them are characterize by a red shifted peak at 679 nm. **(B)** CD spectra of LHCSR1 (black line) compared to CP29 protein from *Z.mays* (red line). Chl major peaks are shown. **(C)** LHCSR1 fluorescence emission at 300K with excitation at 440 nm (black line, Chl a), 475 nm (red line,Chl b), and 500 nm (blue line, Cars) **(D)** HPLC chromatogram of pigments bound to LHCSR1.

Pigment analysis of LHCSR1

High performance liquid chromatography (HPLC) analysis shows that LHCSR1 binds Chl a, Chl b, lutein and violaxanthin whereas no neoxanthin was detected. On the basis of the conservation of six to eight Chl-binding residues (Fig.5) it is proposed a stoichiometry of six Chls per apoprotein as previously reported for LHCSR3 protein reconstituted *in vitro* with pigments (Bonente et al., 2011a). Pigment profiling showed that LHCSR1 is characterized by a high Chl a/b ratio. Furthermore, based on previous data which

demonstrated that LHC proteins bind xanthophylls into specific sites, as sites L1 , L2 , N1 and V1 it is possible to hypothesized that LHCSR1 is able to bind two/three carotenoids. It is possible to assume that LHCSR1 possess two binding site occupied by violaxanthin and lutein , probably L1 and L2 and a third site partially unoccupied. This third Car binding site is probably a V1 type as no neoxanthin is present in LHCSR1 protein, as previously reported for LHCSR3 (Bonente et al., 2011a).

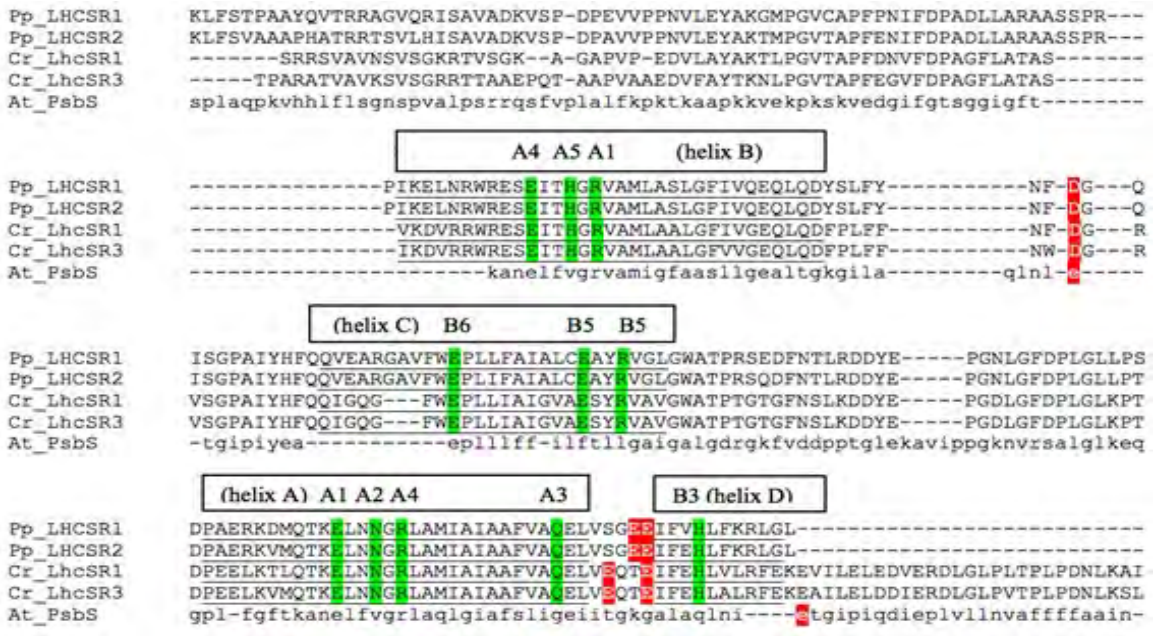

Figure 4 Sequence alignment of LHCSR1/2 from *P.patens*, LHCSR1/3 from *C.reinharditii* and PSBS from *A.thaliana***.** Chl-coordinating residues (green line) and dicyclohexylcarbodiimide (DCCD)–binding glutamate residues (red line) are conserved between all LHCSR proteins. Pp*, P.patens*, Cr, *C.reinharditii*, At, *A.thaliana*

	Chl (a+b) Normalization	Chl a	Chl b	Violaxanthin	Lutein	Chl/Car	Chl a/b
LHCSR1	100	98,25±0,02	1,75±0,02	24,37±0,41	23,08±0,24	2,11±0,01	56,06±0,65
LHCSR1	6	5,89±0,001	0,11±0,001	1,46±0,02	1,39±0,01	2,11±0,01	56,06±0,065

Table 1. Pigment content (in picomoles) of LHCSR1 isolated from *N.benthamiana* leaves. Data are normalized to the suggested number of Chls reported in the first column. Data are means of at least 3 replicas.

Discussion

Recently it has been demonstrated by various knock out and over-expressing lines that two different proteins PSBS and LHCSR are fully able to induce NPQ in *P.patens* additively and independently (Alboresi et al., 2010; Gerotto et al., 2012). However until now only few information is available about their biochemical and structural properties as they are membrane proteins and present in little amounts with respect to other LHC proteins, properties that makes their purification from thylakoids extremely difficult. These data are important to better describe LHCSR structure and therefore mechanism of action. In this work we proposed a strategy to isolate LHC-like proteins in their native state overcoming the limitations of the traditional protocol of expression of LHC as apoprotein following refolding *in vitro* with pigments (Giuffra et al., 1996; Pagano et al., 1998). Indeed, we have exploited the possibility of expression of LHCSR1 protein in an heterologous system like *Nicotiana benthamiana* plants synthesizing both chlorophyll a and b and carotenoids and able to correctly fold antenna protein–pigment complexes. Furthermore LHCSR1 has been expressed with a Histidine tail at its C-terminus allowing LHCSR1 purification using milder conditions than previously required for preparation of native complexes, mitigating potential pigment loss.

By applying this strategy LHCSR1 was correctly expressed as folded protein in thylakoids membrane of *N.benthamiana* leaves at the fourth day post agroinfiltration. The level of accumulation is similar to that of LHCSR1 *P.patens* thylakoids, suggesting that there are limitations due to the size of the compartment where the protein accumulates. LHCSR1 was purified in native state from *N.benthamiana* thylakoids using a milder procedure taking advantages of the His-Tag sequence. This allowed allowing description of its light absorption and pigment binding properties. As previously reported also for LHCSR3 proteins reconstituted *in vitro* with pigments (Bonente et al., 2011a). Even if the possibility of dimeric aggregation state has been reported for LHCa1/4 (Schmid et al., 1997) and for LHSCR3 protein (Bonente et al., 2011) LHCSR1 with histidine tail migrate as monomeric LHC protein in native gel confirming the previously observation reported for *P.patens* (Pinnola et al., 2013). LHCSR1 form a stable and specific complex with Chls and xanthophylls chromophores as demonstrated by the spectral shift induced by pigments-protein interaction, by the capacity for excitation energy transfer from Chl b and xanthophylls to Chl a and by the strong optical activity. All these data clearly indicates the goodness of milder purification procedure using affinity column allowing purification of protein that retain all pigments as previously reported for CP24 protein (Passarini et al., 2014). Starting from the conservation of six pigment binding residues with respect to the other LHC protein members and considering the stoichiometry of six Chls per LHCSR3 apoprotein (Bonente et al., 2011a). On this basis, LHCSR1 has a very high Chl a/b ratio with a Chl b complement slightly below one per polypeptide. This low level of Chl b per polypeptide is consistent with Chl b composition of LHCSR3 (Bonente et al., 2011a) and with the finding of *Lhcsr* orthologs in diatoms which totally lack of Chl b (Zhu and Green, 2010).

Furthermore, HPLC analysis revealed that LHCSR1 binds only lutein and violaxanthin while neoxanthin, the major component of LHCb proteins, is absent according to its role in ROS scavenging and not in qE (Dall'Osto et al., 2007). Based on hypothesis of six Chls per polypeptide, it is possible to propose the binding of three xanthophylls per polypeptide. Base on the conservation of localization with other LHC proteins, Lutein and violaxanthin are likely to bind to L1 and L2 binding sites, respectively, while the additional xanthophyll ligand is probably bound to a third V1-like site.

Even if LHCSR1 from *N.benthamiana* has been isolated in its epoxidated state, it can bind zeaxanthin in the L2 site as reported for other monomeric LHCb proteins (Morosinotto et al., 2003) . This binding is likely to induce allosteric conformational changes leading to a new chromophore–chromophore interaction favouring the formation of intramolecular quenching sites and the reorganization of PSII supercomplex (Ahn, 2008; Ruban et al., 2007; Betterle et al., 2010). As recently shown, LHCSR1 protein in *P. patens* is able to bind zeaxanthin upon excess light stress and this bound is strictly necessary to induce qE (Pinnola et al., 2013) different from the case of LHCSR3 from *C.reinhardtii* (Bonente et al., 2011).

The differential behaviour of zeaxanthin in activating LHCSR depicts an evolutionary scenario according to which from an aquatic unicellular free-living organism, to a plant pioneering colonization to the sub aerial environment, distinct photoprotection mechanisms became integrated through the involvement of zeaxanthin in activation of NPQ.

Overall the data obtained suggest that *N.benthamiana* could represent a good choice for clarify biochemical and structural properties of LHCSR1 protein. The use of *N.benthamiana* as heterelogous system could overcome limitation on biomass accumulation for protein purification while the utilization of the His-tag for purification allowed for milder conditions mitigating potential pigment loss. .

Conclusion

It is shown that *N.benthamiana* could be considered a good alternative for the production of heterologous LHC proteins. In particular, the possibility of expressing LHCSR1 protein from *P.patens* in *N.benthamiana* leaves was demonstrated. Moreover, LHCSR1 carrying and histidine tail could be easily purified directly from thylakoids where it is expressed as a monomeric pigment-binding protein. Spectroscopic and HPLC analysis shown that LHSR1 is correctly folded with pigments as demonstrated by the spectral shift induced by pigments-protein interaction, by the capacity for excitation energy transfer by the strong optical activity.

Materials and methods

Construction of vector for plant expression

P.patens protonemal cDNA has been extracted (Allen et al., 2007) and used as a template to construct the pENTR™/D-TOPO based vector. Lhcsr1 gene was amplified using the following primers: the forward primer 5'-CACCCTCGCTCTGCAACTTTCCTTT-3' and the reverse primer 5-TCAGTGGTGGTGATGATGATGGCTGCCGCGCGGCACCAGCAGGCCCAATCTCTTGAACAA-3' which harbour a sequence coding for 6 histidine tail and a thrombin claveage site. The pENTR.LHCSR1 vector obtained was used for LR recombination reactions with the GATEWAY destination vector pK7WG2, generating the final vector pK7WG2.LHCSR1-HisTag.

Agroinfiltration of *N.benthamiana* leaves

The vector pK7WG2.LHCSR1 was transferred in *A.tumefaciens* strain which was used for *N. benthamiana* agroinfiltration. Bacterial suspension in infiltration buffer (10 mM MES, 10 mM $MgCl_2$, 100 µM acetosyringone , pH 5,6) was use for syringe infiltration of 5-6 weeks-old *N.benthamiana* plants, 5 leaves were infiltrated for each plants. The recombinant protein time-course accumulation of LHCSR1 protein has been estimated by immunoblotting on total protein extract starting from disc of infected leaves collected for 7 days after agroinfiltration and frozen in liquid nitrogen immediately after harvesting. Discs were all grinded directly in Loading Buffer (LB; Tris pH 6,8, 10% glycerol, 2% SDS and 3% β-mercaptoethanol) just before SDS-PAGE analysis.

Thylakoid extraction and purification of LHCSR1 protein

Thylakoids were purified from *N.benthamiana* leaves following a protocol for seed plants with minor modifications. Leaves were harvested and homogenized in extraction buffer (0.5% milk powder, 0.4 M NaCl, 0.02 M Tricine-KOH, pH 7.8, and 0.005M e -aminocaproic acid, 0.001 phenyl-methylsulfonyl fl uoride and 0.001 benzamidine as protease inhibitors). After filtration, samples were precipitated by centrifugation at 1500g for 15 min at 4°C and then resuspended in hypotonic buffer (0.15 M NaCl, 0.005 M $MgCl_2$, 0.02 M Tricine-KOH, pH 7.8, and protease inhibitor). After centrifugation for 10 min at 10,000g at 4°C, thylakoids were resuspended in a buffer containing 0.4 M sorbitol, 0.015 M NaCl, 0.005 M $MgCl_2$, and 0.01 M HEPES-KOH, pH 7.5. All this procedure was done in the dark at 4°C. Finally, thylakoids were either used directly or frozen in liquid nitrogen and stored at – 80°C until use.

Thylakoids were washed with 5 mM EDTA and resuspended at a final concentration of 1 mg/ml in 10 mM Hepes, pH 7,5. Samples were then solubilised at a final concentration of 0,5 mg/ml adding 2% α-DM and 10 mM Hepes, pH 7,5 and vortexing for 1 min. After 10 min of ice incubation, thylakoids membranes were centrifuged at 15.000 g for 10 min to eliminate unsolubilized materials. Solubilized material was loaded

onto a Ni^{2+}-NTA agarose column (GE healthcare) previously equilibrated with buffer A containing 10 mM Hepes pH 7,5, 0,15 mM NaCl, 0,03% α-DM and 10 mM Imidazole. After several washing steps with buffer A supply with increasing concentration of Imidazole (25 and 50 mM), LHCSR1 was eluted using 250 mM Imidazole in buffer A.

SDS-PAGE and immunoblotting analysis

SDS-PAGE analyses were performed as described by Laemmli (1970) An acrylamide/bis-acrylamide ratio of 75: 1 and a total concentration of acrylamide of 4.5 and 15% was used respectively, for stacking and running gel. Urea (6 M) was also added into the running gel. Polypeptides, following SDS-PAGE, were transferred onto an Immobilon PVDF membrane (Millipore) using a Mini Trans-Blot cell (Bio-Rad) and detected by commercial monoclonal antibodies

Deriphat-PAGE

Non-denaturating Deriphat-PAGE was performed using 3.5% (w/v) acrylamide (38:1 acrylamide/bisacrylamide) in the stacking gel and in the resolving gel and an acrylamide concentration gradient from 4.5 to 11.5% (w/v) stabilized by a glycerol gradient from 8 to 16%. Thylakoids concentrated at 1 mg/mL chlorophyll were solubilized with a final 0.8% α-DM, and 60 mg of chlorophyll were loaded in each lane.

Spectroscopy

Samples collected from the sucrose gradients were analyzed by SLM-Aminco DW-2000 spectrophotometer at room temperature collecting absorption measurements. CD spectra were obtained with a Jasco J-600 spectropolarimeter with scan rate of 200 nm/min. Fluorescence spectra were obtained at room temperature with a Fluoromax 3 fluorometer (Horiba Jobin Yvon)

Pigment analysis

Pigments were extracted and then separated and quantified by HPLC as previously described (Gilmore and Yamamoto, 1991). Chl a/b and Chl/Car ratios were corrected through fitting analysis of the absorption spectrum.

References

Ahn, T.K. (2008). Architecture of a charge-transfer state regulating light harvesting in a plant antenna protein. Science (80-.).

Alboresi, A., Gerotto, C., Giacometti, G.M., Bassi, R., and Morosinotto, T. (2010). Physcomitrella patens mutants affected on heat dissipation clarify the evolution of photoprotection mechanisms upon land colonization. Proc. Natl. Acad. Sci. U. S. A.

Allen, G.C., Flores-vergara, M.A., Krasnyanski, S., Kumar, S., and Thompson, W.F. (2007). A modified protocol for rapid DNA isolation from plant tissues using cetyltrimethylammonium bromide. **1**: 2320–2326.

Ballottari, M., Girardon, J., Dall'osto, L., and Bassi, R. (2012). Evolution and functional properties of photosystem II light harvesting complexes in eukaryotes. Biochim. Biophys. Acta **1817**: 143–57.

Bellafiore, S., Barneche, F., Peltier, G., and Rochaix, J.-D. (2005). State transitions and light adaptation require chloroplast thylakoid protein kinase STN7. Nature **433**: 892–895.

Betterle, N., Ballottari, M., Hienerwadel, R., Dall'Osto, L., and Bassi, R. (2010). Dynamics of zeaxanthin binding to the photosystem II monomeric antenna protein Lhcb6 (CP24) and modulation of its photoprotection properties. Arch. Biochem. Biophys. **504**: 67–77.

Bonente, G., Ballottari, M., Truong, T.B., Morosinotto, T., Ahn, T.K., Fleming, G.R., Niyogi, K.K., and Bassi, R. (2011a). Analysis of LhcSR3, a protein essential for feedback de-excitation in the green alga Chlamydomonas reinhardtii. PLoS Biol. **9**: e1000577.

Bonente, G., Ballottari, M., Truong, T.B., Morosinotto, T., Ahn, T.K., Fleming, G.R., Niyogi, K.K., and Bassi, R. (2011b). Analysis of LhcSR3, a protein essential for feedback de-excitation in the green alga Chlamydomonas reinhardtii. PLoS Biol. **9**: e1000577.

Caffarri, S., Croce, R., Breton, J., and Bassi, R. (2001). The Major Antenna Complex of Photosystem II Has a Xanthophyll Binding Site Not Involved in Light Harvesting. J. Biol. Chem. **276**: 35924–35933.

Dainese, P. and Bassi, R. (1991). System and Aggregation State of the Component Chlorophyll u / b.: 8136–8142.

Dall'Osto, L., Cazzaniga, S., North, H., Marion-Poll, A., and Bassi, R. (2007). The Arabidopsis aba4-1 mutant reveals a specific function for neoxanthin in protection against photooxidative stress. Plant Cell **19**: 1048–1064.

Dall'Osto, L.C. (2005). A Mechanism of Nonphotochemical Energy Dissipation , Independent from PsbS , Revealed by a Conformational Change in the Antenna Protein CP26. **17**: 1217–1232.

Demmig-Adams, B. et al (1996). demmig-adam 1996.pdf.

Flachmann, R. and Kühlbrandt, W. (1996). Crystallization and identification of an assembly defect of recombinant antenna complexes produced in transgenic tobacco plants. Proc. Natl. Acad. Sci. U. S. A. **93**: 14966–14971.

Georgakopoulou, S., van der Zwan, G., Bassi, R., van Grondelle, R., van Amerongen, H., and Croce, R. (2007). Understanding the changes in the circular dichroism of light harvesting complex II upon varying its pigment composition and organization. Biochemistry **46**: 4745–54.

Gerotto, C., Alboresi, A., Giacometti, G.M., Bassi, R., and Morosinotto, T. (2012). Coexistence of plant and algal energy dissipation mechanisms in the moss Physcomitrella patens. New Phytol.: 763–773.

Gilmore, A.M. and Yamamoto, H.Y. (1991). Zeaxanthin Formation and Energy-Dependent Fluorescence Quenching in Pea Chloroplasts under Artificially Mediated Linear and Cyclic Electron Transport1.: 635–643.

Giuffra, E., Cugini, D., Croce, R., Bassi, R., Verona, U., and Mm, S. (1996). Reconstitution and pigment-binding properties of recombinant CP29. Eur. J. Biochem. **120**: 112–120.

Horton, P. (2012). Optimization of light harvesting and photoprotection: molecular mechanisms and physiological consequences. Philos. Trans. R. Soc. Lond. B. Biol. Sci. **367**: 3455–65.

Jansson, S. (1999). A guide to the Lhc genes and their relatives in Arabidopsis. Trends Plant Sci. **4**: 236–240.

Kargul, J. and Barber, J. (2008). Photosynthetic acclimation: Structural reorganisation of light harvesting antenna - Role of redox-dependent phosphorylation of major and minor chlorophyll a/b binding proteins. FEBS J. **275**: 1056–1068.

Kovács, L., Damkjaer, J., Kereïche, S., Ilioaia, C., Ruban, A. V, Boekema, E.J., Jansson, S., and Horton, P. (2006). Lack of the light-harvesting complex CP24 affects the structure and function of the grana membranes of higher plant chloroplasts. Plant Cell **18**: 3106–3120.

Kühlbrandt, W., Wang, D.N., and Fujiyoshi, Y. (1994). Atomic model of plant light-harvesting complex by electron crystallography. Nature **367**: 614–621.

Morosinotto, T., Caffarri, S., Dall, L., and Bassi, R. (2003). Mechanistic aspects of the xanthophyll dynamics in higher plant thylakoids.: 347–354.

Niyogi, K.K. (2000). Safety valves for photosynthesis.: 455–460.

Pagano, A., Cinque, G., and Bassi, R. (1998). In Vitro Reconstitution of the Recombinant Photosystem II Light-harvesting Complex CP24 and Its Spectroscopic Characterization *. **273**: 17154–17165.

Passarini, F., Xu, P., Caffarri, S., Hille, J., and Croce, R. (2014). Towards in vivo mutation analysis: Knock-out of specific chlorophylls bound to the light-harvesting complexes of Arabidopsis thaliana - The case of CP24 (Lhcb6). Biochim. Biophys. Acta - Bioenerg. **1837**: 1500–1506.

Paulsen, H., Finkenzeller, B., and Kühlein, N. (1993). Pigments induce folding of light-harvesting chlorophyll a/b-binding protein. Eur. J. Biochem. **215**: 809–816.

Peers, G., Truong, T.B., Ostendorf, E., Busch, A., Elrad, D., Grossman, A.R., Hippler, M., and Niyogi, K.K. (2009). An ancient light-harvesting protein is critical for the regulation of algal photosynthesis. Nature **462**: 518–21.

Pinnola, A., Dall'Osto, L., Gerotto, C., Morosinotto, T., Bassi, R., and Alboresi, A. (2013). Zeaxanthin binds to light-harvesting complex stress-related protein to enhance nonphotochemical quenching in Physcomitrella patens. Plant Cell **25**: 3519–34.

Ruban, a. V., Lee, P.J., Wentworth, M., Young, a. J., and Horton, P. (1999). Determination of the Stoichiometry and Strength of Binding of Xanthophylls to the Photosystem II Light Harvesting Complexes. J. Biol. Chem. **274**: 10458–10465.

Ruban, A. V, Berera, R., Ilioaia, C., van Stokkum, I.H.M., Kennis, J.T.M., Pascal, A. a, van Amerongen, H., Robert, B., Horton, P., and van Grondelle, R. (2007). Identification of a mechanism of photoprotective energy dissipation in higher plants. Nature **450**: 575–578.

Sandonà, D., Croce, R., Pagano, A., Crimi, M., and Bassi, R. (1998). Higher plants light harvesting proteins. Structure and function as revealed by mutation analysis of either protein or chromophore moieties. Biochim. Biophys. Acta - Bioenerg. **1365**: 207–214.

Schmid, V.H., Cammarata, K. V, Bruns, B.U., and Schmidt, G.W. (1997). In vitro reconstitution of the photosystem I light-harvesting complex LHCI-730: heterodimerization is required for antenna pigment organization. Proc. Natl. Acad. Sci. U. S. A. **94**: 7667–7672.

Standfuss, J., Terwisscha van Scheltinga, A.C., Lamborghini, M., and Kühlbrandt, W. (2005). Mechanisms of photoprotection and nonphotochemical quenching in pea light-harvesting complex at 2.5 A resolution. EMBO J. **24**: 919–928.

Zhu, S.H. and Green, B.R. (2010). Photoprotection in the diatom Thalassiosira pseudonana: Role of LI818-like proteins in response to high light stress. Biochim. Biophys. Acta - Bioenerg. **1797**: 1449–1457.

Conclusions

This PhD thesis has been devoted to the optimization of different expression systems for different bio-products like nanoparticles and recombinant proteins.

In the first part of this thesis a prokaryotic system has been used for its natural capacity to produce magnetic nanoparticles called magnetosomes, developing biochemical system for its purification and testing its possible application as magnetic nanoparticles for diagnosis and therapy. Indeed recently attention has been devoted to multifunctional nanostructured magnetic particles as suitable compounds for biomedical application. Taking advantages of the physical phenomenon of superparamagnetism, magnetic nanoparticles are nowadays largely adopted in magnetic hyperthermia of tumour as a small quantity of magnetic nanoparticles delivered to tumours is able to release heat upon the application of a suitable alternate magnetic field in the range 100-500 KHz. By such heat the cancer cells are brought up to 40-45°C and partially destroyed, an event that requires combining chemo- or radioing therapy to MFH. Among materials used for hyperthermia tumour treatment magnetic nanoparticles, called magnetosomes, gestated by bacteria are arising curiosity. Magnetosomes nanoparticles (MNs) are naturally synthesized by bacteria as iron oxide nanoparticles (size range 35-50 nm) organized in long chains which are used as compass to move in water sediments. Magnetosome mineral crystal have high chemical purity, narrow size ranges, species-specific crystal morphologies and exhibit specific arrangements within the cell indicating that the formation of magnetosomes by magnetotactic bacteria is under precise biological control and is mediated by a mineralization process. Furthermore magnetosome crystals are surrounded by a phospholipidic membrane which allows the system to be biocompatible giving also the possibility to penetrate within the tumour cells heating them up from inside.

In this thesis magnetosomes nanoparticles extracted from *Magnetospirillum gryphiswaldense* in shape of long chain has been tested for their interaction with cellular elements and anti-neoplastic activity both *in vitro* and *in vivo*, with the aim of developing new thermo-therapeutic agents. Magnetosomes were tested against two different neoplastic cell lines demonstrating that:

a. **Magnetosomes could be considered a nanostructured material suitable for theranostics.**

   From structural analysis, it has been verified that magnetosomes magnetic cores are composed by magnetite single crystals arranged in chains and coated with a phospholipid membrane. The oxide phase is stable over months thanks to the shielding effect of the membrane. This was confirmed by the magnetic measurements, which showed an evident and stable Verwey transition around 105 K. Due to the particles size, the blocking temperature is above 300 K.

   The great potentiality of MNs as mediators for magnetic fluid hyperthermia was verified: the specific absorption rate (SAR) obtained after the application of an alternate magnetic field is 482.7

W/g, among the highest reported in literature. The NMRD profiles, acquired for MNs dispersed both in agarose gel and water, demonstrated good contrast efficiency as negative MRI contrast agents. This work has been submitted to Contrast media and molecular imaging journal.

b. Magnetosomes nanoparticles increase the efficacy of thermotherapy against colon carcinoma.

Magnetosomes were efficiently purified from bacteria as long chain and tested in vitro for their detectable increasing of temperature by exposing to an alternate magnetic field. In vivo analysis demonstrated that magnetosomes injected in living tissue are easily detectable in living tissue due to their iron content suggesting a possible use of these nanoparticles as negative contrast agents in magnetic resonance imaging. Finally it has been demonstrated the possibility of using magnetosomes as thermo-therapeutic agents against colon carcinoma cells for which even if we did not observe a reduction of tumor mass, areas of fibrosis and necrosis were visible at microscopic level. This work has been published in Plos One Vol

c. Magnetosomes inhibits the growth of a xenograft model of glioblastoma

Magnetosomes purified as previously reported were tested in vivo against glioblastoma model applying a method minimally invasive. Also in this case magnetosomes purified from bacteria were delivered by intratumoural injection remaining within the tumour masses for the whole period of treatment with alternate magnetic field. Even if the hyperthermic temperature gained by magnetosomes in the tumor was lower compared to values commonly reported in the literature, a marked reduction of tumors growing was observed. The progressive disappearance of the tumor has been also recorded in two mice during the treatment, with mild signs of burn on the skin and more severe effects in the core portion of tumor, caused by thermal energy release.

All these data demonstrated that magnetosomes nanoparticles lead to a distinct reduction in tumor growing with significant therapeutic effects.

In the second part of this PhD thesis I focused my attention on the use of plant eukaryotic systems for expression of LHCSR protein, which have a crucial role for the regulation of photoprotection in eukaryotic photosynthetic organisms such as plant and algae. This protein is involved in thermal dissipation of excited chlorophyll singlet states ($^1Chl^*$) a faster mechanism of protection, activated upon exposure to excess light. LHCSR is LHC-like membrane proteins present in small amount in thylakoid membranes. LHCSR has been found in many algae taxa, such as brown and green algae but not in vascular plants..

Until now information on thise protein is are still scarce as it is present in small amount in thylakoids membrane and are to the difficult to purify in native state. In order to to shed light on LHCSR1 biochemical

and spectroscopic properties a heterelogous expression of LHCSR1 in *Nicotiana tabacum* and *Nicotiana benthamiana* was established reaching the following results*:*

a. **Heterologous expression of *P.patens* LHCSR1 protein in *N.tabacum* and *N.benthamiana*.**

LHSCR1 was expressed as a mature LHC protein in thylakoid membranes of both expression systems. Applying a non-denaturing Deriphat gel system LHCSR1 has been purified in its native state. Spectral properties of native LHCSR1 fit those previously reported for recombinant *C. reinhardtii* and CD spectra confirm that LHCSR1 isolated is correctly well folded with pigments. LHCSR1 pigment composition has been described indicating that LHCSR1 is characterized for a high Chl a/b ratio and no neoxanthin-binding capacities. Furthermore *in vitro* de-epoxidation confirms that LHCSR1 is able to bind zeaxanthin. Finally the positive correlation of LHCSR1 accumulation and NPQ maximum reported for *N.tabacum* plants suggest that the protein is fully able to induce NPQ.

b. Purification of LHCSR1 protein from *N.benthamiana* thyalkoid membranes.

It is shown that *N.benthamiana* could be considered a good alternative for the production of heterologous LHC proteins. In particular, the possibility of expressing LHCSR1 protein from *P.patens* in *N.benthamiana* leaves was demonstrated . Moreover, LHCSR1 carrying and histidine tail could be easily purified directly from thylakoids where it is expressed as a monomeric pigment-binding protein. Spectroscopic and HPLC analysis shown that LHSR1 is correctly folded with pigments as demonstrated by the spectral shift induced by pigments-protein interaction, by the capacity for excitation energy transfer and by the strong optical activity.

Glossary

AMF (Alternate magnetic field) : a continuous electric current that periodically reverses direction usually sinusoidally.

DLS (Dynamic light scattering) : Dynamic light scattering (also known as photon correlation spectroscopy or quasi-elastic light scattering) is a technique in physics that can be used to determine the size distribution profile of small particles in suspension or polymers in solution.

HT-29 cell line: Human colorectal adenocarcinoma cell line with epithelial morphology. These cells are sensitive to the chemotherapeutic drugs 5-fluorouracil and oxaliplatin, which are standard treatment options for colorectal cancer. In addition to being a xenograft tumor model for colorectal cancer, the HT-29 cell line is also used as an *in-vitro* model to study absorption, transport, and secretion by intestinal cells. Under standard culture conditions, these cells grow as a non polarized, undifferentiated multilayer.

Mam proteins: magnetosome membrane proteins assigned a letter in the order of their discovery or a number referring to their apparent molecular mass (e.g., MamA, Mms6). All magnetosome membrane proteins belong to characteristic protein families, which include TPR (tetratricopeptide repeat) proteins (MamA), CDF (cation diffusion facilitators) transporters (MamB and MamM), HtrA-like serine proteases (MamE, P, O), Actin-like proteins (MamK), generic transporters (MamH,N), and MTB-specific proteins with no homology to other proteins in nonmagnetic organisms (MamG, F, D, C, J, W, X, Y, Mms6, MmeA, MtxA)

MFH (magnetic fluid hyperthermia): Magnetic hyperthermia is the name given to an experimental cancer treatment, although it has also been investigated for the treatment of other ailments, such as bacterial infections. It is based on the fact that magnetic nanoparticles, when subjected to an alternating magnetic field, produce heat. As a consequence, if magnetic nanoparticles are put inside a tumor and the whole patient is placed in an alternating magnetic field of well-chosen amplitude and frequency, the tumor temperature would rise.

MRI (magnetic resonance imaging): Magnetic resonance imaging (MRI), nuclear magnetic resonance imaging (NMRI), or magnetic resonance tomography (MRT) is a medical imaging technique used in radiology to investigate the anatomy and physiology of the body in both health and disease. MRI scanners use strong magnetic fields and radio waves to form images of the body. MRI involves imaging of the proton, the positively charged spinning nucleus of hydrogen atoms that are abundant in tissues containing water, lipids, proteins and other macromolecules. Because of its spin and charge a proton has a minute magnetic field and assume an alignment respect the magnetic field. When radiofrequency energy at the appropriate frequency is applied (called the Larmor frequency) protons aligned with the magnetic field absorb the energy and reverse its direction. The protons release the absorbed energy and relax back to the original alignment. During this process of relaxation the photons produce a voltage in a radio antenna that surrounds the patient body.

MTT test: The MTT assay is a colorimetric assay for assessing cell viability. NAD(P)H-dependent cellular oxidoreductase enzymes may, under defined conditions, reflect the number of viable cells present. These enzymes are capable of reducing the tetrazolium dye MTT 3-(4,5-dimethylthiazol-2-yl)-2,5-diphenyltetrazolium bromide to its insoluble formazan , which has a purple color. Tetrazolium dye assays can also be used to measure cytotoxicity (loss of viable cells) or cytostatic activity (shift from proliferation to quiescence) of potential medicinal agents and toxic materials. MTT assays are usually done in the dark since the MTT reagent is sensitive to light.

TEM (Transmission electron microscopy) : Transmission electron microscopy (TEM) is a microscopy technique in which a beam of electrons is transmitted through an ultra-thin specimen, interacting with the specimen as it passes through. An image is formed from the interaction of the electrons transmitted through

the specimen; the image is magnified and focused onto an imaging device, such as a fluorescent screen, on a layer of photographic film, or to be detected by a sensor such as a CCD camera. TEM is used to examine fine detail—even as small as a single column of atoms, which is thousands of times smaller than the smallest resolvable object in a light microscope. TEM forms a major analysis method in a range of scientific fields, in both physical and biological sciences. TEMs find application in cancer research, virology, materials science as well as pollution, nanotechnology, and semiconductor research.

T1 and T2 relaxation time: the term relaxation describes how signals change with time. In general signals deteriorate with time, becoming weaker and broader. The deterioration of an NMR signal is analyzed in terms of two separate processes, each with their own time constants. One process, associated with T_1, is responsible for the loss of signal intensity. The other process, associated with T_2, is responsible for the broadening of the signal. Stated more formally, T_1 is the time constant for the physical processes responsible for the relaxation of the components of the nuclear spin magnetization vector **M** parallel to the external magnetic field, $\mathbf{B}_0$ (which is conventionally oriented along the *z* axis). T_2 relaxation affects the components of **M** perpendicular to $\mathbf{B}_0$.

Prussian blue staining: a stain employing acid potassium ferrocyanide to demonstrate iron presence in histological section. Ferric iron deposits in tissue (present mostly as ferric iron within the storage protein ferritin) then react with the soluble ferrocyanide in the stain, to form insoluble Prussian blue dye (a complex hydrated ferric ferrocyanide substance) *in situ*. They are then visualizable microscopically as blue or purple deposits, within cells.

SAR (specific absorption rate): it a measure of the rate at which energy is absorbed by the human body when exposed to a radio frequency (RF) electromagnetic field; although, it can also refer to absorption of other forms of energy by tissue, including ultrasound. It is defined as the power absorbed per mass of tissue and has units of watts per kilogram (W/kg).

U87mg cell line: U87 is a human primary glioblastoma cell line formally known as U-87 MG. It has epithelial morphology, and was obtained from a stage four 44 year-old cancer patient. U87MG cell line is known to have a highly aberrant genomic structure based on karyotyping .

Verwey transition: a Verwey transition is classified today, in recognition of Verwey's pioneering work on the prototype of this class of transitions, first observed in magnetite (Fe3O4), as the occurrence of a spontaneous, inter correlated change of both lattice symmetry and electric conductivity in certain ionic crystals. Typically, such an abrupt change of crystallographic structure at a critical temperature, in Fe_3O_4 near Tv ~125 K, is accompanied by further anomalies in a series of related parameters controlling the magnetic, thermodynamic, electric and mechanical interactions in the solid.

X-ray microanalysis: an analytical technique used for the elemental analysis or chemical characterization of a sample. It relies on an interaction of some source of X-ray excitation and a sample. Its characterization capabilities are due in large part to the fundamental principle that each element has a unique atomic structure allowing unique set of peaks on its X-ray emission spectrum. To stimulate the emission of characteristic X-rays from a specimen, a high-energy beam of charged particles such as electrons or protons, or a beam of X-rays, is focused into the sample being studied.

Glossary

Antenna system: component of photosystems responsible for light harvesting and energy transfer to the reaction centre. For both PSI and PSII two antenna systems are present: an inner antenna system located in the core complex and a peripheral antenna system composed by LHC proteins. In particular the peripheral antenna systems are formed by LHCa and LHCb proteins for PSI and PSII respectively. Antenna systems are responsible for light harvesting and photoprotection**.**

^{1}Chl*: singlet chlorophyll excited states. This specie is formed upon light absorption or excitonic energy transfer; singlet chlorophyll excited states can decay to the ground states through several pathways: fluorescence emission, heat production, intersystem crossing or photosynthetic reactions.

^{3}Chl*: triplet chlorophyll excited states. This specie is formed through intersystem crossing from singlet chlorophyll excited states. Triplet Chl excited state is a long-lived state (~ms time scale) and thus can react with triplet oxygen, converting it to singlet oxygen ($^1O_2$), a highly reactive oxygen specie. Carotenoid have a determinant role in 3Chl* quenching .

Grana: the stacked structures formed by thylakoids.

L1: carotenoid binding site, located in the inner part of antenna proteins close to helix A. L1 site is prevalently filled by lutein in all plant species and in all LHC proteins.

L2: carotenoid binding site, located in the inner part of antenna proteins close to helix B. L2 sites is prevalently filled by lutein in LHCII trimers, while in monomeric antenna proteins L2 can be occupied by lutein, violaxanthin, neoxanthin and zeaxanthin. In LHCI and Lhcb minor complexes L2 binds the product of the xanthophyll cycle.

LHC proteins: antenna proteins of photosystem I and II responsible for light harvesting and photoprotection. They bind pigments chlorophyll a, chlorophyll b and xanthophylls. LHC proteins are encoded by nuclear genes forming a multigenic family.

LHCII: the trimeric more abundant antenna complex associated to PSII. Each trimmer is a heterotrimer composed by Lhcb1, 2, 3 subunits. Each monomer is constituted by three transmembrane and one amphypathic helices, indicated respectively as A-C and D. Each monomer binds 14 chlorophylls and 4 carotenoids.

LHCSR: it is a LHC-like protein present only in algae and moss where it is responsible for qE activation. LHCSR share with PSBS protein the ability to bind DCCD but differently it is able to bind pigments. LHCSR appears to function as both a sensor of excess light and a site of quenching.

Lumen: the soluble compartment in the chloroplast delimited by thylakoids: in the lumen protons are pumped during photosynthetic light phase, forming a transmembrane ΔpH which constitutes the force used by ATP-ase to produce ATP.

Minor complexes: monomeric antenna proteins associated to PSII. Minor complexes are composed by CP24, CP26 and CP29 antenna proteins and bind 2-3 carotenoids per molecule. These proteins are located between PSII core and the peripheral LHCII trimers.

N1: carotenoid binding site, located close to helix C of antenna proteins. N1 site is present in LHCII and it's specific for neoxanthin, even if violaxanthin or lutein binding was found therein. This binding site is stabilized by a Tyrosine residue which can form hydrogen bounds with the carotenoid therein. N1 site is also stabilized by the chlorophylls located near Helix C and D.

NPQ: Non Photochemical Quenching. It's a light-induced photoprotective process by which plants are able to rapidly dissipate the excess absorbed energy as heat. When light is absorbed in excess the photosynthetic electron transport establish a low lumenal pH, which activate the mechanisms inducing NPQ. This process could be detectable monitoring the decrease of leaf fluorescence during illumination.

Photoprotection: the whole mechanisms developed by photosynthetic organisms in order to avoid photoinhibition. Two different types of photoprotection mechanisms, depending on the time-scale of action, can be described: a) short-term photoprotective mechanisms and b) long-term photoprotective mechanisms.

PSBS: an integral membrane protein component and member of the LHC-protein superfamily, even if it doesn't bind pigments. It is fundamental for NPQ induction in plants, and in particular for the qE component. PsbS has two conserved glutamic acid exposed to the lumen) which substitution results is PsbS inactivation.

qE: the faster component of leaf fluorescence decrease due to NPQ induction; it's associated to the reduction of lumenal pH upon exposition to excess light intensity. In plants qE is strongly dependent to the presence of the PSII associated protein PSBS and from zeaxanthin accumulation. On the contrary in algae qE depends to the presence of LHCSR proteins. qE component of NPQ has relaxation time of few minutes.

Stroma lamellae: the interconnecting regions of thylakoids between grana.

Stroma: the soluble compartment of the chloroplast. In the stroma are present the enzymes involved in the dark phase of photosynthesis, that use the ATP and NADPH produced during light phase in order to produce biomass.

Thylakoids: the inner membranes of the chloroplast. . Thylakoids are organized into two membrane domains: 1) cylindrical stacked structures called grana, and 2) interconnecting regions, the stroma lamellae. Thylakoids confine a compartment called lumen: in the lumen protons are pumped during photosynthetic light phase, forming a transmembrane ΔpH which constitutes the force used by ATP-ase to produce ATP. The complexes involved into the light phase of the photosynthesis (PSI, PSII, ATP-ase, Cytochrome b6f) are located in the thylakoids membranes.

V1: carotenoid binding site, located at the peripheral part of antenna proteins LHCII. V1 site is a specific site for violaxanthin and it is involved in xanthophyll cycles product binding in LHCII.

Xanthophyll cycle: a series of enzymatic reactions by which the carotenoid violaxanthin is de-epoxidated to zeaxanthin, through the intermediate antheraxanthin. This process is catalyzed by the Violaxanthin de-epoxidase enzyme (VDE), which is activated at acid pH around 5.2. Saturation of photosynthetic reactions induce the reduction of lumenal pH is reduced by proton pumping: this event activates VDE enzyme which induces the xanthophyll cycle. Accumulation of zeaxanthin is responsible for activation of several photoprotective mechanism as NPQ, ^{3}Chl* quenching and ROS scavenging.